Inversion methods for fast-ion diagnostics in fusion plasmas

Schmidt, Bo Simmendefeldt

Publication date:
2023

Document Version
Publisher's PDF, also known as Version of record

Technical University of Denmark

A collaboration between
plasma physics and fusion energy (dtu)
swiss plasma center (epfl)

Inversion methods for fast-ion diagnostics in fusion plasmas

Ph.D. Dissertation

Bo Simmendefeldt Schmidt

Supervisors:

Professor Mirko Salewski (DTU)
Dr. Marcelo Baquero-Ruíz (EPFL)

31 May, 2023

Title:	Inversion methods for fast-ion diagnostics in fusion plasmas
Author:	Bo Simmendefeldt Schmidt
Supervisors:	Professor Mirko Salewski (DTU) Dr. Marcelo Baquero-Ruíz (EPFL)
Period:	June 2020 - May 2023
University:	Technical University of Denmark
Department:	DTU Physics, Department of Physics Plasma Physics and Fusion Energy, DTU Swiss Plasma Center, EPFL

Abstract

The present dissertation presents my Ph.D. research on inversion methods for fast-ion diagnostics in fusion plasmas. This work is part of a collaboration between the Technical University of Denmark and École Polytechnique Fédérale de Lausanne. My research focused on developing mathematical methods for solving ill-posed inverse problems in velocity-space tomography applied to synthetic and experimental data from projections of fast-ion velocities, ion cyclotron emission, and fast-ion loss detectors.

A main objective in diagnostics of fusion plasmas is to determine the fast-ion velocity-space distribution function. As part of my research, a technique called "slowing-down physics regularization" was developed to determine the fast-ion velocity-space distribution function throughout the fusion plasma from projections of velocities of the fast ions. This technique was applied to synthetic data from the TCV tokamak and the W7-X stellarator.

Extensive modelling of the physical systems is required to determine the fast-ion velocity-space distribution function. In fast-ion parlance, such models are built into a "weight function matrix". For point-wise determination of the velocities of the fast ions emitting ion cyclotron emission, 2D weight functions and reconstruction techniques using them were developed.

The ill-posed inverse problem can be solved using regularization methods. Tikhonov regularization has been the standard regularization method in velocity-space tomography for the past decade. Other regularization techniques were investigated and evaluated. In particular, algebraic iterative reconstruction techniques were applied to synthetic and experimental measurements from fast-ion loss detectors and compared with Tikhonov regularization.

When diagnosing fusion plasmas, simulations are performed to model the physical processes. Measurements from fast-ion loss detectors are simulated using a code called "FILDSIM". A raised cosine model was proposed as an alternative to the standard Gaussian model. The resulting improvements in weight functions and reconstructions were obtained for the TCV tokamak. A model based on these improvements achieves higher precision and faster calculations, making it possible to compute reconstructions of measurements from fast-ion loss detectors between repeated experiments.

In addition, neural networks were used to perform velocity-space tomography. Neural networks were trained to suggest an optimal value of the regularization parameter for Tikhonov regularization and to compute reconstructions directly from synthetic and experimental measurements from fast-ion loss detectors. The neural networks provide instantaneous reconstructions of the fast-ion velocity-space distribution function, which can supplement reconstruction methods for diagnostics of fast ions in fusion plasmas and contribute to improved control of fusion plasmas.

Resumé (Danish)

Nærværende afhandling præsenterer min ph.d.-forskning i inverse metoder til diagnostik af hurtige ioner i fusionsplasmaer. Dette arbejde er en del af et samarbejdsprojekt mellem Danmarks Tekniske Universitet og École Polytechnique Fédérale de Lausanne. Min forskning fokuserede på at udvikle matematiske metoder til at løse ikke-velformulerede inverse problemer inden for tomografi af hastighedsrum anvendt på syntetiske og eksperimentelle data fra projektioner af hastigheder af hurtige ioner, ioncyklotronsemission og detektorer af undslupne hurtige ioner.

Et hovedformål inden for diagnostik af fusionsplasmaer er at bestemme hastighedsfordelingsfunktionen af hurtige ioner. Som led i min forskning blev udviklet en metode kaldet "slowing-down physics regularization" til at bestemme fordelingsfunktionen af rum og hastigheder i hele fusionsplasmaet fra projektioner af hastigheder af de hurtige ioner. Denne metode blev anvendt på syntetiske data fra TCV-tokamakken og W7-X-stellaratoren.

For at bestemme fordelingsfunktionen af de hurtige ioner kræves omfattende modellering af de fysiske systemer. I hurtig-ion sprogbrug er sådanne modeller indbygget i en vægtfunktionsmatrix. Til punktvis bestemmelse af værdierne af hastighederne af de hurtige ioner, der udsender ioncyklotronsemission, blev udviklet 2D-vægtfunktioner samt rekonstruktionsmetoder, som anvender disse.

Det ikke-velformulerede problem kan løses ved hjælp af metoder baseret på regularisering. Tikhonov-regularisering har været standardregulariseringsmetoden inden for tomografi af hastighedsrum i det seneste årti. Andre regulariseringsmetoder blev undersøgt og vurderet. Især blev algebraiske iterative rekonstruktionsmetoder anvendt på syntetiske og eksperimentelle målinger fra detektorer af undslupne hurtige ioner, og deres fordele og ulemper blev sammenlignet med Tikhonov-regularisering.

Ved diagnostik af fusionsplasmaer udføres simuleringer til at modellere de fysiske processer. Målinger fra detektorer af undslupne hurtige ioner simuleres med en kode kaldet FILDSIM. En forhøjet cosinusfunktion blev foreslået som et alternativ til Gauss-modellen. Forbedringer i vægtfunktioner og rekonstruktioner blev opnået for TCV-tokamakken. Med modellen baseret på disse forbedringer opnås højere præcision og hurtigere beregninger, hvilket gør det muligt at bestemme rekonstruktioner af målinger fra detektorer af undslupne hurtige ioner mellem gentagne eksperimenter.

Desuden blev neurale netværk anvendt til at udføre tomografi af hastighedsrum. Neurale netværk blev trænet til at foreslå en optimal værdi af regulariseringsparameteren til Tikhonov-regularisering og til at beregne tomografiske rekonstruktioner direkte fra syntetiske og eksperimentelle målinger fra detektorer af undslupne hurtige ioner. Herved opnås øjeblikkelige bestemmelser af hastighedsfordelingsfunktionen af hurtige ioner, hvilket kan væsentligt supplere inverse metoder til diagnostik af hurtige ioner i fusionsplasmaer samt bidrage til forbedret kontrol af fusionsplasmaer.

Acknowledgements

The presented achievements would have been unattainable without the support and guidance of a number of individuals to whom I owe a great debt of gratitude.

I am deeply indebted to my supervisor at the Technical University of Denmark, Professor Mirko Salewski, who has been a source of unwavering encouragement throughout my Ph.D. His faith in my abilities and his willingness to allow me to pursue the directions I found most interesting have fostered a unique environment of exploration and research. His insights, attention to details, and patience have been invaluable in my development as a physicist. I hope our collaboration will continue.

Also, I express my sincere gratitude to my supervisor Dr. Marcelo Baquero-Ruíz at the Swiss Plasma Center at École Polytechnique Fédérale de Lausanne. His pivotal role in smoothly integrating me into the research group, combined with his mentorship and guidance, has shaped my academic trajectory and personal development.

I would also like to extend my gratitude to my colleagues, particularly the members of the fast ion group at the Plasma Physics and Fusion Energy section at DTU and the fast ion diagnostic group at the Swiss Plasma Center at EPFL. Their camaraderie, intellectual contributions, and spirit of collaboration have enriched my doctoral experience.

Contents

Chapter 1

Introduction

This Ph.D. dissertation contributes to nuclear fusion research aimed at making fusion energy a viable energy source. The current climate crisis and the world's increasing energy demand are two major motivational factors. These two problems are briefly addressed, illustrating how fusion energy can contribute to the solution.

1.1 General remarks

Alternative energy sources to fossil fuels are in high demand. According to the International Energy Agency, the year 2021 added a record renewable electricity of 290 GW, and projected acceleration of electricity production from solar panels, wind turbines, and other renewables.[1] Additionally, according to the International Labour Organisation, jobs related to renewable energy will grow despite multiple crises.[2] The current alternative energy sources can only operate intermittently, and battery storage is insufficient.[3] One alternative energy source to fossil energy that can provide a continuous energy supply is fusion energy. Fusion reactions, such as those occurring in the Sun, release energy due to the mass defect of the products relative to the reactants.[4] This energy release occurs for all fusion reactions for which the products have higher mass numbers A than the reactants and when the mass numbers satisfy $A \leq 62$.[5] Since the 1950s, fusion research has investigated ways to harness the energy of fusion reactions.[6] While the Sun achieves its thermonuclear fusion through gravitation, the two current approaches to achieving controlled fusion energy on Earth are magnetic and inertial confinement fusion.

1.2 Global warming

Numerous scientific associations including the American Physical Society, the U.S. Global Change Research Program, the American Geophysical Union, and the Intergovernmental Panel on Climate

[1] IEA (2021).
[2] ILO (2022).
[3] Cf. Section 1.3.
[4] The *pp* chain in the Sun can be summarized by the reaction

$$4H \rightarrow {}^{4}\mathrm{He} + 2e^{+} + 2\nu_e. \tag{1.1}$$

See, e.g., Adelberger et al. (2011).
[5] The nucleus with the highest mean binding energy per nucleon is ^{62}Ni, not ^{56}Fe as typically stated; see Sree Harsha (2018), p. 1.
[6] ITER (2014).

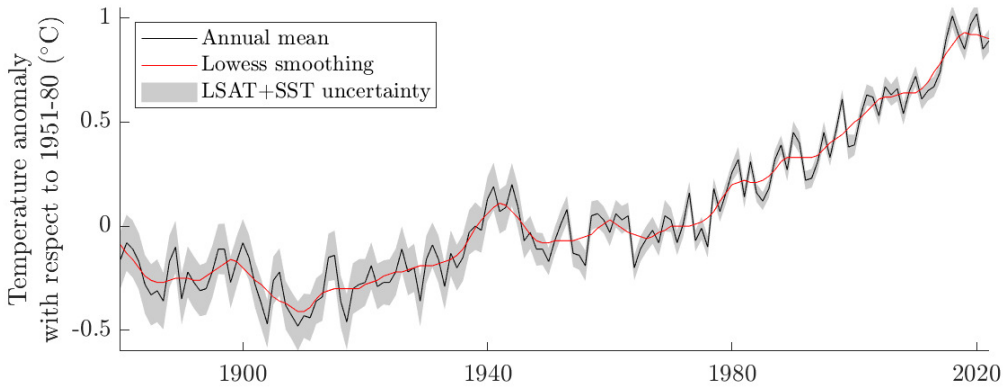

Figure 1.1: Temperature index for the land and ocean from 1880 to 2022. The base period is 1951-1980. The red line is obtained using locally weighted scatterplot smoothing (lowess). The gray shading represents the total land surface air temperature (LSAT) and sea surface temperature (SST) annual uncertainty at a 95% confidence interval.
Source: GISS, Global Annual Mean Surface Air Temperature Change dataset.[16]

Change (IPCC), have issued statements on the critical issue of Earth's changing climate and the significant evidence for the change being due to anthropogenic activities.[7] IPCC, comprising more than 1,000 independent scientific experts from countries all over the world, concluded in its Fifth Assessment Report[8] that there is a probability of more than 95% that the current climate change is the result of human activities over the last 50 years. Further, out of 1,372 climate researchers, 97% support the tenets of anthropogenic climate change outlined by the IPCC.[9]

Measurements from ice cores, rocks, tree rings, and from satellites all indicate a changing climate.[10] Greenland and Antarctica are losing ice masses on average of more than a hundred billion tonnes per year,[11] the global sea level rises much faster, and the rate is increasing with a probability of less than 1% that the acceleration is zero,[12] each major ocean basin has warmed at nearly all latitudes,[13] and the global temperature is rising, with the past nine years being the warmest years since recordkeeping began in 1880; see Fig. 1.1.[14] Earth is now about 1.1 °C warmer than the late 19th century average.[15]

The primary reason for global warming is human emission of greenhouse gases into the atmosphere, intensifying the greenhouse effect,[17] with carbon dioxide emission being the highest on record in 2022.[18] For the last 800,000 years, the carbon dioxide level has never been above approximately 300 ppm, whereas the current level (2022) is close to 420 ppm.[19] Further, the correlation between the atmospheric carbon dioxide concentration and Earth's surface temperature

[7] See, e.g., APS (2007), Reidmiller et al. (2018), AGU (2019), and IPCC (2022).
[8] IPCC (2022).
[9] Anderegg et al. (2010).
[10] NASA (2023a)
[11] Velicogna et al. (2020).
[12] Nerem et al. (2018).
[13] Levitus et al. (2012).
[14] NASA (2023c).
[15] NASA (2023c).
[16] Team (2023).
[17] NASA (2023c).
[18] Friedlingstein et al. (2022).
[19] Earth System Research Laboratories (2023).

has been well-documented for the last 60 million years.[20]

The primary culprit for the increased atmospheric carbon dioxide levels is the burning of fossil fuels such as coal and oil, where the burning process combines carbon from the fuel with oxygen in the atmosphere to make CO_2.[21] Other industrial processes, such as the production of cement, also contribute.[22] The increased CO_2 levels can be seen to be a result of human activity due to the isotopic fingerprint left by the carbon from fossil fuels.[23] Data also shows that the variation in the Sun's irradiance is not the cause of global warming.[24]

1.3 The need for energy

Global energy consumption has increased drastically since the beginning of the Industrial Revolution dominated by exploration of coal and iron in mid-18th century Great Britain.[25] This increase in demand is mainly due to economic and technological developments and a rising population.[26] Projections from the International Energy Agency (IEA) include increased use of renewable energy sources, improved energy efficiency, and a shift toward electric vehicles.[27] However, the transition to these energy sources is relatively slow, as evidenced by the IEA projection of an identical demand for oil and natural gas in 2050 as today, with the demand for coal only decreasing slightly.[28]

Thus, clean energy generation is necessary. Currently, the two primary alternative energy sources are wind and solar power; the most significant increase in electricity generation from 2021 to 2030 will come from an increase in solar and wind energy, and the primary investments in renewables are directed toward improving these two technologies.[29] However, solar and wind technologies have several problems.

Due to changing weather, wind and solar power are currently backed up by fossil fuels. In 2021, wind speeds were significantly milder than usual,[30] leading to an increased demand for natural gas for electricity production from thermal plants, significantly increasing electricity prices.[31] Flexible operation of power systems is necessary, as also stressed by IEA in their *World Energy Outlook 2022*-report.[32] Paradoxically, studies indicate that countries with modern fossil fuel capacity are more likely to invest in renewable energy generation since modern fossil fuels provide a reliable backup capacity to hedge against the variability of supply.[33]

The variability of wind power in, e.g., Germany is well-documented.[34] Low wind power events lasting half a day are relatively frequent, and low wind power events lasting up to 5 and 8 days occur every 5 and 10 years.[35] The problem of intermittency is apparent. To compound the problem, it seems that the use of batteries cannot resolve the intermittency issue; batteries are currently able to supply 1.25 minutes of the world's electricity requirements, and current

[20] Rae et al. (2021).
[21] NASA (2023d).
[22] Salewski (2019), p. 5.
[23] NASA (2023d).
[24] NASA (2023b).
[25] Our World in Data (2023).
[26] Internet Geography (2023).
[27] International Energy Agency (2022a).
[28] See International Energy Agency (2022b). The global oil demand grows by less than 1% before peaking in the mid-2030s, depending on the scenario.
[29] International Energy Agency (2022b).
[30] Germany experienced a 16% drop in combined output from on and offshore wind farms, see Buli and Jacobsen (2021).
[31] Buli and Jacobsen (2021).
[32] International Energy Agency (2022a), p. 30 f.
[33] Verdolini et al. (2018), p. 251 ff.
[34] See, e.g., Ohlendorf and Schill (2020).
[35] Ohlendorf and Schill (2020), p. 9 f.

projections indicate that having ten times as many batteries in 2030 as today will supply 10.6 minutes.[36] Sisternes et al. (2016) also concluded that substantial cost reductions in battery storage are needed to justify large-scale deployment.

1.4 Fusion energy and fast ions

Fusion energy is a promising candidate for a sustainable and continuous energy source. One key to realizing fusion energy is understanding fast ions. The fast ions carry a significant amount of the energy of the plasma in fusion reactors, making them challenging to control. Understanding what happens to the fast ions and why is crucial for fast-ion confinement and control of future discharges. In particular, the fast-ion velocity space distribution function is of interest.

The fast-ion velocity-space distribution function can be obtained by modelling the physical processes of various fast-ion diagnostics and subsequently solving inverse problems. Solving such problems is typically not straightforward, with the primary complication being that the inverse problem is ill-posed due to measurement noise. To compare the obtained distribution functions with known physics, the results are compared with results from simulations using codes such as TRANSP[37], ASCOT[38], and BEAMS3D[39].

The forward problem for measurements of fast ions can be written as a Fredholm integral equation of the first kind

$$s = \iint w f \, \mathrm{d}\boldsymbol{x} \, \mathrm{d}\boldsymbol{v}, \tag{1.2}$$

where s is the measurement, w a function describing the precise relation between s and f, and f the fast-ion distribution function to be determined. The variable dependencies in Eq. (1.2) have been omitted since it varies with the diagnostic. The inverse problem is to obtain f given s and w. By discretizing the continuous spatial and velocity dimensions, the forward problem can be written as the linear matrix-vector equation

$$s = W f \tag{1.3}$$

for $W \in \mathbb{R}^{m \times n}$, $f \in \mathbb{R}^n$, and $s \in \mathbb{R}^m$.[40] The signal vector s contains the measured data, the matrix W contains the physics of the problem, and the distribution function vector f is the solution, either the velocity-space or phase-space distribution function to be determined.

Throughout this work, vectors and matrices are written in italics, with vectors written using lower-case letters, and matrices using upper-case letters. A few exceptions are made such as when discussing electric and magnetic fields, in which case they are written using boldface. Greek letters are used to indicate scalars.

This work is concerned with ways to determine the distribution function f in Eq. (1.3).

[36] These estimates are made by Dr. Bjørn Lomborg, director of Copenhagen Consensus Center and visiting professor at Copenhagen Business School, using data from Wood Mackenzie Global Energy Storage Outlook H2 2021, the U.S. Energy Information and Administration, and the IEA World Energy Outlook 2021; see his infographic from 2022 at `https://pbs.twimg.com/media/FJnv9NoXOAMqRZa?format=png&name=large`. Accessed: 11-02-2023.

[37] See, e.g., Budny et al. (1995) for TRANSP simulations of alpha parameters (alpha heating, pressure, and distributions in energy and pitch) in a TFTR DT supershot with high fusion power and Pankin et al. (2004) for a description of the the NUBEAM module.

[38] Hirvijoki et al. (2014).

[39] See Lazerson et al. (2020) for validation of the BEAMS3D neutral beam deposition model on W7-X, and Lazerson et al. (2021) for a comparison of the energetic particle slowing-down model in the BEAMS3D stellarator neutral beam code to analytic models and experimental data from W7-X.

[40] The discretization is performed as described in Salewski et al. (2012), p. 3 ff.

1.5 Definition of problems

This dissertation explores the following fast-ion diagnostic topics:

- Development of **slowing-down physics regularization** [2].
- Development of **weight functions for ion cyclotron emission** [1], [3].
- Application of **algebraic iterative reconstruction techniques** [4], [6].
- Characterization of **fast ion loss detectors** [4], [6].
- Application of **deep neural networks** [1], [5].
- Development of the **raised cosine FILDSIM model** [6].
- Investigation of the **reconstruction error dependence** on the forward and inverse grid size [7].

The numbers refer to the papers indicated on the following page.

1.6 Publications

The publications resulting from the research conducted during this Ph.D. are listed below.

First author:

[7] **B. S. Schmidt** et al. (2023): *Grid-dependent reconstruction error for solving ill-posed inverse problems in nuclear fusion science* (to be submitted).

[6] **B. S. Schmidt** et al. (2023): *A raised cosine FILDSIM model and faster tomographic reconstructions of fast ion loss detector measurements for inter-shot analysis* (to be submitted).

[5] **B. S. Schmidt** et al. (2023): *Tomographic reconstructions of fast ion loss detector measurements using deep neural networks* (to be submitted).

[4] **B. S. Schmidt** et al. (2023): *Reconstruction methods for velocity-space tomography of fast-ion loss detectors* (to be submitted).

[3] **B. S. Schmidt** et al. (2023): *Velocity-space sensitivity and tomography of ion cyclotron emission* (submitted to Physics of Plasmas).

[2] **B. S. Schmidt** et al. (2023): *4D and 5D phase-space tomography using slowing-down physics regularization*, Nuclear Fusion, Volume 63, Issue 7, pp. 076016.

[1] **B. S. Schmidt** et al. (2021): *Determining 1D fast-ion velocity distribution functions from ion cyclotron emission data using deep neural networks*, Review of Scientific Instruments, Volume 92, Issue 5, pp. 053528

Coauthor:

- J. Galdon-Quiroga et al. (2023): *Mitigation of TAE-induced ICRF fast-ion losses using deuterium NBI in the ASDEX Upgrade tokamak*, to be submitted.
- H. Järleblad et al. (2023): *A Framework for Synthetic Diagnostics using Energetic-particle Orbits in Tokamaks*, submitted to Computer Physics Communications.
- J. Poley-Sanjuán et al. (2023): *Simultaneous measurement of co- and counter-current ions with a Fast Ion Loss Detector on the TCV tokamak*, 5th European Conference on Plasma Diagnostics (ECPD).
- Mencke, J. E. et al. (2022): *Characterization of correlations of fast-ion H-alpha measurement volumes in Wendelstein 7-X by particle tracking*, Review of Scientific Instruments, Volume 93, Issue 12, pp. 123503.
- H. Reimerdes et al. (238 other authors) (2022): *Overview of the TCV tokamak experimental programme*, Nuclear Fusion, Volume 62, Issue 4, pp. 042018.
- Järleblad, H. et al. (2022): *Fast-ion orbit sensitivity of neutron and gamma-ray diagnostics for one-step fusion reactions*, Nuclear Fusion, Volume 62, Issue 11, pp. 112005.
- Moseev, D. et al. (2021): *Development of the ion cyclotron emission diagnostic for the W7-X stellarator*, Review of Scientific Instruments, Volume 92, Issue 3, pp. 033546.
- Järleblad, H. et al. (2021): *Fast-ion orbit sensitivity of neutron emission spectroscopy diagnostics*, Review of Scientific Instruments, Volume 92, Issue 4, pp. 043526.

1.7 Relevance for the International Thermonuclear Experimental Reactor (ITER)

The International Thermonuclear Experimental Reactor (ITER) will be the world's largest tokamak once construction is complete. It seeks to prove the feasibility of fusion energy as a safe and environmentally friendly source of energy. A project of immense complexity, ITER's construction and operation hinge on the contributions of seven partners: the European Union, India, Japan, China, Russia, South Korea, and the United States. The milestone of first plasma is anticipated in the early 2030s.

The weight functions for ion cyclotron emission improve the understanding of the processes generating the signal. Reconstruction techniques can be used to determine the emission location in velocity space of the ions generating the ion cyclotron emission. Specifically, since one goal of the ITER project is to achieve a D-T plasma sustained mostly by internal alpha particle heating[41], analysis of the behaviour of the alpha particles through their ion cyclotron emission signature may provide useful insights.

Several projects are currently ongoing using slowing-down physics regularization to obtain the phase-space distribution function of fast ions. This includes using slowing-down physics regularization on neutron emission spectroscopy data and obtaining a spatially finer resolved fast ion velocity-space distribution along injected neutral beams. The interpretation developed in this dissertation solidifies the slowing-down physics regularization technique independent of modelling dimensions, and the applications demonstrate its usefulness in obtaining 4D and 5D phase-space distribution functions for both tokamaks and stellarators.

A fast-ion loss detector will be installed at ITER.[42] The improved reconstruction techniques for fast-ion loss detector measurements will improve their analysis, contributing to a better understanding of fast-ion interactions with, e.g., MHD modes. Further, the velocity-space sensitivity of the fast-ion loss detector probe(s) at ITER can be evaluated using the newly-developed gross strike map and gross weight function ideas.

The faster algebraic iterative reconstruction techniques allow for faster reconstructions of FILD signals with a detailed trade-off between reconstruction quality and computation time. These signals can be used for fast analysis, potentially together with a trained neural network.

The demonstration of direct calculations of reconstructions using neural networks shows that further development and application of neural networks can provide improved and faster reconstructions when the training process of the neural network progresses. This prospect of improved and fast reconstructions applies potentially to all diagnostics.

1.8 Remarks on used notation

Citations are included in footnotes indicated by numbered subscripts in the main text to comment on and discuss the contents of the source without affecting the main text. Additional authors are mentioned when citing a source if required to distinguish between sources with the same first author published in the same year.

Petit sections are used to make the text more clear. These sections are reserved for examples, considerations, and side notes not otherwise suitable for the main text or footnotes.

[41] ITER (2022d). See also McClements et al. (2015).
[42] See ITER (2022c) and Garcia-Munoz et al. (2016).

1.9 Dissertation outline

The dissertation is structured as follows:

Chapter 2 introduces the necessary background theory in plasma physics and fusion energy related to the research presented in this Ph.D. dissertation.

Chapters 3 to 9 contain the research papers produced during this Ph.D.

Chapter 3 presents slowing-down physics regularization and demonstrates the technique applied to synthetic measurements from TCV and W7-X.

Chapter 4 presents 1D weight functions for ion cyclotron emission and reconstructions of fast ion velocity distribution functions using deep neural networks.

Chapter 5 presents 2D ICE weight functions for LHD and three reconstruction techniques for obtaining the location in velocity-space of the ions emitting the ICE.

Chapter 6 presents new ways to characterize a FILD based on FILDSIM-simulated weight functions and strike maps and algebraic iterative reconstruction techniques to obtain the velocity-space distribution function at the fast-ion loss detector pinhole.

Chapter 7 presents a raised-cosine FILDSIM model, applies it on synthetic and experimental data from TCV, and develops an optimization framework for FILD reconstructions using algebraic iterative reconstruction techniques.

Chapter 8 presents applications of deep neural networks to analyse measurements from fast ion loss detectors by determining the optimal value of the regularization parameter for Tikhonov regularization and by computing reconstructions of the fast ion velocity space distribution function.

Chapter 9 presents investigations of the dependence of the reconstruction error on the grid size in ill-posed inverse problems.

Chapter 10 presents a conclusion and an outlook.

Chapter 2

Plasma physics and fusion energy

The following sections present relevant theory and select research results that this work extends. Topics include magnetic confinement fusion, ion cyclotron emission, fast ion loss detectors, and ill-posed inverse problems.

2.1 Magnetic confinement fusion

The fuel for future fusion reactors comprises deuterium (D) and tritium (T). The fusion of deuterium and tritium produces an alpha particle and a neutron with kinetic energies of approximately 14.1 MeV and 3.5 MeV:

$$\mathrm{D} + \mathrm{T} \rightarrow \overbrace{{}^4\mathrm{He}}^{3.5\,\mathrm{MeV}} + \overbrace{\mathrm{n}}^{14.1\,\mathrm{MeV}} \tag{2.1}$$

The total energy released of approximately 17.6 MeV is due to the mass defect $\Delta m \approx 0.019 \mathrm{m}_p$.

D-T fuel is considered optimal for future fusion reactors for several reasons. One reason is the availability of fuel. Since deuterium is an isotope of hydrogen, it is a constituent of water molecules and can be extracted by electrolysis.[1] Tritium is rarer than deuterium, but the neutrons from the reaction in Eq. (2.1) can generate tritium from lithium through tritium breeding:

$$^6\mathrm{Li} + \mathrm{n} \rightarrow ^4\mathrm{He} + \mathrm{T}. \tag{2.2}$$

This breeding is accomplished by placing lithium, which exists in large reserves, in the blanket of the fusion reactor.[2] The neutrons generated from fusion reactions in the plasma are used as reactants. Another reason for considering D-T the optimal fuel is that the reactivity of the D-T reaction is several orders of magnitude above that of the other reactions for attainable temperatures.[3] The other possible fusion reactions are

$$\mathrm{D} + \mathrm{D} \rightarrow {}^3\mathrm{He} + \mathrm{n} + 3.27\,\mathrm{MeV} \tag{2.3a}$$

$$\mathrm{D} + \mathrm{D} \rightarrow \mathrm{T} + \mathrm{H} + 4.03\,\mathrm{MeV} \tag{2.3b}$$

$$\mathrm{D} + {}^3\mathrm{He} \rightarrow {}^4\mathrm{He} + \mathrm{H} + 18.3\,\mathrm{MeV} \tag{2.3c}$$

$$\mathrm{D} + \mathrm{T} \rightarrow {}^4\mathrm{He} + \mathrm{n} + 17.6\,\mathrm{MeV}. \tag{2.3d}$$

[1] The ratio of deuterium to hydrogen isotopes is 1:6,700 in nature; see Friedman (1953), p. 89. However, with the abundance of water molecules on Earth, sufficient deuterium can easily be extracted; cf. ITER (2022a).

[2] ITER (2022b).

[3] Wesson (2004), p. 5 ff.

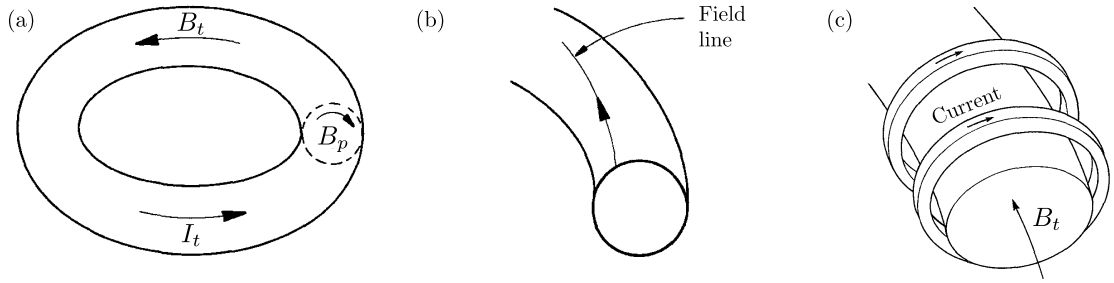

Figure 2.1: (a) The toroidal magnetic field B_t and poloidal magnetic field B_p generated by the toroidal current I_t. (b) A twisted field line from the sum of B_t and B_p. (c) Current in toroidal field coils generate the toroidal magnetic field B_t. From Wesson (2004), p. 16.

2.1.1 Tokamaks

The temperatures sought for D-T fusion are around 10-20 keV corresponding to 100-200 $\times$ 10^6 °C. Material walls cannot contain plasmas at such high temperatures, so other confinement methods are needed. The tokamak is an example of such a confinement configuration.

A magnetic field confines the ions of the plasma to move in a toroidal region in a tokamak plasma. The plasma pressure $p = nT$ is immense due to the high temperatures, so a magnetic pressure is required to balance it. This balance requires both a toroidal magnetic field B_t and a poloidal magnetic field B_p; see Fig. 2.1(a). The magnetic field lines of the total magnetic fields are twisted, as illustrated in Fig. 2.1(b). The poloidal magnetic field strength is typically an order of magnitude smaller than the toroidal magnetic field strength.[4] The toroidal magnetic field B_t is generated by currents in coils wrapping around the toroidal vessel, and the poloidal field is generated by a plasma current I_t. The plasma current is typically driven by a toroidal electric field induced by a flux change through the torus center from a changing current through a coil called "transformer action". This configuration results in relatively good plasma confinement since the axisymmetric magnetic field automatically confines collisionless particle orbits, but the transformer action may induce current-driven instabilities and makes it challenging to operate steady state. Other ways of generating the plasma current are expensive and limit plasma parameters.[5]

2.1.1.1 Confinement

A measure of the confinement of plasma pressure by the magnetic field is given by the ratio

$$\beta = \frac{p}{B^2/(2\mu_0)}. \tag{2.4}$$

Coulomb collisions give an upper bound on the confinement, but often the confinement is worse. The particle and energy transport can be calculated classically, but the observed transport does not agree with these calculations. This "anomalous transport" occurs due to plasma instabilities causing particles and energy to escape at a higher rate.[6] Thus, empirical methods have been used to predict the confinement time by collecting data from various machines and using statistical

[4] Wesson (2004), p. 16. This strength difference is mainly due to stability reasons since increasing the poloidal magnetic field strength too much causes the safety factor q to be too small, where q is the ratio of the number of times a magnetic field line traverses around toroidally to the number of times it traverses poloidally.

[5] Helander (2014), p. 2.

[6] Wesson (2004), p. 150 f.

methods to find the dependence between the confinement time and relevant parameters. This approach allows for extrapolation to tokamaks with different parameter values.

Under certain conditions, a discontinuous improvement in confinement occurs as heating power is increased. This regime is called "H-mode", and the lower confinement level "L-mode". Typically, the confinement time increases by a factor of two.[7]

2.1.1.2 Tokamak à Configuration Variable

The Tokamak à Configuration Variable (TCV) is part of the Swiss Plasma Center at the École Polytechnique Fédérale de Lausanne in Lausanne, Switzerland, and was built in 1992. The machine has a rectangular vacuum vessel with a height-to-width ratio of 2.9 and 16 shaping coils. Further details of the machine are given in Table 2.1. TCV has a large degree of flexibility in plasma shaping and positioning and in high-power-density electron cyclotron resonance heating (ECRH) and electron cyclotron current drive (ECCD) in addition to neutral beam injection (NBI).[8]

The scientific programme investigates the creation and control of plasmas with different shapes, in particular highly elongated plasmas, investigating their confinement and MHD properties, with many of the plasma shapes not able to be investigated in any other tokamak. Thus, research at TCV contributes to optimizing tokamaks as a reactor concept and to preparing ITER operations.[9] One example is the knowledge gained about high-elongation plasmas. Such plasmas allow investigation of large plasma currents since $I_t \propto (1+\kappa^2)/2$, where κ is the elongation. Higher currents increase the β limit and improve confinement, and a direct improvement in confinement has also been observed with increasing elongation. A notable recent result includes Degrave et al. (2022) in which a deep neural network trained using reinforcement learning autonomously commanded the full set of control coils for different plasma shapes.

2.1.2 Ignition

Deuterium and tritium are positively charged, so the mutual electrostatic repulsion must be overcome to induce fusion. Thus, the reaction cross-section is small at low temperatures but increases with temperature. A positive total power balance can be attained if the ions at these temperatures can react before they lose their energy.[11] A positive total power balance occurs when the sum of the externally supplied heating power P_H and the alpha-particle heating power P_α is greater than the power loss P_L, i.e., $P_\mathrm{H} + P_\alpha > P_\mathrm{L}$. This can be achieved by heating the D-T fuel to sufficiently high temperatures.

The fraction of alpha particle heating increases as a function of the temperature. Ignition happens when the plasma temperature can be sustained only by internal heating against the energy losses. With total plasma energy E, the power loss P_L is characterized by the energy confinement time τ_E according to

$$P_\mathrm{L} = \frac{E}{\tau_\mathrm{E}}. \tag{2.5}$$

Let the energy of the alpha particles be E_α and $\langle\sigma v\rangle$ the reactivity. Power balance considerations show that the ignition condition is[12]

$$n\tau_\mathrm{E}T > \frac{12}{\langle\sigma v\rangle}\frac{T^2}{E_\alpha}. \tag{2.6}$$

[7] Wesson (2004), p. 152.
[8] SPC (2023a).
[9] Wesson (2004), p. 589 f.
[10] SPC (2023b).
[11] Wesson (2004), pp. 2 and 150 ff.
[12] Wesson (2004), p. 10 ff.

Table 2.1: Parameters for TCV.
Source: SPC Wiki: Technical data.[10]

Operational parameter	**TCV**
Major/minor plasma radius	0.89 m/0.25 m
First wall	Graphite
Aspect ratio	3.5
Plasma elongation	0.9 - 2.8
Maximmal on axis magnetic field	1.54 T
Maximal plasma current	1.2 MA
Triangularity range	-0.8 / +0.9
Pulse duration	2.6 s (ohmic)
	4.0 s (ECCD)
Main ion component	H, D, He
Core electron density	1-20 $\times$ 10^{19} m^{-3}
Core electron temperature	$\leq$ 1 keV (ohmic)
	$\leq$ 15 keV (ECRF)
Core ion temperature	$\leq$ 1 keV
Current and field directions	Both can be flipped between shots
ECRF	4.5 MW (6×0.5 MW + 3×0.5 MW)
NBI	NBI-1: 23(28) keV, 1(1.3) MW H(D)
	NBI-2: 46(47) keV, 900(900) kW H(D)
	Diagnostic (DNBI): 50 keV, 80 kW

The graph of the product $n\tau_\mathrm{E}$ as a function of temperature has a minimum at $T \approx 30$ keV, but the ignition temperature is somewhat lower at 10-20 keV. In this temperature range,

$$\langle \sigma v \rangle \approx 1.1 \times 10^{-24}\, T^2\, \mathrm{m}^3\, \mathrm{s}^{-1}, \tag{2.7}$$

with the temperature in keV. For flat density and temperature profiles, the ignition condition becomes

$$nT\tau_\mathrm{E} > 3 \times 10^{21}\, \mathrm{keV\, s\, m}^{-3}, \tag{2.8}$$

whereas parabolic profiles give

$$nT\tau_\mathrm{E} > 5 \times 10^{21}\, \mathrm{keV\, s\, m}^{-3}. \tag{2.9}$$

Values that satisfy the criterion are, e.g., $n = 10^{20}$ m^{-3}, $T = 10$ keV, and $\tau_\mathrm{E} = 5$ s.

2.1.3 Ion motion

The motion of charged particles in electromagnetic fields is governed by the Lorentz equation of motion:

$$m\frac{\mathrm{d}\boldsymbol{v}}{\mathrm{d}t} = q(\boldsymbol{v} \times \boldsymbol{B} + \boldsymbol{E}), \tag{2.10}$$

where m is the mass of the particle, q the charge, $\boldsymbol{v}$ the velocity, and $\boldsymbol{B}$ and $\boldsymbol{E}$ the magnetic and electric fields. The velocity components $v_\parallel$ and $v_\perp$ are the components of v parallel and perpendicular to $\boldsymbol{B}$. Thus, Lorentz' equation for $\boldsymbol{E} = 0$ and uniform $\boldsymbol{B}$ can be decomposed into

the two equations

$$m\frac{\mathrm{d}v_\parallel}{\mathrm{d}t} = 0, \tag{2.11}$$

$$m\frac{\mathrm{d}\boldsymbol{v}_\perp}{\mathrm{d}t} = q\boldsymbol{v}\times\boldsymbol{B}. \tag{2.12}$$

Hence, $v_\parallel$ is constant in a collisionless plasma, and the perpendicular motion is circular. Thus, the ions in a plasma have a helical trajectory, gyrating around a magnetic field line with the axis called the "guiding center". From the harmonic solutions to Eq. (2.12), it follows that the frequency of the oscillations of species s in the poloidal plane is the cyclotron frequency

$$\Omega_\mathrm{s} = \frac{qB}{m}. \tag{2.13}$$

The radius of the gyromotion is

$$\rho = \frac{v_\perp}{\Omega_\mathrm{s}} = \frac{mv_\perp}{qB}, \tag{2.14}$$

also called the "Larmor radius".

2.1.3.1 Ion drifts

A force $\mathbf{F}$ leads to a drift of the guiding center according to the equation[13]

$$\boldsymbol{v} = \frac{1}{q}\frac{\mathbf{F}\times\boldsymbol{B}}{B^2}. \tag{2.15}$$

Thus, the ions drift perpendicularly to the force and the local magnetic field. In particular, the following three drifts are relevant: the $\boldsymbol{E}\times\boldsymbol{B}$-drift, the $\nabla\boldsymbol{B}$ drift, and the curvature drift.

If there is an electric field $\boldsymbol{E}$ with associated force $\mathbf{F} = q\boldsymbol{E}$, then

$$\boldsymbol{v}_{\boldsymbol{E}\times\boldsymbol{B}} = \frac{\boldsymbol{E}\times\boldsymbol{B}}{B^2}, \tag{2.16}$$

independent of the ion charge. This drift increases the gyroradius in half of the gyromotion and decreases it in the other half, leading to a drift perpendicular to the local $\boldsymbol{E}$ and $\boldsymbol{B}$ fields.

Since $\nabla\boldsymbol{B} \neq \mathbf{0}$ in a tokamak, in particular, $B_t \propto 1/R$ so $\nabla\boldsymbol{B}$ points towards the center of the torus, the ions experience the force

$$\mathbf{F} = -\mu\nabla\boldsymbol{B}, \tag{2.17}$$

where $\mu = IA$ is the magnetic moment associated with the gyromotion of the ion. Thus,

$$\boldsymbol{v}_{\nabla\boldsymbol{B}} = \frac{mv_\perp^2}{2q}\frac{\boldsymbol{B}\times\nabla\boldsymbol{B}}{B^3}. \tag{2.18}$$

The drift is perpendicular to the local magnetic field gradient and the local magnetic field and depends on the charge, leading to opposite drifts for ions and electrons.

Finally, the magnetic field lines are curved in tokamaks and stellarators. Thus, the ions following the magnetic field lines feel the centrifugal force

$$\mathbf{F} = mv_\parallel^2\frac{\mathbf{R}}{R^2} \tag{2.19}$$

[13] Salewski (2022), p. 37.

for the radius R of the field lines, leading to the drift

$$\mathbf{v}_c = \frac{mv_\parallel^2}{qB^2}\frac{\mathbf{R}\times\boldsymbol{B}}{R^2}, \tag{2.20}$$

where $\mathbf{R}$ points from the center of the radius of curvature towards the outside.

For a toroidal magnetic field satisfying Maxwell's equations,[14]

$$\frac{\nabla \boldsymbol{B}}{B} = -\frac{\mathbf{R}}{R^2}, \tag{2.21}$$

so

$$\boldsymbol{v}_{\nabla \boldsymbol{B}} + \boldsymbol{v}_c = \frac{m}{q}\frac{\mathbf{R}\times\boldsymbol{B}}{R^2B^2}\left(v_\parallel^2 + \frac{1}{2}v_\perp^2\right). \tag{2.22}$$

It follows that ions and electrons drift in opposite directions giving rise to an electric field $\boldsymbol{E}$ from charge separation, resulting in an $\boldsymbol{E}\times\boldsymbol{B}$-drift accelerating the plasma towards the walls. This loss of confinement is why a poloidal magnetic field component B_p is needed.

2.1.3.2 Orbits

Under adiabatic conditions, i.e., when the spatial and temporal variation of the magnetic field are small compared to the gyroradius and the gyrofrequency,

$$\frac{|\nabla B|}{B} \ll \rho, \quad \frac{\dot{B}}{B} \ll \Omega_\mathrm{s}, \tag{2.23}$$

the magnetic moment

$$\mu = \frac{mv_\perp^2}{2B} \tag{2.24}$$

is conserved. Thus, $v_\perp$ must increase as the ion moves into a stronger magnetic field. Since the energy

$$E = \frac{1}{2}m\left(v_\parallel^2 + v_\perp^2\right) \tag{2.25}$$

is conserved, $v_\parallel$ decreases. For a strong enough magnetic field, $v_\parallel$ decreases to 0, and the ion is reflected from the high-magnetic field region towards the low-magnetic field region.

This effect is present in tokamaks due to the $1/R$-gradient of the toroidal magnetic field from the high-field side to the low-field side near the outer wall and leads to trapped orbits with a typical banana shape for ions with sufficiently low initial $v_\parallel$, corresponding to a large pitch angle α defined according to

$$\lambda = \cos\alpha = \frac{v_\parallel}{v}, \tag{2.26}$$

and passing orbits whose parallel velocities are not reduced to zero at the high-magnetic field. Examples of ion orbits are illustrated in Fig. 2.2. The magnetic axis is at $R_0 = 3.13$ m and the last closed flux surface at $R = 4$ m. Fig. 2.2(a) shows a passing orbit of an alpha particle with a birth pitch angle of 54.8°, and Fig. 2.2(b) a trapped orbit with birth pitch angle 55.2° with maximum ion orbits intercepting $R = 4$ m.

[14] See, e.g., Chen (2016), p. 28 ff.

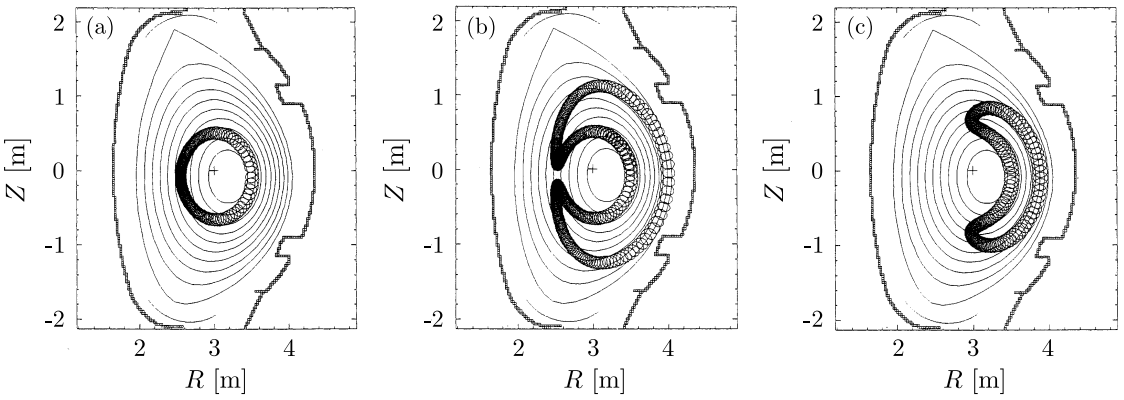

Figure 2.2: Poloidal projectiosn of simulated ion orbits for 3.5 MeV alpha particles for D-T pulse No. 26148 at JET related to the early investigations of ion cyclotron emission. The flux surface geometry is from $t = 13.2$ s. From Cottrell et al. (1993), p. 1378 f.

2.1.4 Energetic particle physics

Fast ions, or energetic ions, are the superthermal ions in a plasma with energies of approximately 30 keV to several MeVs,[15] significantly above the temperatures of the bulk plasma ions with energies around 10 keV. The average energy of the bulk plasma is referred to as the 'thermal energy' and is given by $E_\mathrm{s} = 3T_\mathrm{s}/2$ with $T_\mathrm{s} = m_\mathrm{s} v_\mathrm{ts}^2/2$, where the thermal velocity v_ts for species s is determined by the collision frequency ν_s and mean free path $\lambda_\mathrm{mfp,s}$ by $v_\mathrm{ts} = \lambda_\mathrm{mfp,s}\nu_\mathrm{s}$.[16]

Three different energetic ion populations can be distinguished as generated (1) by injected neutrals with energies approximately 30 keV - 1 MeV, (2) from electromagnetic wave heating in the ion cyclotron range of frequencies (ICRF) with energies up to 2-3 MeVs, or (3) from fusion reactions, where the alpha particles from D-T fusion reactions have birth energies of 3.5 MeV.[17] The fast ions are essential to the operation of a future fusion power plant since they will provide more than 2/3 of the total heating by transferring their energy to the bulk plasma.[18]

2.1.4.1 Neutral beam injection

Neutral beam injection (NBI) systems are used to heat the fusion plasma and to investigate the behaviour of energetic ions in different plasma configurations and plasma devices. In NBI systems, ions, typically hydrogen or deuterium, are accelerated to high energies, neutralized, and subsequently injected into the plasma as neutrals. The neutral atoms ionize due to, e.g., impact ionization or charge exchange. The ions then transfer energy to the bulk plasma through Coulomb collisions. The type of collisions depends on the energies, where collisions with electrons dominate at higher energies and collisions with ions at lower energies, resulting in pitch-angle scattering processes. There is a crossover energy E_c between the two energies where the heating rate is equal for electrons and ions. If the injection energy is above the crossover energy, more energy is transferred to the electrons, and conversely, if the injection energy is below the crossover energy, more energy is transferred to the ions.

The time it takes for the beam ions to slow down is called the "slowing-down time" and is

[15] Salewski, Geiger, et al. (2015), p. 1.
[16] Salewski (2022), p. 84 ff.
[17] Salewski, Geiger, et al. (2015), p. 1. See also Salewski et al. (2011).
[18] Salewski et al. (2011), p. 1.

typically on the order of milliseconds. For ASDEX Upgrade, typical slowing-down times for 90 keV NBI ions are around 90 ms.[19]

> Zhang et al. (2013) investigated the slowing-down times of neutral-beam injected energetic ions in HL-2A plasmas with different electron temperatures T_e and densities n_e by use of 5 ms D-NBI blips with an injection energy of 30 keV. The deuterium ions were injected into a deuterium plasma at an angle of 32 °with respect to the plasma current at the magnetic axis, producing 2.45 MeV D-D fusion neutrons. TRANSP runs showed approximately 70% of the neutrons produced by beam-target reactions and 30% by beam-beam reactions. As the energies of the beam ions decrease, the reaction cross section falls, and hence the neutron emission decays. The decay time is therefore related to the slowing-down time of the energetic ions. They found slowing-down times around 12 ms and longer slowing-down times for lower-density plasmas compared to higher-density plasmas as predicted by classical slowing-down physics.

The injection geometry of the beam and the magnetic equilibrium configuration determines the NBI birth distribution function. The NBI distribution functions are typically anisotropic. A more tangential injection will create more passing ions, and a more perpendicular injection will create a larger fraction of trapped particles on the low-field side.[20] On-axis injection refers to the deposition of the energetic ions near the magnetic axis and off-axis deposition further from the magnetic axis.

"Shine through" occurs when the injected neutrals travel through the plasma and hit the opposite wall. This undesirable consequence is investigated at different machines.[21]

2.1.4.2 Electromagnetic wave heating in the ion cyclotron range of frequencies (ICRF)

Due to the harmonic motion of the ion, an ion can gain energy by resonating with an electromagnetic wave with frequency ω, if the resonance condition

$$\omega = n\Omega + k_{\parallel} v_{\parallel} \tag{2.27}$$

is satisfied. The parameter $k_{\parallel}$ is the wavenumber parallel to the magnetic field, and n is a positive integer. Such an electromagnetic wave can be generated by external antennae outside the reactor vessel and propagate through the plasma. Since $\Omega = qB/m$, the resonance occurs at radii with specific values of B. Since $B_t \propto 1/R$, the radial location of the ions to be heated can be determined. Changing the frequency of the wave changes the resonance position in the plasma. The resonance location is also referred to as a resonance layer since the radial location can be considered a 2D plane.

The ions satisfying the resonance condition in Eq. (2.27) gain or lose energy as they pass through the resonance layer multiple times during their orbit. Thus, ICRF-heated fast-ion distributions gain energy over time, which can be up to MeVs.

> Discharges #21011 and #21083 at ASDEX Upgrade investigated the behaviour of fast ions during high-frequency MHD phenomena induced by ICRF heating.[22] MHD-induced fast ion losses with energies in the MeV range were observed using fast-ion loss detectors. The lost ions were trapped protons with energies in the range 0.3-1.6 MeV heated using ICRF heating.

[19] Galdon-Quiroga (2018), p. 15 ff.
[20] Galdon-Quiroga (2018), p. 15 ff.
[21] Examples include Lazerson et al. (2020) discussing shine through related to the validation of the BEAMS3D neutral beam deposition model on W7-X, and the presentation by Karpushov (2022) mentioning the first-wall protection at TCV against overheating from shine through.
[22] Garcia-Munoz (2006), p. 73 ff, and Mantsinen et al. (2007).

2.1.4.3 Fusion reactions

The reactions in modern experimental fusion plasmas depend on the species mix. The possible reactions are given in Eqs. (2.3). These reactions can result from beam-target reactions, i.e., between NBI ions and the bulk plasma, beam-beam reactions, i.e., between ions from the beam, or thermonuclear reactions, i.e., between ions from the bulk plasma. The birth profile distributions from the thermonuclear reactions depend on the kinetic profiles of the plasma, and the beam-target and beam-beam reactions depend on the NBI geometry.

2.1.5 Slowing-down physics

Fast ions partake in binary Coulomb collisions with the bulk plasma. The cross section of the collisions is determined by the relative velocity of the scatterers. Since the fast ion velocity v_f, in general, satisfies $v_\mathrm{Th,e} \gg v_\mathrm{f} \gg v_\mathrm{Th,i}$, the Coulomb collision rate with thermal electrons is largely determined by $v_\mathrm{Th,e}$ and that with thermal ions by v_f.

The fast ion energy at which the electron and ion friction is balanced is the crossover energy E_c, which is given by[23]

$$E_\mathrm{c} = 14.8 T_\mathrm{e} \left(\frac{A^{3/2}}{n_\mathrm{e}} \sum_i \frac{n_i Z_i^2}{A_i} \right)^{2/3}, \tag{2.28}$$

where the sum is over the ion species of the plasma.[24] Thus, when $E_\mathrm{f} > E_\mathrm{c}$, electron drag dominates, and the fast ions transfer energy and momentum primarily to electrons, and, hence, slow down due to electrons. Due to the mass difference, the ions decelerate without pitch-angle scattering. When $E_\mathrm{f} < E_\mathrm{c}$, collisions with thermal ions dominate and the fast ions slow down primarily due to collisions with thermal ions with appreciable pitch-angle scattering.

The slowing-down time τ_SD for a fast ion with energy E_f can be written as[25]

$$\tau_\mathrm{SD} = \frac{\tau_\mathrm{se}}{3} \log \left(1 + \left(\frac{E_\mathrm{f}}{E_\mathrm{c}} \right)^{3/2} \right), \tag{2.29}$$

with $\tau_\mathrm{se} \propto T^{3/2}/n_\mathrm{e}$ the slowing-down time for ions on electrons.[26]

2.2 Ion cyclotron emission

Experimentally, ion cyclotron emission (ICE) is identified as peaks at cyclotron harmonic frequencies $n\Omega_s$ for a species s in a frequency spectrum; see Fig. 2.3 for an example of an ICE spectrum measured at the Tokamak Fusion Test Reactor (TFTR). The frequencies of such measurements provide information about the ICE-emitting species. For example, the radial location of the energetic ions emitting the ICE can be determined by relating the measured frequencies to the radial location corresponding to the correct magnetic field strength.[27] Studies on ion cyclotron emission in magnetically-confined fusion plasmas can roughly be categorized into three groups: theoretical studies, experiments, and simulations.

Theoretical studies on ICE are primarily concerned with the magnetoacoustic cyclotron instability (MCI) as the driver of ICE and investigate its growth rate.[28] This is done by solving

[23] Heidbrink and Sadler (1994), p. 550.
[24] Only the temperature of the thermal electrons enter Eq. (2.28) due to the relative velocities of the species.
[25] Stix (1972), p. 374.
[26] Stix (1972), p. 374, cf. Spitzer (1962).
[27] See Cottrell and Dendy (1988), p. 33 ff., and Cottrell et al. (1993), p. 1373 ff.
[28] See, e.g., Dendy et al. (1994).

for perturbative solutions of the dispersion relation by letting

$$\omega = \omega_0 + \delta\omega, \tag{2.30}$$

where ω_0 is a real frequency and $\delta\omega$ complex satisfying $|\delta\omega| \ll \omega_0$. Positive values of the growth rate $\gamma \equiv \mathrm{Im}(\delta\omega)$ indicate wave growth, and negative values wave damping.

Experiments have been performed on almost all tokamaks. In these experiments, ICE has been found to originate from different plasma locations, primarily the plasma core and the edge termed "core ICE" and "edge ICE". ICE has been observed from fusion products, neutral-beam injection, and ICRF heating.

Plasma simulations utilizing a particle-in-cell (PIC) code have investigated the linear and non-linear saturated phases of the MCI using a fully kinetic and a hybrid approach. The plasma simulation results support contemporary theory and agree with experiments, which provides support for the plasma simulation assumptions and implementation.

2.2.1 Spectral characteristics

Ion cyclotron emission is characterized as radiation in the ion cyclotron range of frequencies. The radiation is typically strongly superthermal since its intensity is several orders of magnitude above the background radiation from the thermal ions.[29] ICE is observed in narrow bands at integer multiples of the fundamental cyclotron frequency

$$f_\mathrm{s} = \frac{\Omega_\mathrm{s}}{2\pi} = \frac{Z_s e B}{2\pi m_s}. \tag{2.31}$$

A fundamental cyclotron frequency of 15 MHz is around the value expected for edge ICE from protons, as the magnetic field is typically around 1 T near the edge. For core ICE, the fundamental proton cyclotron frequency is closer to 40 MHz, as the on-axis magnetic field strength is typically around 2.0-4.0 T.[30] The fundamental deuterium cyclotron frequency is one-half of the fundamental proton cyclotron frequency, for ^{3}He it is two-thirds of the fundamental proton cyclotron frequency, and for alpha particles one-half of the fundamental proton cyclotron frequency. Thus, the second cyclotron harmonic of deuterium equals that of the fundamental cyclotron frequency of hydrogen. This can give rise to degeneracy in the frequency spectra, as was observed in discharge #73255 at TFTR; see Fig. 2.3. Note the high intensity of the second deuterium harmonic and the third tritium harmonic.

Since the toroidal field strength depends on the radial location in the machine, which to a good approximation follows a $1/R$-dependence for tokamaks,[31] the frequencies of the cyclotron harmonics depend on the radial location of the ions. Thus, depending on the experimental conditions, the peaks of an ICE spectrum will occur at different frequencies. Typical frequencies comprise the range 0-150 MHz.[32]

[29] Cottrell and Dendy (1988) report that the ICE from hydrogen NBI result in intensities up to 10^4 above the background. See also the introduction in Chapman et al. (2020).

[30] Wesson (2011), pp. 14, 630, and 633 ff.

[31] See, for example, Wesson (2011), p. 13 ff., Cairns, 1985, p. 32, and Cottrell and Dendy (1988), p. 34, where this assumption was made to determine the approximate radial locations of the ICE-emitting ions for the first four hydrogen cyclotron harmonics.

[32] Cf. Cottrell et al. (1993), p. 1369, and Cauffman et al. (1995), p. 1598. See also Ochoukov, Bilato, Bobkov, Chapman, et al. (2019), Ochoukov, McClements, et al. (2019), Thome et al. (2018), and Thome et al. (2019) for measurements in the same frequency range. Lower frequencies of 2-3 MHz have been reported at NSTX and NSTX-U; see Fredrickson et al. (2019) and Fredrickson et al. (2021). ICE chirping on sub-microsecond timescales in the range 500-900 MHz have been measured at KSTAR; see Chapman et al. (2018).

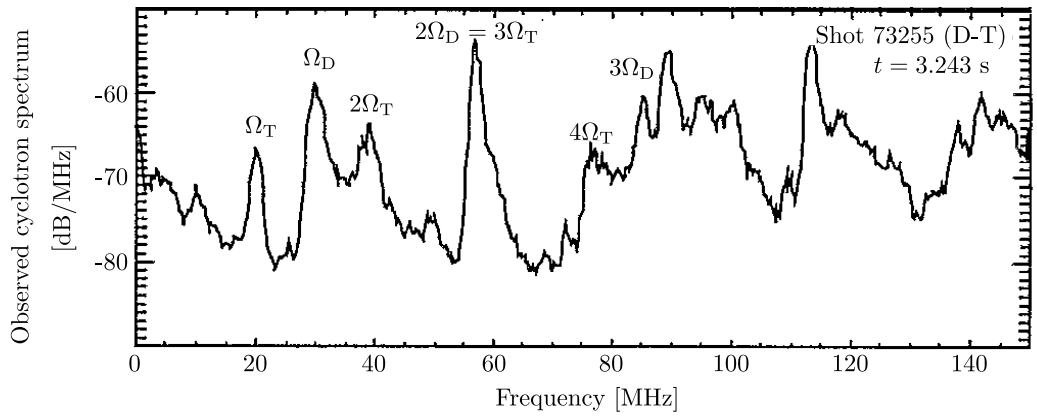

Figure 2.3: Spectrum showing ion cyclotron emission at harmonics of Ω_D and Ω_T observed in discharge #73255 at $t = 3.243$ s at TFTR. From Cauffman and Majeski (1995), p. 818.

Cottrell et al. (1993) reported ICE data from the Preliminary Tritium Experiment (PTE) at JET with spectral peaks at multiples of 17 ± 0.5 MHz. Matching the measured frequency with the theoretically predicted value of the fundamental cyclotron frequency of the alpha particles required approximately 1.2 T, corresponding to ICE originating from the edge at $R \approx 4.0$ m.

Measurements of ICE at the fundamental hydrogen cyclotron frequency in the plasma core at ASDEX Upgrade during discharge #34561 were reported in Ochoukov, Bilato, Bobkov, Chapman, et al. (2019). A signal at 39.6 MHz matches the fundamental hydrogen cyclotron frequency for a field of 2.6 T in the spectrogram in Fig. 2, where frequencies $f/\text{MHz} \in \{36, 42\}$ detected using B-dot probes are shown for the time interval $t = 4.0$ s to $t = 5.0$ s. This indicated that the ICE originated from the core since the on-axis magnetic field strength was 2.6 T.

2.2.2 Line broadening

The peaks in ICE spectra are generally characterized by being narrow in frequency, typically having a relative width of $\Delta f/f \simeq 0.1$, where Δf is the width of a peak at half of the maximal intensity.[33] The width of the peaks vary depending on the ion source, with fusion products typically producing narrower peaks compared to beam-injected ions. This is seen particularly well for ICE at JT-60U as reported by Ichimura et al. (2008), where modes at the fundamental and second harmonic helium cyclotron frequencies from fusion-born ^{3}He produce sharp peaks, and perpendicularly-injected deuterium ions result in broad peaks at the fundamental, second, and third harmonic deuterium cyclotron frequencies. Cottrell and Dendy (1988) also report peaks of varying widths for the measured ICE during an ohmic-heating phase and a 58° NBI injection of protons into a deuterium plasma, with the NBI-induced emission lines being much more sharply peaked. The difference in relative width $\Delta f/f$ of the spectral peaks in the Ohmic-heating phase and the NBI-heating phase was approximately a factor of two. This difference may be due to the radial extent of the gyroradii of the ICE-emitting ions, where a relative width of $\Delta f/f \lesssim 0.1$ corresponds to a radial extent of $\Delta R \simeq 20$ cm in JET. The Larmor radii of the energetic fusion products (3.5 MeV α particles and 3.0 MeV protons) from the PTE discharge at the edge were around 12 cm, so ΔR could hardly be any smaller.

[33] This was reported by Cottrell and Dendy (1988) and by Cottrell et al. (1993) for ICE at JET with the peaks satisfying $\Delta f/f \simeq 0.1 \ll a/R = 0.4$. All other reports of ICE show similar ICE spectral widths.

Several factors besides the width in the radial location from the gyroradius may contribute to the width of the spectral peaks, including Doppler broadening, relativistic effects, collisions, radiation damping, and quantum effects, but their contributions are all small.[34] The contribution to the spectral width from the Doppler effect depends on the angle of propagation of the ICE defined by $\cos\theta = \mathbf{k}\cdot\mathbf{B}/kB$ with $\mathbf{k}$ the wave vector of the emission, where an estimate is

$$\Delta\omega_n \approx n\omega_\mathrm{c}\frac{v_\mathrm{t}}{c}\left|N\cos\theta\right| \lesssim 0.01\,\omega_c \tag{2.32}$$

for perpendicular propagation and a velocity spread $v_\mathrm{t} = 10^6\ \mathrm{m\,s^{-1}}$. Similarly, relativistic effects contribute

$$\Delta\omega_n \approx n\omega_\mathrm{c}\left(\frac{v_\mathrm{t}}{c}\right)^2 \approx 10^{-4}\,\omega_\mathrm{c}. \tag{2.33}$$

Thus, relativistic effects are on the order of the Doppler effects if and only if $|N\cos\theta| < v_\mathrm{t}/c$, which is only satisfied for propagation angles close to 90°. Even in that case, the line broadening is negligible. The line broadening due to collisions is on the order of the collision frequency, so

$$\Delta\omega_n \approx \nu \approx \omega_p\frac{\ln\Lambda}{\Lambda} \approx 10^{-4}\,\omega_\mathrm{c} \tag{2.34}$$

for $\omega_p = 10^{10}$ Hz and $\Lambda = 10^8$ the number of particles in the Debye sphere. For radiation damping, the line broadening is

$$\Delta\omega_n \approx \frac{\omega_\mathrm{c}}{3\pi}\frac{\omega_\mathrm{c}}{\omega_\mathrm{p}}\frac{1}{\Lambda}\left(\frac{v_\mathrm{th}}{c}\right)^3 \approx 10^{-10}\,\mathrm{Hz}. \tag{2.35}$$

The line broadening contributed by quantum effects is even smaller.

In conclusion, the dominant line broadening effect is from the radial location dependence of the toroidal field strength affecting the harmonic cyclotron frequencies.

2.2.3 Excitation mechanism

Ion cyclotron emission occurs when one or more of the following three conditions are satisfied: (i) instabilities expel beam ions to the plasma edge, (ii) there is an anisotropic fast-ion population in the plasma edge, and (iii) when initializing neutral-beam injection so the minority energetic ion distribution function is non-monotonic with energy.[35] Common to all three scenarios is either an inversion in velocity space of the fast-ion distribution function, i.e., $\partial f/\partial v_\perp > 0$, or anisotropies from gradients in pitch, triggering the magnetoacoustic cyclotron instability (MCI), with the MCI being the most likely mechanism for the generation of ICE.

2.2.3.1 The magnetoacoustic cyclotron instability

The suggested excitation mechanism for ICE has been the magnetoacoustic cyclotron instability since the 1990s.[36] The magnetoacoustic cyclotron instability excites fast Alfvén waves at multiple cyclotron harmonics of a non-Maxwellian energetic ion population when in the presence of a more numerous thermal ion species. The fast Alfvén waves are excited collectively through wave-particle cyclotron resonance with the free energy available to excite the waves provided by anisotropy or population inversion.

[34] See Bornatici et al. (1983) for the approximations of the line broadening effects for cyclotron emission from electrons in fusion plasmas.

[35] W. W. Heidbrink et al. (2006), p. 324. See also Cottrell et al. (1993), p. 1380.

[36] See Dendy et al. (1992), Dendy et al. (1993), and Dendy et al. (1994). See also McClements et al. (2015) and Dendy and McClements (2015).

The MCI comprises fast Alfvén waves propagating at large angles (close to 90°) to the magnetic field at cyclotron harmonics of an energetic ion population with a non-Maxwellian velocity-distribution.[37] This results in an instability with growth rates at the cyclotron harmonic frequencies. The MCI occurs at locations where an energetic ion population has an inverted velocity gradient, i.e., $\partial f/\partial v > 0$, where wave-particle cyclotron resonances may occur between the energetic ions and waves on the compressional Alfvén branch, with the waves supported by the bulk plasma and propagating close to perpendicular to the magnetic field. Furthermore, studies suggest that ICE emission depends on the perpendicular fast-ion to local Alfvén speed ratio $v_\perp/v_\mathrm{A}$, where the MCI is more readily excited for super-Alfvénic energetic ion populations, i.e., when $v_\perp/v_\mathrm{A} \gtrsim 1$.[38]

At the early experiments at JET measuring ICE,[39] distributions with such local inverted gradients were detected from marginally-trapped alpha particles in the outer midplane plasma, born from fusion reactions in the core, on trapped orbits just above the trapped-passing boundary, whose drift orbits had large radial excursions to the edge; see Fig. 2.2.

These same experiments observed a linear relation between the measured ICE intensity P_ICE and the neutron emission rate R_N over six decades of intensity with a best fit of $P_\mathrm{ICE} \propto R_\mathrm{N}^{0.9\pm0.1}$. This linear relation strongly indicates that the measured ICE was emitted by the alpha particles from the fusion reactions in the core.

2.2.4 Ring beams

Models for velocity-space distributions containing non-Maxwellian features able to provide the free energy to drive the MCI have, for the case of perpendicular propagation, included shells, extended shells, and rings.[40] The ring model was motivated by the velocity-space distribution of the large-excursion trapped orbits observed at JET during the PTE, where only the trapped orbits born in a narrow pitch range around 55° were able to make sufficiently large radial excursions to emit ICE at the measured location.[41]

Since the details of the underlying velocity-space structure does not affect the underlying character of the magnetoacoustic cyclotron instability in terms of excitation of fast Alfvén waves at ion cyclotron harmonics, a velocity-space distribution of energetic ions with a drifting Maxwellian distribution of velocities parallel to the magnetic field and a unique velocity perpendicular to the magnetic field has typically been used.[42] Such velocity-space distributions may be written as

$$f(v_\parallel, v_\perp) = \frac{1}{2\pi^{3/2} u v_r} \exp\left(-\frac{(v_\parallel - v_\mathrm{d})^2}{v_r^2}\right) \delta(v_\perp - u), \tag{2.36}$$

where u is the unique perpendicular speed, v_d the average parallel drift speed, and v_r the parallel velocity spread of the ions. Variations of Eq. (2.36) have been used in analytical investigations

[37] McClements et al. (1996), p. 546.
[38] See Carbajal et al. (2014).
[39] See, for example, the discharges mentioned in Cottrell and Dendy (1988), Dendy et al. (1992), and Cottrell et al. (1993).
[40] Dendy et al. (1994), p. 1919. See also Belikov and Kolesnichenko (1975), Dendy et al. (1992), Dendy et al. (1993), and McClements and Dendy (1993).
[41] Cottrell et al. (1993), p. 1379 f.
[42] Dendy et al. (1994), p. 1919. Drifting rings are also used as initial distributions for most PIC simulations.

and PIC plasma simulations, such as

$$f(v_\parallel, v_\perp) \propto \exp\left(-\frac{(v_\parallel - v_\mathrm{d})^2}{v_r^2}\right) \exp\left(\frac{(v_\perp - u)^2}{u_\mathrm{r}^2}\right), \tag{2.37}$$

$$f(v_\parallel, v_\perp) \propto \delta(v_\parallel - v_\mathrm{d})\delta(v_\perp - u), \tag{2.38}$$

sometimes with $v_\mathrm{d} = 0$.

Modelling the ICE measurements from KSTAR made during discharge #11513, Chapman et al. (2017) argued that the fusion-born protons driving the ICE could be represented by a delta-function ring distribution. Still, driving the MCI is possible only if $v_\perp$ is comparable to the local Alfvén velocity, as has been demonstrated by analytical and simulation studies, see, e.g., Dendy et al. (1992), Dendy et al. (1993), Dendy et al. (1994), McClements et al. (1996), Cook et al. (2013), Carbajal et al. (2014), and Carbajal et al. (2017). Thus, in their simulations, initial $v_\perp$ was chosen corresponding to an energy of 150 keV which was approximately 5% of the birth energy at 3.0 MeV and comparable to the local Alfvén speed.

2.3 Fast-ion loss detectors

In a fast-ion loss detector (FILD), fast ions pass through a pinhole in a probe head, are collimated by a slit, and impinge on a plate. FILDs are located in the far scrape-off layer and are positioned at different toroidal and poloidal angles depending on the machine. FILDs with two different working mechanisms exist: one is a Faraday cup FILD measuring the current from ions impacting and passing through a stack of thin foils, and another is a scintillator FILD measuring photons emitted by a scintillating material at the ion impact locations. Faraday cup FILDs are installed at JET[43] and W7-X[44]. Scintillator FILDs are installed at ASDEX Upgrade[45], TCV[46], and other machines[47]. JET also has a scintillator FILD supplementing the data from the Faraday cup fast-ion loss detector array.[48] FILDs for ITER[49], JT-60SA[50], and W7-X[51] are being designed. The investigations contained in this dissertation concerns scintillator FILDs, so the Faraday cup technique will not be discussed.

The scintillator FILD design dates back to 1987 at TFTR, and the working principle remains the same.[52] The strike position on the scintillator plate indicates the gyroradius ρ and pitch angle α: ions with larger ρ impinge further away vertically from the pinhole, and a larger α further away horizontally. Thus, the FILD measures 2D velocity-space, since the (α, ρ)-coordinates are

[43] Darrow et al. (2004) and Bonofiglo et al. (2020).
[44] Ogawa et al. (2019).
[45] Garcia-Munoz (2006), Garcia-Munoz et al. (2009), Garcia-Munoz et al. (2010), and Galdon-Quiroga, Garcia-Munoz, Sanchis-Sanchez, et al., 2018.
[46] Stipani (2021) and Poley-Sanjuan et al. (2023).
[47] See Chapter 6, p. 88.
[48] Bonofiglo et al. (2020).
[49] Garcia-Munoz et al. (2016).
[50] Ayllon-Guerola et al. (2021).
[51] Jansen Van Vuuren et al. (2022).
[52] Zweben (1989) and Zweben et al. (1990).

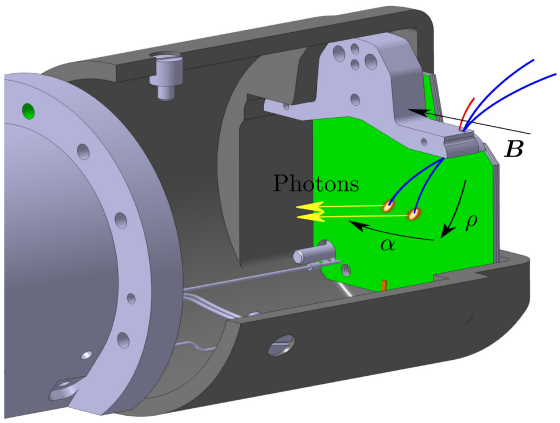

Figure 2.4: Working principle of a FILD. The blue trajectories pass through the pinhole, and the red is blocked. From Poley-Sanjuan et al. (2023).

equivalent to $(v_\parallel, v_\perp)$. This follows from the expressions

$$v_\perp = \frac{eB}{m}\rho, \tag{2.39a}$$

$$v_\parallel = v_\perp \frac{\lambda}{(1-\lambda^2)^{1/2}}, \tag{2.39b}$$

$$E = \frac{eB}{2m(1-\lambda^2)}\rho^2, \tag{2.39c}$$

where $\lambda = \cos(\alpha) = v_\parallel/v$ is the pitch. Depending on the local magnetic field strength, the gyroradii of the ions are around 2-3 cm for TCV[53], 3-6 cm for FILD1 at ASDEX Upgrade,[54] and 7 cm for fusion-born alpha particles at ITER[55]. An illustration of a FILD probe head is illustrated in Fig. 2.4.

After passing through the FILD pinhole, the lost fast ions are collimated to allow only ions within a small range of gyrophases to pass through. The gyrophase interval of the ions able to pass through the pinhole is called the "gyrophase acceptance cone" and is typically relatively limited in width; see Fig. 2.5. The collimation minimizes the distribution in gyroradius and pitch angle as a result of the ions having different gyrophases when entering through the FILD slit.

The width and length of the FILD probe head determines the gyroradius and the pitch angles of the ions measurable by the FILD. The width of the pinhole determines the accepted gyroradii, and the length determines the accepted pitch angles. A wider slit may also result in a larger gyrophase acceptance cone and thus a lower resolution. Thus, designing a FILD requires careful consideration of these factors.

Earlier FILDs were designed using a single slit that ions could pass through; see Fig. 2.6(a). Newer models are equipped with a double-slit system to detect both co- and counter-going lost fast ions. This is useful at TCV since ions can be injected from two NBIs pointing in opposite directions. This principle is also used for the conceptual design of the scintillator-based FILD for

[53] Stipani (2021), p. 56.

[54] See Galdon-Quiroga, Garcia-Munoz, Sanchis-Sanchez, et al. (2018), p. 7 ff., where a study of reconstructions for FILD1 using Tikhonov regularization was performed for lost fast ions with gyroradii of 3.1 cm, 4.3 cm, and 5.4 cm from NBI prompt losses.

[55] Garcia-Munoz et al. (2016), p. 2.

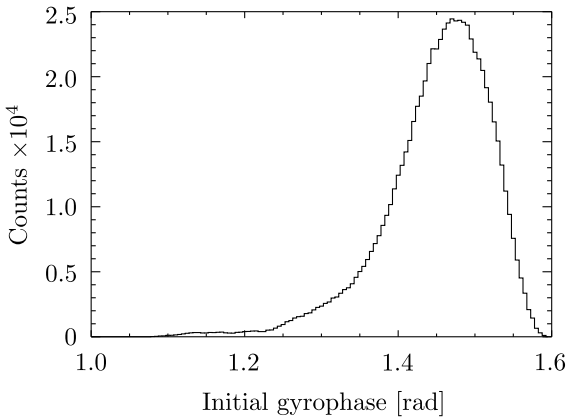

Figure 2.5: A histogram of the markers' initial gyrophase not blocked by the collimator in FILD1 at ASDEX Upgrade. Note that the gyrophase acceptance cone is unique to this FILD and is given by its probe head and slit geometries. From Galdon-Quiroga (2018).

W7-X.[56] The double-slit probe head configuration is illustrated in Fig. 2.6(b).

The probe head is oriented with the local magnetic field in the plane of the scintillator. This avoids an angle between the local magnetic field and the scintillator plate, which results in trajectories not representing the gyroradii and pitch angles. Perfect alignment is impossible in practice and especially during a campaign, so the velocity space measurements are always based on calibration using FILDSIM.

The scintillator plate is coated with a scintillating material emitting photons when impacted by fast ions. The optimal choice of coating has been assessed to be TG-Green due to several optimal properties such as high sensitivity to fast ions, low sensitivity to neutrons, electrons, and gamma rays, reliable light emission of 540 nm in the required temperature range of 400-700 K without quenching, fast response to identify MHD fluctuations, longer lifetime under intense ion flux compared to other materials, and high saturation levels. The decay time for TG-Green is 490 ns, allowing for detection of photons from MHD activity with frequencies below 2 MHz.[57] The photon yield per unit length dY/dx of the TG-Green material has been determined experimentally for protons, deuterium, and α particles at an acceleration facility for a 9 μm thick coating[58] and follows to a good approximation Birks's model[59] given by

$$\frac{dY}{dx} = \frac{\epsilon \frac{dE}{dx}}{1 + k \frac{dE}{dx}} \tag{2.40}$$

for (almost all) energies relevant for fast ions.[60] The fraction dE/dx is the energy released per unit length by the ion, ϵ is a measure of the material efficiency, and k is a measure of the material quenching. If the quenching is low, the relation between the photon yield per unit length and the energy deposition per unit length becomes linear. The relationship between the yield and the energy of alpha particles for TG-Green is almost linear; see Fig. 2.7.

[56] Jansen Van Vuuren et al. (2022).
[57] Garcia-Munoz et al. (2009), p. 4.
[58] See Jiménez-Ramos et al. (2014), Rodriguez-Ramos et al. (2017), and Galdon-Quiroga, Garcia-Munoz, Salewski, et al. (2018).
[59] Birks (1951).
[60] The yield per unit length is characterized for energies in the range 0.6 MeV to 3.0 MeV. Thus, the range does not include 3.5 MeV alpha particles.

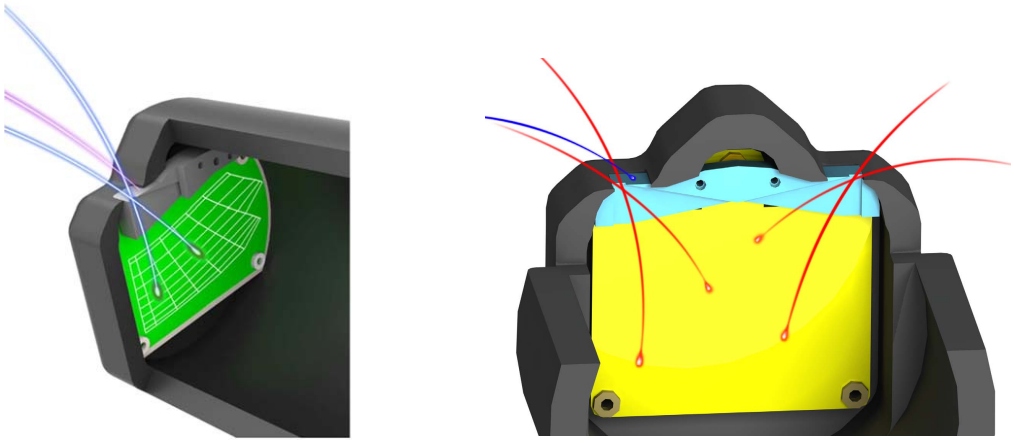

(a) (b)

Figure 2.6: (a) One slit and (b) double slit FILD probe head configurations. From Galdon-Quiroga, Garcia-Munoz, Salewski, et al. (2018) and Jansen Van Vuuren et al. (2022).

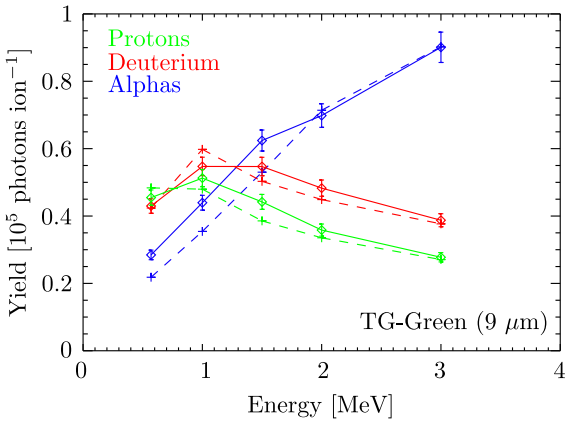

Figure 2.7: The yield for protons (green), deuterium (red), and alpha particles (blue) for energies in the range 0.6-3.0 MeV. Adapted from Galdon-Quiroga, Garcia-Munoz, Salewski, et al. (2018).

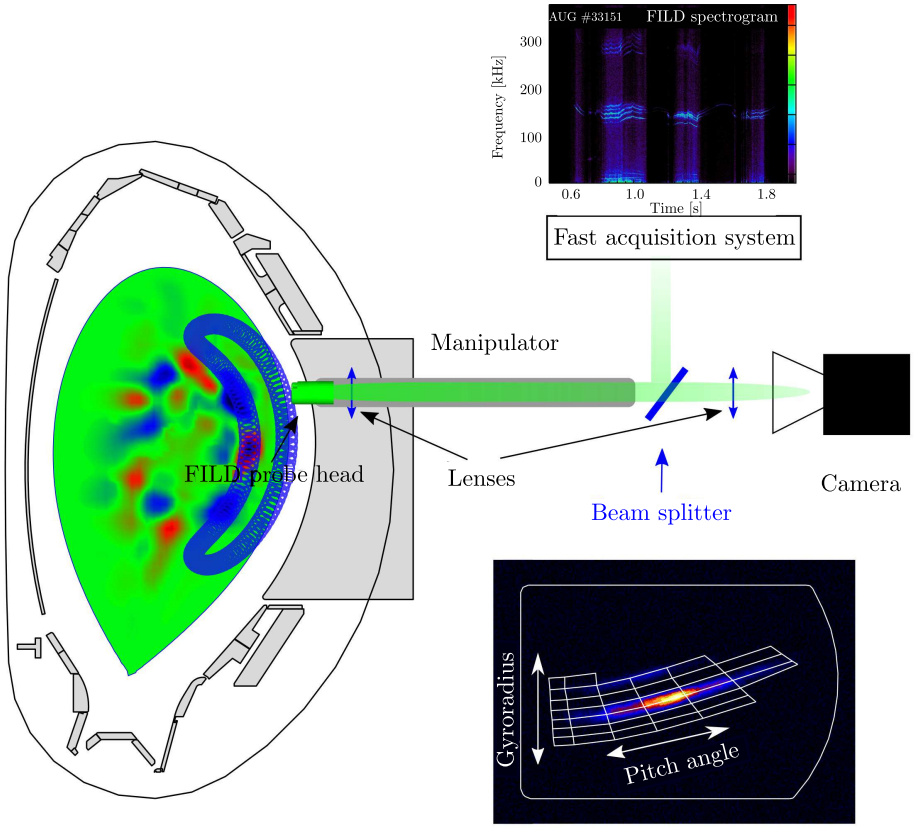

Figure 2.8: Elements of a FILD diagnostic illustrated for FILD1 at ASDEX Upgrade: the FILD probe head, the camera, and a fast acquisition system. Adapted from Galdon-Quiroga (2018).

The photons emitted by the scintillator material is imaged onto a charge-coupled device (CCD) with high spatial resolution to image the measured velocity space and a photomultiplier tube (PMT) array.[61] The PMTs enable time-resolved measurements of fast-ion losses with bandwidth of at least 1 MHz. The individual PMTs are distributed over the scintillator plate to observe time-resolved events occurring at specific locations on the scintillator. Measurements from PMTs can be Fourier transformed to obtain the frequency of the fast-ion losses.[62] A schematic of the FILD1 setup at ASDEX Upgrade is shown in Fig. 2.8.

The slit and scintillator plate are enclosed by a graphite shield. The graphite shield protects against heat loads and must do so without blocking the ions with gyroradii and pitch angles in the desired range. The latest estimates show that the same material as used in today's FILDs is sufficient for ITER operations with the detector aperture positioned approximately 11 cm outside the diagnostic first wall, where the heat load is comparable to that in present devices.[63]

The measurement process adds a blurring effect to the true velocity space distribution function of the fast ions. The velocity space distribution function of the fast ions passing through the pinhole can be obtained by solving an inverse problem to be discussed in subsequent chapters.

[61] The FILD at TCV initially used a PMT setup, which has recently been changed to a 128 avalanche photodiode matrix camera allowing for a temporal resolution up to 4 MHz; cf. Poley-Sanjuan et al. (2023).
[62] Garcia-Munoz et al. (2009) and Galdon-Quiroga (2018), p. 30 ff.
[63] Garcia-Munoz et al. (2016).

A thorough understanding of fast-ion confinement is crucial to attain burning plasmas in the future. Experiments investigating the behaviour of fast ions resulting from NBI, ICRH, and fusion reactions provide information on fast-ion confinement for future operations, including planned ITER operations. Scenarios resulting in fast-ion losses are important to understand since fast-ion losses reduce a fusion reactor's performance by reducing the internal heating power and cause damage to plasma-facing components.

Damage to a FILD probe head in ASDEX Upgrade was reported by Galdon-Quiroga, Garcia-Munoz, Sanchis-Sanchez, et al. (2018), where the FILD1 probe head was damaged during discharge #30810 due to fast-ion losses from MHD activity. An automatic pneumatic positioning system has been installed for the FILD at TCV allowing a positioning closer to the plasma and automatic retraction to avoid heating past 300 °C.[64] A similar retracting system is considered in the conceptual design of the ITER FILD.[65]

2.4 Ill-posed inverse problems

The need to solve inverse problems arises in many different scientific disciplines and applications. One example is image reconstruction from projections as done in medical imaging, geoscience, and materials science. Another example is fault inspection of, e.g., pipes to detect defects and cracks using X-ray scanning to compute cross-sectional images. To perform the reconstructions requires, e.g., the physics of X-ray attenuation, the strength of the X-ray source, and a specification of the geometry of the object. A third example is rotational image deblurring as used in star cameras for satellite navigation, where the center of rotation and rotation angle is required to perform the reconstruction.[66] Common to the three examples is using a mathematical model to infer hidden features from indirect measurements. This same approach can be used to obtain the velocity-space distribution function of fast ions at specific locations in a magnetically confined fusion device using a large range of fast ion diagnostics.[67]

Inverse problems belong to the class of ill-posed problems.[68] A problem is ill-posed if it violates at least one of three requirements: (i) existence, (ii) uniqueness, and (iii) stability. Thus, a solution must exist, it must be unique, and the solution must depend continuously on the data. Examples violating the three requirements are as follows:[69]

(i) The overdetermined system

$$\begin{pmatrix} 1 & 1 \\ 1 & 2 \\ 1 & 3 \end{pmatrix} x = \begin{pmatrix} 2.1 \\ 3.0 \\ 3.9 \end{pmatrix} \tag{2.41}$$

has no solution, but the least-squares solution $x_{\mathrm{LS}} = \operatorname{argmin}_x \|Ax - b\|_2 = (1.2, 0.9)^{\mathrm{T}}$ can be defined.

(ii) The system

$$\begin{pmatrix} 1 & 2 \\ 1 & 2 \end{pmatrix} \begin{pmatrix} x_1 \\ x_2 \end{pmatrix} = \begin{pmatrix} 3 \\ 3 \end{pmatrix} \tag{2.42}$$

[64] Stipani (2021), p. 63 ff. and Poley-Sanjuan et al. (2023).
[65] Garcia-Munoz et al. (2016).
[66] See Hansen (2019), p. 3 ff. for a brief description of these three examples.
[67] See, e.g., Salewski et al. (2011) describing analytically the first computation of weight functions for CTS.
[68] Hansen (2010), p. 2.
[69] Hansen (2019).

has infinitely many solutions, but the minimum-norm solution $x_0 = (0.6, 1.2)^{\mathrm{T}}$ defined by $x_0 = \operatorname{argmin}_x \|x\|_2$ subject to $Ax = b$ can be defined.

(iii) The unperturbed system $Ax = b$ with

$$A = \begin{pmatrix} 1.0 & 2.1 & 3.0 \\ 4.0 & 5.0 & 5.9 \\ 7.0 & 8.0 & 9.0 \end{pmatrix}, \quad x = \begin{pmatrix} 1 \\ 1 \\ 1 \end{pmatrix}, \quad \text{and} \quad b = Ax = \begin{pmatrix} 6.1 \\ 14.9 \\ 24.0 \end{pmatrix}, \tag{2.43}$$

can be perturbed by adding a small "noise" component to b, so $\tilde{b} = b + (0, 0.001, 0)$. The naïve solution $\tilde{x}$ is then

$$\tilde{x} = A^{-1}\tilde{b} = \begin{pmatrix} 0.927 & 1.171 & 0.904 \end{pmatrix}, \tag{2.44}$$

which is far from the original solution $x = (1, 1, 1)^{\mathrm{T}}$.

Inverse problems are *always* ill-posed.[70] Therefore, as was done for the above three examples, the problem can be reformulated so a solution can be found. In the case of the solutions sensitivity to perturbations, the problem is regularized to stabilize the solution.

2.4.1 Fredholm integral equation of the first kind

The forward model typically used to model the signal containing information about the fast-ion velocity-space distribution function in magnetically confined nuclear fusion has the general form of a Fredholm integral equation of the first kind

$$s = \iint W f \, \mathrm{d}\boldsymbol{x} \, \mathrm{d}\boldsymbol{v}. \tag{2.45}$$

Such integral equations have a smoothing effect on s, i.e., high-frequency components of f are damped.[71] It follows that the inverse problem, computing f from s and W, amplifies high-frequency components, with higher-frequency components receiving more amplification. In fact, the perturbation of f can be arbitrarily large if the perturbation δs has a sufficiently high frequency component.

2.4.2 Degree of ill-posedness

The singular value decomposition (SVD) can provide useful insights into the characteristics of a matrix. The SVD of W takes the form

$$W = U\Sigma V^T = \sum_{i=1}^{r} u_i \sigma_i v_i^T, \tag{2.46}$$

where $r \leq \min(m, n)$ is the rank of W, $U \in \mathbb{R}^{m \times n}$ consists of the left singular vectors $U = (u_1, \ldots, u_n)$, $\Sigma \in \mathbb{R}^{n \times n}$ with $\Sigma = \operatorname{diag}(\sigma_1, \ldots, \sigma_n)$ and $\sigma_1 \geq \sigma_2 \geq \cdots \geq \sigma_n$, and $V \in \mathbb{R}^{n \times n}$ consists of the right singular vectors $V = (v_1, \ldots, v_n)$. The left and right singular vectors comprise orthonormal sequencies $\{u_i\}$ and $\{v_i\}$ satisfying

$$W v_i = \sigma_i u_i, \quad W^T u_i = \sigma_i v_i, \tag{2.47}$$

[70] Hansen (2019).

[71] This result follows from the Riemann-Lebesgue lemma. See Goldberg (1964), p. 370 ff.

and σ_i are the singular values of Σ.[72] The singular values decay towards zero with increasing i. Thus, the right singular vectors v_i contain information about the behaviour of the solution to the inverse problem. Right singular vectors with higher indices correspond to higher frequency components, which may be amplified when solving the inverse problem.

The degree of ill-posedness of Eq. (2.45) can be defined in terms of the singular values of W. According to the Picard condition, the equation $Wf = s$ is solvable if and only if[73]

$$\sum_{i=1}^{\infty} \frac{\left(u_i^T s\right)^2}{\sigma_i^2} < \infty, \tag{2.48}$$

and the solution to the equation is

$$f = \sum_{i=1}^{\infty} \frac{u_i^T s}{\sigma_i} v_i. \tag{2.49}$$

It follows that perturbing the signal s by $s^\delta = s + \delta v_i$, the solution is $f^\delta = f + \delta\sigma_i^{-1}u_i$. Hence

$$\frac{\left\|f^\delta - f\right\|}{\left\|s^\delta - s\right\|} = \frac{\left\|\delta\sigma_i^{-1}u_i\right\|}{\|\delta v_i\|} = \frac{1}{\sigma_i}. \tag{2.50}$$

Since σ_i tends to zero with increasing i, the ratio $\left\|f^\delta - f\right\| / \left\|s^\delta - s\right\|$ can be made arbitrarily large. The influence of noise in the data vector s in the solution is controlled by the rate of decay to zero of the singular values. Thus, the slower the decay to zero, the less ill posed the equation. The terminology is "mildly ill-posed" for slow decay to zero and "severely ill-posed" for very rapid decay.[74]

Observe that for discrete ill-posed problems, the norm of the solution is always bounded due to the sum being finite. Thus, there is, strictly speaking, no Picard condition. However, it is possible to introduce a discrete Picard condition as follows.[75] At some point, the numerical values of the singular values reach the noise level or machine precision, typically 10^{-16}, below which the singular values cannot decay any further. Denote this level by τ. The discrete Picard condition is then satisfied if, for all singular values larger than τ, the coefficients $\left|u_i^T s\right|$ decay faster than σ_i on average.[76]

A Picard plot illustrates the degree of ill-posedness by plotting the singular values σ_i, $\left|u_i^T s\right|$, and $\left|u_i^T s\right| / \sigma_i$. A Picard plot of a synthetic ICE measurement with 10% noise is shown in Fig. 2.9(c). Observe that the discrete Picard condition is satisfied for the first ~ 30 components, indicating a need for regularization when computing the location of the ions emitting the ICE in velocity space to limit the influence of the components associated with small singular values. The problem is mildly ill posed due to the slow rate of decay of the singular values.

The signal without noise is denoted s^{exact} and the synthetic/measured signal thus $s = s^{\text{exact}} + e$, where $Wf^{\text{true}} = s^{\text{exact}}$. The noise and the exact measurement are assumed to be uncorrelated. The influence from the noise on the SVD coefficients can be seen to be

$$u_i^T s = u_i^T (s^{\text{exact}} + e) = u_i^T s^{\text{exact}} + u_i^T e, \quad 1 = 1, \ldots, n. \tag{2.51}$$

[72] Some mathematical details in this exposition are omitted, cf. Kress (2014), p. 309 ff. See also Hansen (2010), p. 28 ff.
[73] Kress (2014), p. 311 ff.
[74] Kress (2014), p. 312.
[75] Hansen (2008), p. 16 ff.
[76] Hansen (2008), p. 16 ff. and Hansen (2010), p. 37.

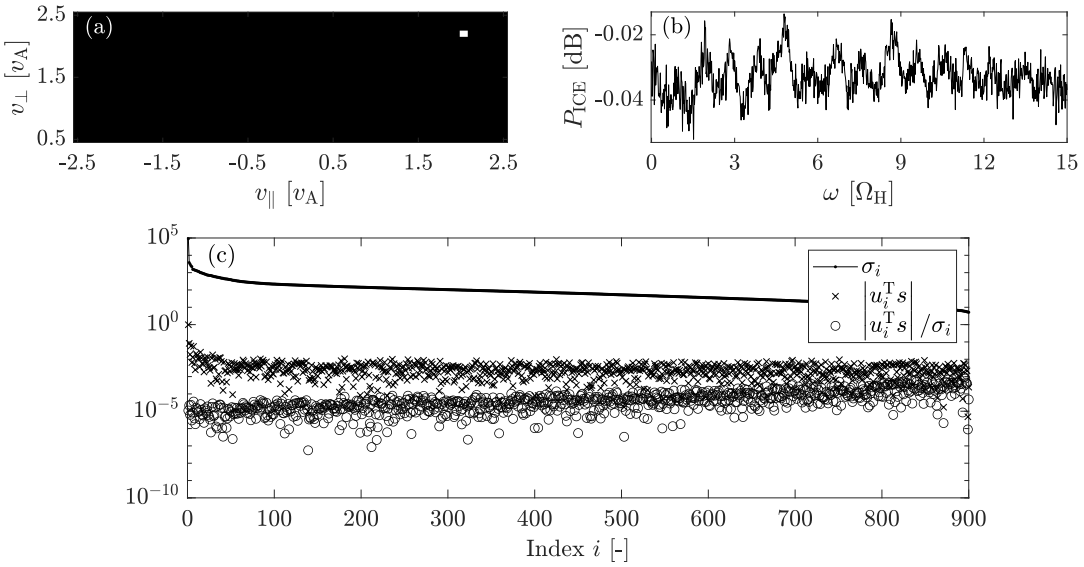

Figure 2.9: (a) Location in velocity space of an energetic ion species at $(v_\parallel, v_\perp) = (2.2\,v_\mathrm{A}, 2.2\,v_\mathrm{A})$ emitting ion cyclotron emission. (b) Normalized ion cyclotron emission spectrum with 10% noise emitted by the ions at the velocity-space location in (a). (c) Picard plot for (a) and (b).

Depending on the size of either term, the SVD coefficients satisfy[77]

$$u_i^T s \approx \begin{cases} u_i^T s^\mathrm{exact}, & \left|u_i^T s^\mathrm{exact}\right| > \left|u_i^T e\right|, \\ u_i^T e, & \left|u_i^T s^\mathrm{exact}\right| < \left|u_i^T e\right|. \end{cases} \tag{2.52}$$

Thus, the coefficients $\left|u_i^T s\right| \gg \sigma$ corresponding to larger singular values σ_i contain information about the exact data s^exact. The coefficients $\left|u_i^T s\right| \approx \sigma$ corresponding to smaller singular values are influenced by the noise. Extremely large errors in the naïve solution $f = W^\dagger s$ are a result from the noisy SVD components. Thus, regularization is needed to obtain a useful solution.

2.4.3 Previously applied reconstruction techniques

This section summarizes the reconstruction techniques that have been applied to obtain velocity-space distribution functions previously.[78] These techniques comprise truncated SVD, zeroth and first-order Tikhonov regularization, minimum Fisher information, and maximum entropy.[79]

2.4.3.1 Truncated singular value decomposition

From the above discussion, it is seen that the large errors in the naïve solution $f = W^\dagger s$ is due to the noisy SVD components of the form $u_i^T s/\sigma_i \approx u_i^T e/\sigma_i$. Assuming the equation satisfies the

[77] See Hansen (2010), p. 41 ff. for a rigorous derivation.

[78] See Jacobsen et al. (2016a) and Jacobsen (2015), Chapter 4, for an investigation of these methods for velocity-space tomography from FIDA measurements. The primary reconstruction method used prior to the publication was the truncated singular value decomposition, cf. Salewski et al. (2013). Since then, the primary technique has been Tikhonov regularization, cf. Salewski et al. (2017), Salewski, Geiger, Jacobsen, et al. (2018), Galdon-Quiroga, Garcia-Munoz, Salewski, et al. (2018), Madsen, Salewski, et al. (2020), and Madsen, Huang, et al. (2020).

[79] These techniques were already considered for X-ray tomography in 1996, cf. Anton et al. (1996).

Picard condition, the SVD components of the exact solution are those coefficients with small indices i satisfying $u_i^T s/\sigma_i \approx u_i^T s^{\text{exact}}/\sigma_i$. So, obtaining a solution close to the exact solution can be obtained by truncating the solution in Eq. (2.49) after the first k components:

$$f_k \coloneqq \sum_{i=1}^{k} \frac{u_i^T s}{\sigma_i} v_i. \tag{2.53}$$

The value of k is ideally chosen so all noise-dominated SVD components are removed. This can typically be determined by an inspection of a Picard plot. Figure 2.10 shows the reconstructions from synthetic CTS/FIDA data from four views as a function of including additional SVD components.[80] The reconstruction improves with an increasing number of SVD components until noise becomes apparent at around 280 SVD components.

2.4.3.2 Tikhonov regularization

The problem formulation using Tikhonov regularization incorporates the regularity requirement of the solution, defining the solution f^* as

$$f^* = \underset{f}{\operatorname{argmin}} \left\{ \|Wf - s\|_2^2 + \lambda^2 \|Lf\|_2^2 \right\}, \tag{2.54}$$

where $L \in \mathbb{R}^{n \times n}$ is a regularization matrix chosen to specify which aspects of f should be regularized. For $L = I$, which is zeroth-order Tikhonov regularization, the norm of f is controlled, thereby suppressing the large noise components of f.

The first term in Eq. (2.54) controls how well the solution fits the data s. This term cannot be too large, since f would not solve the problem in that case, but the term should also not be too small, since then the solution fits to the noise. The balance between the goodness-of-fit and the regularity of the solution is determined by the value of the regularization parameter λ. Smaller values of λ give more weight to the goodness-of-fit term, whereas larger values of λ give more weight to the regularity of the solution.

For first-order Tikhonov regularization, gradients of the solution are penalized. For velocity-space tomography, a natural function to regularize is therefore

$$\mathcal{R} = (\Delta_{v_\parallel} f)^{\mathrm{T}} (\Delta_{v_\parallel} f) + (\Delta_{v_\perp} f)^{\mathrm{T}} (\Delta_{v_\perp} f) \tag{2.55}$$

$$= \left\| f_{v_\parallel} \right\|_2^2 + \left\| f_{v_\perp} \right\|_2^2, \tag{2.56}$$

where $\Delta_{v_\parallel}$ and $\Delta_{v_\perp}$ represent the differential operators with respect to $v_\parallel$ and $v_\perp$, and $f_{v_\parallel}$ and $f_{v_\perp}$ denotes differentiation of f with respect to $v_\parallel$ and $v_\perp$. Since $\|Lf\|_2^2 = (Lf)^{\mathrm{T}} Lf = f^T L^T L f$, it follows that

$$L^T L = \nabla_{v_\parallel}^{\mathrm{T}} \nabla_{v_\parallel} + \nabla_{v_\perp}^{\mathrm{T}} \nabla_{v_\perp}. \tag{2.57}$$

Depending on the finite difference approximations chosen for the derivatives, different versions of L are obtained.[81]

Since

$$\|a\|_2^2 + \|b\|_2^2 = a^{\mathrm{T}} a + b^{\mathrm{T}} b = \begin{pmatrix} a \\ b \end{pmatrix}^{\mathrm{T}} \begin{pmatrix} a \\ b \end{pmatrix} = \left\| \begin{pmatrix} a \\ b \end{pmatrix} \right\|_2^2, \tag{2.58}$$

[80] Salewski et al. (2013), p. 6.

[81] See Jacobsen (2015), p. 51 ff., for an example using the backwards finite difference approximation $\frac{\partial f_{i,j}}{\partial v_\perp} \simeq \frac{f_{i,j} - f_{i-1,j}}{\Delta v}$.

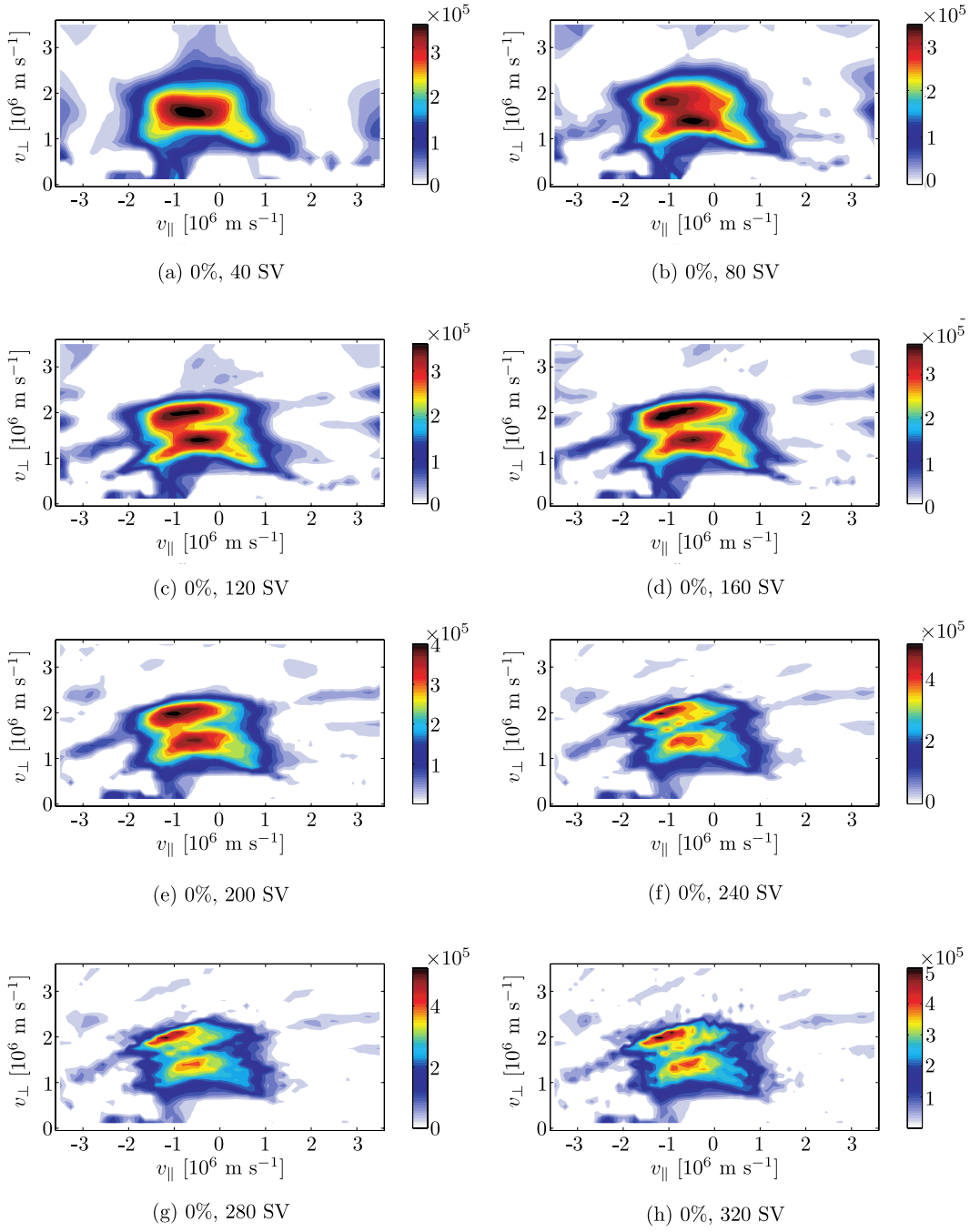

(a) 0%, 40 SV

(b) 0%, 80 SV

(c) 0%, 120 SV

(d) 0%, 160 SV

(e) 0%, 200 SV

(f) 0%, 240 SV

(g) 0%, 280 SV

(h) 0%, 320 SV

Figure 2.10: Reconstructions of a fast ion velocity space distribution function from noiseless synthetic CTS/FIDA data from four views as a function of including additional SVD components. From Salewski et al. (2013), p. 6.

Eq. (2.54) can be written in the form

$$f^* = \underset{f}{\operatorname{argmin}} \left\| \begin{pmatrix} W \\ \lambda L \end{pmatrix} f - \begin{pmatrix} s \\ 0 \end{pmatrix} \right\|_2, \tag{2.59}$$

which is the most computationally efficient and numerically stable implementation.[82] The normal equations are

$$\begin{pmatrix} W \\ \lambda L \end{pmatrix}^{\mathrm{T}} \begin{pmatrix} W \\ \lambda L \end{pmatrix} f = \begin{pmatrix} W \\ \lambda L \end{pmatrix}^{\mathrm{T}} \begin{pmatrix} s \\ 0 \end{pmatrix}, \tag{2.60}$$

so the solution can be computed as

$$f^* = (W^{\mathrm{T}} W + \lambda^2 L^{\mathrm{T}} L)^{-1} W^{\mathrm{T}} s. \tag{2.61}$$

To illustrate the effect of the regularization for zeroth-order Tikhonov regularization, inserting the SVD of W in Eq. (2.61) for $L = I$ gives[83]

$$f = V(\Sigma^2 + \lambda^2 I)^{-1} \Sigma U^{\mathrm{T}} s \tag{2.62}$$

$$= \sum_{i=1}^{n} \varphi_i^{[\lambda]} \frac{u_i^{\mathrm{T}} s}{\sigma_i} v_i, \tag{2.63}$$

where

$$\varphi_i^{[\lambda]} = \frac{\sigma_i^2}{\sigma_i^2 + \lambda^2} \approx \begin{cases} 1, & \sigma_i \gg \lambda, \\ \sigma_i^2/\lambda^2, & \sigma_i \ll \lambda, \end{cases} \tag{2.64}$$

are filter factors. It follows that the Tikhonov solution can be interpreted as a filtered solution similar to the TSVD solution. The filter factors are close to one for singular values larger than λ, and close to zero for singular values smaller than λ. Thus, λ controls the filtering.

2.4.3.3 Minimum Fisher information regularization

For the model $Wf = s$, minimum Fisher information regularization can be written as the solution to the equation

$$f^* = \underset{f}{\operatorname{argmin}} \left\{ \|Wf - s\|_2^2 + \lambda I(f) \right\}, \tag{2.65}$$

similar to Tikhonov regularization with regularization term $\lambda I(f)$. The Fisher information $I(f)$ is defined as[84]

$$I(f) = \mathbb{E}\left[\left(\frac{\partial \log p\,(s \mid f)}{\partial f} \right)^2 \right]. \tag{2.66}$$

Thus, minimum Fisher information regularization seeks the model with minimum Fisher information fitting the data well. The exact form of Eq. (2.65) depends on the distributions of the likelihood $p(s \mid f)$ and the prior $p(f)$. In some cases, it might even equal Tikhonov regularization if $I(f)$ takes a form similar to a squared norm.

> Based on the characteristics of solutions with minimum Fisher information, Anton et al. (1996) argue that minimum Fisher information regularization is suitable for soft x-ray tomography, where low-emissivity regions are expected to be smooth, and less smoothness is expected in the centre of the plasma where emissivity is high.

[82] Hansen (2010), p. 61.
[83] Hansen (2010), p. 62.
[84] See Frieden (1988), p. 1299 ff. and Fisher (1959).

The MFI principle can be implemented as an iterative procedure with convergence after just a few number of iterations.[85] This is achieved by modifying the $L^{\mathrm{T}}L$ term in Tikhonov regularization with a diagonal weight matrix $W^{[k]}$, where k indicates the iteration number, so

$$L^{\mathrm{T}}L = \Delta_{v_\parallel}^{\mathrm{T}} W^{[k]} \Delta_{v_\parallel} + \Delta_{v_\perp}^{\mathrm{T}} W^{[k]} \Delta_{v_\perp}. \tag{2.67}$$

The zeroth iteration is performed with $W^{[0]} = I$, which is equivalent to first-order Tikhonov regularization. Computations with $k > 0$ are then performed as for Tikhonov regularization with

$$W_{ij}^{[k]} = \begin{cases} \frac{1}{f_i^{[k]}}\delta_{ij}, & f_i^{[k]} > 0, \\ W_{\max}\delta_{ij}, & f_i^{[k]} \leq 0, \end{cases} \tag{2.68}$$

where $W_{\max}$ is an upper bound for the weights. Note that this is no longer a linear algebra problem. Typically, only a few iterations are needed for convergence. In this case, MFI enforces smoothing similar to first-order Tikhonov regularization. Minimum Fisher regularization has been implemented in this form for soft x-ray tomography on TCV[86] and COMPASS[87] and used for velocity-space tomography[88].

2.4.3.4 Maximum entropy regularization

Maximum entropy (ME) regularization can be formulated as the minimization problem

$$f^* = \underset{f}{\operatorname{argmin}} \left\{ \|Wf - s\|_2^2 + \lambda H \right\}, \tag{2.69}$$

similar to Tikhonov regularization and minimum Fisher information regularization, now regularizing the information entropy

$$H = -\sum_{i=1}^{N} \left(f_i - m_i - f_i \ln(f_i/m_i) \right). \tag{2.70}$$

ME algorithms find the solution maximizing the information entropy with respect to a default model $m = (m_i)$. The default model can be chosen as some appropriate theoretical model, e.g., slowing-down distributions, or simply as some constant. The minimum of H is attained for $f_i = m_i$ for all i, i.e., when the solution is equal to the default model.

The motivation for maximum entropy regularization follows from the entropic prior

$$P(f \mid I) = \left(\frac{\lambda}{2\pi}\right)^{n/2} \frac{1}{\sqrt{\prod_i f_i}} \exp\left(\lambda H\right). \tag{2.71}$$

being the most uninformative unbiased prior, where I is some *a priori* information.[89] Regularizing using this prior therefore imposes the least possible assumptions about the solution. It follows

[85] See Anton et al. (1996), p. 1857, where their iterative scheme is converged after two iterations, and Jacobsen (2015), p. 55 ff., with convergence after at most four iterations. According to Anton et al. (1996), the iteration scheme presented here minimizes the Fisher information of f.

[86] See Anton et al. (1996).

[87] See Loffelmann et al. (2016), where a fast implementation of a minimum Fisher Tikhonov regularization algorithm suitable for real-time control of the plasma position is presented.

[88] Jacobsen (2015), p. 55 ff.

[89] Skilling (1989), p. 45 ff.

that the posterior $p(f \mid s, I)$ can be written as[90]

$$P(f \mid s, I) \propto P(s \mid f, I) P(f \mid I) \tag{2.72}$$

$$\propto \exp\left(-\|Wf - s\|\right) \exp\left(\lambda H\right). \tag{2.73}$$

The maximum of the posterior probability is therefore determined as the maximum of

$$\phi(\lambda, f) = -\|Wf - s\|_2^2 + \lambda H, \tag{2.74}$$

where $\lambda > 0$ is a regularization parameter.

The five methods of truncated SVD, minimum Fisher regularization, maximum entropy regularization, and zeroth and first-order Tikhonov regularization were compared by Jacobsen et al. (2016a) applied to synthetic and experimental data of a sawtooth crash at ASDEX Upgrade. Typically, zeroth and first-order Tikhonov regularization is used as the benchmark against which other techniques are measured.[91] Here, the reconstructions for a synthetic NBI distribution are highlighted; see Fig. 2.11. Three different noise levels were investigated: $k = 0.1$, $k = 0.5$, and $k = 0.9$, where k corresponds to η in Eq. (9.21). The NBIs comprise two co-current beams with injection energies at 70 and 80 keV and one counter-current beam with injection energy at 70 keV. Thus, the reconstructed distribution should have non-zero values at higher energies for positive pitch compared to negative pitch. This is observed for most of the reconstructions irrespective of method and noise level. The first-order Tikhonov solution and the minimum Fisher solution result in smooth solutions. The truncated SVD and zeroth-order Tikhonov solutions are very similar as expected from the above discussion. For $k = 0.1$, the truncated SVD, zeroth-order Tikhonov regularization, and maximum entropy solutions distinguish between the full and half injection energy peaks. The smooth solutions from first-order Tikhonov regularization and minimum Fisher regularization do not. For first-order Tikhonov regularization, this is likely due to the value of the regularization parameter being selected according to the L-curve criterion, which tends to overregularize. Also, first-order Tikhonov regularization attenuates sharp NBI peaks.[92]

2.4.4 Choosing the regularization parameter

The reconstructions computed using the above techniques are dependent on the value of the regularization parameter. At present, there does not exist a general-purpose parameter-choice algorithm to determine the optimal k for TSVD or λ for Tikhonov, MF, or ME.[93] Different methods exist which produce different values of λ, which, depending on W and s, may produce good or bad results. Thus, typically, in practice, not a single method is used to determine the value of the regularization parameter, but different values are tested and the best solution then chosen based on a variety of factors. Such factors are both positive and negative, e.g., an important criterion is if the solution *looks* real and if it has the characteristics expected of the solution as computed by, e.g., simulation codes such as TRANSP, and if the solution does not have what are clearly incorrect artefacts. For example, a reconstruction of the velocity-space distribution function from neutral beam injection must have a peak at the injection energy, and it cannot have peaks at higher energies.[94] Reconstructions that do not satisfy such criteria can be disregarded immediately.

[90] See Anton et al. (1996), p. 1858 ff. for details. See also Salewski (2019), p. 61 ff.

[91] See, e.g., Galdon-Quiroga, Garcia-Munoz, Salewski, et al. (2018), Madsen, Salewski, et al. (2020), and Madsen, Huang, et al. (2020).

[92] Salewski, Geiger, Jacobsen, et al. (2016), p. 6.

[93] Hansen (2010), p. 85 ff.

[94] See, e.g., Madsen, Salewski, et al. (2020), p. 5 f. where the value of the regularization parameter is chosen to suppress "spurious features" without oversmoothing.

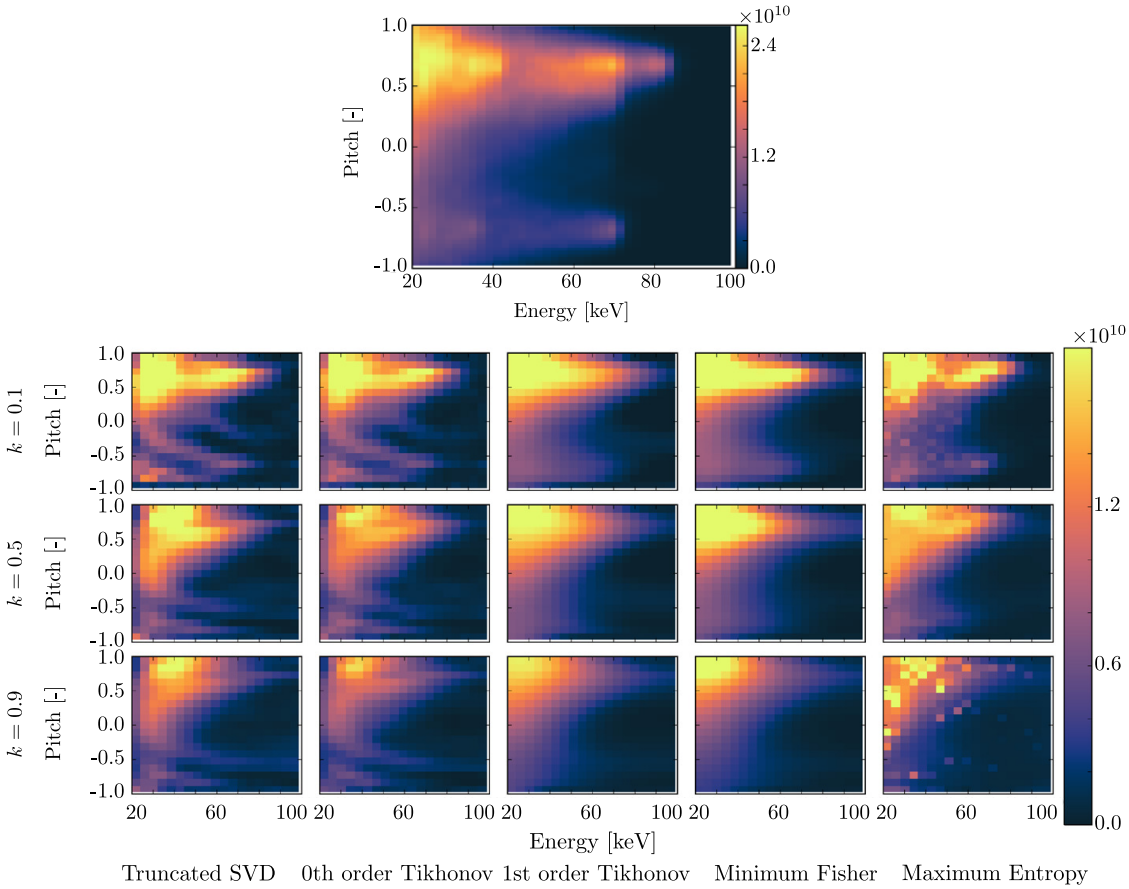

Figure 2.11: The first row shows the true velocity distribution of NBI with two co-current beams with injection energies at 70 and 80 keV and one counter-current beam with injection energy at 70 keV. Rows two to four show the reconstructions for different noise levels for the five regularization techniques: truncated SVD, zeroth- and first-order Tikhonov, minimum Fisher regularization, and maximum entropy. From Jacobsen et al. (2016a), pp. 5 and 9.

The process for determining the optimal regularization parameter is therefore more heuristic than quantitative. Still, the two methods called the "discrepancy principle" and the "L-curve" are most commonly used as a guide in velocity-space tomography[95] and for reconstructing velocity space distributions[96].

2.4.4.1 Discrepancy principle

According to the discrepancy principle,[97] the truncation parameter k and the regularization parameter λ should be chosen such that the residual norm satisfies

$$\left\| Wf^{[k]} - s \right\|_2 \geq \nu_{\mathrm{DP}} \left\| e \right\|_2 > \left\| Wf^{[k+1]} - s \right\|_2 , \tag{2.75}$$

where ν_{DP} is a safety factor ensuring that none of the noisy SVD components contaminate the solution. The same equation applies for a Tikhonov solution or other regularization techniques using λ as a regularization parameter with f^{λ} replacing $f^{[k]}$. By requiring the residual norm to be above the norm of the error e, it is ensured that the solution does not fit the noise.

> Truncated SVD was initially used for velocity-space tomography from CTS and FIDA measurements with a manual search over the number of SVD components.[98] Such a manual search has likely identified a value of the truncation parameter close to that found from Eq. (2.75). One reason for not using the discrepancy principle is the difficulty in estimating $\left\| e \right\|_2$. The solution is very sensitive to the accuracy of $\left\| e \right\|_2$, where a too small estimate will lead to significant oversmoothing.[99] Later, Tikhonov-regularized solutions with an intuitive choice of λ were preferred.[100]

2.4.4.2 L-curve

Information about the regularized solution f is contained in the quantities $\left\| Wf - s \right\|_2$ and $\left\| Lf \right\|_2$. Thus, a plot of $\left\| Lf \right\|_2$ as a function of the residual norm $\left\| Wf - s \right\|_2$ computed for different values of the regularization parameter shows information about the regularized solution. For any λ, the plot shows the compromise between the minimization of the two quantities. The L-curve is then defined as the continuous curve consisting of all points $(\left\| Wf - s \right\|_2, \left\| Lf \right\|_2)$ for $\lambda \in [0, \infty)$.[101] It is possible to show that $\left\| Lf \right\|_2$ is a monotonically decreasing function of $\left\| Wf - s \right\|_2$.[102] Thus, the L-curve divides the first quadrant into two separate region where any regularized solution must lie on or above it.

The L-curve has two distinctly different parts that, when plotted in double-logarithmic scale, has the shape of an "L". One part occurs for large values of the regularization parameter, where it is possible to show that[103]

$$\left\| f \right\|_2 \approx \left\| f^{\mathrm{true}} \right\|_2 \text{ (a constant)} \quad \text{and} \quad \left\| Wf - s \right\|_2 \text{ increases with } \lambda. \tag{2.76}$$

[95] Jacobsen (2015), p. 58 ff.
[96] See, e.g., Galdon-Quiroga, Garcia-Munoz, Salewski, et al. (2018), p. 8, where the L-curve criterion was used to perform reconstructions of FILD measurements.
[97] Usually attributed to Morozov, cf. Hansen (1992), p. 570, cf. Morozov (1984).
[98] Salewski et al. (2013) and Salewski, Geiger, A. S. Jacobsen, et al. (2014).
[99] Hansen (2010), p. 90 f.
[100] Salewski, Geiger, Jacobsen, et al. (2016), p. 2 ff.
[101] Hansen (1992), p. 564 ff.
[102] Hansen (1992), p. 564, Theorem 1, and Hansen (2010), p. 71 ff.
[103] Hansen (2010), p. 73.

This corresponds to the horizontal line of the L. For small values of the regularization parameter, the solution is dominated by the errors from the noise, and

$$\|f\|_2 \text{ increases with } 1/\lambda \quad \text{and} \quad \|Wf - s\|_2 \approx \|e\|_2 \text{ (a constant)}. \tag{2.77}$$

This corresponds to the vertical line of the L. The corner of the line is roughly located at

$$\left(\log \|e\|_2 , \log \left\|f^{\text{true}}\right\|_2\right). \tag{2.78}$$

For very large values of the regularization parameter, the solution norm is forced toward zero, so the L-curve bends towards the x-axis. For very small values of the regularization parameter, the L-curve becomes less steep and bends towards the y-axis.

The properties of the L-curve can be illustrated by the following numerical example.[104] Consider the discrete ill-posed problem obtained by discretizing a Fredholm integral equation of the first kind given by

$$\int_a^b K(s,x) f(x)\,\mathrm{d}x = g(s), \quad a \le s \le b, \tag{2.79}$$

where K is the kernel, g are some measurements, and f is the sought solution. The problem corresponds to a one-dimensional model problem in image reconstruction, where the desired solution is

$$f(x) = 2\exp\left(-4(x-0.5)^2\right) + \exp\left(-4(x+0.5)^2\right), \quad -\frac{\pi}{2} \le x \le \frac{\pi}{2}, \tag{2.80}$$

and the kernel is

$$K(s,x) = \left((\cos s + \cos x)\frac{\sin \psi_{s,x}}{\psi_{s,x}}\right)^2, \quad -\frac{\pi}{2} \le s \le \frac{\pi}{2}, \tag{2.81}$$

corresponding to an image blurred by a known point-spread function with $\psi_{s,x} = \pi(\sin s + \sin x)$. The matrix W and true solution vector f^{true} is derived by discretizing the interval $[-\pi/2, \pi/2]$ with $n = 64$ equidistantly spaced points. The exact measurement is then obtained by computing $s^{\text{exact}} = Wf^{\text{true}}$. White noise is subsequently added.[105] The L-curve for this problem can then be computed for $\lambda \in [0, \infty)$ using a regularization matrix L equal to the second derivative operator, $L = \text{tridiag}(1, -2, 1)$ as illustrated in Fig. 2.12.

The L-curve criterion is to choose the value of the regularization parameter that corresponds to the corner of the L-curve. This corner can be defined as the point with maximum curvature. Note, however, that a discrete L-curve can have many small local corners, so it is not straightforward to compute the location of the "true" corner of the L-curve.[106] A numerical scheme for determining the value of the regularization parameter at the true corner has been constructed using an adaptive pruning algorithm.[107]

The L-curve criterion has been used to determine the optimal value of the regularization parameter for velocity-space tomography[108] and FILD reconstructions[109] of both synthetic and experimental data with good results. An example of a FILD reconstruction from FILD1 at ASDEX Upgrade from discharge #32081 at $t = 1.14$s is shown in Fig. 2.13. In practice, the L-curve criterion is known to produce overregularized solutions, and the value of the regularization parameter from the L-curve criterion remains a guide. In Jacobsen et al. (2016a), the authors mention that "different regularization levels were chosen rather than set by the L-curve method"

[104] See Hansen (1992), p. 574 ff.
[105] See Hansen (1992), p. 575, for details.
[106] Hansen (2010), p. 93.
[107] Hansen et al. (2007).
[108] Jacobsen et al. (2016a).
[109] Galdon-Quiroga, Garcia-Munoz, Salewski, et al. (2018).

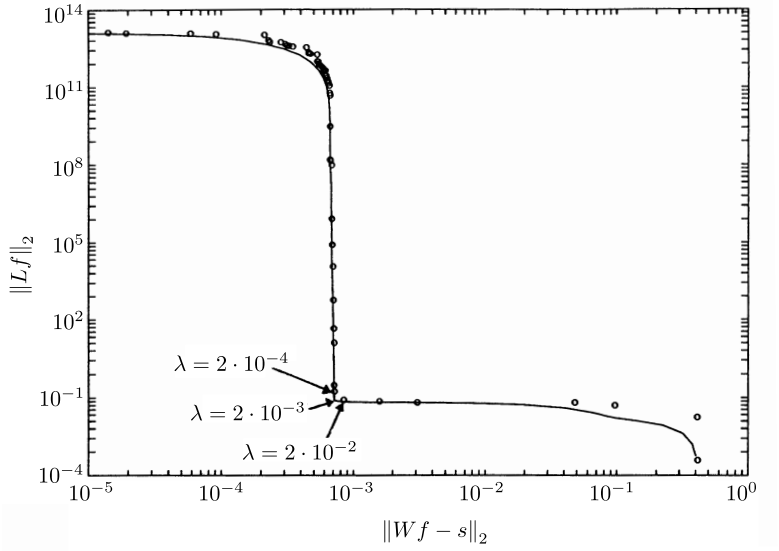

Figure 2.12: The L-curve for Tikhonov solutions $(\|Wf - s\|_2, \|Lf\|_2)$ for an image deblurring problem with white noise. The circles are truncated SVD solutions. Note that those solutions are either on or above the L-curve. From Hansen (1992), p. 576.

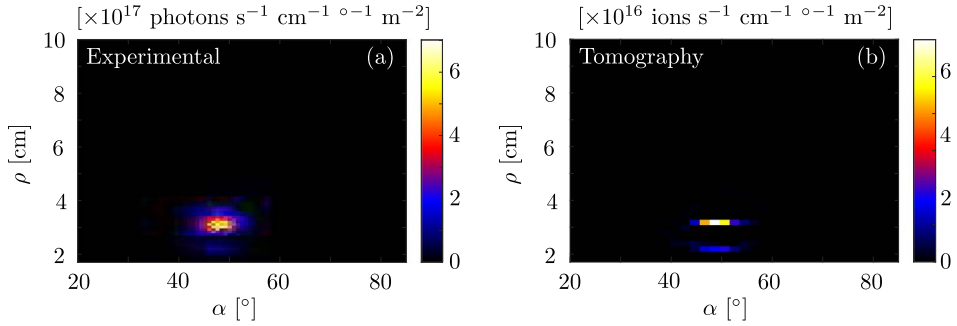

Figure 2.13: (a) Velocity space of lost fast ions measured by FILD1 at ASDEX Upgrade from discharge #32081 at $t = 1.14$ s. (b) Reconstruction of pinhole velocity space obtained using zeroth-order Tikhonov regularization with the optimal value of the regularization parameter determined using the L-curve criterion. From Galdon-Quiroga, Garcia-Munoz, Salewski, et al. (2018), p. 11.

for velocity-space tomography of experimental data from before and after a sawtooth crash in ASDEX Upgrade discharge #31557 at $t = 2.25$ s.[110]

[110] Jacobsen et al. (2016a), p. 11.

Chapter 3

Slowing-down physics regularization

This chapter presents the paper "4D and 5D phase-space tomography using slowing-down physics regularization", in press at *Nuclear Fusion*.

3.0 Abstract

We compute reconstructions of 4D and 5D fast-ion phase-space distribution functions in fusion plasmas from synthetic projections of these functions. The fast-ion phase-space distribution functions originating from neutral beam injection (NBI) at TCV and Wendelstein 7-X (W7-X) at full, half, and one-third injection energies can be distinguished and particle densities of each component inferred based on 20 synthetic spectra of projected velocities at TCV and 680 at W7-X. Further, we demonstrate that an expansion into a basis of slowing-down distribution functions is equivalent to regularization using slowing-down physics as prior information. Using this technique in a Tikhonov formulation, we infer the particle density fractions for each NBI energy for each NBI beam from synthetic measurements, resulting in six unknowns at TCV and 24 unknowns at W7-X. Additionally, we show that installing 40 LOS in each of 17 ports at W7-X, providing full beam coverage and almost full angle coverage, produces the highest quality reconstructions.

3.1 Introduction

A complete understanding of fast-ion distributions and fast-ion dynamics is imperative for future operation of fusion reactors, thus necessitating the development of ways to diagnose fast ions in both tokamaks and stellarators. Tomography is used in magnetic fusion plasma science to obtain information about fast-ion distributions, typically visualized as cross-sectional images. Assuming tokamaks to be toroidally symmetric, 3D position space (R, θ, Z) can be reduced to two dimensions (R, Z). Similarly, the fast gyration of the ions leads to azimuthal symmetry in 3D velocity space, since the gyroangle γ becomes ignorable, so the velocity space reduces to $(v_\parallel, v_\perp)$.[1] Here, $v_\parallel$ is the magnitude of the velocity component parallel to the magnetic field and $v_\perp$ the magnitude of the velocity component perpendicular to the magnetic field. Hence, the 6D phase space consisting of 3D position space and 3D velocity space is usually reduced to a 4D phase space,

[1] Moseev and Salewski (2019).

as can be done in the TRANSP or ASCOT codes.[2] Since stellarators do not possess toroidal symmetry in position space, the phase space in stellarator plasmas can only be reduced to 5D, as in the BEAMS3D code.[3] Here, we consider 4D and 5D phase-space distributions at TCV and W7-X as examples for tokamaks and stellarators.

Position-space tomography provides spatial information about fast-ion distributions. For example, the spatial location of neutron emission has been reconstructed using the 19 available neutron cameras at JET.[4] During the last decade, fast-ion velocity-space tomography was developed, which provides insight into the fast-ion velocity-space distribution functions from experimental data. This technique has been applied to several diagnostics, including FIDA spectroscopy,[5] collective Thomson scattering (CTS),[6] neutron emission spectrometry (NES),[7] γ-ray spectrometry (GRS),[8] and scintillator-based fast-ion loss detectors (FILDs)[9] at the tokamaks ASDEX Upgrade, JET, EAST, MAST, and DIII-D. Velocity-space tomography has also been used to estimate 1D velocity distribution functions[10]. While the 1D and 2D techniques infer velocity distribution functions in a small volume in the plasma, orbit tomography infers a 3D phase-space distribution of all fast ions in the plasma.[11] This technique uses fast-ion orbits as prior information and exploits that velocity distribution functions can, assuming toroidally symmetric plasmas, be parametrized in terms of fast-ion drift orbits by three parameters: the energy, the magnetic moment, and the canonical toroidal angular momentum. In this paper, we develop techniques to infer 4D and 5D phase-space distribution functions based on slowing-down physics regularization. The idea is to use the known physics of the slowing-down process of fast ions in plasmas as a prior in the ill-posed inference problem. This allows for reconstruction of the velocity space distribution function for all spatial locations and not just a single diagnostic locations as has been the case for previous tomographic and reconstruction techniques. This approach was demonstrated for 2D velocity-space tomography[12], which we here extend up to 5D.

Reconstructing 4D and 5D phase-space distribution functions in magnetically confined plasmas has never been attempted. A standard 4D or 5D inference appears out of reach due to the large number of unknowns, for example, discretizing each dimension by 30 points yields on the order of 10^6 grid points in 4D and 10^7 in 5D. Standard regularization techniques, such as Tikhonov regularization without additional prior information, can work in 1D, 2D, or 3D, but additional prior information is needed at present to enable the inference of the larger number of parameters in the 4D or 5D phase-space distributions. Here, we develop slowing-down physics regularization in 4D and 5D based on projected velocity spectra to show that this technique can obtain the 4D and 5D fast-ion phase-space distribution functions for plasmas heated by NBI at TCV and W7-X. Slowing-down physics regularization also works for other plasma heating schemes such as ICRF. The slowing down of energetic ions by collisions always occurs in plasmas, irrespective of any other processes occurring in addition to the slowing down. Thus, this project investigates neoclassical slowing-down with the possibility of extending to non-neoclassical regimes.

In section 2, we describe the beam configurations at TCV and W7-X. In sections 3 and 4,

[2] Budny et al. (1995), Pankin et al. (2004), Hirvijoki et al. (2014), and Grierson et al. (2018).
[3] Lazerson et al. (2020) and Mencke et al. (2022).
[4] Moseev et al. (2018), Kazakov et al. (2020), Nocente, Kazakov, et al. (2020), and Nocente, Molin, et al. (2020).
[5] Salewski, Geiger, A. S. Jacobsen, et al. (2014), Jacobsen et al. (2016b), Salewski, Geiger, Jacobsen, et al. (2016), Weiland et al. (2016), Weiland et al. (2017), Madsen et al. (2018), Madsen, Salewski, et al. (2020), and Madsen, Huang, et al. (2020).
[6] Jacobsen et al. (2016b).
[7] Salewski et al. (2017) and Salewski, Nocente, Jacobsen, Binda, Cazzaniga, et al. (2018).
[8] Salewski et al. (2017) and Salewski, Nocente, Madsen, et al. (2018).
[9] Galdon-Quiroga, Garcia-Munoz, Sanchis-Sanchez, et al. (2018) and Galdon-Quiroga, Garcia-Munoz, Salewski, et al. (2018).
[10] Salewski (2019) and Schmidt et al. (2021).
[11] Stagner et al. (2022).
[12] Madsen, Huang, et al. (2020).

we describe the forward problem and the Tikhonov regularization approach typically used for velocity-space tomography. In section 5, we develop the slowing-down physics regularization technique. In section 6, we describe the synthetic dataset used for our investigations. In section 7, we show and interpret the results from applying slowing-down physics regularization to synthetic data from TCV and W7-X. In section 8, we present a conclusion and outlook.

3.2 NBI configurations at TCV and W7-X

NBIs inject energetic particles, typically hydrogen isotopes, which have been accelerated to energies in the 10 - 100 keV range. In the acceleration stage, in addition to the neutral deuterium atoms, deuterium dimers and trimers are formed. As all three species are accelerated in the same potential, the energy of the injected dimers and trimers is the same as for the deuterium monomers. Hence, the velocity is reduced by a factor of $1/\sqrt{2}$ for the dimers and $1/\sqrt{3}$ for the trimers. The dimers and trimers are ionized as they exit the NBI beam and enter the plasma. Thus, when the dimers and trimers split into single deuterium ions inside the plasma due to collisions, the resulting deuterium monomers continue moving at lower velocities.

TCV has two NBIs positioned as shown in Fig. 3.1(a) for a top view of TCV. The NBIs are oriented tangentially to the magnetic axis in the midplane ($Z = 0$). The diagnostic FIDA lines of sight considered in this study are those used for shot 68407 consisting of 10 horizontal and 10 vertical FIDA views. A crucial parameter for the velocity-space sensitivity of diagnostics is the viewing angle ϕ between the line of sight and the magnetic field. The viewing angle intervals for the horizontal and vertical fans are $\phi_{\text{hor}} \in [45°, 90°]$ and $\phi_{\text{vert}} \in [75°, 90°]$. The intersections of the NBIs and the FIDA lines of sight are illustrated in Fig. 3.1(a) as the points where the magenta lines meet the black and red lines and in Fig. 3.2 as the black dots. The nominal power fractions of the injected deuterium species at full, half, and one-third injection energy for NB1 and NB2 at TCV are 0.73:0.22:0.05 and 0.59:0.33:0.08 at the nominal energies 25 keV and 47 keV.

W7-X is designed with two NBI boxes with four beams in each.[13] The two NBI boxes are positioned to achieve different injection angles for the eight beams with the local toroidal magnetic field. Beams 2, 3, 6, and 7 are pointed more radially and beams 1, 4, 5, and 8 more tangentially. The diagnostic FIDA lines of sight intersect beams 7 and 8 (Q7 and Q8); see Fig. 3.1(b) for an illustration of the experimental setup. Each FIDA view is part of one of three fans, originating from ports AEA21, AEM21, and AET21. We will refer to them as fans A21, M21, and T21 with corresponding viewing angle intervals $\phi_{\text{A21}} \in [2°, 10°], \phi_{\text{M21}} \in [125°, 135°]$, and $\phi_{\text{T21}} \in [35°, 45°]$. In addition to these three fans, we investigate how much information can be gained by installing additional FIDA views. Seventeen ports located in the first- and second half-modules of the second module are available for installing diagnostic FIDA views on Q7 and Q8. Figure 3.2 shows the spatial fast-ion distribution at TCV and W7-X along with the measurement volumes. The possible viewing angles for each port along NBI Q7 and Q8 are illustrated in Fig. 3.3. For a given port, the median viewing angle is displayed as a circle and maximum and minimum viewing angles are indicated by the top and bottom bars. Observe that with the 17 ports combined, coverage of all viewing angles is attained except for the viewing angles between approximately 10° and 20°. The power fractions of the injected deuterium species at full, half, and one-third injection energy at W7-X are 0.45:0.45:0.10 with full injection energy of 55 keV.

[13] McNeely et al. (2020) and Lazerson et al. (2021).

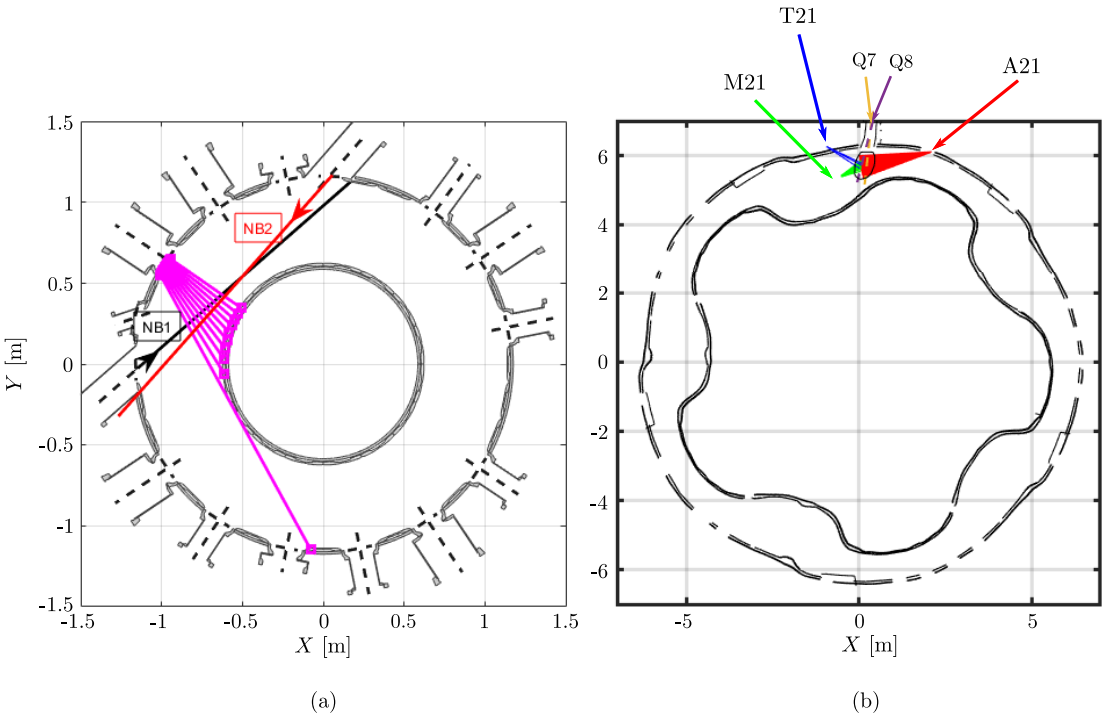

Figure 3.1: Neutral beam (NB) locations at (a) TCV and (b) W7-X. For TCV, the black and red lines indicate NB1 and NB2. The magenta lines indicate the lines of sight of the FIDA views. For W7-X, Q7 and Q8 correspond to the 7th and 8th NBs out of eight in total. The three fans 'A21', 'M21', and 'T21' indicate FIDA lines of sight located in the first half-module of the second module.

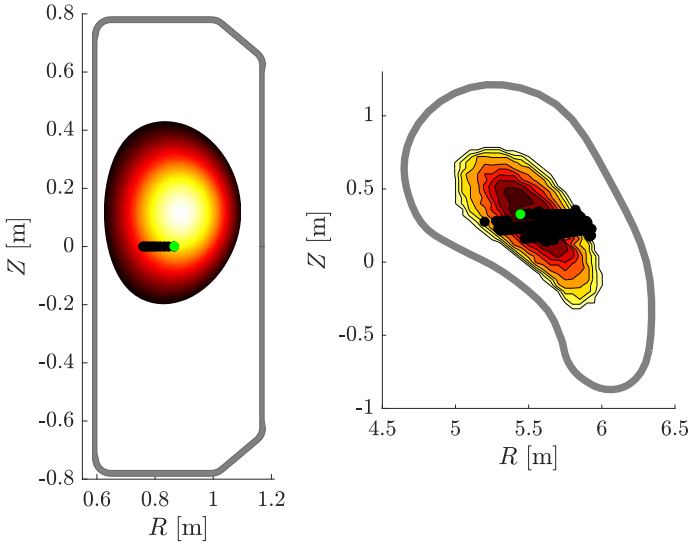

(a) (b)

Figure 3.2: Poloidal cross sections and simulated fast-ion density distributions in (a) TCV and (b) W7-X at $\theta \approx 90°$. The black dots indicate the measurement volumes. The green dots indicate the locations for the distributions in Figs. 3.4 and 3.5.

3.3 Forward model

The goal in this study is to obtain the 4D and 5D fast-ion phase-space distribution function from projections of the velocity distribution function. Such projections serve as a proxy for CTS and FIDA spectra, since the projected velocity is proportional to the Doppler shift, which is the key effect leading to the spectrum formation. However, other details such as Stark splitting are neglected.

The projections s are obtained as the integral over phase-space of the product wf, where $w = w(\lambda_1, \lambda_2, \phi, \boldsymbol{x}, \boldsymbol{v})$ is the weight function and $f = f(\boldsymbol{x}, \boldsymbol{v})$ is the phase-space distribution function.[14]. Hence,

$$s(\lambda_1, \lambda_2, \phi) = \iint w(\lambda_1, \lambda_2, \phi, \boldsymbol{x}, \boldsymbol{v}) f(\boldsymbol{x}, \boldsymbol{v}) \, \mathrm{d}\boldsymbol{x}\mathrm{d}\boldsymbol{v} \tag{3.1}$$

for a detected signal $s(\lambda_1, \lambda_2, \phi)$ in the wavelength bin $\lambda_1 < \lambda < \lambda_2$ with projection angle ϕ originating from a small measurement volume. A weight function, the kernel in Eq. (3.1), indicates the sensitivity of the given diagnostic at a specific location in phase-space for a projection angle ϕ and a wavelength bin with lower wavelength λ_1 and upper wavelength λ_2. Such weight functions have also been calculated for neutron emission spectroscopy,[15] gamma-ray spectroscopy,[16] fast-ion loss detectors,[17] ion cyclotron emission,[18] and MeV-proton diagnostics[19].

[14] W. W. Heidbrink et al. (2007), Heidbrink (2010), Salewski et al. (2011), and Salewski, Geiger, Moseev, et al. (2014).
[15] Jacobsen et al. (2015), Jacobsen et al. (2017), Järleblad et al. (2021), and Järleblad et al. (2022).
[16] Salewski, Nocente, Gorini, et al. (2015) and Salewski, Nocente, Gorini, et al. (2016).
[17] Galdon-Quiroga, Garcia-Munoz, Sanchis-Sanchez, et al. (2018).
[18] Schmidt et al. (2021).
[19] W. Heidbrink et al. (2021).

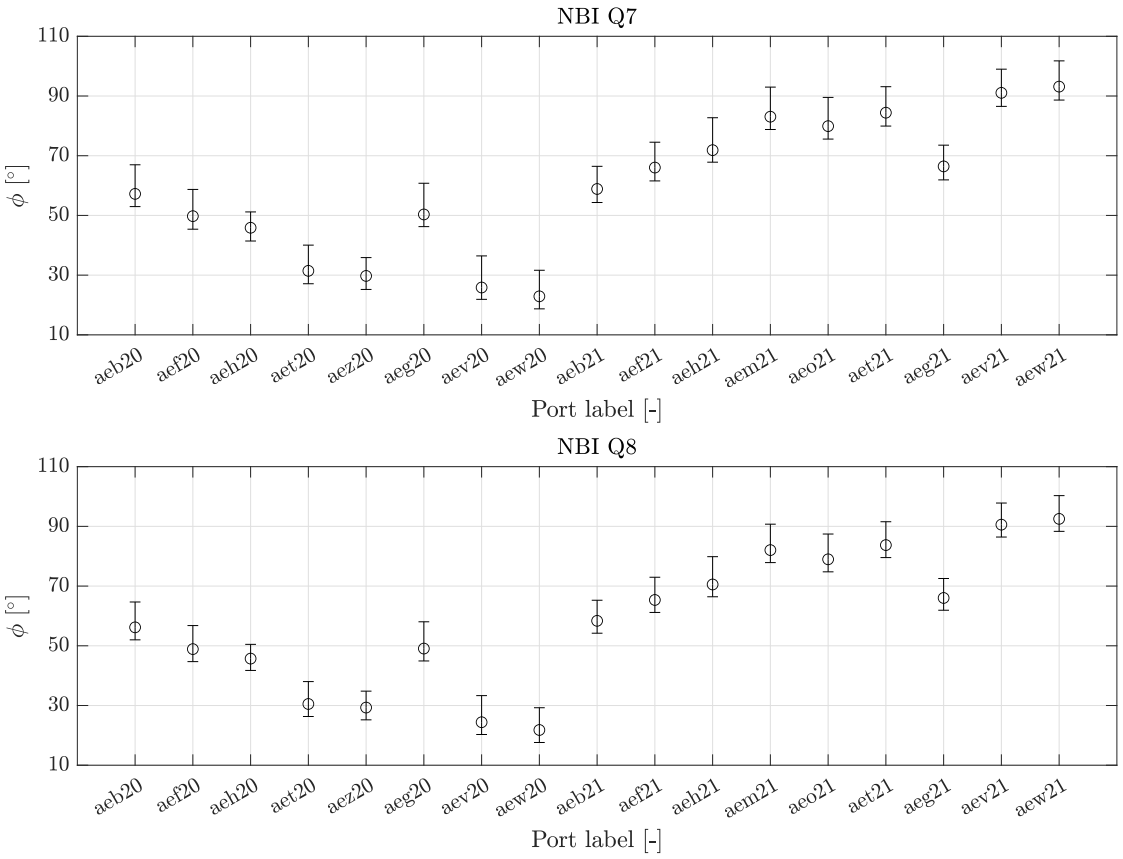

Figure 3.3: 17 diagnostic ports could be used for FIDA views at W7-X. The upper figure shows the viewing angles ϕ of the lines of sight and the magnetic field for NBI Q7, and the lower for NBI Q8. The circles represent the median viewing angle, and the vertical bar represents the angle range.

Discretizing position and velocity space transforms the equation into the matrix-vector equation

$$Wf = s, \tag{3.2}$$

where f is the vector corresponding to the fast-ion phase-space distribution function and s the measurement data vector corresponding to the projections. The problem formulation assumes the underlying problem to be linear. Equation (3.2) for 4D and 5D phase space distributions is the same as the 2D velocity-space tomography[20] and 3D orbit tomography[21] formulations. The fast-ion distribution vector f has dimension n, the measurement data vector s has dimension m and contains all spectral data from all lines of sight, and W has dimension $m \times n$. The fast-ion distribution function is obtained by solving the inverse problem given by Eq. (3.2), i.e., computing f given s and W.

[20] Salewski et al. (2012) and Salewski et al. (2013).
[21] Stagner et al. (2022).

3.4 Tikhonov regularization

The accuracy of the solution to the matrix equation $Wf = s$ is bounded by its condition number $\kappa(W) = \sigma_1/\sigma_n$ defined as the ratio of the largest singular value σ_1 to the lowest singular value σ_n. The condition number expresses the maximum ratio of the relative error in f to the relative error in s. Therefore, a large condition number implies that a small change in s can cause a large change in f. For both TCV and W7-X, $\kappa(W) \gg 10^{15}$, so even little noise in s can cause large changes in f. Such large condition numbers result from the underlying continuous problems, described, e.g., by Eq. (3.1), being notoriously ill-posed inverse problems. Condition numbers on the order of 10^{15} are typical for such ill-posed problems. Well-conditioned problems typically have $\kappa(W) \lesssim 10^4$.

Meaningful solutions to such problems can be found by regularization, which penalizes undesired features in f so that small changes in s lead to small changes in f. This can be achieved by regularizing on f with a matrix L such that $\|Ls\|_2$ is a prior for the sought solution, e.g., smoothness by choosing L to be a gradient operator. With this approach, the inverse problem can be written as the following minimization problem:

$$f^* = \underset{f}{\operatorname{argmin}} \|Wf - s\|_2^2 + \lambda^2 \|Lf\|_2^2 . \tag{3.3}$$

The value of the regularization parameter λ controls how well the solution fits the noisy data and the degree to which the regularization influences the solution. To illustrate how Eq. (3.2) is solved in practice, Eq. (3.3) can be written as

$$f^* = \underset{f}{\operatorname{argmin}} \left\| \begin{pmatrix} W \\ \lambda L \end{pmatrix} f - \begin{pmatrix} s \\ 0 \end{pmatrix} \right\|_2^2 . \tag{3.4}$$

This is the most stable formulation of the inverse problem and the best suited for numerical computations[22].

Typically, it is helpful to use additional prior information to find a better solution. Previous work in velocity-space tomography in fusion plasmas has implemented non-negativity of the fast-ion distribution function, penalty matrices with different properties, null-measurement regions, specification of NBI locations, and numerical simulations as prior information.[23] Here, we implement prior information by constraining the solution to lie in the vector space spanned by the expected 4D or 5D slowing-down distribution functions of fast ions assuming neoclassical transport.

3.5 Slowing-down physics regularization

We reconstruct simulated fast-ion phase-space distribution functions from NBI at TCV and W7-X. The ions are born by ionization of neutrals from the neutral beams at full, half, and one-third injection energies. The fast-ion distribution in velocity space is anisotropic due to the narrow pitch range of injected particles determined by the geometry of the NBI relative to the magnetic field. The fast ions are assumed to follow neoclassical slowing down due to collisions with electrons and ions in a thermal background plasma. In 2D velocity space assuming a spatially homogeneous plasma, velocity distributions arising in these situations can be modeled as anisotropic slowing-down velocity distributions[24]. Here, we use ASCOT[25] and BEAMS3D[26] to calculate 4D and 5D

[22] Hansen (2010) and Salewski, Geiger, Jacobsen, et al. (2016).
[23] Salewski, Geiger, Jacobsen, et al. (2016), Salewski, Geiger, Jacobsen, et al. (2018), Madsen et al. (2018), Madsen, Salewski, et al. (2020), and Madsen, Huang, et al. (2020).
[24] Moseev and Salewski (2019).
[25] Hirvijoki et al. (2014).
[26] Lazerson et al. (2020) and Mencke et al. (2022).

phase-space distribution functions assuming only the neoclassical slowing-down physics. In the remainder of this paper, we will simply call them 'slowing-down distributions'.

Thus, we postulate that the solution to Eq. (3.4) must be closely related to the anisotropic slowing-down distributions from the NBI sources at full, half, and one-third injection energies. Madsen et al. followed a similar approach for computing 2D fast-ion velocity distribution functions resulting from co- and counter-current NBIs at EAST with good results[27].

We denote the N_{sd} phase-space slowing-down distribution functions by $\psi_1, \psi_2, \ldots, \psi_{N_{\mathrm{sd}}}$ defined for the 4D and 5D phase spaces at TCV and W7-X, where N_{sd} is the desired number of vectors in the slowing-down physics basis. In slowing-down physics regularization, the phase-space distribution function is assumed to lie in the space spanned by the set $\{\psi_j\}, j = 1, 2, \ldots, N_{\mathrm{sd}}$, so

$$f = \sum_{j=1}^{N_{\mathrm{sd}}} c_j \psi_j, \tag{3.5}$$

where $c_j \in \mathbb{R}$ is the coefficient corresponding to the jth slowing-down distribution. Thus, we enforce slowing-down physics on the regularized solution. The energy components of the neutral beams at TCV are illustrated in Fig. 3.4. The full energy component of all eight beams at W7-X is illustrated in Fig. 3.5. Observe the sign difference of the peaks in $v_\parallel$ indicating the difference in injection direction with respect to the local magnetic field. The spatial locations for the velocity distributions are from the central locations marked by green dots in Fig. 3.2.

To enable the detection of anomalous phenomena based on experimental data, future work will use thousands of slowing-down distribution functions. The greater flexibility of the model should allow modelling anomalous transport. A single neutral beam injects fast ions with three different energies. Thus, for TCV, two neutral beams result in $2 \times 3 = 6$ distinct slowing-down basis functions ψ_j. For W7-X, eight neutral beams result in $8 \times 3 = 24$ distinct slowing-down basis functions.

Let Ψ be a matrix containing sampled values of the slowing-down distribution functions as column vectors, and let c be a column vector containing the coefficients c_j corresponding to each ψ_j. Then

$$f = \Psi c, \tag{3.6}$$

so

$$s = Wf = W(\Psi c) = (W\Psi)\, c. \tag{3.7}$$

According to Eq. (3.7), we can calculate a synthetic measurement, given the coefficients c, using the weight function matrix as always used in velocity-space tomography and the matrix containing the slowing-down distribution basis functions as columns. Thus, to solve the original inverse problem in Eq. (3.3), we need to determine the 6 and 24 slowing-down distribution function coefficients for TCV and W7-X. Thus, our problem is to infer the densities of the NBI sources at full, half, and one-third energies from projections in velocity space at the position-space locations of the measurement volumes. These coefficients are found by solving the inverse problem in Eq. (3.7), which is to determine the coefficient vector c given s and the matrix $W\Psi$. This inverse problem will be solved by regularizing the coefficient vector c for solutions $f \in \operatorname{span}\{\psi_j\}$ using Tikhonov regularization. The underlying complexity of the modelled systems with dimensionality of 4D or 5D for TCV and W7-X therefore does not affect the solution.

[27] Madsen, Huang, et al. (2020).

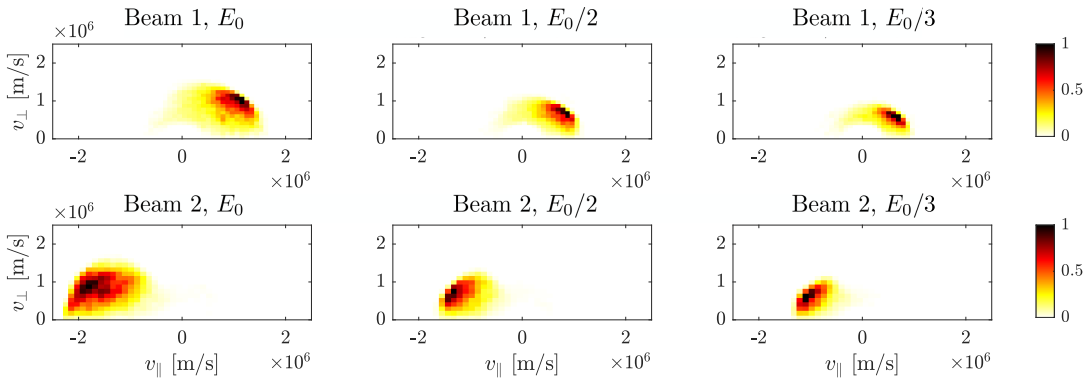

Figure 3.4: 2D velocity distribution functions for the full, half, and one-third energy for NB1 (top row) and NB2 (bottom row) at TCV. The distributions originate from the green dot in Fig. 3.2(a).

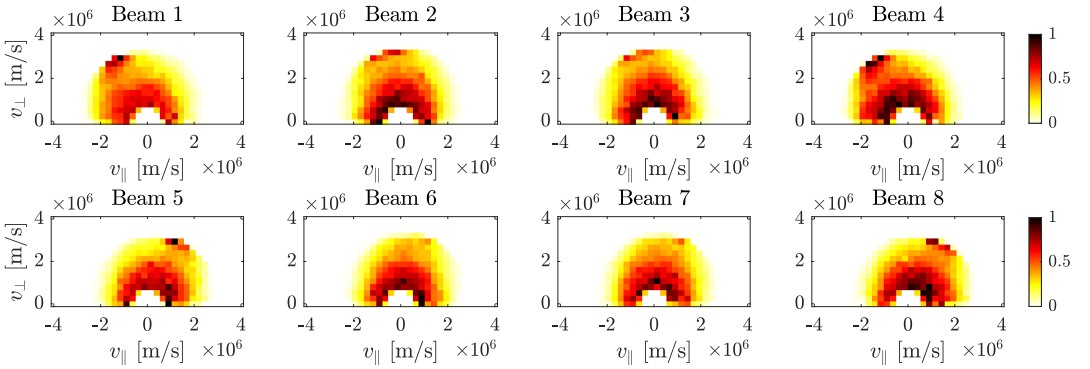

Figure 3.5: 2D velocity distribution functions for the full energy neutral beam injections at W7-X. The distributions originate from the green dot in Fig. 3.2(b).

3.6 Interpretation of the expansion in slowing-down functions as slowing-down physics regularization

The traditional formulation of the problem with Tikhonov regularization, with a non-negativity constraint on the solution, is

$$f^* = \underset{f}{\operatorname{argmin}} \left\{ \|Wf - s\|_2^2 + \lambda^2 \|Lf\|_2^2 \right\} \quad \text{subject to} \quad f \geq 0. \tag{3.8}$$

Here, the matrix L determines the type of regularization that is applied; L can be the identity matrix or a discrete approximation to a derivative operator.[28]

We can expand the solution in terms of this basis and write $f = \Psi c$. Here, $\Psi \in \mathbb{R}^{n \times N_{\text{sd}}}$ is the matrix whose N_{sd} columns are the discretized slowing-down functions, and $c \in \mathbb{R}^{N_{\text{sd}}}$ is a vector of the coefficients in this basis. Thus, the problem in Eq. (3.8) can be reformulated as

$$c^* = \underset{c}{\operatorname{argmin}} \left\{ \|W\Psi c - s\|_2^2 + \lambda^2 \|L\Psi c\|_2^2 \right\} \quad \text{subject to} \quad \Psi c \geq 0. \tag{3.9}$$

In this formulation, $W\Psi$ is the matrix connecting the coefficient vector c to the measurements, and $L\Psi$ is the regularization matrix. The two formulations (3.8) and (3.9) are equivalent when we set $f = \Psi c$.

In this work, we take a different approach that utilizes the physics-informed basis vectors in Ψ as a prior. Specifically, instead of enforcing regularization directly on f we regularize the coefficient vector c via a regularization term $\|c\|_2^2$. This is needed since the problem $\min \|W\Psi c - s\|_2^2$ is ill-posed. Enforcing this regularization ensures that all the expansion coefficients are bounded and that the solution expressed in the slowing-down basis is physically meaningful for the given measurement scenario. The physics-informed Tikhonov regularization problem then takes the form

$$c^* = \underset{c}{\operatorname{argmin}} \left\{ \|W\Psi c - s\|_2^2 + \lambda_c^2 \|c\|_2^2 \right\} \quad \text{subject to} \quad \Psi \boldsymbol{c} \geq 0. \tag{3.10}$$

from which we determine the regularized 4D or 5D fast-ion phase-space distribution function f^* from

$$f^* = \Psi c^*. \tag{3.11}$$

The number of rows of the matrix $W\Psi$ is determined by the number of lines of sight and the spectral resolution. For $N = 250$ lines of sight, each with a spectral resolution of 84 measurement bins in a spectrum, $W\Psi$ has 21000 rows. Since the matrix Ψ with the slowing-down basis consists of six simulated fast-ion phase-space slowing-down distribution functions for TCV, and 24 simulated fast-ion phase-space slowing-down distribution functions for W7-X, the matrix $W\Psi$ has six columns for TCV and 24 columns for W7-X. The interpretation of the regularization procedure by imposing the slowing-down basis prior depends on the dimension of the slowing-down basis N_{sd} compared to the number of rows n of Ψ, i.e., how many grid points the slowing-down function is resolved in.

First, consider the simplest case $N_{\text{sd}} = n$. This case appears when every grid point in the discretization of phase-space is considered as a source for a slowing-down basis function. This is the approach previously demonstrated in the 2D velocity-space tomography problem[29]. If $N_{\text{sd}} = n$, the matrix Ψ is square, and numerical testing shows it has full rank. Then $f = \Psi c \;\Leftrightarrow\; c = \Psi^{-1} f$, and therefore Eqs. (3.10) and (3.11) are equivalent to the problem

$$f^* = \underset{f}{\operatorname{argmin}} \|Wf - s\|_2^2 + \lambda_c^2 \left\|\Psi^{-1} f\right\|_2^2 \quad \text{subject to} \quad f \geq 0. \tag{3.12}$$

[28] Hansen (2010) and Salewski, Geiger, Jacobsen, et al. (2016).
[29] Madsen, Huang, et al. (2020).

A comparison of equations (3.12) and (3.3) shows that the expansion in slowing-down basis functions can be interpreted as a regularizer $L = \Psi^{-1}$ in the regularization term in Eq. (3.3). We shall now demonstrate that the same interpretation holds when $N_{\mathrm{sd}} \neq n$.

We first consider the case $N_{\mathrm{sd}} > n$ where we use more slowing-down basis functions than the number of grid points (an overcomplete system) we have chosen to discretize the distribution function. In this case, numerical testing shows that the matrix Ψ has full row rank, i.e., the $n \times N_{\mathrm{sd}}$ matrix has rank n. We still assume that $f = \Psi c$. Then it follows from the theory in Section 8.4, case 2 in Hansen (2010) that the matrix L in (3.9) must satisfy $L^\dagger = \Psi$, where the superscript † denotes the pseudoinverse. This, in turn, implies that $L = \Psi^\dagger$. Thus, regularizing on the coefficient vector c can be interpreted as using the regularizer $\Psi^\dagger$ for f in the regularization term in the original problem formulation.

Next, consider the case $N_{\mathrm{sd}} < n$ where we use fewer slowing-down basis functions, and hence fewer coefficients, than the number of grid points. In this case, numerical testing shows Ψ has full column rank, i.e., the $n \times N_{\mathrm{sd}}$ matrix has rank N_{sd}. To analyze this case, we cannot use the theory in Hansen (2010) and instead we introduce the QR factorization

$$\Psi = \begin{pmatrix} Q \,,\, Q_0 \end{pmatrix} \begin{pmatrix} R \\ 0 \end{pmatrix} = QR, \tag{3.13}$$

where R is an upper triangular matrix, Q and Q_0 have orthonormal columns, $Q^{\mathrm{T}} Q_0 = \mathbf{0}$, and $\mathrm{range}\,(Q_0) = \mathrm{range}\,(\Psi)^\perp = \mathrm{null}\left(\Psi^{\mathrm{T}}\right)$. Let $\mathcal{P} = Q_0 Q_0^{\mathrm{T}}$ be the orthogonal projector on $\mathrm{null}\left(\Psi^{\mathrm{T}}\right)$. For a general f and some vector w of appropriate dimension, $f = \Psi c + Q_0 w$, so

$$\Psi c = QRc = f - Q_0 w \quad \Leftrightarrow \quad c = R^{-1} Q^{\mathrm{T}} f = \Psi^\dagger f. \tag{3.14}$$

We want $f \in \mathrm{range}\,(\Psi)$, so $Q_0 w = \mathcal{P} f = 0$. Thus, the problem formulation becomes

$$f^* = \underset{f}{\mathrm{argmin}} \, \|Wf - s\|_2^2 + \lambda^2 \left\|\Psi^\dagger f\right\|_2^2 \quad \text{subject to} \quad \mathcal{P} f = 0. \tag{3.15}$$

Again, regularization on the coefficient vector c can be interpreted as a regularizer $L = \Psi^\dagger$ for f in the regularization term in the original problem formulation with the additional requirement that $\mathcal{P} f = 0$. This requirement corresponds to finding solutions in the vector space ψ_j described by slowing-down physics. The requirement is automatically satisfied when we compute $f = \Psi c = QRc$.

We have thus shown that we can interpret the regularization on the coefficient vector c as regularization on f in terms of slowing-down physics for any combination of n and N_{sd}. In reconstruction problems without using basis functions, we choose the number of grid points n based on the number of available measurements. Specifically, n should be similar to the number of measurements m. (It does not have to be the exact same number of unknowns as equations since the regularization provides additional requirements on the solution.) Following the same reasoning, we can choose the number of slowing-down basis functions to be similar to the number of measurements (where the data points of a measured spectrum are counted individually). The preceding analysis shows that we can choose the number of grid points in the basis functions as we like. For any choice, finely resolved or coarsely resolved basis functions, our interpretation of the expansion of the distribution function into slowing-down basis functions as slowing-down physics regularization holds.

3.7 Generation of synthetic data based on the ground truth

The study of slowing-down physics regularization using Tikhonov regularization is performed on synthetic measurement data based on ASCOT5 and BEAMS3D simulations for TCV and W7-X.

In both simulations, particles slow down due to Coulomb collisions until they reach twice the thermal energy. For TCV, phase space was discretized using a grid of size $(50, 150, 40, 40)$ for $(R, Z, v_\parallel, v_\perp)$ with corresponding ranges $([0.62, 1.14]\,\mathrm{m}, [-0.75, 0.75]\,\mathrm{m}, [-1.8 \times 10^6, 1.8 \times 10^6]\,\mathrm{m\,s^{-1}}, [0, 1.8 \times 10^6]\,\mathrm{m\,s^{-1}})$. For W7-X, phase space was discretized using a grid of size $(41, 34, 51, 32, 16)$ for $(R, \theta, Z, v_\parallel, v_\perp)$ with corresponding ranges $([4.5, 6.5]\,\mathrm{m}, [0, 2\pi], [-1, 1]\,\mathrm{m}, [-4 \times 10^6, 4 \times 10^6]\,\mathrm{m\,s^{-1}}, [0, 4 \times 10^6]\,\mathrm{m\,s^{-1}})$. The synthetic measurement data is generated by computing $Wf = s$ for known f which we refer to as the ground truth. The fast-ion phase-space distribution functions f are generated by specifying the values in the coefficient vector c and performing the multiplication $f = \Psi c$. Due to the generation mechanisms of the deuterium ions in the neutral beams, the density fractions for the distribution functions of deuterium monomers, dimers, and trimers are 0.73:0.22:0.05 and 0.59:0.33:0.08 for NB1 and NB2 at TCV at the nominal energies 25 keV and 47 keV and 0.45:0.45:0.10 for the NBIs at W7-X at the nominal energy 55 keV. The values in c are generated with a 10% variation of these values for each energy beam coefficient. This value for the variation was chosen since it is larger than the expected experimental error of the injected density fractions of the NBIs and typical for experimental error. The projection data comprise spectra from many lines of sight, and these are stacked in a single vector s. The values of the sought coefficients and example spectra are illustrated in Fig. 3.6.

If the same model is used to compute the synthetic spectra and the inference of the distribution function, the inference is unrealistically easy. This is sometimes called an 'inverse crime'[30]. To avoid committing an inverse crime when solving the inverse problem $W\Psi c = s$, the dimensions of the weight function matrix used to solve the inverse problem must be different from the dimensions of the weight function matrix used to generate the data. For TCV, the grid size used to generate the data was [40, 40] and the inversion grid size [37,37]. For W7-X, the corresponding grid sizes were [32, 16] and [33, 17]. Furthermore, noise is added to each measurement to simulate actual measurements, such that the signal-to-noise ratio is up to 10%.

For W7-X, we investigate two scenarios: one with 250 lines of sight and one with 680 lines of sight, with viewing angles calculated for FIDA views located in available ports. Each line of sight passes through NBIs Q7 and Q8, so a spectrum measured by one spectrometer is the sum of the signals from FIDA emission from its intersections with Q7 and Q8. Thus, the signal $s_i = W_7 f_7 + W_8 f_8$ for the weight functions W_7 and W_8 associated with NBIs Q7 and Q8 for the specific FIDA view i.

3.8 Simulation results

The difficulty of determining the correct coefficient vector $\boldsymbol{c}$ increases with the number of active beams. Therefore, we show the reconstructions with all beams active: two at TCV and eight at W7-X–and noting that reconstructions for fewer active beams are as accurate or better.

3.8.1 TCV with 20 lines of sight and W7-X with 250 lines of sight

The 4D and 5D phase-space distribution functions are determined by solving the equation

$$c^* = \underset{c}{\operatorname{argmin}} \left\{ \|W\Psi c - s\|_2^2 + \sum_k \lambda_k^2 \|L_k c\|_2^2 \right\} \quad \text{subject to} \quad \Psi c \geq 0 \tag{3.16}$$

and subsequently computing $f^* = \Psi c^*$. With this notation, $k \in \{0, 1\}$ corresponding to 0th-order and 1st-order Tikhonov regularization. For all techniques, the optimal values of λ_0 and λ_1 are

[30] Hansen (2010).

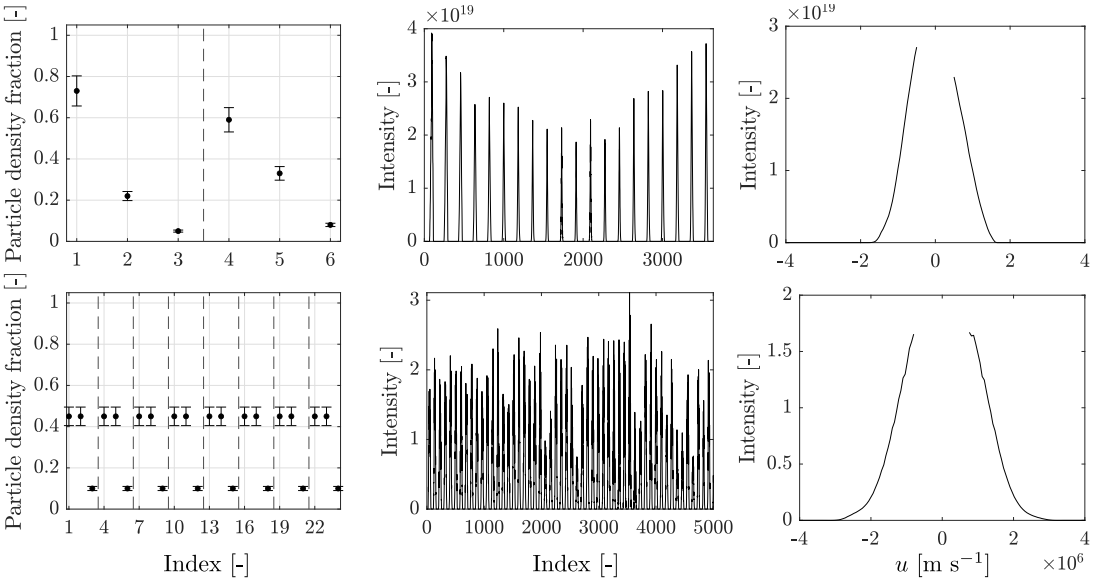

Figure 3.6: Essential aspects of the dataset for TCV (top row) and W7-X (bottom row). The first column shows the values of the densities of each beam component with 10% variation in each coordinate. The 'Index' label refers to the energy beam components in each neutral beam injector. The second column shows example data vectors $\boldsymbol{s}$ with all projected spectra ordered sequentially in a single vector. The 'Index' label here refers to each measurement bin in the projected spectra. The third column shows a single spectrum illustrating the shape of the spectral peaks as a function of the projected velocity u cut off at $\pm 0.5 \times 10^6$ m s^{-1}.

determined by choosing the solution to Eq. (3.16) with the lowest mean 2-norm deviation

$$\Delta_2 := \frac{1}{N} \left\| c^* - c^{\text{exact}} \right\|, \tag{3.17}$$

where c^{exact} is the ground truth and N the number of coefficients; $N = 6$ for TCV and $N = 24$ for W7-X.

The case of $k = 0$ called '0th-order Tikhonov regularization' corresponds to solving

$$c^* = \underset{c}{\operatorname{argmin}} \left\{ \|W\Psi c - s\|_2^2 + \lambda_0^2 \|L_0 c\|_2^2 \right\} \quad \text{subject to} \quad \Psi \boldsymbol{c} \geq 0 \tag{3.18}$$

with λ_0 a scalar, and $L_0 = I$. The reconstructions for TCV and W7-X using 0th-order Tikhonov regularization are illustrated in Figs. 3.7 and 3.8. In a perfect reconstruction, the red circles (reconstructions) enclose the black dots (ground truth). Note that the reconstruction is systematically biased: penalizing the 2-norm of the coefficient vector c tends to decrease the largest values, here the half-energy beam component values of 0.45, and tends to increase the lowest values. This is a deficiency that the 0th-order Tikhonov regularization always has. We can observe this tendency in our inversions, though the regularization parameter can be so low that the data dictates otherwise, as is the case for the one-third energy components. However, decreasing the regularization parameter λ_0 to allow more variation in the coefficient values decreases the accuracy of the reconstruction further. To avoid this tendency of the 0th-order Tikhonov regularization, we use prior information or 1st-order Tikhonov regularization.

We may use the prior information that the expected values of the nominal beam coefficients are particle density fractions obtained by other means, e.g., by measurement of the beam emission or physics of the acceleration phase of the atoms in the neutral beam injectors. In our numerical test, we can use the ground truth. Note that this is not the ground truth of a given test case since 10% noise is added to each coefficient before generating the signal. Thus, this prior has the tendency to bias the solution towards this prior information. We view this as an advantage over biasing larger values downwards.

Denote by $\boldsymbol{c}_0$ the vector with the values of the nominal beam coefficients for each beam component. Then, the 4D and 5D phase-space distribution functions are determined by solving

$$c^* = \underset{c}{\operatorname{argmin}} \left\{ \|W\Psi c - s\|_2^2 + \lambda_0^2 \|L_0 (c - c_0)\|_2^2 \right\} \quad \text{subject to} \quad \Psi c \geq 0. \tag{3.19}$$

We call this technique '0th-order Tikhonov regularization with prior'; see Fig. 3.7 and 3.8 for the reconstructions for TCV and W7-X using this technique. The 0th-order Tikhonov regularization with prior reconstructions is better than the one without prior for both TCV and W7-X. The regularization strengths used for 0th-order Tikhonov regularization with and without prior information are different due to the numerical differences of c and $c - c_0$.

An alternative to the 0th-order Tikhonov regularization is 1st-order Tikhonov regularization which, in general, penalizes differences between neighboring pixels. Here, our prior information is that the NBI's installed at W7-X are constructed and operated in the same way and, therefore, have the same species mix, i.e., the full-energy coefficients are likely the same for all NBIs, as are the half-energy coefficients, and the third energy coefficients. Since the two beams at TCV have different particle density fractions for the full, half, and third energy components, this regularization cannot be performed for the current beam setup at TCV.

Thus, a relevant prior for the 24 coefficients at W7-X is

$$c_{3n+1} \approx c_1, \tag{3.20}$$

$$c_{3n+2} \approx c_2, \tag{3.21}$$

$$c_{3n+3} \approx c_3, \tag{3.22}$$

for $n = 1, 2, \ldots, 7$. This prior belief can be written as the penalty matrix

$$L_1 = \begin{pmatrix} 1 & 0 & 0 & -1 & 0 & \cdots & 0 \\ 0 & 1 & 0 & 0 & -1 & \cdots & 0 \\ & & \ddots & & & \ddots & \\ 0 & 0 & \cdots & 1 & 0 & 0 & -1 \end{pmatrix}. \tag{3.23}$$

Since this matrix penalizes differences between similar energy components among different beams, we call this '1st-order Tikhonov regularization.' Thus, for $k = 1$, the equation to be solved is

$$c^* = \min_c \left\{ \|W\Psi c - s\|_2^2 + \lambda_1^2 \|L_1 c\|_2^2 \right\} \quad \text{subject to} \quad \Psi c \geq 0 \tag{3.24}$$

with λ_1 a scalar.

The 1st-order Tikhonov regularization solution is much better than that found by 0th-order Tikhonov regularization. The third energy components are determined almost perfectly, and the full- and half-energy components from the solution are around the correct values. However, the values of the solutions for the full- and half-energy beam components are biased in the direction of the majority of the beam components. For example, if more than four of the true full-energy beam component coefficients are larger than 0.45 due to noise, the 1st-order Tikhonov regularized solution for the full-energy beam components will be greater than 0.45 for all beams. The situation is the same for the half-energy beam component. However, this behavior could be an advantage since the eight NBIs are assumed to be constructed identically and, therefore, any systematic effects will be found by 1st-order Tikhonov regularization. See a reconstruction example for W7-X in Fig. 3.8.

Further, a 0th-order Tikhonov prior can be imposed on the 1st-order Tikhonov regularization. This corresponds to solving

$$c^* = \min_c \left\{ \|W\Psi c - s\|_2^2 + \lambda_0^2 \|L_0 (c - c_0)\|_2^2 + \lambda_1^2 \|L_1 c\| \right\} \quad \text{subject to} \quad \Psi c \geq 0. \tag{3.25}$$

The equation is implemented in the following form

$$c^* = \underset{c}{\operatorname{argmin}} \left\| \begin{pmatrix} W\Psi \\ \lambda_0 I \\ \lambda_1 L \end{pmatrix} c - \begin{pmatrix} s \\ \lambda_0 c_0 \\ 0 \end{pmatrix} \right\|_2. \tag{3.26}$$

See a reconstruction example for W7-X in Fig. 3.8. The prior improves the 1st-order Tikhonov regularized solution by mitigating the bias in the solution: the amplitudes of the full- and half-energy components are closer to the actual values, and the third-energy components are determined perfectly.

The spatial and velocity distribution functions corresponding to the reconstructed coefficient vectors are illustrated in Fig. 3.9 for 0th-order Tikhonov regularization. Observe that the reconstructed distributions are almost identical to the true distributions, indicating the applicability of the technique to determine coefficient vectors corresponding to the underlying true distributions.

3.8.2 W7-X with 680 lines of sight

Physical constraints such as port access and space for spectrometers within ports restrict the available measurement volumes and the corresponding viewing angles. At W7-X, 17 ports located in the first- and second half-modules of the second module are here considered suitable for the installation of additional FIDA views. Thus, we investigate the maximal reconstruction quality

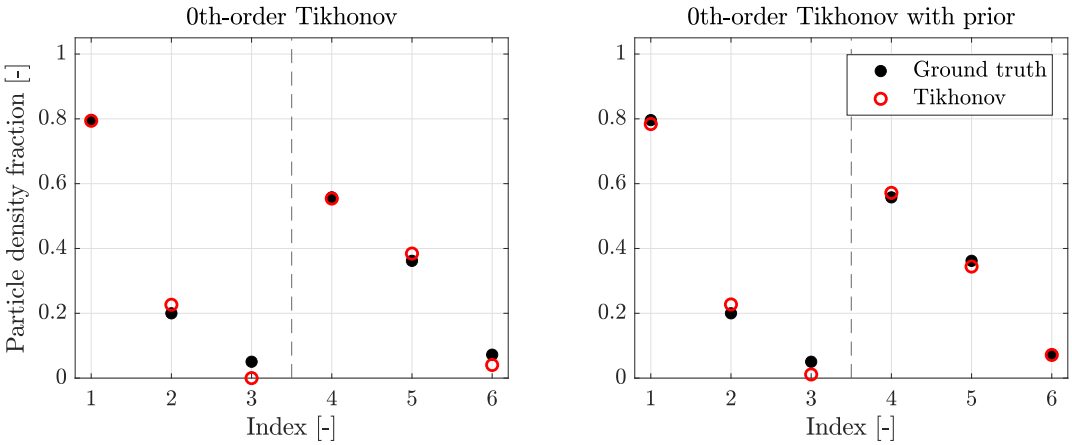

Figure 3.7: Reconstructions from synthetic measurements from TCV. The black dots indicate the actual densities (ground truth) for each beam energy component, and the red circles correspond to the density computed using 0th-order Tikhonov with and without priors.

using all 17 ports with full beam coverage, i.e., the FIDA views in each port can span the full length of the Q7 and Q8 NBIs. Each port is chosen to have 40 lines of sight. This corresponds to $17 \times 40 = 680$ spectra with a resolution of 84 measurement bins for a total of 57,120 measurement points, a 270% increase in the amount of data available for reconstructions. We refer to Fig. 3.3 for the viewing angles of the 17 ports.

Tikhonov-regularized reconstructions from the data described above are illustrated in Fig. 3.10. Observe the significant improvement in the 0th-order regularized solution compared to that in Fig. 3.8. Of all the reconstructions shown in this paper, the 0th- and 1st-order Tikhonov reconstructions here produce the best results, as the values of the coefficients in the reconstructions are the closest to the ground truth using no prior information.

3.9 Conclusion and outlook

Reconstructing 4D and 5D fast-ion phase-space distribution functions at TCV and W7-X requires an approach beyond traditional Tikhonov regularization used for velocity-space tomography. The slowing-down physics regularized solution f^* lies in the vector space spanned by slowing-down distributions $\psi_1, \psi_2, \ldots, \psi_{\text{sd}}$ such that $f^* = \sum_j c_j \psi_j$. The slowing-down distribution functions are calculated using ASCOT5 for TCV and BEAMS3D for W7-X. The slowing-down distribution functions ψ_j were calculated for the full, half, and one-third beam energy components for two neutral beams at TCV and eight neutral beams at W7-X.

In slowing-down physics regularization, the sought quantity is the column vector c containing the slowing-down distribution coefficients c_j. This column vector was obtained using Tikhonov regularization. We showed that for any number of grid points n and any number of slowing-down distribution functions N_{sd}, the expansion in slowing-down basis functions is equivalent to regularizing after slowing-down physics, i.e., using the regularizer $\Psi^\dagger$ on f in Tikhonov regularization.

Slowing-down physics regularization can be successfully applied to synthetic measurements s to obtain the column vector c very close to the known ground truth. As a consequence, the reconstructed fast-ion phase-space distribution functions $f = \Psi c$ are very similar to the ground

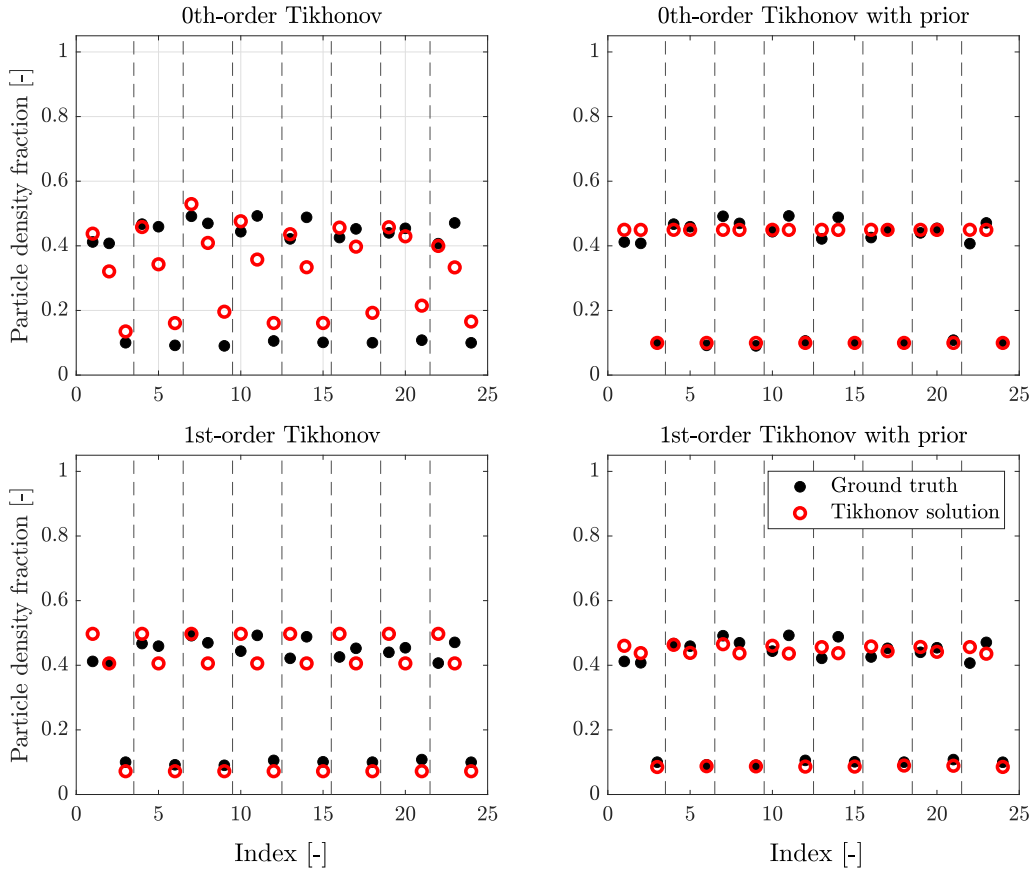

Figure 3.8: Reconstructions from synthetic measurements from W7-X. The black dots indicate the actual particle density fractions (ground truth) for each beam energy component, and the red circles correspond to the particle density fractions computed using 0th-order Tikhonov with and without priors (top row) and 1st-order Tikhonov with and without priors (bottom row).

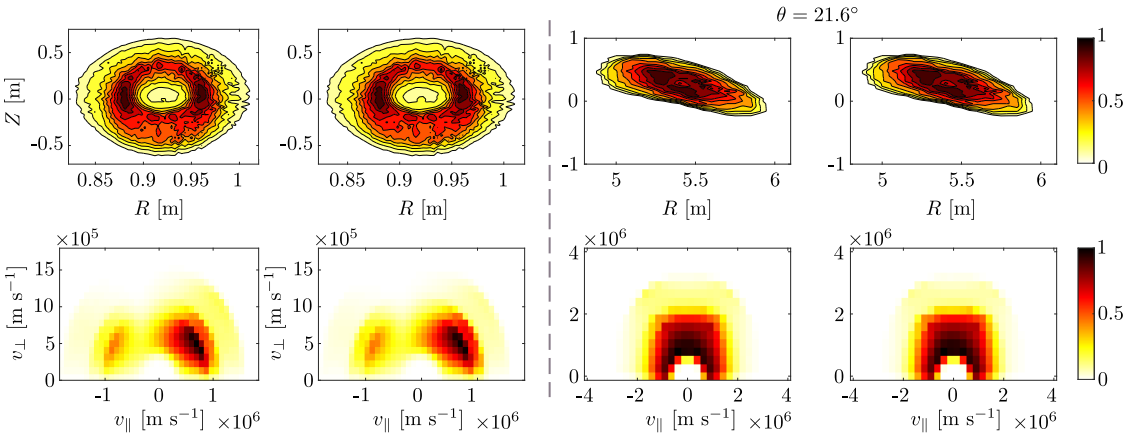

Figure 3.9: The first row contains spatial distributions for TCV (to the left of the dashed line) and W7-X (to the right of the dashed line), and the second row contains velocity distributions. The first and third columns show the actual distribution functions, and the second and fourth columns show the reconstructed solutions from Tikhonov regularization.

truths. The best reconstructions are obtained with a larger amount of data. Therefore, we suggest installing as many views as possible in the available ports.

The next step is to increase the number of simulated slowing-down distribution functions along the neutral beam paths. Adding more slowing-down distribution functions corresponds to adding additional basis vectors to Ψ, hence increasing the available fast-ion phase-space distribution functions that can be reconstructed. A very large numbers of lines of sight are expected to be crucial for this approach adding further support to the suggestion of installing as many views as possible.

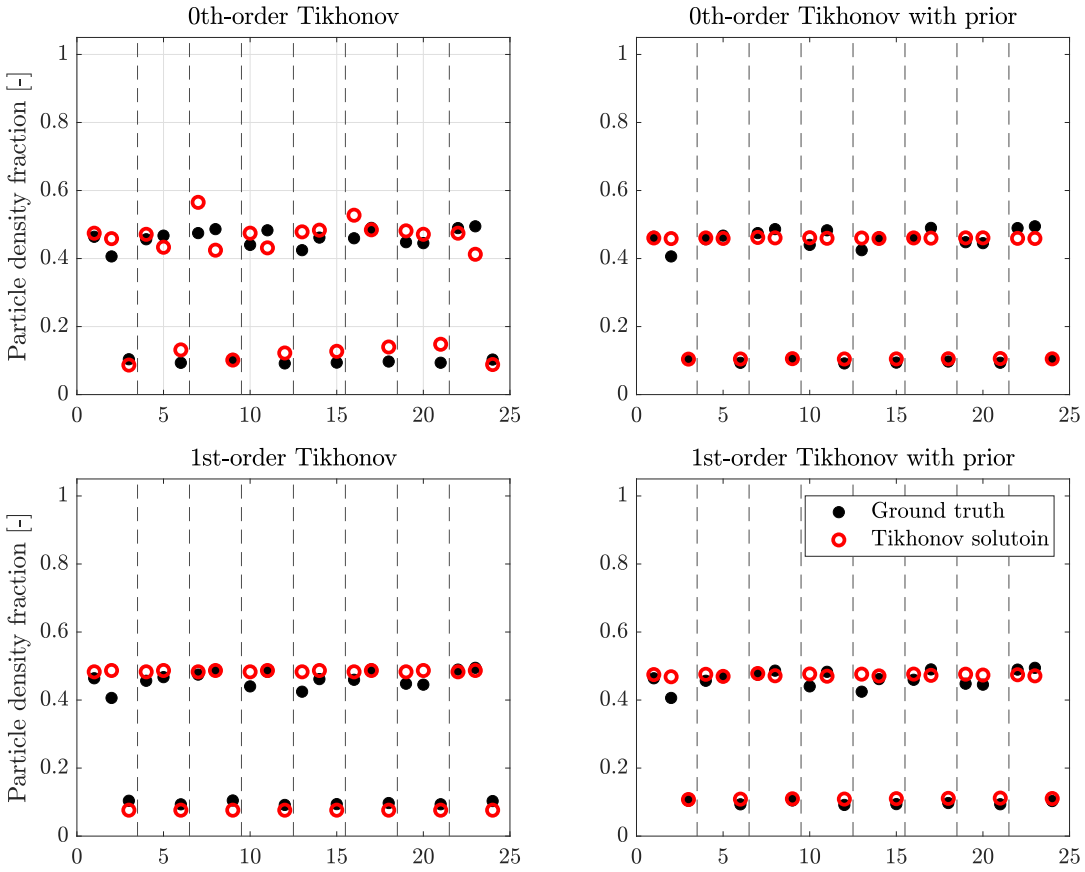

Figure 3.10: Reconstructions for a diagnostic setup at W7-X with 680 lines of sight distributed across 40 lines of sight in all 17 available ports in the first and second half-module of the second module.

Chapter 4

1D ICE weight functions and reconstructions using deep neural networks

This chapter presents the paper "Determining 1D fast-ion velocity distribution functions from ion cyclotron emission data using deep neural networks", published in the journal *Review of Scientific Instruments*.

4.0 Abstract

The relationship between simulated ion cyclotron emission (ICE) signals s and the corresponding 1D velocity distribution function $f(v_\perp)$ of the fast ions triggering the ICE is modelled using a two-layer deep neural network. The network architecture (number of layers and number of computational nodes in each layer) and hyperparameters (learning rate and number of learning iterations) are fine-tuned using a bottom-up approach based on cross-validation. Thus, the optimal mapping $g(s;\theta)$ of the neural network in terms of the number of nodes, the number of layers, and the values of the hyperparameters, where θ is the learned model parameters, is determined by comparing many different configurations of the network on the same training and test set and choosing the best one based on its average test error. The training and test sets are generated by computing random ICE velocity distribution functions f and their corresponding ICE signals s by modelling the relationship as the linear matrix equation $Wf = s$. The simulated ICE signals are modelled as edge ICE signals at LHD. The network predictions for f based on ICE signals s are on many simulated ICE signal examples closer to the true velocity distribution function than that obtained by 0th-order Tikhonov regularization, although there might be qualitative differences in which features one technique is better at predicting than the other. Additionally, the network computations are much faster. Adapted versions of the network can be applied to future experimental ICE data to infer fast-ion velocity distribution functions.

4.1 Introduction

In recent years, it has become possible to infer 2D fast-ion velocity distribution functions from fast-ion measurement data in magnetically confined plasmas.[1] This traditionally requires a formulation of the diagnostic forward models in terms of so-called weight functions that have been developed for collective Thomson scattering[2], fast-ion D-alpha spectroscopy[3], gamma-ray spectroscopy[4], neutron emission spectroscopy[5], and fast-ion loss detectors[6]. Here, we apply this approach to simulated ion cyclotron emission (ICE)[7] data and formulate a 1D inversion problem to infer a 1D fast-ion velocity distribution function. Further, we take an entirely new approach based on deep neural networks.

A deep neural network is a computational model comprising a network of functions capable of representing complex linear and non-linear relationships to translate input data into output data. Such networks are well-suited for analysing data from experiments where the quantities of interest are not directly measurable but must be inferred by modelling. The mathematical formulation of the problem may introduce systematic bias, and the inherent noise of the measurements increases the difficulty in obtaining a solution representative of the true solution by using traditional mathematical methods. Specifically, the linear inverse problem $Wf = s$ of finding a distribution function f given a forward model encoded in W and the measurement data s, is ill-posed. Regularization is needed in order to find an approximate solution. This is often done by Tikhonov regularization.[8]

An alternative approach is to use deep neural networks to model the relationship between the measured signal s and the distribution function f. The networks are trained using a supervised training approach on datasets consisting of an input and known true solution such that the predictions by the network $g(s;\theta)$ come as close as possible to the true solutions. The network learns to predict f by optimizing its internal parameters θ. In effect, training a neural network is a calibration of the network (the equipment) by comparing its output values (the measurements) to known values (the calibration standard).

Deep neural networks can be applied to ICE data analysis to assist and improve current analysis techniques for measurements of velocities, densities, and energies of fast ions. Such analysis is of crucial importance for ITER.[9] Further, such measurements require no additional measurement equipment since the future ICRH antennas at ITER can be used as receivers to measure ICE.[10] Thus, the easy access to ICE data and the inclusion of such diagnostic systems in ITER provide a strong incentive to develop ICE data analysis techniques.

Typically, fast ions drive instabilities at the ion cyclotron frequency and higher harmonics in the $5-100$ MHz range. Such instabilities occur when the distribution function f becomes inverted in velocity space, i.e., when $\partial f/\partial v > 0$, since free energy becomes available to drive the instabilities.[11] The magnetoacoustic cyclotron instability (MCI) produces ICE[12], and compressional Alfvén

[1] Salewski, Geiger, Moseev, et al. (2014), Salewski, Geiger, Jacobsen, et al. (2016), Weiland et al. (2016), Salewski et al. (2017), Weiland et al. (2017), Madsen et al. (2018), Madsen, Salewski, et al. (2020), and Madsen, Huang, et al. (2020).

[2] Salewski et al. (2011).

[3] W. W. Heidbrink et al. (2007), Stagner and Heidbrink (2017), and Salewski, Geiger, Moseev, et al. (2014).

[4] Salewski, Nocente, Gorini, et al. (2015) and Salewski, Nocente, Gorini, et al. (2016).

[5] Jacobsen et al. (2015) and Jacobsen et al. (2017).

[6] Galdon-Quiroga, Garcia-Munoz, Salewski, et al. (2018).

[7] McClements et al. (2015).

[8] Salewski, Geiger, Jacobsen, et al. (2016), Weiland et al. (2016), Salewski et al. (2017), Weiland et al. (2017), Madsen et al. (2018), Madsen, Salewski, et al. (2020), and Madsen, Huang, et al. (2020).

[9] Donné et al. (2007) and Salewski, Nocente, Madsen, et al. (2018).

[10] Dendy et al. (1994).

[11] Ochoukov, McClements, et al. (2019)

[12] Ochoukov, McClements, et al. (2019) and Liu et al. (2021).

eigenmodes (CAEs) and global Alfvén eigenmodes (GAEs) occur in the ion cyclotron frequency range.[13] Therefore, analysis of data from ICE is important since CAEs and GAEs may redistribute the energy from fusion-born alpha particles to the bulk plasma faster than Coulomb collisions. Furthermore, ICE may cause pitch angle scattering of beam ions when using NBI as heating source.[14]

4.2 1D ICE weight functions

We calculate 1D ICE weight functions by running a hybrid particle-in-cell (PIC) self-consistent Maxwell-Lorentz computation of the relaxation of an energetic ion population with given values of $v_\perp$ and $v_\parallel$ in the presence of an MCI. The computations result in power spectra of the excited fields in the non-linear saturated regime of the MCI. Each horizontal line in Fig. 4.1 constitutes such a power spectrum for the specified value of $v_\perp$ while $v_\parallel$ is held constant. Thus, Fig. 4.1 illustrates the signal intensities for a given $v_\perp$ and $v_\parallel$ of the ions for the frequencies ω. 1D weight functions for ICE appear as vertical lines in Fig. 4.1 and indicate the 1D velocity-space sensitivity of the detector to ions at a given ω. The 1D weight functions are analogous to the 2D weight functions for the previously mentioned fast-ion diagnostics. The data array W displayed in Fig. 4.1 provides a mapping from ICE signals to distribution functions on the basis that $Wf = s$, where f is the distribution function and s the ICE signal. This approach assumes that the physics embodied in the PIC-hybrid simulations dominates the generation of the observed ICE signals, and this appears to be well grounded.[15]

The relationship between the distribution function and the ICE signal is modelled as follows. Let $f \in \mathbb{R}^n$ be the distribution function and let $s \in \mathbb{R}^m$ be the signal. The relationship between f and s is then given by the linear equation

$$Wf = s, \tag{4.1}$$

where $W \in \mathbb{R}^{m \times n}$, $m = 451$, and $n = 22$. The matrix W contains the known physics of the problem and is calculated numerically from the Maxwell-Lorentz system of equations as follows: A non-linear 1D3V PIC-hybrid code follows the velocity-space trajectories (including the gyromotion of fully kinetic energetic and thermal ions) together with the three components of the electric and magnetic fields in an isothermal massless neutralising electron fluid. The kinetic ions, fluid electrons, and fields are coupled self-consistently through the Lorentz force and Maxwell's equations in Darwin's approximation.[16] These simulations are followed through the linear phase of the MCI and then deeply into its non-linear saturated phase.

The calculations are initialized with physical parameters representative of tokamak and stellarator edge plasmas. In these simulations, we used parameters relevant for LHD. The thermal deuterons are loaded using a quiet start method[17] while the energetic protons are initialised uniformly and randomly in space with velocities following a cold-ring distribution $n_H \delta\left(v_\parallel\right) \delta\left(v_\perp - u_\perp\right)$ to generate the inversion.[18] The background magnetic field $B_0 = 1.75T$ is oriented at 89° with respect to the periodic simulation domain that consists of 2048 cells of length $\Delta x = 1.30 r_D$, where r_D is the deuteron Larmor radius. 500 macroparticles per energetic and per thermal ion species are loaded in each cell and $n_H/n_e = 0.002$ to achieve a high signal-to-noise ratio. The spatio-temporal fast Fourier transform of the perturbed magnetic field $\delta B_z\left(x,t\right)$

[13] Fredrickson et al. (2001), W. W. Heidbrink et al. (2006), Appel et al. (2008), and Gorelenkov (2016).
[14] Ochoukov et al. (2020).
[15] Cook et al. (2013).
[16] Darwin (1920).
[17] Sydora (1999).
[18] Moseev and Salewski (2019).

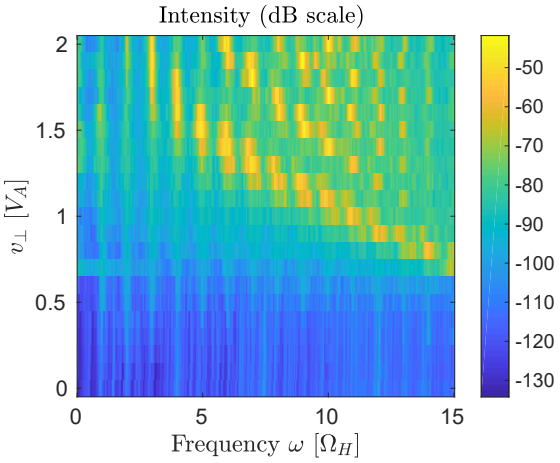

Figure 4.1: The weight function matrix W in the formulation $Wf = s$. V_A is the Alfvén speed, and Ω_H is the proton cyclotron frequency.

provides the 2D dispersion relation $\delta B_z\,(k, \omega)$, where k and ω are the wavenumber and frequency, respectively. In this specific case, the relaxation of the energetic protons through the MCI generates self-consistent excitations of the magnetic fields at multiple cyclotron harmonics on the fast-Alfvén branch. Summing over wavenumber-space k yields the synthetic power spectra. Each simulation corresponds to a different value of $v_\perp \in [0\,V_\mathrm{A}, 2\,V_\mathrm{A}]$. The power spectra are illustrated in Fig. 4.1.

4.3 Inversion by deep neural networks

We use a trained deep neural network to predict the distribution functions from simulated ICE signals. Note that the simulated ICE signals closely mimic actual ICE signals from edge ICE in LHD. The network is trained using a stochastic gradient descent method based on adaptive estimation of first-order and second-order moments called Adam in the Keras API. The network is trained on a large number of simulated datasets where each ICE spectrum is directly matched with a distribution function. Gaussian noise is added to the measurements to obtain a signal-to-noise ratio of 5% which is similar to the expected noise level in ICE measurements at LHD. Fig. 4.2 shows a simulated ICE signal and the corresponding distribution function.

The network performs its computations according to a predetermined architecture, initial values of network parameters, and user-specified values of hyperparameters to produce the network output. The network output is compared to the true solution, and the internal parameters are updated by backpropagation. The network is then trained again on the same data with its updated internal parameters. The number of times this is repeated is called the number of iterations.

The cost function that the network minimizes during training is chosen to be the mean squared error

$$\mathrm{MSE} = \frac{1}{N}\sum_{i=1}^{N}\left(f_i - \hat{f}_i\right)^2, \tag{4.2}$$

where f_i corresponds to the ith entry in the true solution f, and $\hat{f}_i$ corresponds to the ith entry in the network output vector $\hat{f}$. Letting p_data be the true data generating distribution, the problem

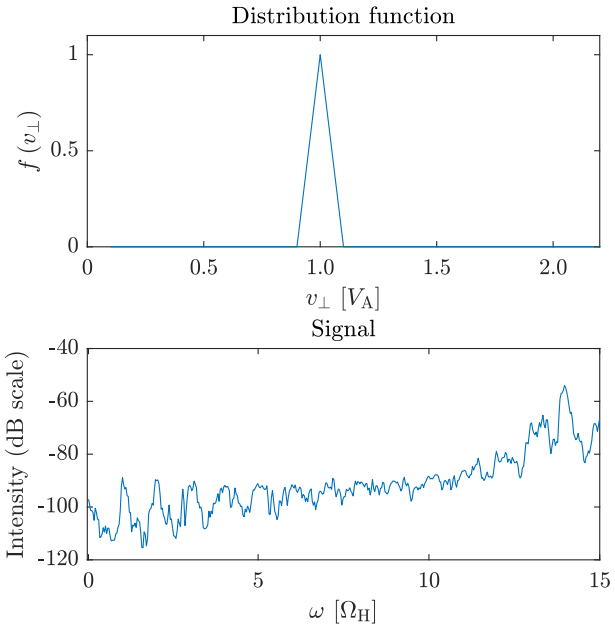

Figure 4.2: An example of a simulated distribution function $f(v_\perp)$ along with its corresponding simulated signal as measured by an ICE detector.

that the network solves is

$$g^* = \underset{g}{\operatorname{argmin}}\, \mathbb{E}_{s,f\sim p_{\text{data}}} \|f - g(y)\|^2 \tag{4.3}$$

with the solution

$$g^*(s) = \mathbb{E}_{f\sim p_{\text{data}}(f|s)}(f), \tag{4.4}$$

derived using calculus of variations[19]. This result shows that by training the network on infinitely many samples from the true data generating distribution p_{data} by minimizing the MSE cost function, the network prediction is the mean of f for each s. Other possible cost functions include how well the predictions match the width and height of the peaks of the ice distribution or just focusing on the location of the peaks. Such measures will be explored in future works.

The dataset used for training the network consists of 400.000 simulated ICE signal-distribution function pairs. The dataset includes distribution functions with up to three normal distributions with random center, width, and amplitude to mimic possible ICE distributions. As an example, consider Fig. 4.2 but with three distributions with random locations, amplitude, and width.

The optimal network architecture is determined in a bottom-up manner by first comparing the MSE loss for a network consisting of a single layer and an output layer using the default learning rate of $\alpha = 0.0001$ for the Adam optimizer. This comparison is made using $K = 5$ cross-validation, thereby ensuring that the training and validation set is the same for all network models. The performance of a specific network architecture is determined by the mean and standard deviation of the MSE across the 5 tests. The number of nodes in the first layer is varied from 100 to 5000, and the number of nodes in the best performing network is chosen as the number of nodes in the first layer. A second layer is then added between the input and output layer and the optimal

[19] Goodfellow et al. (2016).

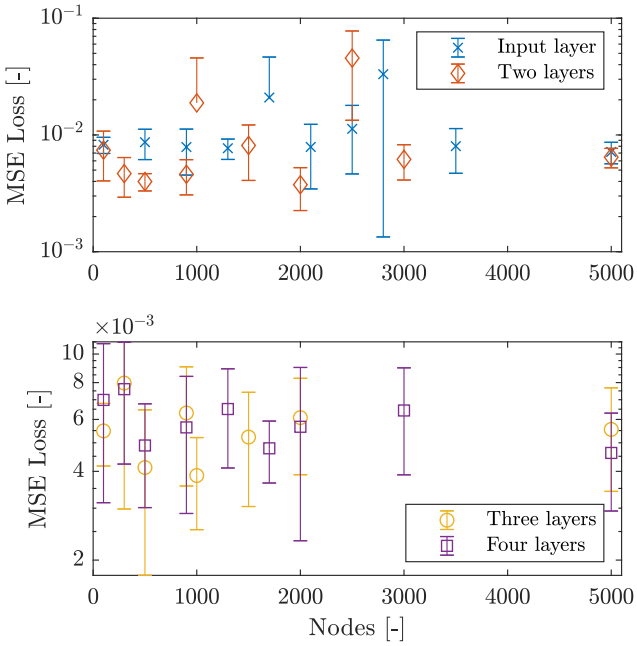

Figure 4.3: MSE loss of the network for a different number of layers and nodes.

number of nodes determined in a similar manner. These calculations were performed for up to four layers excluding the output layer. See Fig. 4.3 for the performance of each network architecture. The optimal number of nodes in the input layer is 1300. Including a second layer improves the model, and its optimal number of nodes is 500 or 2000. Here, 500 is chosen since the mean value of the loss is slightly lower and to save computational resources. The model gets worse when including additional layers.

Similar cross-validation investigations show that adding a dropout layer improves model performance. The optimal choice of dropout fraction is 0.4 after the first layer and no dropout after the second layer. The mean value of the loss in 5-fold cross-validation is improved from 7.6×10^{-3} to 4.0×10^{-3} corresponding to an improvement of approximately 52 %.

Finally, the learning rate α is optimized by performing the learning rate range test as described by Smith[20] and implemented by Wittmann.[21] The learning rate range test determines the values of the learning rate for which training improves the initial loss value. This range is then used to implement a triangular cyclical learning rate policy to achieve better and faster convergence of the model towards the optimal training state. The training for the range test is generally run for a low number of iterations. Here a single iteration is used with a batch size of 500. The results for the MSE loss is shown in Fig. 4.4. A good value of the learning rate occurs when the loss decreases. This occurs approximately for any $\alpha \in \left[10^{-5}, 2 \times 10^{-3}\right]$, which is chosen to be the lower and upper bounds for the learning rate in the cyclical learning rate policy. The cyclical learning rate is implemented by using the code developed by Kenstler.[22]

[20] Smith (2017).
[21] Wittmann (2019).
[22] Kenstler (2016).

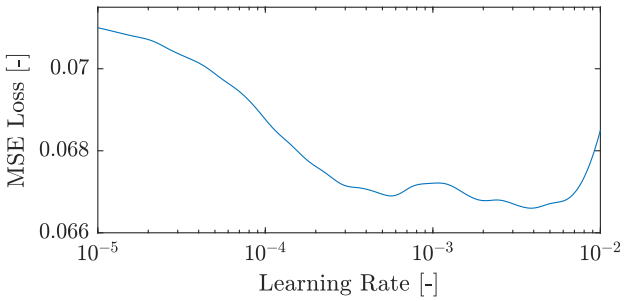

Figure 4.4: MSE loss from the learning rate range test to determine the optimal minimum and maximum values for the learning rate when employing a cyclical learning rate strategy.

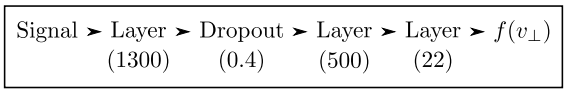

Figure 4.5: The structure of the neural network to obtain distribution functions from simulated ICE data.

4.4 Results and Discussion

Based on the investigation described in the previous section, the optimal network has the following properties. The network has three layers: one layer with 1300 nodes, a second layer with 500 nodes, and an output layer with 22 nodes. A 40 % dropout layer is placed between the first and second layer. Finally, the Adam optimizer is used in training the network with a cyclical learning rate policy with $\alpha \in \left[10^{-5}, 2 \times 10^{-3}\right]$. This network is illustrated in Fig. 4.5.

The network is trained for 1500 iterations as the network has converged to the best possible model at this point. This is shown by the training loss curve, see Fig. 4.6. Two signals and their distribution function predictions by the network, the best Tikhonov inversions, and the true solutions are displayed in Fig. 4.7. The network finds a more accurate distribution function than Tikhonov regularization as shown by the lower MSE value, although the distribution functions are quantitatively similar.

The neural network is trained to analyse simulated ICE spectra from LHD. In order to apply the trained neural network to other ICE spectra such as ICE spectra from JET and TFTR, the neural network needs to be trained for these scenarios. Since the weight function matrix depends on the ion species, the magnetic field, and other parameters, the weight function matrix for other machines, and even for other discharges in LHD, will differ from the ones used here. However, we expect the same methods to be applicable.

The computation speed of the network surpasses that of the Tikhonov inversions by at least $\mathcal{O}\left(10^3\right)$: the neural network performs one prediction on the order of ms, and Tikhonov inversions on the order of a second or slower. The problem with Tikhonov regularization is the need for determining a value of the regularization parameter in order to obtain a good inversion. This either costs extra computation time or must be done manually. Computation speed is relevant for both on-site and off-site analyses since the data analysis speed is often a bottleneck in determining how to proceed with a given experiment. Fast inversions for in-between shot analysis would be a large advantage.

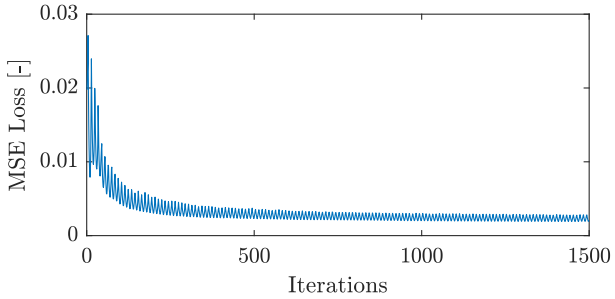

Figure 4.6: Convergence of the network as a function of the number of training iterations for the MSE loss using the cyclical learning rate policy.

4.5 Conclusion

A trained deep neural network can be used to model the relationship between simulated edge ICE signals from LHD due to fast ions and their 1D velocity distribution function in $v_\perp$. The network is more accurate than Tikhonov regularization on many of the ICE signal validation examples. Application of the neural network to ICE measurements and not simulated ICE data requires specific training of the network and the sensitivity of how exactly the simulated training data must mimic the measurement data has not been studied here. Thus, criteria for when a training set is good enough needs to be investigated further. Future work also involves expanding the neural network to predict the 2D velocity distribution in $v_\perp$ and $v_\parallel$ of fast ions, or even the 3D phase-space distribution,[23] from ICE signals.

[23] Järleblad et al. (2021).

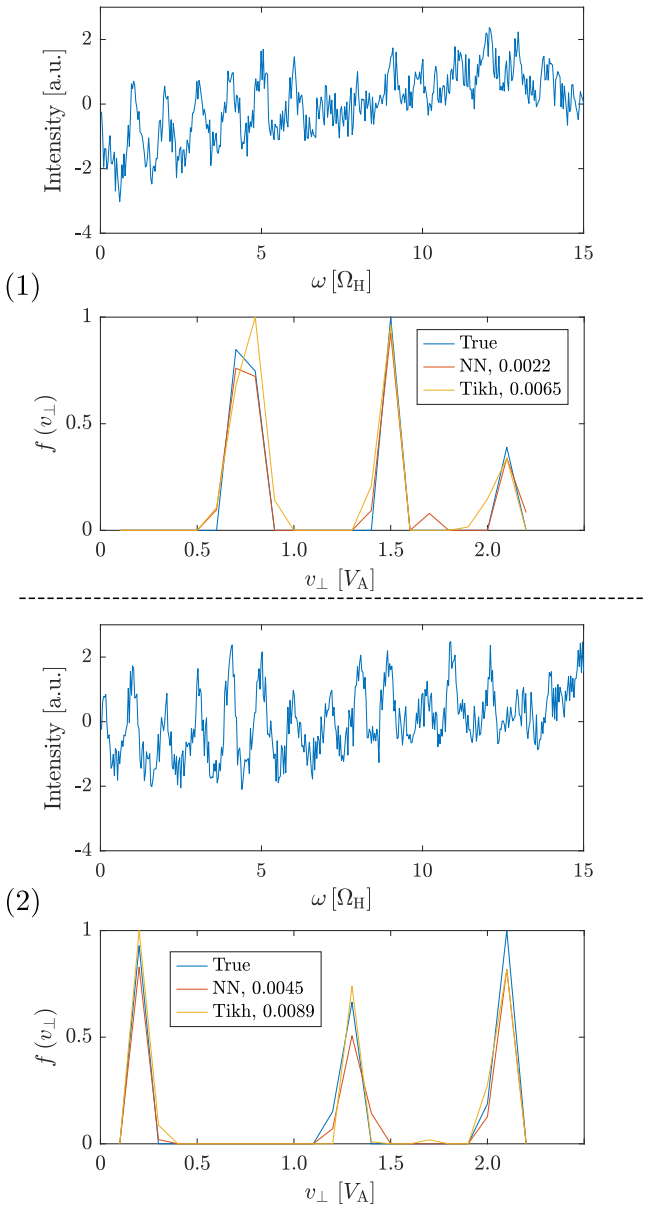

Figure 4.7: Two signals with the deep neural network ("NN") and Tikhonov inversion ("Tikh") predictions compared to the true solutions ("True"). The MSE is indicated. Note that the signals are normalized so that the y-axis is the normalized intensity in arbitrary units.

Chapter 5

2D ICE weight functions and reconstruction techniques for ion cyclotron emission

This chapter presents the paper "Velocity-space sensitivity and inversions of synthetic ion cyclotron emission", submitted to the journal *Physics of Plasmas*.

5.0 Abstract

This paper introduces a new model to find the velocity-space location of energetic ions generating ion cyclotron emission (ICE) in plasmas. ICE is thought to be generated due to inverted gradients in the $v_\perp$ direction of the velocity distribution function or due to anisotropies, i.e., strong gradients in the pitch direction. Here, we invert synthetic ICE spectra generated from first principles PIC-hybrid computations to find the locations of these ICE-generating ions in velocity space in terms of a probability distribution function. To this end, we compute 2D ICE weight functions based on the magnetoacoustic cyclotron instability which reveals the velocity-space sensitivity of ICE measurements. As an example, we analyze the velocity-space sensitivity of synthetic ICE measurements near the first 15 harmonics for plasma parameters typical for the Large Helical Device. Further, we investigate the applicability of a least-square subset search, Tikhonov regularization, and Lasso regularization to obtain the locations in velocity space of the ions generating the ICE.

5.1 Introduction

Ion cyclotron emission (ICE) refers to strongly superthermal radiation in the ion cyclotron range of frequencies (ICRF), typically with well-defined power spectral peaks associated with harmonics of the local cyclotron frequency of a minority energetic ion population within the plasma. ICE has been detected using externally mounted antennas and probes, and also recently by internal scattering.[1] It can exhibit both predominantly electromagnetic or electrostatic characteristics;[2] in both cases, it appears to be driven by collective relaxation of the energetic ions under the

[1] Crocker et al. (2022).
[2] Dendy et al. (1992) and Dendy et al. (1994).

magnetoacoustic cyclotron instability (MCI). In tokamaks, MCIs can, for example, be driven by marginally-trapped fusion products born in the center of the plasma with a radial drift to the outer edge of the plasma.[3] The velocity distribution of the fusion products from the location emitting the ICE contains anisotropies or inverted gradients in the form of a local maximum in pitch or energy. Such anisotropies and inverted gradients contain free energy to drive the MCI.

An ICE diagnostic is a passive non-invasive diagnostic. It is possible to measure characteristics of fast ions and of phenomena producing signals in the ion-cyclotron frequency range such as compressional Alfvén eigenmodes (CAEs) and global Alfvén eigenmodes (GAEs) with ICE detectors.[4] The diagnostic is compatible with high-radiation environments such as in ITER, e.g., by using the antennas for electromagnetic wave heating in the ion cyclotron range of frequencies (ICRF) as receivers.[5]

ICE refers to the signal generated at integer multiples of the ion cyclotron frequency of the ion species generating it. Including the Doppler shift, the resonance condition of the ICE-generating ions is

$$\omega = n\Omega_\mathrm{s} + v_\parallel k_\parallel, \tag{5.1}$$

where n is a positive integer, Ω_s is the cyclotron frequency for the ion species s, $v_\parallel$ is the velocity of the ions parallel to the magnetic field, and $k_\parallel$ is the parallel wave number. Typically, the frequency of the fundamental harmonic is around 10 MHz depending on the magnetic field and species.[6]

Studies at JET in the early 1990s discovered a linear relationship between the ICE signal intensity and the neutron emission rate from DT reactions by comparing ICE from DD and DT plasmas heated using neutral beam injection (NBI).[7] They concluded that fusion alpha particles were responsible for providing the free energy to generate ICE localized at the outer midplane edge of the plasma, near the last closed flux surface. Measurements at LHD also detected ICE from lost ions at the plasma edge during perpendicular hydrogen NBI and from ions lost due to toroidicity-induced Alfvén eigenmode (TAE) bursts.[8] Recently, an ICE detector has been installed at Wendelstein 7-X.[9] Further, beam-heated plasmas on several tokamaks emit core ICE signals generated by the MCI driven by the velocity-space inversion of sub-Alfvénic beam-injected ions.[10] Thus, ICE signals provide helpful information for diagnosing fast-ion behavior.

We want to infer the location of the source of the ICE in velocity space from measured ICE signals. Research over the last decade has inferred 2D fast-ion velocity distribution functions for diagnostics such as FIDA spectroscopy[11], collective Thomson scattering (CTS)[12], neutron emission spectrometry (NES)[13], γ-ray spectrometry (GRS)[14], and scintillator-based fast-ion loss detectors (FILDs)[15] at tokamaks such as ASDEX Upgrade, JET, EAST, DIII-D, and MAST. For these diagnostics, the 2D fast-ion velocity distribution function is determined from measurements

[3] McClements et al. (1999).

[4] Cottrell et al. (1993), Fredrickson et al. (2001), W. W. Heidbrink et al. (2006), Appel et al. (2008), Saito et al. (2013), Gorelenkov (2016), Ochoukov et al. (2020), and Ochoukov et al. (2023).

[5] Dendy et al. (1994) and McClements et al. (2015).

[6] Ochoukov, McClements, et al. (2019).

[7] Cottrell et al. (1993).

[8] Saito et al. (2013).

[9] Moseev et al. (2021).

[10] Ochoukov, McClements, et al. (2019), Liu et al. (2021), and Liu et al. (2023).

[11] Salewski, Geiger, Moseev, et al. (2014), Weiland et al. (2016), Salewski, Geiger, Jacobsen, et al. (2016), Weiland et al. (2017), Madsen et al. (2018), Madsen, Salewski, et al. (2020), Madsen, Huang, et al. (2020), and Su et al. (2021).

[12] Jacobsen et al. (2016b).

[13] Salewski et al. (2017) and Salewski, Geiger, Jacobsen, et al. (2018).

[14] Salewski et al. (2017) and Salewski, Geiger, Jacobsen, et al. (2018).

[15] Galdon-Quiroga, Garcia-Munoz, Sanchis-Sanchez, et al. (2018) and Galdon-Quiroga, Garcia-Munoz, Salewski, et al. (2018).

by solving an inverse problem. The technique is called 'velocity-space tomography.' In addition to 2D velocity distribution functions, velocity-space tomography has inferred 1D velocity distribution functions of FIDA[16] measurements, synthetic ICE measurements[17], and 3D phase-space distributions of all energetic particle orbits based on FIDA measurements.[18] Such inversions require knowledge of the velocity-space sensitivity of the diagnostics, which is encoded in weight functions. Weight functions have been developed for most of the above-mentioned diagnostics, including FIDA[19], neutral particle analyzers (NPA)[20], CTS[21], FILDs[22], GRS[23], NES[24], and 3 MeV proton diagnostics[25].

The conceptual framework, interpretation, and practical implementation of the 2D ICE weight function formalism to obtain the locations of the ions generating the ICE in velocity space from ICE signals are developed in this paper. In section 2, it is argued, based on results from ICE experiments and simulations, that ICE weight functions can be computed for ICE arising from a single ring-beam fast ion distribution function. In section 3, a new model for the inference of the location of the ICE source is presented. In section 4, the generation of the 2D weight functions is explained. In section 5, the velocity-space sensitivity quantified by ICE weight functions is interpreted. In section 6, the locations of the ions generating the ICE in velocity space are obtained by applying a subset search, Tikhonov regularization, and Lasso regularization to synthetic ICE signals. In section 7, a conclusion and future outlook are given.

5.2 Modelling of ICE

ICE is thought to be generated by inverted gradients in velocity space or anisotropies. Often a ring distribution is used to model ICE.[26] It is then investigated if this ring distribution drives ICE by solving a dispersion relation or Maxwell-Vlasov equations, and this rests on the identification of a subset of energetic ions. This is the case for the analysis of ICE in JET[27] and TFTR[28] DT plasmas, KSTAR[29], ASDEX-U[30], LHD[31], JT-60U[32], DIII-D[33], and EAST[34]. Additionally, the emission location or resonance condition needs to be identified. When several peaks are present, this is usually inferred from the spectral spacing taken to correspond to the fundamental cyclotron frequency of the emitting species under the assumption of drive by a single species at a given location. Disambiguation of ICE has been achieved in the presence of one single spectral peak,[35]

[16] Salewski (2019).
[17] Schmidt et al. (2021).
[18] Stagner et al. (2022)
[19] W. W. Heidbrink et al. (2007) and Salewski, Geiger, Moseev, et al. (2014).
[20] W. W. Heidbrink et al. (2007).
[21] Salewski et al. (2011).
[22] Galdon-Quiroga, Garcia-Munoz, Sanchis-Sanchez, et al. (2018).
[23] Salewski, Nocente, Gorini, et al. (2015) and Salewski, Geiger, Jacobsen, et al. (2016).
[24] Jacobsen et al. (2015), Eriksson et al. (2019), Järleblad et al. (2021), and Järleblad et al. (2022).
[25] W. Heidbrink et al. (2021).
[26] Moseev and Salewski (2019).
[27] Cottrell et al. (1993)
[28] Cauffman et al. (1995)
[29] Thatipamula et al. (2016), Chapman et al. (2017), and Chapman et al. (2019).
[30] Ochoukov, McClements, et al. (2019) and Chapman et al. (2020).
[31] Saito et al. (2009), Veshchev et al. (2009), Bustos et al. (2011), Ozaki et al. (2012), Reman (2018), and Reman et al. (2019).
[32] Sumida et al. (2017), Sumida et al. (2018), Sumida et al. (2021).
[33] Thome et al. (2019), Zalzali et al. (2021), and DeGrandchamp et al. (2022).
[34] Liu et al. (2023).
[35] See, for example, Ochoukov, McClements, et al. (2019) and Sumida et al. (2021).

and in the presence of multiple energetic ion species.[36] Once a likely emission location with an inversion or a strong anisotropy has been identified, a particle-in-cell (PIC) simulation in the local approximation can be set up to study the fast collisionless relaxation of energetic ions under the MCI[37] from which the linear phase is compared with theory[38], synthetic spectra are calculated, and the non-linear phase investigated by higher order spectral methods[39].

Complementary to comparing measured ICE spectra to simulated ICE spectra, obtained in the nonlinear saturated regime from PIC-type computations, one may also compare the time evolution of measured ICE spectra to linear growth rates obtained from MCI theory. Such an approach was first applied[40] for TFTR (for sub-Alfvénic MCI with finite $k_\parallel$) and more recently in ASDEX Upgrade core ICE driven by sub-Alfvénic energetic deuterons in deuterium plasmas[41] and by sub-Alfvénic fast hydrogen in helium plasmas[42]. In these studies at ASDEX Upgrade, TRANSP simulations of NBI show three peaks at the full, half, and third of the injection energy. In the modelling, the growth rates were evaluated using cold ring distributions located at the full-energy beam peak in velocity space. The propagation angle of the ICE was constrained by maximising growth rate and avoiding strong wave reabsorption in the plasma. Recent PIC simulations have shown that several energetic ion populations can simultaneously drive the MCI and also interact with it. This is true for beam-driven MCI and the beam ions interacting with the MCI[43] but also for beam ions driving the MCI interacting with an energetic thermal ion population (100 keV helium ash α-particles).[44] Therefore, this questions the relaxation of single ring distributions for NBI studies. However, the beam deposition profile is energy dependent, so two fast ion populations may not reach their maximum density at the same radial position, thereby minimising such interactions.[45] If one is interested in finding where in velocity space instability occurs, it will usually be dictated by the maximum energy component, provided an inverted gradient in velocity space exists in that region. Therefore, as indicated by simulations, ICE in the presence of beam interaction will still be strongly driven, possibly affecting the spectral properties, but not as much if the beam density profiles peak at different locations. This motivates the calculation of weight functions arising from a single ring distribution of fast ions in this work.

The physical parameters correspond to those of the LHD edge given in Schmidt et al. (2021) and Reman et al. (2022): the magnitude of the background magnetic field is $B_0 = 1.75$ T, electron density $n_e = 0.9 \times 10^{19}$ m^{-3}, and thermal electron and deuteron temperatures $T_\mathrm{e} = 800$ eV and $T_D = 900$ eV. The hybrid-PIC simulations initialise the background thermal deuterons and ring distributed protons on a 1D grid consisting of 2048 cells using a quiet start for the thermal deuterons. Each ion species is represented by 500 macroparticles per cell. The code follows the velocity-space trajectories, including the gyromotion of the fully-kinetic energetic and thermal ions, together with the three components of the electric and magnetic fields in an isothermal massless neutralizing electron fluid. The three velocity components of ions are sampled randomly (1D3V PIC simulations). This approach assumes that the physics embodied in the PIC-hybrid simulations dominates the generation of the observed ICE signals, and this appears to be well grounded[46]. These simulations are followed through the linear phase of the MCI and then deeply

[36] See, for example, Cauffman and Majeski, 1995, Ichimura et al. (2008), Sato et al. (2010), and L. N. Liu et al. (2019).
[37] Cook et al. (2013) and Carbajal et al. (2014).
[38] Belikov and Kolesnichenko (1975) and Dendy et al. (1992).
[39] Carbajal et al. (2014) and Chapman et al. (2018).
[40] McClements et al. (1996).
[41] Ochoukov, McClements, et al. (2019).
[42] Liu et al. (2021).
[43] Reman (2018).
[44] Dendy et al. (2023).
[45] Wesson (2011).
[46] Cook et al. (2013).

into its non-linear saturated phase. The energetic protons are initialized uniformly and randomly in space with velocities following a cold ring distribution $f_{\mathrm{CR}}(v_\parallel, v_\perp) = n_{\mathrm{H}}\delta\left(v_\parallel - u_\parallel\right)\delta\left(v_\perp - u_\perp\right)$ to generate the inversion with $u_\perp = [0.6 : 0.1 : 2.6]\ v_{\mathrm{A}}$ and $u_\parallel = [-2.6 : 0.1 : 2.6]\ v_{\mathrm{A}}$, where $v_{\mathrm{A}} = 0.9 \times 10^7$ m s^{-1} is the Alfvén speed at the emission location. Carrying out a full scan over $(u_\parallel, u_\perp)$ equates to scanning over $(v_\parallel, v_\perp)$ and for convenience we use the latter variables from here on. The calculations are carried over 60 proton gyroperiods, ensuring saturation of the MCI across every simulation for a relative energetic proton density $n_{\mathrm{H}}/n_{\mathrm{e}} = 1.75 \times 10^{-3}$. The relaxation of the energetic protons through the MCI generates excitations of the magnetic fields at multiple cyclotron harmonics on the fast-Alfvén branch. The spatiotemporal fast Fourier transform of the perturbed magnetic field $\delta B_z\left(x,t\right)$ calculated over the whole grid and simulation duration provides the 2D dispersion relation $\delta B_z\left(k,\omega\right)$ where k and ω are the wavenumber and frequency. One-dimensional power spectra are obtained by summing over wavenumber-space. The power spectra consist of 900 points spanning the first 15 hydrogen harmonics.

5.3 A model for finding probabilities of ICE emission in velocity space

The relation between the signal $s \in \mathbb{R}^m$ as measured by a given diagnostic and the corresponding velocity distribution $f \in \mathbb{R}^n$ in velocity-space tomography is typically modelled as the matrix-vector equation

$$Wf = s^{\mathrm{exact}} + e \tag{5.2}$$

for a weight function matrix $W \in \mathbb{R}^{m\times n}$ unique for the diagnostic and Gaussian white noise vector e. The signal vector s^{exact} is the true signal, and $s = s^{\mathrm{exact}} + e$ the measured signal including noise. The weight function matrix contains the sensitivities of the diagnostic in velocity space for every measured data point.

Previous work on ICE weight functions computed the 1D weight functions to find the location of the source of the ICE described by the velocity distribution function $\boldsymbol{f} = f\left(v_\perp\right)$ from ICE signals by solving the inverse problem in Eq. (5.2).[47] It has since been shown that the ICE signal can be Doppler-shifted due to the parallel velocities of the ions[48]. Hence, we here include the parallel velocities and compute the 2D weight functions used to obtain the locations of the ions generating the ICE in velocity space under the same conditions.

5.3.1 The inverse problem for ICE

Typically, velocity-space tomography is viewed as the inference of a 2D velocity distribution function f from a signal s. For example, consider a Maxwellian distribution f. The noise free signal of the diagnostic is then $s = Wf$. However, a Maxwellian distribution has no inverted velocity-space gradients or anisotropy, so it will not generate an ICE signal. ICE requires a highly non-Maxwellian subpopulation often modelled as a cold ring distribution $f_{\mathrm{CR}}(v_\parallel, v_\perp) = n_{\mathrm{H}}\delta\left(v_\parallel - u_\parallel\right)\delta\left(v_\perp - u_\perp\right)$ corresponding to a single point in velocity space.[49] The goal of ICE reconstructions is to infer the location of the ICE-generating cold ring distribution from the ICE signal and not the entire fast-ion velocity distribution function.

The probability density function $p\left(v_\parallel, v_\perp \mid p_s(\omega)\right)$ of the velocities of the ICE-generating ions with velocity components $(v_\parallel, v_\perp)$ is related to the probability that the source of the ICE occupied a given location in velocity space at the time of emission. The latter probability is contained in

[47] Schmidt et al. (2021)
[48] Reman et al. (2022).
[49] Moseev and Salewski (2019).

the ICE probability density function $p_s(\omega)$. Thus, the question becomes: given a measured ICE signal $p_s(\omega)$, what is the probability that $p_s(\omega)$ originated from certain $v_\parallel$ and $v_\perp$?

From Bayes' theorem, the probability density function $p\left(v_\parallel, v_\perp \mid p_s(\omega)\right)$ satisfies

$$p\left(v_\parallel, v_\perp \mid p_s(\omega)\right) = \frac{p\left(p_s(\omega) \mid v_\parallel, v_\perp\right) p\left(v_\parallel, v_\perp\right)}{p\left(p_s(\omega)\right)}, \tag{5.3}$$

where | means 'given'. The sought quantity is the posterior $p\left(v_\parallel, v_\perp \mid p_s(\omega)\right)$ giving the probability of the source location being at the coordinates $(v_\parallel, v_\perp)$ given the measured signal $p_s(\omega)$. This, in turn, is given by the product of the likelihood $p\left(p_s(\omega) \mid v_\parallel, v_\perp\right)$ and the prior $p\left(v_\parallel, v_\perp\right)$. The likelihood states the probability of observing such a signal $p_{\boldsymbol{s}}(\omega)$ given the signal originated from ions at $(v_\parallel, v_\perp)$. The prior states the probability of the signal being generated from this location in velocity space before having any measurements (our prior belief). The occurrence of a specific event given a point estimate of $v_\parallel$ and $v_\perp$ is obtained by maximizing the posterior $p\left(v_\parallel, v_\perp \mid p_s(\omega)\right)$ as determined by maximum a posteriori (MAP) estimation. Thus,

$$\max_{v_\parallel, v_\perp} p\left(v_\parallel, v_\perp \mid p_s(\omega)\right) = \max_{v_\parallel, v_\perp} \frac{p\left(p_s(\omega) \mid v_\parallel, v_\perp\right) p\left(v_\parallel, v_\perp\right)}{p\left(p_s(\omega)\right)}. \tag{5.4}$$

Let f be the vector containing the locations of the ions generating the ICE in velocity space, i.e., a 1D array reshaped from the 2D velocity distribution of the ions generating the ICE, and s the measured ICE signal. Furthermore, assume the noise in s is independent and normally distributed. Based on the forward model $Wf = s$, the likelihood then satisfies

$$p\left(p_s(\omega) \mid v_\parallel, v_\perp\right) \propto \exp\left(-\frac{1}{2}\left\|Wf - s\right\|_2^2\right). \tag{5.5}$$

Suppose the prior follows a multivariate Gaussian distribution, so

$$p\left(v_\parallel, v_\perp\right) \propto \exp\left(-\frac{1}{2}\lambda \left\|f\right\|_2^2\right), \tag{5.6}$$

where $\lambda > 0$ is a width-scaling for the distribution. Substituting Eqs. (5.5) and (5.6) in Eq. (5.4), we obtain

$$\max_{v_\parallel, v_\perp} p\left(v_\parallel, v_\perp \mid p_s(\omega)\right) \propto \max_{f} \left[\exp\left(-\frac{1}{2}\left\|Wf - s\right\|_2^2 - \frac{1}{2}\lambda \left\|f\right\|_2^2\right)\right] \tag{5.7}$$

Since the maximum is attained if and only if the negative logarithm is minimized, we may write

$$\max_{v_\parallel, v_\perp} p\left(v_\parallel, v_\perp \mid p_s(\omega)\right) = \min_{v_\parallel, v_\perp} \left\{-\log\left(p\left(p_s(\omega) \mid v_\parallel, v_\perp\right)\right) - \log\left(p\left(v_\parallel, v_\perp\right)\right)\right\} \tag{5.8}$$

$$\Leftrightarrow$$

$$\max_{v_\parallel, v_\perp} p\left(v_\parallel, v_\perp \mid p_s(\omega)\right) = \min_{f} \left\{\frac{1}{2}\left\|Wf - s\right\|_2^2 + \frac{1}{2}\lambda \left\|f\right\|_2^2\right\}. \tag{5.9}$$

Equation (5.9) is the 0th-order Tikhonov regularization formulation used to great success in computing the 2D velocity distributions for the diagnostics mentioned in the introduction. Thus, the interpretation of the velocity distribution of the ions generating the ICE as a probability density function $p\left(v_\parallel, v_\perp \mid p_s(\omega)\right)$ given the ICE emission probability density function $p_s(\omega)$ is equivalent to solving the equation $Wf = s$ using 0th-order Tikhonov regularization.

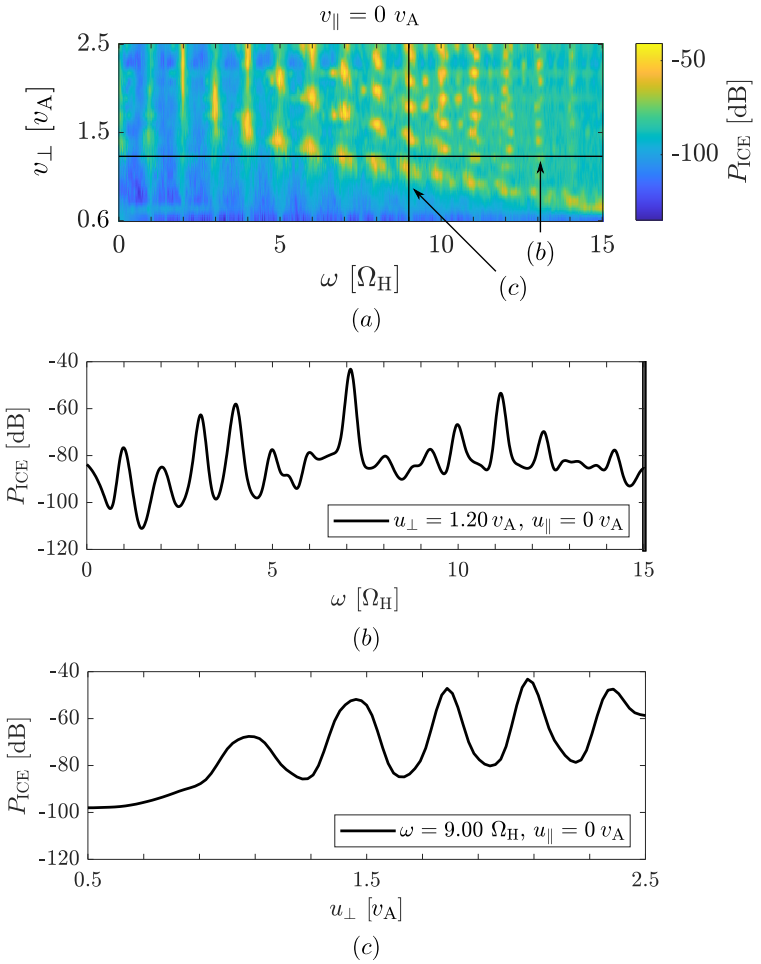

Figure 5.1: (a) Power spectra computed for $v_\parallel = 0\ v_A$ and $v_\perp \in [0.6, 2.6]\ v_A$ and combined into one figure computed for an MCI at LHD. (b) An example power spectrum for $v_\perp = 1.20\ v_A$ and $v_\parallel = 0\ v_A$. (c) A 1D weight function in $v_\perp$ for $v_\parallel = 0\ v_A$.

5.4 2D ICE weight functions

The physics relating an ICE signal to the location of its driving source in 2D velocity space is contained in the weight function matrix W. The weight function matrix is obtained by computing 1D power spectra for a range of $v_\parallel$ and $v_\perp$ which are then subsequently combined appropriately as explained in this section. Recall that a power spectrum contains the signal intensities for all frequencies for a given $v_\parallel$ and $v_\perp$. Collecting the power spectra from low to high $v_\perp$ for a given $v_\parallel$ produces a set of 1D weight function as illustrated in Fig. 5.1 for $v_\parallel = 0\, v_A$ computed for an ICE detector at LHD, as was done in previous work.[50] The 1D weight functions provide the detector sensitivity at a given frequency for a given parallel velocity, which was assumed to be zero.

To obtain the weight function matrix to be used for reconstructions, the power spectra are stacked as shown in Fig. 5.2. The result is the matrix W_{ijk}. The i index corresponds to $v_\parallel$, the j

[50] Schmidt et al. (2021).

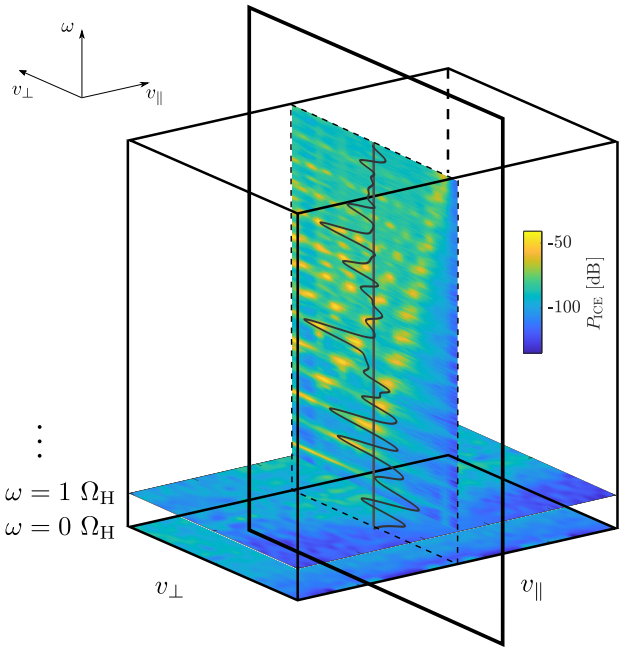

Figure 5.2: The 3D weight function matrix W_{ijk} is obtained by stacking the 1D power spectra according to the location of the ring distribution $f(v_\parallel, v_\perp)$. The intersection of the black square with the cube indicated by a dashed line is a cross section of the 3D matrix at a specific $v_\parallel$. Each vertical line corresponds to a power spectrum, as indicated by the vertical central line.

index to $v_\perp$, and the k index to ω (not to be confused with the wavenumber k). Cross-sections across the frequency dimension of W_{ijk} result in 2D weight functions in $v_\parallel$ and $v_\perp$. The dashed line in Fig. 5.2 indicates a cross-section of the 3D array for $v_\parallel = 0\ v_{\mathrm{A}}$, showing the 1D power spectrum from Fig. 5.1. The horizontal cross sections are the 2D weight functions.

The $v_\parallel$-resolution is 0.1 v_{A}, and the frequency resolution is $\Omega_{\mathrm{H}}/60 \approx 0.6$ MHz. The frequency range of ω is 0 to 15 Ω_{H}, where Ω_{H} is the fundamental hydrogen cyclotron frequency. This frequency range equals that used in prior work on ICE weight functions.[51] Each signal peak around the harmonics contains around 10-15 frequency measurements corresponding to $6-9$ MHz. This resolution is equal to that expected for ICE detectors at ITER.

5.5 Characteristics of 2D ICE weight functions in $v_\parallel$ and $v_\perp$

In this section we discuss the characteristics of the 2D ICE weight function formalism to infer the probability density function of the ICE-generating ions in velocity space. This development includes analysis of the characteristics of the 2D ICE weight functions in the spectral vicinity of harmonics and for increasing harmonic number.

Figure 5.3 shows the 2D ICE weight functions at several frequencies close to the fourth harmonic. ICE weight functions quantify the expected signal given an ion at a location $(v_\parallel, v_\perp)$. The high-sensitivity areas occur in bands wide in $v_\parallel$ and narrow in $v_\perp$. At 3.83 Ω_{H}, the sensitivity is largest for positive $v_\parallel$. The closer the frequency is to the fourth harmonic, the smaller $v_\parallel$ of the most sensitive region, until right at the fourth harmonic where the sensitivity is largest for $v_\parallel = 0$.

[51] Schmidt et al. (2021).

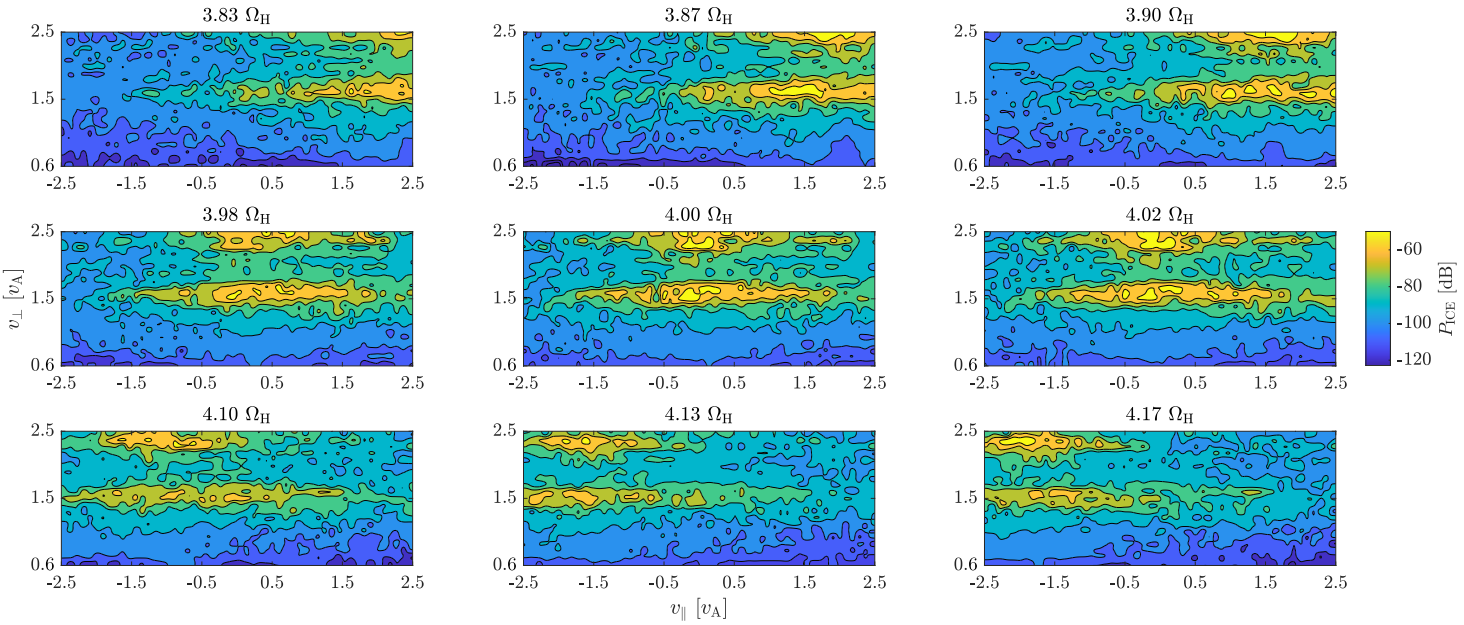

Figure 5.3: 2D weight functions in $v_\parallel$ and $v_\perp$ around the fourth hydrogen harmonic. The high-sensitivity regions are indicated by a bright yellow colour. Note the movement of the center of the highest sensitivity region for $v_\perp \approx 1.5\ v_\mathrm{A}$ from around $v_\parallel \approx 2.0\, v_\mathrm{A}$ at $3.83\,\Omega_\mathrm{H}$ to $v_\parallel = 0\, v_\mathrm{A}$ at $4\,\Omega_\mathrm{H}$ to $v_\parallel \approx -1.5\, v_\mathrm{A}$ at $4.17\,\Omega_\mathrm{H}$. Note also how the second band occurs for progressively lower $v_\perp$ as the frequency increases.

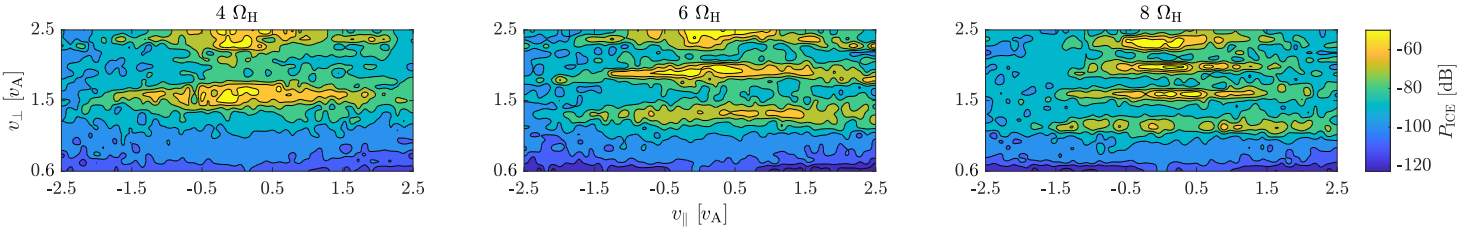

Figure 5.4: 2D weight functions for the $\omega = 4\ \Omega_\mathrm{H}, 6\ \Omega_\mathrm{H}$, and $8\ \Omega_\mathrm{H}$. Note that the number of sensitivity bands increases by one every second harmonics. The width of the bands in $v_\perp$ decrease for higher harmonics.

The same pattern is seen for frequencies larger than the fourth harmonic, where $v_\parallel$ of the most sensitive region increases in the negative direction with the frequency shift. This is due to the Doppler shift term $k_\parallel v_\parallel$ in the resonance condition

$$\omega = n\Omega_\mathrm{H} + k_\parallel v_\parallel. \tag{5.10}$$

The sensitivity patterns illustrated in Fig. 5.3 occur for every harmonic. Fig. 5.4 illustrates examples of higher harmonics. For $v_\perp \in [0.6\,v_\mathrm{A}, 2.6\,v_\mathrm{A}]$, the number of high-sensitivity bands increases by 1 every second harmonic with no high-sensitivity band occurring at the first harmonic. Thus, for lower frequencies, only specific $v_\perp$ can contribute to the signal generation. For higher frequencies, several bands in $v_\parallel$ with different values of $v_\perp$ can contribute to the signal generation. Further, the width of the bands decreases with increasing harmonic number, and they occur for lower values of $v_\perp$.

5.6 Inversion methods for ICE

The goal of ICE reconstructions is to infer the velocity-space location of the ICE-generating ions from an ICE signal. This is achieved by solving the inverse problem in $\boldsymbol{Wf} = \boldsymbol{s}$, and the resulting 2D probability distribution of the location of ICE emission $\boldsymbol{f}$ is called a 'reconstruction'. A regular least-square inversion fails since the problem is ill-posed. Here, we illustrate three different techniques to compute reconstructions: (i) 0th-order Tikhonov regularization, (ii) a least-square subset search, and (iii) Lasso regularization. In the following, we consider values of $v_\parallel \in [-2.6\,v_\mathrm{A}, 2.6\,v_\mathrm{A}]$ and $v_\perp \in [0.6\,v_\mathrm{A}, 2.6\,v_\mathrm{A}]$. The grid discretizes velocity space into single pixels of size approximately $0.1\ v_\mathrm{A} \times 0.1\ v_\mathrm{A}$. To avoid performing inverse crime when reconstructing the 2D velocity-space distributions of the ICE-generating ions, a finer grid is used to create the ICE signals in the forward model; see Ref [80] p. 139 ff. for details. This grid is five times as fine, i.e., $0.02\ v_\mathrm{A} \times 0.02\ v_\mathrm{A}$.

In the following calculations, it is assumed that ICE is likely to be generated at only one or a few locations in velocity space. This is well motivated, as current theory suggests the primary generation mechanism of ICE is given by a cold ring distribution[52], cf. the discussion in Section 5.2.

5.6.1 Tikhonov regularization

As shown above in Eq. (5.9), 0th-order Tikhonov regularization solves the problem

$$f^* = \underset{f}{\operatorname{argmin}} \|Wf - s\|_2^2 + \lambda \|f\|_2^2 \tag{5.11}$$

for some non-negative value of the regularization parameter λ, where the factors of $1/2$ have been removed. The noise e in the measured signal $s = s^\mathrm{exact} + e$ influences the accuracy of the reconstruction f^*. The weight function matrix W determines how much the noise affects the reconstruction. An upper bound on the error in the reconstruction is

$$\frac{\|\delta f\|_2}{\|f\|_2} \leq \kappa(W) \frac{\|\delta s\|_2}{\|s\|_2}, \tag{5.12}$$

where $\kappa(W) = s_1/s_n$ is the condition number defined in terms of the largest and smallest singular values s_1 and s_n of W. For our weight function matrix, $\kappa(W) \approx 10^4$, so the problem is not

[52] Dendy et al. (1995).

well-conditioned, but it is also not terribly ill-conditioned. For other inverse problems such as velocity-space tomography of CTS or FIDA signals, $\kappa(W) > 10^{15}$ indicating a significant need for regularization. However, in the case of ICE generated by an MCI at LHD, observation-relevant noise levels of around 10% might not impact the reconstruction f^* to a significant degree due to the relatively low value of $\kappa(W)$. The insignificant influence of the noise in the reconstruction is reflected in some synthetic signals having $\lambda \approx 10^{-7}$ as the optimal regularization parameter.

Characteristics of the solution are reflected in the singular vectors v_i of the singular value decomposition (SVD) of W.[53] For any matrix $W \in \mathbb{R}^{m\times n}$, the SVD can be written as

$$W = U\Sigma V^{\mathrm{T}} = \sum_{i=1}^{r} u_i \sigma_i v_i^{\mathrm{T}}, \tag{5.13}$$

where $r \leq \min(m, n)$ is the rank of W, $U \in \mathbb{R}^{m\times m}$ and $V \in \mathbb{R}^{n\times n}$ are unitary matrices, and $\Sigma \in \mathbb{R}^{m\times n}$ is a rectangular matrix with positive real numbers σ_i, $i = 1, \ldots, r$, on the diagonal ($m = n$). These numbers, called the 'singular values', satisfy $\sigma_1 \geq \sigma_2 \geq \cdots \geq \sigma_r$. The matrices U and V contain the left and right singular vectors,

$$U = (u_1, u_2, \ldots, u_m)\,, \quad V = (v_1, v_2, \ldots, v_n)\,. \tag{5.14}$$

Without any regularization, the naïve solution to Eq. (5.2) can be written in terms of the SVD components as

$$f = W^{\dagger} s = \sum_{i=1}^{n} \frac{u_i^{\mathrm{T}} s}{\sigma_i} v_i, \tag{5.15}$$

where $W^{\dagger}$ is the Moore-Penrose pseudo-inverse of W. Several regularization methods can be written as a filtered SVD expansion of the form

$$f_{\mathrm{reg}} = \sum_{i=1}^{n} \varphi_i \frac{u_i^{\mathrm{T}} s}{\sigma_i} v_i, \tag{5.16}$$

where φ_i are the filter factors of the given regularization method. For 0th-order Tikhonov regularization, the filter factors in terms of the regularization parameter λ are

$$\varphi_i^{[\lambda]} = \frac{\sigma_i^2}{\sigma_i^2 + \lambda^2} \approx \begin{cases} 1, & \text{for } \sigma_i \gg \lambda, \\ \sigma_i^2/\lambda^2, & \text{for } \sigma_i \ll \lambda. \end{cases} \tag{5.17}$$

Thus, for all i such that the singular values σ_i are larger than λ, the SVD components contribute almost fully to the solution. For all i such that the singular values σ_i are much smaller than λ, the SVD components are damped and do not contribute as much to the solution. Hence, the right singular vectors v_i corresponding to the largest singular values contribute the most to a Tikhonov-regularized solution. The characteristics of these vectors will therefore be reflected in the solutions found.

The first nine right singular vectors are shown in Fig. 5.5. Observe that the first five have areas spanning a wide range of $v_{\parallel}$ and $v_{\perp}$ with approximately equal intensity within the given range. The right singular vectors numbered six to nine have clear bands in the $v_{\parallel}$ direction for a small range of $v_{\perp}$. These properties indicate that the sensitivity in $v_{\perp}$ is good and the sensitivity in $v_{\parallel}$ worse. Thus, we expect to do better in finding the location of the ICE-generating ions in the $v_{\perp}$-direction than in the $v_{\parallel}$-direction.

[53] Hansen (2010)

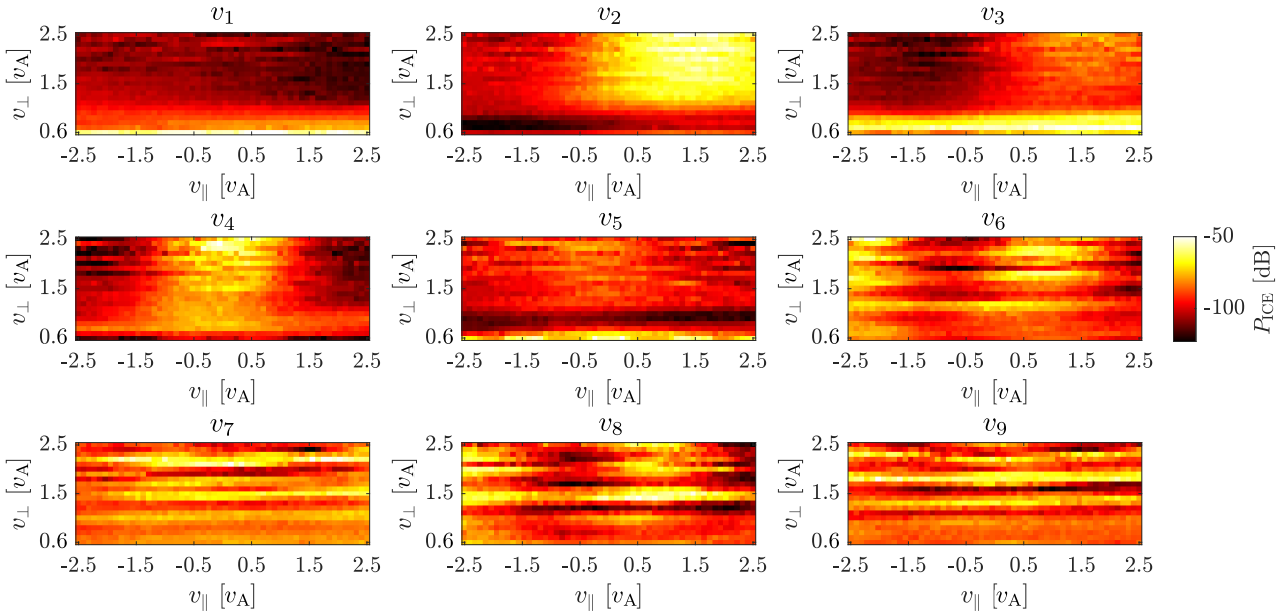

Figure 5.5: The first nine right singular vectors $\boldsymbol{v}_i$ from the SVD of $\boldsymbol{W}$. They reflect the dominant components of the regularized solution found using Tikhonov regularization. Observe the large areas with the same sensitivity for the first five vectors and the bands in the $v_\parallel$-direction for the singular vectors numbered six to nine. These properties reflect the sensitivity of the regularized solutions in $v_\parallel$ and $v_\perp$.

5.6.2 The least-square subset search

Since we are looking for a particular location in velocity space rather than for an entire distribution function, it might be feasible to simply compare synthetic data from all possible locations in velocity space with the actual data. For ICE-generating ions at any location in velocity space, we can calculate the corresponding ICE signal using the forward model in Eq. (5.2). Thus, we compute a signal $\sigma^{[i]}$ for every possible location of ICE emission in velocity space $\varphi^{[i]}$ (not to be confused with the singular values and filter factors defined above) and store it in an array $D_\sigma = [\sigma^{[1]}, \ldots, \sigma^{[N]}]$, where the superscript '$[i]$' indicates the number in the array, while also storing the corresponding velocity distributions in the array $D_\varphi = [\varphi^{[1]}, \ldots, \varphi^{[N]}]$. The number N is the total number of simulated ICE signals and velocity distributions. The elements in the arrays satisfy $W\varphi^{[i]} = \sigma^{[i]}$.

Consider then the subset $V \subseteq D_\varphi \oplus D_\sigma$ consisting of all physically relevant $(\sigma^{[i]}, \varphi^{[i]})$-pairs. A measured ICE signal $s = s^{\text{exact}} + e$ consisting of the underlying exact signal s^{exact} and noise vector e being additive white and Gaussian with $e \sim \mathcal{N}\left(0, \eta^2 I\right)$ is then compared against the first entry of all elements in V by calculating

$$\Delta_2(s, \sigma^{[i]}) \equiv \left\| s - \sigma^{[i]} \right\|_2^2 \tag{5.18}$$

for all i. The signal $\sigma^{*[i]}$ with lowest Δ_2 is chosen to be s^{exact}. The corresponding distribution $\varphi^{*[i]}$ used to generate $\sigma^{*[i]}$ is then considered to contain the location of the ions that generated the signal. If the exact signal is not in the subset, the closest match is chosen by minimizing Δ_2.

Several challenges are associated with this technique: (i) the noise e may corrupt the measured signal s so the best-fitting signal $\sigma^{*[i]}$ suggested by the least-square subset search is incorrect, (ii) if ICE originates from more than one location, the subset may be too large to be stored on a server, and (iii) computations may take too long due to the large size of the subset. We suggest ways to overcome these challenges below.

For the least-square subset search, it is impractical to assign locations in velocity space continuous probabilities. Thus, we need only consider a subset. Since the primary goal of ICE reconstructions is to infer the location of the ions generating the ICE in velocity space, we may assume that the values of a pixel are binary: '0' indicates that no part of the ICE signal was generated from this location in velocity space, and '1' indicates that this location of velocity space generated part of or all of the ICE signal.

To avoid dependency of the synthetic ICE signals $\sigma^{[i]}$ and measured ICE signals s on the intensity of the pixels in discretized velocity space, $\sigma^{[i]}$ and s are normalized before being stored. This also removes any experimental calibration errors. Thus, in the synthetic data generation, a power spectrum $\sigma^{[i]} = W\varphi^{[i]}$ is first generated using the fine discretization of velocity space, then noise added, and the spectrum normalized.

5.6.3 Lasso regularization

Letting the regularization term in Eq. (5.9) be the one-norm instead of the Euclidean norm, we obtain the so-called 'Lasso' regularization[54],

$$f^* = \underset{f}{\operatorname{argmin}} \frac{1}{2} \|Wf - s\|_2^2 + \frac{1}{2}\lambda \|f\|_1 . \tag{5.19}$$

Note that Eq. (5.19) is a MAP estimate with a Laplace prior on f, so the model for finding probabilities of ICE emission in velocity space derived in Section 5.3 holds. If the regularization

[54] Tibshirani (1996).

parameter λ is sufficiently large, some of the entries in f are driven to zero. Thus, the Lasso regularization promotes sparsity in the solution. This is especially desirable when reconstructing ICE-generating distributions localized to a single pixel. This regularization method sometimes avoids the jitter in the Tikhonov-regularized solutions, as shown below. Lasso-regularized solutions are determined using the implementation of Lasso in MATLAB.

5.7 Reconstructions of the locations of the ions generating the ICE in velocity space

To generate the arrays for one ring beam least-square subset searches, a single non-zero pixel with a value of 1 was placed at each grid point in velocity space. The corresponding signal was then generated by computing $W\varphi^{[i]} = \sigma^{[i]}$ and the normalized $\varphi^{[i]}$ and $\sigma^{[i]}$ stored in D_φ and D_σ.

We want to determine how well the least-square subset search, Tikhonov regularization, and Lasso regularization can reconstruct a given one ring beam distribution for a synthetic ICE signal with 10% noise. The reconstructions found by the three different techniques are compared to the ground truth source location of ICE emission. Further, they are multiplied with W to obtain the signal for the reconstructed solution to locate deviations from the noise-free signal corresponding to the ground truth distribution.

We begin by considering a velocity distribution consisting of a single pixel in velocity space; see the first row in Fig. 5.6 for an example of a ground truth and the corresponding ICE signal. Ten percent noise is added to the ICE signal. The three techniques are then used to determine the locations of the ions generating the ICE in velocity space.

From the ICE signal with added noise, the least-square subset search is able to perfectly reconstruct the ground truth; see the second row in Fig. 5.6. The small differences in the database solution compared to the ground truth occur due to the different grid sizes used to generate the signals in the database compared to the grid used to generate the ground truth signal to avoid performing inverse crime.

The optimal reconstruction from 0th-order Tikhonov regularization is also close to the ground truth distribution. A few non-zero pixels with low intensities adjacent to the correct location in velocity space which should not be a part of the velocity distribution occur. However, the correct location of the ground truth distribution is found and clearly indicated in the figure by the high-intensity pixel; see the third row of Fig. 5.6. The occurrence of a number of pixels with low intensities, which we call 'jitter', occurs for all ICE Tikhonov reconstructions to a smaller or larger degree. The amount of jitter depends on the complexity of the ground truth distribution as demonstrated below. However, as is clear from Fig. 5.6, the signal corresponding to the reconstruction found using Tikhonov regularization is almost identical to the ground truth.

The optimal reconstruction using Lasso regularization is quite similar to the Tikhonov or the least-square subset reconstructions: for a sufficiently large value of λ, only the true location in the velocity distribution remains. However, it is clear that the Lasso solution is more sparse than the Tikhonov solution.

5.7.1 Noise investigation

Two investigations were performed to identify the impact of different noise levels in the signal on the accuracy of the reconstructions: for a ring distribution of size $0.5 \times 0.2\ v_\mathrm{A}$, (i) 0th-order Tikhonov regularization and Lasso regularization were performed for the corresponding ICE signal with 1-10% noise added, and (ii) reconstructions with all three methods for 0-100% noise added; see Figs. 5.7 and 5.8.

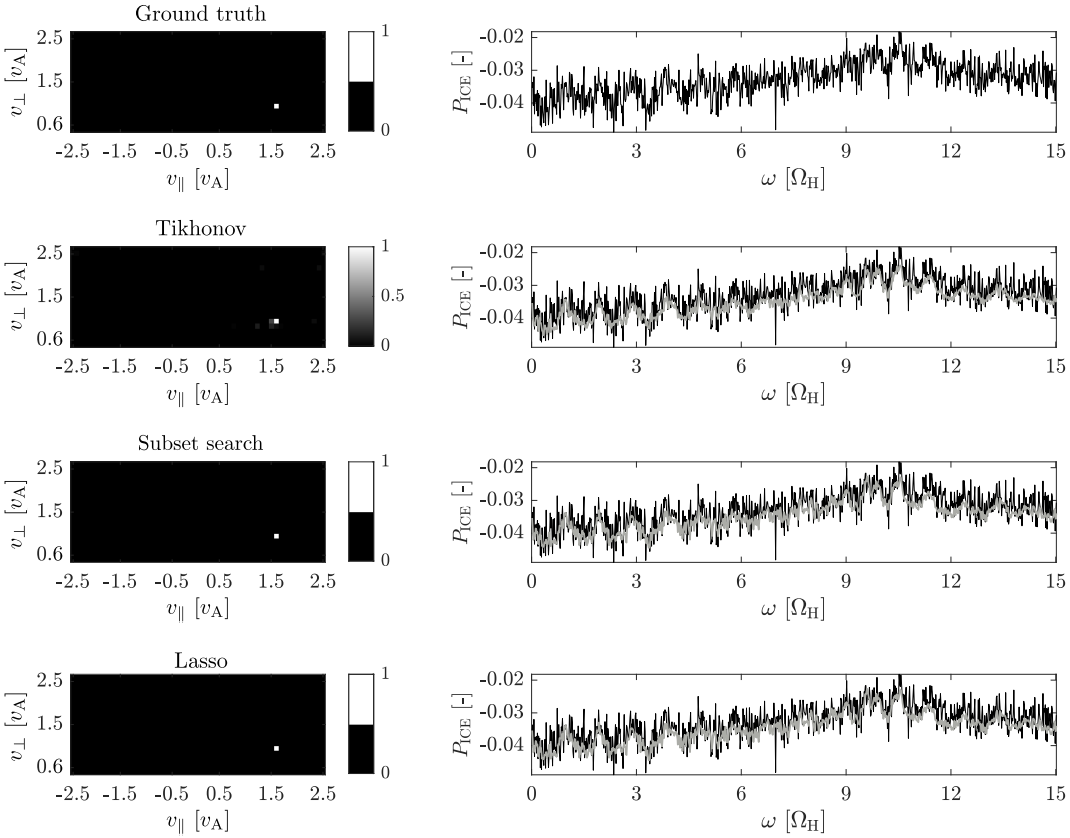

Figure 5.6: The velocity-space distribution of ICE-generating ions shown to the left in the first row was used to generate the ICE signal to its right. The same signal with 10% noise was then used to compute the reconstructions using the least-square subset search (second row), 0th-order Tikhonov regularization (third row), and Lasso regularization (fourth row). The signals for the three different techniques are plotted in the second column as a grey signal on top of the black ground truth signal.

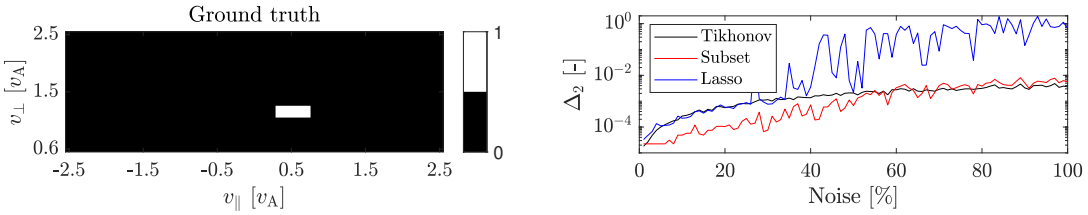

Figure 5.7: The least-square subset search is superior to Tikhonov and Lasso regularization for up to around 60% noise and is able to find the exact locations of the ions generating the ICE for at least up to 10% noise in the ICE signal. The reconstructions found using 0th-order Tikhonov regularization and Lasso regularization are almost identical up to 30% noise as indicated by the almost identical value of Δ_2 for 0-30% noise. Lasso regularization remains the worst technique for all other noise levels.

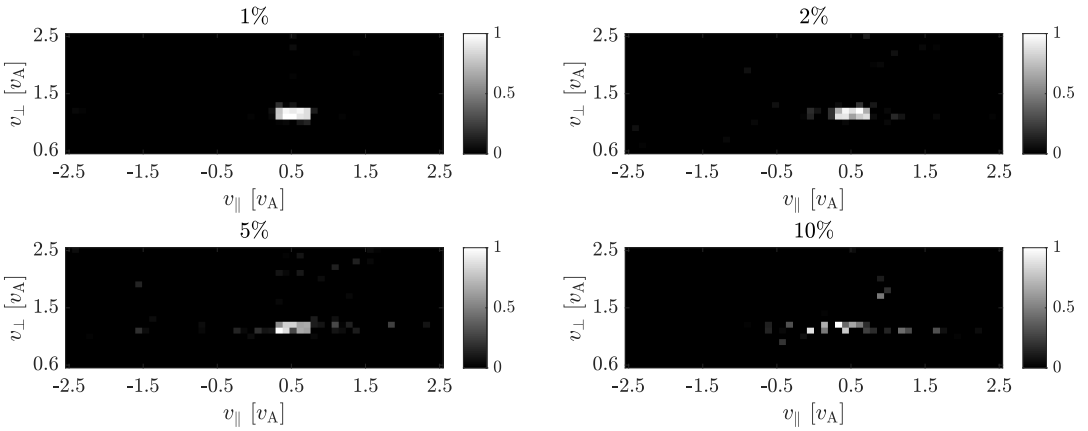

Figure 5.8: The reconstructions from the ground truth ICE emission location shown in Fig. 5.7 using 0th-order Tikhonov regularization as a function of the noise percentage in the signal (1-10%). Lasso regularization produces almost identical reconstructions and are therefore not illustrated.

Fig. 5.7 shows the investigated ground truth signal and the Δ_2 value for Tikhonov regularization, the subset search, and Lasso regularization as a function of the noise percentage. The subset D_φ consists in this case of every one ring distribution in velocity space with size 0.5×0.2 v_A. The subset search is the preferred reconstruction method up to around 60% noise, where it then remains on par with Tikhonov regularization. The correct central locations are found by the subset search for at least up to 10% noise. The best reconstructions found using Tikhonov and Lasso regularization for 1-5% noise compare to the reconstruction found using the subset search with around 30% noise.

As shown in Fig. 5.8, close to perfect reconstructions with a small amount of jitter are found for the lowest levels of noise, whereas more jitter occurs for 10% noise, indicating a larger uncertainty of the extent of the velocity distribution. Note that only Tikhonov solutions are shown, as the Lasso solutions are almost identical; see also the Δ_2 values for both methods in Fig. 5.7. The jitter is mostly spread in $v_\parallel$, which is in line with the interpretation from the SVD; see Fig. 5.5. The central location of the distribution in velocity space is clear for all noise levels in the range of 1-10% indicated by the highest intensity pixels.

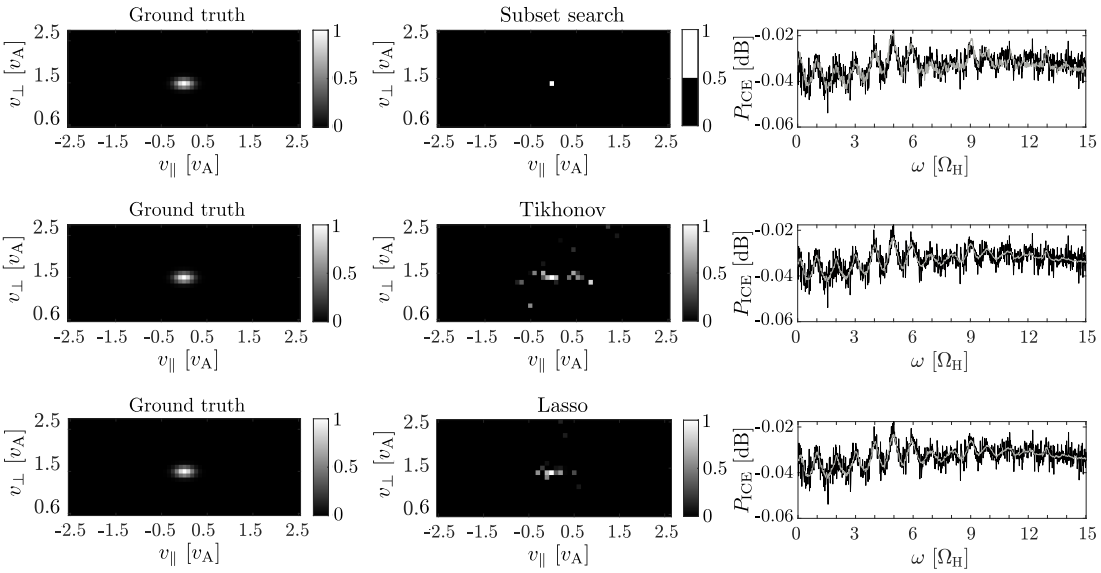

Figure 5.9: The subset least-square search (top row), 0th-order Tikhonov regularization (middle row), and Lasso regularization (bottom row) solutions for a Gaussian distribution. The ground truths are shown on the left, the reconstructions in the middle, and the signals for the reconstructions on the right. The subset search finds the correct central location of the Gaussian blob. Tikhonov and Lasso regularization also finds the correct location of the distribution with some jitter.

5.7.2 Reconstructions of Gaussian distributions in $v_\parallel$ and $v_\perp$

A natural follow-up to the above investigations is how well distributions with shapes other than rectangular and no longer binary but with values in the interval $[0, 1]$ can be reconstructed by the subset search, Tikhonov regularization, and Lasso regularization. Here, we consider distributions with Gaussian blobs specified by a central location $(\mu_{v_\parallel}, \mu_{v_\perp})$ in velocity space and the standard deviations $\sigma_{v_\parallel}$ and $\sigma_{v_\perp}$. Further, the quality of the reconstructions from each method for Gaussian distributions indicates the quality of reconstructions of other shapes.

The Gaussian blob shown in Fig. 5.9 has standard deviations of $\sigma_{v_\parallel} = 0.2\, v_A$ and $\sigma_{v_\perp} = 0.1\, v_A$. A 1-pixel subset search can identify the central location of a single Gaussian distribution; see the top row in Fig. 5.9. The subset search can identify the correct central location for such a distribution anywhere in velocity space. Also, the distribution can be of any size, and the subset search correctly finds the location in velocity space. A solution found using Tikhonov regularization produces results similar to those shown above for rectangular signals; see the middle row of Fig. 5.9. In the Tikhonov solution, the highest intensity pixels are located at the central locations of the Gaussian blob with jitter mostly within the original distribution. The dominant error in the solution is in the $v_\parallel$ direction as predicted from the SVD; see Fig. 5.5. The same conclusions hold for the solution found using Lasso regularization. In conclusion, all three techniques successfully identify the location of the ions generating the ICE in all velocity space for a single Gaussian blob of any size.

We conclude that the solutions from the subset search, Tikhonov regularization, and Lasso regularization behave similarly, independent of the shape of the velocity-space distributions of the ions generating the ICE: the subset search finds the pixel at the central locations of the distributions, and similarly for Tikhonov regularization and Lasso regularization but with small

amounts of erroneously placed jitter.

5.8 Discussion and conclusion

Prior work has computed and validated the weight functions needed to reconstruct the 2D fast-ion velocity distribution function for measurements from diagnostics such as CTS, FIDA, GRS, NES, and FILDs. However, the recently developed weight functions and reconstructions for ICE were limited to 1D in $v_\perp$, assuming $v_\parallel = 0$.

In this study, we computed the 2D weight functions for edge ICE caused by the MCI for conditions at LHD using a non-linear 1D3V PIC-hybrid code. We compute power spectra for a specific value of $v_\parallel$ in the range -2.6 to 2.6 v_A and $v_\perp$ in the range 0.6 to 2.6 v_A. The weight functions are obtained by stacking the power spectra appropriately to obtain ascending values of $v_\perp$ and $v_\parallel$ in the first and second dimensions and the angular frequency ω in the third dimension. The result is a 3D array with 2D weight functions for every frequency.

The weight functions exhibit a particular pattern for frequencies close to the cyclotron harmonics. For frequencies below the harmonics, the highest signal sensitivities occur for positive $v_\parallel$. Conversely, for frequencies above the harmonics, the highest signal intensities occur for negative $v_\parallel$. At the frequency of the harmonic, ions with $v_\parallel = 0$ have the highest sensitivity. This effect is due to the Doppler shift. Also, the sensitivities occur in horizontal bands in $v_\perp$ so only some specific values of $v_\perp$ contribute to the measured signal. Tikhonov and Lasso-regularized reconstructions have good resolution in $v_\perp$ for this reason.

Reconstructions can be performed for synthetic velocity distributions for the ions generating the ICE using a least-square subset search, 0th-order Tikhonov regularization, and Lasso regularization for noise realizations at least up to 10%. The least-square subset search is able to correctly identify the central locations of the distributions independent of the level of noise added, but the drawback is the requirement of large storage space if the subset is to consist of anything but single-pixel functions generating the ICE.

Tikhonov and Lasso reconstructions are accurate for localized distributions in velocity space. With increasing size of the distributions, the reconstructions are corrupted by erroneous jitter occurring at incorrect locations in velocity space. Still, Tikhonov and Lasso reconstructions have high resolution in $v_\perp$ and contain high-intensity pixels in the signal locations of the distributions in velocity space.

We performed our simulations for edge ICE at LHD. Thus, extending the results to other machines requires new simulations to obtain the 2D weight functions. Therefore, future work should investigate whether it is possible to reproduce the results of this study for synthetic ICE signals at other machines. However, this study indicates the feasibility of the ICE diagnostic for use at both current and future machines to diagnose fast-ion behaviour. Thus, our results support the proposal to include the ICE diagnostic at ITER, where it could contribute to integrated data analysis for alpha particle distribution functions.[55]

[55] Salewski, Nocente, Madsen, et al. (2018).

Chapter 6

Reconstruction methods for velocity-space tomography of fast-ion loss detectors

This section presents the paper "Reconstruction methods for velocity-space tomography of fast-ion loss detectors", submitted to the journal *Plasma Physics and Controlled Fusion*.

6.0 Abstract

This paper proposes a new way to characterize different fast-ion loss detectors (FILDs) in terms of a gross weight function and a gross strike map for the pinhole-scintillator relation computed from the FILDSIM-modeled weight function matrix. We show that the gross weight function and gross strike map indicate the largest sensitivities to ions with pitch around 30-45° at 6-8 cm gyroradius for the FILD detector FILD1 at ASDEX Upgrade. Furthermore, we introduce three algebraic iterative reconstruction techniques to obtain reconstructions of velocity distributions in the pinhole of the FILD detector close to the plasma edge. We show that they perform as well as Tikhonov regularization and highlight characteristics that make them preferable to Tikhonov regularization. We also show that the current FILD model for FILD1 at ASDEX Upgrade computes low resolution pinhole reconstructions for ion velocity-space distribution functions with values of the gyroradius above 6 cm.

6.1 Introduction

Ions with superthermal energies are an essential ingredient of fusion plasmas as they heat the plasma. They are generated by neutral beam injection (NBI), electromagnetic wave heating in the ion cyclotron range of frequencies (ICRF), and alpha particles from DT-reactions. Such ions are called 'fast ions' and typically have energies spanning from few tens of keVs to several MeVs. The alpha particles from DT-reactions will be the source of energy to keep a self-sustaining burning plasma. However, uncontrolled fast ions may present a risk if lost to the walls: the efficiency of plasma heating is reduced and plasma-facing components damaged.[1] Such radial transport

[1] Duong et al. (1993) and Fasoli et al. (2007).

can occur due to fast-ion interactions with magnetohydrodynamic (MHD) activity.[2] In present devices, the radial transport of fast ions is intensely studied.[3]

Thus, it is essential to understand the mechanisms resulting in fast-ion losses to reduce their negative impact on the performance of fusion devices. A clear picture of the velocity space of the lost fast ions is helpful to gain this understanding since their orbits may be obtained by backward modelling to identify what caused them to be lost. Local information of the velocity space of lost fast ions can be obtained from measurements at the plasma edge using fast-ion loss detectors (FILDs).[4] FILDs work as magnetic spectrometers by dispersing the lost fast ions onto a plate with the impact locations depending on the pitch angle and gyroradius of the ion. Faraday-cup measure the current induced by fast ions impinging on a conductive plate, and scintillator FILDs measure the light emitted from a scintillating material on a plate.[5]

FILDs are installed at several machines, including ASDEX Upgrade[6], DIII-D[7], JET[8], NSTX[9], MAST-U[10], EAST[11], KSTAR[12], LHD[13], and TCV[14]. FILDs for ITER[15] and JT-60SA[16] are being designed. FILD data is supposed to represent the velocity-space distribution of the ions passing through the pinhole of the FILD. This is obtained by measuring the pitch angles α and gyroradii ρ of the ions passing through the pinhole of the FILD, which can be translated to, e.g., $v_\parallel$ and $v_\perp$, from the relations

$$\alpha = \cos\frac{v_\parallel}{v}, \quad \text{and} \tag{6.1}$$

$$\rho = \frac{mv_\perp}{ZeB}, \tag{6.2}$$

where $v = \sqrt{v_\parallel^2 + v_\perp^2}$. However, ion trajectories with specific values of pitch and gyroradius have a distribution of strike-points on the FILD scintillator plate since ions passing through the pinhole may occupy different positions in the pinhole and have different gyrophases. Thus, the measured velocity distribution is a blurred version of the actual velocity distribution of the ions passing through the pinhole.

An approximate pinhole velocity distribution can be obtained by performing velocity-space tomography on a measured scintillator velocity distribution. Zeroth-order Tikhonov regularization has been used previously with good results.[17]. Here, we use *algebraic iterative reconstruction techniques* (ART) to compute the fast-ion velocity-space distribution function in the pinhole and compare them to the distributions obtained using zeroth-order Tikhonov regularization. ARTs may provide equal or better results for faster computation times compared to zeroth-order Tikhonov regularization. Furthermore, our invesgitations show that using ARTs to compute the tomographic reconstructions removes the need to determine an optimal regularization parameter due to the robustness of the solutions around the point of semi-convergence.

[2] Garcia-Munoz et al. (2010) and Heidbrink and White (2020).
[3] Garcia-Munoz et al. (2013).
[4] Zweben (1989) and Garcia-Munoz et al. (2009).
[5] Jansen Van Vuuren et al. (2022).
[6] Garcia-Munoz et al. (2009), Gonzalez-Martin et al. (2018), and Gonzalez-Martin et al. (2019).
[7] Fisher et al. (2010).
[8] Baeumel et al. (2004).
[9] Darrow (2008)
[10] Rivero-Rodriguez et al. (2018) and Rivero-Rodriguez et al. (2019).
[11] Chang et al. (2016).
[12] Kim et al. (2012).
[13] Nishiura et al. (2004).
[14] Poley-Sanjuan et al. (2023).
[15] Garcia-Munoz et al. (2016).
[16] Ayllon-Guerola et al., 2021.
[17] Galdon-Quiroga, Garcia-Munoz, Sanchis-Sanchez, et al. (2018) and Galdon-Quiroga, Garcia-Munoz, Salewski, et al. (2018).

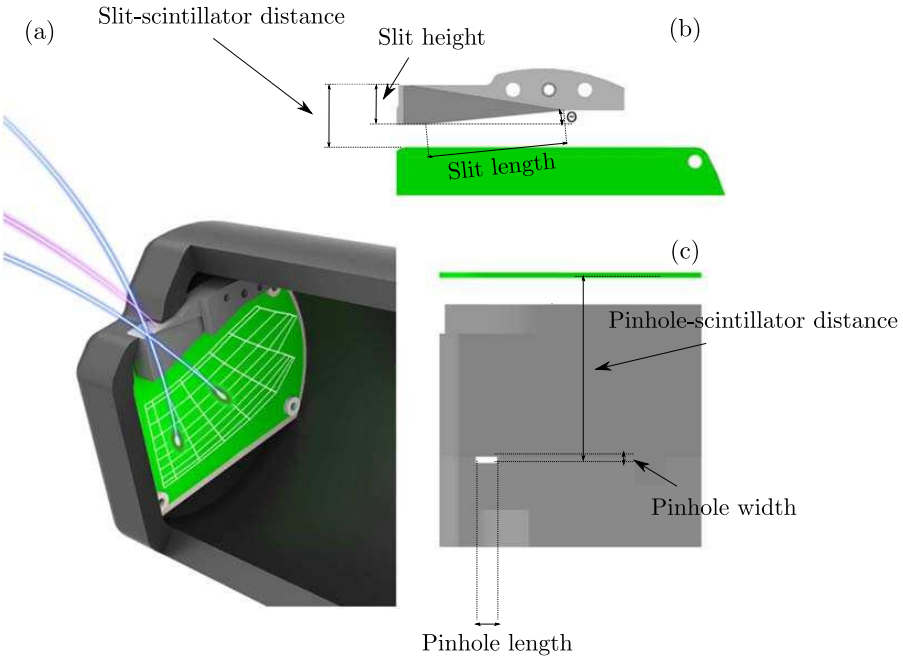

Figure 6.1: Illustration of a scintillator FILD: (a) FILD probe head (dark gray) and scintillator (green). The red fast-ion orbit is blocked by the collimator and the blues are not. The white strike map is overlaid on the scintillator. (b) and (c) show detailed views of the collimator. From Galdon-Quiroga, Garcia-Munoz, Sanchis-Sanchez, et al. (2018).

This paper has the following aims: (i) to derive and explain a novel way to characterize FILDs from a FILDSIM-modeled weight function matrix, (ii) to introduce the algebraic iterative reconstruction techniques, and (iii) to prove their usefulness for performing FILD velocity-space tomography. Section 2 defines the model for the relation between the velocity distribution at the pinhole and the measured velocity distribution on the scintillator. Section 3 derives a gross strike map and gross weight function characterizing the pinhole-scintillator relation in any FILD. Section 4 introduces three algebraic iterative reconstruction techniques with mathematical formulas for each iteration. Section 5 investigates tomographic reconstructions on synthethic data relevant for ASDEX Upgrade using the ARTs. Section 6 concludes and presents an outlook.

6.2 Forward model: the pinhole-scintillator relation

In a scintillator FILD, ions pass through a pinhole with a collimator in a probe placed near the plasma, in the far scrape-off layer, to impact on a scintillator plate. This setup measures the velocity space of the lost fast ions through an estimate of their gyroradii and pitch angles. See Fig. 6.1 for a schematic of a scintillator FILD.

Traditionally, FILD measurements are given in gyroradius ρ and pitch angle α. Pinhole velocity space will be distinguished from scintillator velocity space by adding a subscript p. The FILD signal $s(\alpha_1, \alpha_2, \rho_1, \rho_2)$ in the pitch angle range $[\alpha_1, \alpha_2]$ and gyroradius range $[\rho_1, \rho_2]$ is the number of photons measured at a given location on the scintillator plate. The velocity-space distribution function of the ions passing through the pinhole is $f(\alpha_p, \rho_p)$ for a given pitch angle α_p and gyroradius ρ_p with units [ions $^{\circ -1}$ cm^{-1}]. The relation between the measured signal and

the velocity distribution of the pinhole ions is then[18]

$$s(\alpha_1, \alpha_2, \rho_1, \rho_2) = \int_0^\infty \int_0^\pi w(\alpha_1, \alpha_2, \rho_1, \rho_2, \alpha_p, \rho_p) f(\alpha_p, \rho_p)\, \mathrm{d}\alpha_p\, \mathrm{d}\rho_p, \tag{6.3}$$

where $w(\alpha_1, \alpha_2, \rho_1, \rho_2, \alpha_p, \rho_p)$ is the weight function for the signal in the specified velocity-space ranges on the scintillator given some location (α_p, ρ_p) in pinhole velocity space. The units of w are [photons per ion]. The weight function w for a given range of scintillator velocity-space coordinates $(\alpha_1, \alpha_2, \rho_1, \rho_2)$ indicates the velocity-space coordinates of the ions able to produce a signal at this location in scintillator velocity space. The weight function can be written as the product of a probability function $\Pr(\alpha_1, \alpha_2, \rho_1, \rho_2 \mid \alpha_p, \rho_p)$ of an ion located at (α_p, ρ_p) producing a signal in the interval $(\alpha_1, \alpha_2, \rho_1, \rho_2)$ and the yield of the scintillator $\epsilon(\rho_p)$ for an ion with gyroradius ρ_p. Similar decomposition has been performed for FIDA,[19] NES,[20] and GRS[21]. Thus,

$$w(\alpha_1, \alpha_2, \rho_1, \rho_2, \alpha_p, \rho_p) = \Pr(\alpha_1, \alpha_2, \rho_1, \rho_2 \mid \alpha_p, \rho_p)\, \epsilon(\rho_p). \tag{6.4}$$

The probability function is obtained by modeling a large number of orbit trajectories initiated in the pinhole with random position and gyrophase for a predetermined range in pitch angle and gyroradius using the FILDSIM code[22]. For each initial pitch angle, i.e., the value of the pitch angle of the ions initialized in the pinhole, the gyroradius strike-point distributions can be modelled as skew Gaussians with mean ρ_0 and standard deviation σ_0. The skew Gaussian is a Gaussian multiplied by an error function with a factor β_ρ controlling the skewness. For each initial gyroradius, the pitch-angle strike-point distributions can be modelled as Gaussians with mean α_0 and standard deviation σ_α. Thus, the probability function becomes

$$\begin{aligned}\Pr(\alpha_1, \alpha_2, \rho_1, \rho_2 \mid \alpha_p, \rho_p) = &\frac{f_{\mathrm{col}}}{2\pi\sigma_\alpha\sigma_\rho} \exp\left(-\frac{(\alpha_0 - \alpha)^2}{2\sigma_\alpha^2} - \frac{(\rho_0 - \rho)^2}{2\sigma_\rho^2}\right) \\ &\times \left(1 + \operatorname{erf}\left(\beta_\rho \frac{\rho_0 - \rho}{\sqrt{2}\sigma_\rho}\right)\right)\end{aligned} \tag{6.5}$$

for $\alpha_0 \in [\alpha_1, \alpha_2]$ and $\rho_0 \in [\rho_1, \rho_2]$, where $f_{\mathrm{col}} = N/N_p$ is the number of markers reaching the scintillator N divided by the number of markers initialized at the pinhole N_p for fixed values of pitch angle and gyroradius in pinhole velocity space. The dependence of α_p and ρ_p is through the estimates of $\alpha_0, \rho_0, \sigma_\alpha$, and σ_ρ.

Measurements in an accelerator facility were performed to obtained the yield as a function of energy for protons, deuterium, and α-particles[23]. The relation between the photon yield per unit length $\mathrm{d}Y/\mathrm{d}x$ and the stopping power of the incident particles $\mathrm{d}E/\mathrm{d}x$ follows Birks's model[24]

$$\frac{\mathrm{d}Y}{\mathrm{d}x} = \frac{S\,\frac{\mathrm{d}E}{\mathrm{d}x}}{1 + k\,\frac{\mathrm{d}E}{\mathrm{d}x}}, \tag{6.6}$$

where S and k are constants related to the scintillator efficiency and the degree of quenching.

FILDSIM computes values of $\alpha_0, \rho_0, \sigma_\alpha, \sigma_\rho$, and f_{col} for all (α_p, ρ_p). The probability function can then be computed for all scintillator velocity-space ranges $(\alpha_1, \alpha_2, \rho_1, \rho_2)$ using Eq. (6.5).

[18] W. W. Heidbrink et al. (2007) and Salewski, Geiger, Moseev, et al. (2014).
[19] Salewski, Geiger, Moseev, et al. (2014).
[20] Jacobsen et al. (2015).
[21] Salewski, Nocente, Gorini, et al. (2015) and Salewski, Nocente, Gorini, et al. (2016).
[22] Galdon-Quiroga et al. (2019).
[23] Galdon-Quiroga, Garcia-Munoz, Sanchis-Sanchez, et al. (2018).
[24] Galdon-Quiroga, Garcia-Munoz, Sanchis-Sanchez, et al. (2018).

Combining the probability functions with the yield function for all velocity-space ranges gives the weight functions at all locations in velocity space. The chosen velocity-space ranges are determined by the scintillator velocity-space discretization used. Scintillator velocity space is discretized with resolution $\Delta\alpha$ and $\Delta\rho$, and pinhole velocity space is discretized with resolution $\Delta\alpha_p$ and $\Delta\rho_p$. The discretization of Eq. (6.3) yields

$$s = Wf, \tag{6.7}$$

where $s \in \mathbb{R}^m$, $f \in \mathbb{R}^n$, and $W \in \mathbb{R}^{m\times n}$. The values of m and n depend on the discretizations chosen for the pinhole and scintillator velocity spaces.

Equation (6.7) describes the inverse problem we wish to solve: given a measured signal s and the weight function matrix W, determine f. However, since the condition number $\kappa(W) = \sigma_1/\sigma_n \gg 10^{15}$, the problem is very ill-posed. Thus, noise e in the signal $s = s^{\text{exact}} + e$ may result in large errors in the solution f as shown by the bound[25]

$$\frac{\|f - f^{\text{true}}\|_2}{\|f\|_2} \leq \kappa(W)\frac{\|e\|}{\|s\|}. \tag{6.8}$$

An approximate solution for f can be found by using, e.g., Tikhonov regularization or ARTs.

6.3 Characterization of FILDs

6.3.1 Gross strike map

Consider ions at a specific location in pinhole velocity space, so $f = \delta(\alpha_p, \rho_p)$ for some α_p and ρ_p. Due to differences in gyroangle and the location of the ions in the pinhole, such ions may impact the scintillator at different locations resulting in a spread of locations in velocity space. We call this a 'strike map'; see Fig. 6.2(a) for an example. The black cross in the figure indicates the pinhole velocity-space location of the ions being considered, and the colored areas indicate the possible strike locations on the scintillator. A strike map is obtained by letting f be a delta function corresponding to a single column of the weight function matrix, so $f = \delta(\alpha_p, \rho_p)$. To see where, on average, ions will strike the scintillator, strike maps for all pinhole velocity-space locations can be summed, which is equivalent to letting $f = 1$. Thus, the gross strike map is

$$W_{\text{strike}}(\alpha_1, \alpha_2, \rho_1, \rho_2) = \int_0^\infty \int_0^\pi w(\alpha_1, \alpha_2, \rho_1, \rho_2 \mid \alpha_p, \rho_p)\, \mathrm{d}\alpha_p\, \mathrm{d}\rho_p. \tag{6.9}$$

An illustration of the gross strike map is given in Fig. 6.2(b).

6.3.2 Gross weight function

The pinhole velocity distribution is blurred when measured on the scintillator since ions with a given pitch angle and gyroradius in pinhole velocity space impact on the scintillator as given by the strike map. Knowing the strike maps of all positions in the pinhole, we can determine which positions in the pinhole can reach a given position on the scintillator. This is reflected in a weight function. The weight function for the location $(57°, 5.3\,\text{cm})$ is illustrated in Fig. 6.3(a). Ions at non-zero locations can impact the scintillator at the black cross. As the units of a weight functions are [photon per ion], the weight function indicates the sensitivity of a specific pixel measurement on the scintillator.

In the equation $s = Wf$, each row of W is a weight function containing information about the sensitivity of a measurement point with coordinates (α_s, ρ_s) on the scintillator plate. For

[25] Hansen (2010).

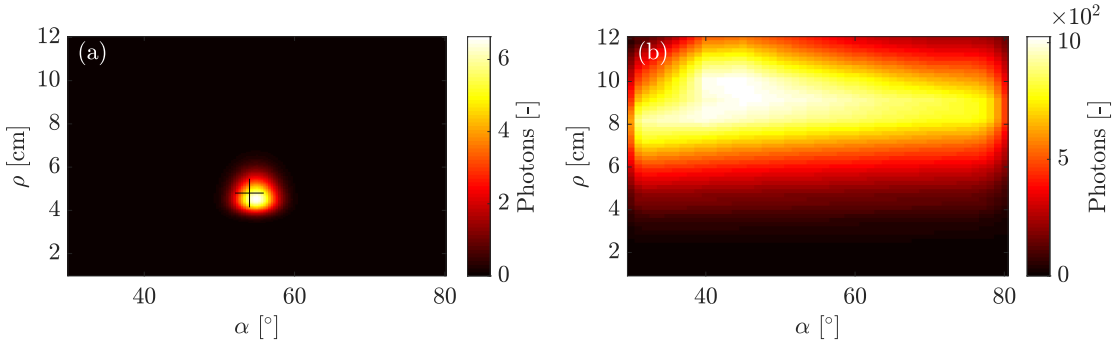

Figure 6.2: (a) Strike map for the location $(57°, 5.3\,\text{cm})$. (b) Gross strike map for FILD1 at ASDEX Upgrade.

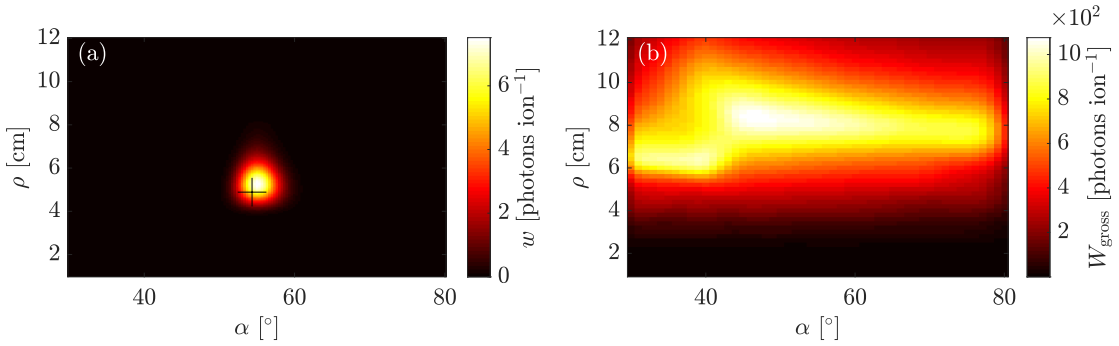

Figure 6.3: (a) The weight function for the location $(57°, 5.3\,\text{cm})$ in scintillator velocity space indicating all locations in pinhole velocity-space that can impinge the scintillator at the black cross in scintillator velocity space. (b) The gross weight function for FILD1 at ASDEX Upgrade.

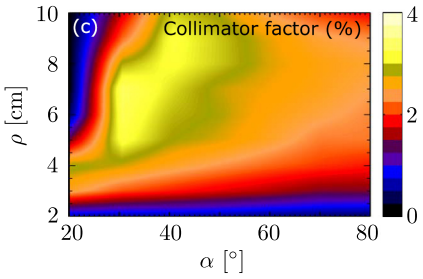

Figure 6.4: The collimator factor map for FILD1 at ASDEX Upgrade. The pitch angle and gyroradius coordinates are in pinhole velocity space. From Galdon-Quiroga, Garcia-Munoz, Sanchis-Sanchez, et al. (2018).

example, the first row of W corresponds to the bottom left corner of the scintillator. The weight function for this location indicates which parts of pinhole velocity space can produce a signal at this location, and how much signal each position in the pinhole velocity space produces on that measurement position on the scintillator plate. The same interpretation can be made for each row of W. This sensitivity is unique to a specific FILD. Taking the sum of all weight functions produces the 'gross weight function' matrix. See Fig. 6.3(b) for the gross weight function for FILD1 at ASDEX Upgrade for the weight functions computed for discharge #38017. It indicates the total amount of photons generated per ions per location in pinhole velocity space. The largest amount of photons are generated from ions with gyroradii of 6-8 cm for all pitch angles, and there are regions where no photons are generated.

The gross weight function matrix is related to the 2D collimator factor map, which provides a map of the ratio $N(\alpha_p, \rho_p)/N_p(\alpha_p, \rho_p)$ for the entire pinhole velocity space, where N is the number of ions impacting the scintillator and N_p the number of ions initialized in the pinhole. See Fig. 6.4 for the collimator factor map for FILD1 at ASDEX Upgrade. The areas with largest collimator factor occur for pitch angles of 30-50° and gyroradii of 5-8 cm. Combining the information from the collimator factor map and the gross weight function matrix may be used to construct FILDs with high sensitivities in specific velocity-space regions.

The high-sensitivity areas in pinhole and scintillator velocity space for W_{gross} and W_{strike} are similar. This is a result of the individual weight functions and strike maps being similar as illustrated in Figs. 6.3(a) and 6.2(a). However, the two matrices provide different information, since the gross weight function indicates the total sensitivity of a point in pinhole velocity space for all measurement locations on the scintillator, and the gross strike map indicates the scintillator measurement for a uniform distribution.

6.4 Tikhonov regularization and algebraic iterative reconstruction techniques

The inverse problem $s = Wf$ is severely ill-posed due to the large condition number. One approach to mitigate this problem is Tikhonov regularization where the inverse problem is the minimization problem[26]

$$f^* = \underset{f}{\operatorname{argmin}} \|Wf - s\|_2^2 + \lambda^2 \|Lf\|_2^2 . \tag{6.10}$$

[26]Salewski, Geiger, Jacobsen, et al. (2016) and Galdon-Quiroga, Garcia-Munoz, Salewski, et al. (2018).

The matrix $L \in \mathbb{R}^{p\times n}$ for $p \in \mathbb{N}$ can be any matrix such that different aspects of the solution are regularized, e.g., smoothness by choosing L to be a gradient operator. The value of the regularization parameter λ controls the weighting between the data fidelity term and the regularization term.

Prior information can also be implemented to find a better solution. Examples include non-negativity of the distribution function, penalty matrices, null-measurement regions, specification of NBI locations, and numerical simulations[27]. Here, we only use non-negativity.

Algebraic iterative reconstruction techniques are used in computed tomography to reconstruct an image from measurement data. ARTs are particularly suited for solving systems such as $Wf = s$, where W is a sparse matrix. The weight function matrix W is sparse for FILDs, indicating that the techniques may be suitable. Given W and s, different ARTs compute the iterative solutions in different ways. Here, we focus on one *row-action method*, one *column-action method*, and one *simultaneous iterative reconstruction technique*. First, we introduce some notation. Denote all rows of W by $r_i = (r_{ij})$ and all columns by $c_j = (c_{ij})$ so

$$W = \begin{pmatrix} \text{—} & r_1 & \text{—} \\ \text{—} & r_2 & \text{—} \\ & \vdots & \\ \text{—} & r_m & \text{—} \end{pmatrix} = \begin{pmatrix} | & | & & | \\ c_1 & c_2 & \cdots & c_n \\ | & | & & | \end{pmatrix}. \tag{6.11}$$

Further, let $W = (w_{ij})$, $f = (f_j)$, and $s = (s_i)$, so

$$Wf = \begin{pmatrix} w_{11}f_1 + w_{12}f_2 + \cdots + w_{1n}f_n \\ w_{21}f_1 + w_{22}f_2 + \cdots + w_{2n}f_n \\ \vdots \\ w_{m1}f_1 + w_{m2}f_2 + \cdots + w_{mn}f_n \end{pmatrix} = \begin{pmatrix} s_1 \\ s_2 \\ \vdots \\ s_m \end{pmatrix}. \tag{6.12}$$

The solution to the system of equations can be interpreted as the intersection of all hyperplanes contained in Eq. (6.12).

All of the iterative methods exhibit *semi-convergence* for noisy measurements S. Thus, the reconstruction error initially decreases for some iterations $k \leq k_0$ but increases for $k > k_0$. The solutions for $k < k_0$ are overly smooth distributions, and the $k > k_0$ solutions are overly noisy distributions due to overfitting the data. The iteration number can therefore be thought of as a regularization parameter. Thus, it is important to implement a stopping criterion that best estimates k_0. However, in the case of FILD data, this is not a problem as shown below.

6.4.1 A row-action method

As an example of a row-action method, we consider *Kaczmarz's method*. In Kaczmarz's method, every iteration vector $f^{(k)}$ for the kth iteration satisfies one of the m equations in Eq. (6.12), i.e., $r_i f^{(k)} = s_i$, where $k \equiv i \pmod m$. If Δf is the next step in the iterations such that equation i is satisfied, then $s_i - r_i(f^{(k)} + \Delta f) = 0$, so

$$\Delta f = r_i^\dagger \left(s_i - r_i f^{(k)}\right) = \frac{s_i - r_i f^{(k)}}{\|r_i\|_2^2}\, r_i^T. \tag{6.13}$$

We consider only cyclic control, i.e., the rows are selected in a cyclic manner, e.g., $i = 1, 2, \ldots, m, 1, 2, \ldots$ Furthermore, a non-negativity constraint to the solution is applied by projecting each iteration

[27] Salewski, Geiger, Jacobsen, et al. (2016), Madsen et al. (2018), Madsen, Salewski, et al. (2020), and Madsen, Huang, et al. (2020).

onto $\mathcal{C} = \mathbb{R}^n_+$. One iteration corresponds to cycling through all rows once. Letting $\omega^{(k)}$ be the relaxation parameter satisfying $0 < \omega^{(k)} \leq 1$, the iterations are

$$f^{(k)} = \mathcal{P}_{\mathcal{C}} \left(f^{(k)} + \omega^{(k)} \frac{s_i - r_i f^{(k)}}{\|r_i\|_2^2} r_i^T \right) \tag{6.14}$$

for $k \equiv i \pmod{m}$.

Each iteration in Kaczmarz's method divides by the row norm $\|r_i\|_2^2$. Some rows have either zero or very small but nonzero norm which may result in noise amplification. To avoid this problem, a small damping parameter $t^{(k)}$ is added to the denominator such that the division in each iterative step is $\|r_i\|_2^2 + t^{(k)}$. This damping parameter is dependent on the iteration step k, but we choose $t^{(k)} = 0.1$ for all k for simplicity.[28]

Algorithm 1 Kaczmarz's method

Initialization: $f^{(0)} \in \mathbb{R}^n$ is arbitrary
for $k = 0, 1, 2, \ldots$ **do**
$k \equiv i \pmod{m}$
$f^{(k)} = \mathcal{P}_{\mathcal{C}} \left(f^{(k)} + \omega^{(k)} \frac{s_i - r_i f^{(k)}}{\|r_i\|_2^2 + t^{(k)}} r_i^T \right)$
end for

6.4.2 The column-action method

The column-action method operates on the columns c_j and not the rows. The column-action method used here performs each iteration step cyclically in the direction of the unit vectors e_j. The unit vector e_j has a 1 at the jth location and 0s elsewhere. The function to minimize is $g(f) = \|Wf - s\|_2^2$. At each iteration, we update $f^{(k+1)} = f^{(k)} + \alpha_k e_j$ with $j \equiv k \pmod{n}$. The step length α_k should be chosen to give the maximum reduction in $g(f)$. Thus,

$$\alpha_k = \underset{\alpha}{\operatorname{argmin}} \left\| W \left(f^{(k)} + \alpha e_j \right) - s \right\|_2^2 \tag{6.15}$$

$$= \underset{\alpha}{\operatorname{argmin}} \left\| \alpha (W e_j) - (s - W f^{(k)}) \right\|_2^2 \tag{6.16}$$

$$= \underset{\alpha}{\operatorname{argmin}} \left\| \alpha c_j - (s - W f^{(k)}) \right\|_2^2, \tag{6.17}$$

where c_j is the jth column of W. The minimizer is

$$\alpha_k = \frac{c_j^T (s - W f^{(k)})}{\|c_j\|^2}. \tag{6.18}$$

Thus, with projection onto $\mathbb{R}^n_+$ and relaxation parameter ω_k, the iterations are

$$f^{(k+1)} = \mathcal{P}_{\mathcal{C}} \left(f^{(k)} + \omega^{(k)} \frac{c_j^T (s - W f^{(k)})}{\|c_j\|^2} e_j \right). \tag{6.19}$$

In each iteration, the updating term divides by the norm of column j, so care must be taken here as for Kaczmarz's method. The same approach by adding a damping parameter $t^{(k)} = 0.1$ was used.

[28] This approach is validated in Andersen and Hansen (2014).

Algorithm 2 A column-action method

Initialization: $f^0 \in \mathbb{R}^n$ is arbitrary
for $k = 0, 1, 2, \ldots$ **do**
$j \equiv k \pmod{n}$
$f^{(k+1)} = \mathcal{P}_{\mathcal{C}} \left(f^{(k)} + \omega^{(k)} \frac{c_j^T (s - W f^{(k)})}{\|c_j\|_2^2 + t^{(k)}} e_j \right)$.
end for

Note a significant difference between Kaczmarz's method and the column-action method: Kaczmarz's method updates the solution vector each iteration such that one of the m equations in $s = Wf$ is satisfied and subsequently dividing by a measure of the total photons per ion at the corresponding location in scintillator velocity space. Conversely, the column-action method updates the solution vector each iteration such that the maximum reduction in the equation $\|s - Wf\|_2^2$ is obtained for the unit vectors e_j and subsequently dividing by the total photons per ion for an ion at a given location in pinhole velocity space. Thus, Kaczmarz's method finds the optimal solution considering the total photons per ion at locations in scintillator velocity space, and the column-action method finds the optimal solution considering the total photons per ion generated per ion at locations in pinhole velocity space.

6.4.3 A simultaneous iterative reconstruction technique

Convex optimization involves minimizing convex functions over convex sets. As before, let $g(f) = \|s - Wf\|_2^2$. Then $\nabla g(f) = -2W^T(s - Wf)$. Then $g(f)$ is a convex function since the Hessian $Hg(f) = 2W^TW$ is positive semi-definite on $\mathbb{R}^n$. Hence, $\operatorname{argmin}_f g(f)$ is an unconstrained convex optimization problem that can be solved by the method of steepest descent by performing the iterations

$$f^{(k+1)} = f^{(k)} - \omega^{(k)} \nabla g(f) = f^{(k)} + \omega^{(k)} W^T (s - W f^{(k)}). \tag{6.20}$$

This method called the *Landweber iteration*[29] is a specific case of a larger part of ARTs called simultaneous iterative reconstruction techniques (SIRT) since the iterations operate on the rows and the columns simultaneously. General SIRT methods have a diagonal matrix $D \in \mathbb{R}^{n \times n}$ and a weighting matrix $M \in \mathbb{R}^{m \times m}$ with iterative steps

$$f^{(k+1)} = f^{(k)} + \omega^{(k)} D W^T M (s - W f^k). \tag{6.21}$$

For simplicity, we choose $D = I^{n \times n}$. To obtain faster convergence, we use a SIRT with

$$M = \operatorname{diag} \left(\frac{1}{m \|r_i\|_2^2} \right) \tag{6.22}$$

instead of Landweber iterations. This method is called *Cimmino's method*. It can be shown that the Landweber solution approaches the Tikhonov solution for increasing k.[30] Since we are interested in ART solutions different from the Tikhonov solution, we choose Cimmino's method instead.
We project onto $\mathcal{C} = \mathbb{R}_+^n$, so the iterations for Cimmino's method are

$$f^{(k+1)} = \mathcal{P}_{\mathcal{C}} \left(f^{(k)} + \omega^{(k)} W^T M (s - W f^{(k)}) \right). \tag{6.23}$$

[29] Hansen (2010).
[30] Hansen (2010).

Algorithm 3 Cimmino's method

Initialization: $f^0 \in \mathbb{R}^n$ is arbitrary
for $k = 0, 1, 2, \ldots$ **do**
$f^{(k+1)} = \mathcal{P}_{\mathcal{C}} \left(f^{(k)} + \omega_k W^T M (s - W f^{(k)}) \right)$.
end for

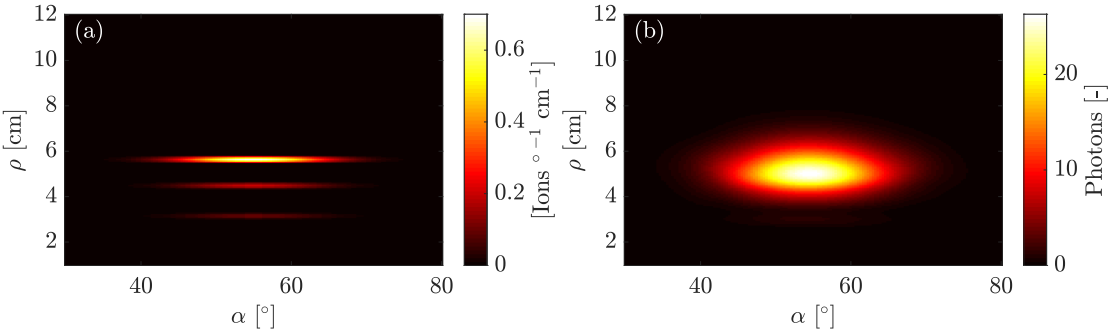

Figure 6.5: (a) Synthetic pinhole distribution consisting of three monoenergetic distributions centralized around a pitch angle of 55°. (b) Corresponding synthetic scintillator measurement.

6.5 Tomographic reconstructions on synthetic data

The three ARTs are tested on a synthetic measurement identical to that used in Galdon-Quiroga, Garcia-Munoz, Sanchis-Sanchez, et al. (2018). This is done since the measurement represents expected FILD measurements at ASDEX Upgrade and to make it possible to compare the results obtained using the ARTs with the results obtained using Tikhonov regularization given in Galdon-Quiroga, Garcia-Munoz, Sanchis-Sanchez, et al. (2018). The synthetic measurement represents expected first-orbit NBI losses for the full, half, and one-third energy components. The synthetic pinhole distribution has three monoenergetic distributions, at $\rho = 3.1, 4.3$, and 5.4 cm, with a Gaussian distribution in pitch angle with $\sigma_\alpha = 7°$. The intensity of each monoenergetic distribution is weighed with the corresponding NBI power fraction, which can be set to approximately 70/20/10% at ASDEX Upgrade[31]. See Fig. 6.5 for an illustration of the pinhole distribution and the corresponding scintillator signal.

In studies reconstructing known functions based on synthetic signals, it is crucial to use different numerical grids for calculating the synthetic signal and the inversion. If not, this produces an artificially good solution due to *inverse crime*. Using a different discretization of velocity space for the reconstruction prevents 'perfect' reconstructions, i.e., an error-free reconstruction of the original pinhole distribution. For the computations shown here, the discretization of velocity space used to compute the synthetic signal s from $Wf = s$ is 51×56, and the discretization used to reconstruct the pinhole distributions f from s is 50×55. The effect of change of discretization is significant and corresponds to adding an average of 15% noise in the signal. Reconstructions of the signal using all three techniques with inverse crime are illustrated in Fig. 6.6. The visible errors disappear for $k \to \infty$.

[31] Hopf (2013).

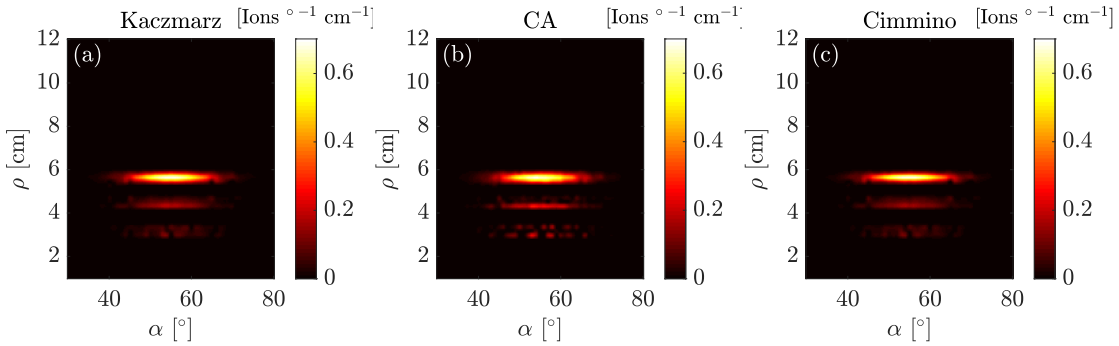

Figure 6.6: Reconstructions using (a) Kaczmarz's method, (b) the column-action method, and (c) Cimmino's method for $k = 10^5$ iterations and committing inverse crime. Note that the reconstructions approach the ground truth for $k \to \infty$, i.e., the small visible errors are removed for larger k.

6.5.1 Number of iterations

The first question to answer is how many iterations should be performed for each technique. The answer is: it depends on the complexity of the signal, the locations of the signals in velocity space, the grid resolution, and the noise level. Thus, it is not possible to give a general answer. However, different stopping criteria have been developed to determine the optimal $\tilde{k}$ such that the reconstruction $f^{(k)}$ achieves semi-convergence at iteration $\tilde{k}$, i.e., the iteration stops such that $f^{(\tilde{k})}$ is as close to the ground truth f^{true} as possible. However, for the synthetic FILD measurements considered here, the reconstructed pinhole distribution $f^{(k)}$ does not change much from one iteration to the next around the semi-convergence point, as illustrated by the flat error histories $\left\| f^{\text{true}} - f^{(k)} \right\|_2$ in Fig. 6.7. Thus, implementing a stopping criterion is not likely to make a difference, and computing the optimal reconstruction becomes a matter of choosing a sufficiently large iteration number.

The next question becomes how well the pinhole distribution can be reconstructed for a noisy signal without committing inverse crime. Thus, we add 10% Gaussian noise to the scintillator signal and use a different grid size for the weight function matrix to perform the reconstructions. First, we investigate the reconstructions depending on the complexity of the synthetic measurement, i.e., how many different monoenergetic distributions are measured on the scintillator. Including just the $\rho = 5.4$ distribution is called 'One peak,' both $\rho = 4.3$ cm and $\rho = 5.4$ cm 'Two peaks,' and all three $\rho = 3.1$ cm, $\rho = 4.3$ cm, and $\rho = 5.4$ cm 'Three peaks.' The error histories are shown in Fig. 6.7. Observe that for one, two, and three peaks, only small improvements occur after $k \approx 1000$ for all methods. This is because the signal is dominated by the full-energy beam component at $\rho = 5.3$ cm. The column-action method achieves convergence the fastest at $k = 1000$ iterations. The corresponding reconstructions for the one, two, and three peaks are shown in Fig. 6.8. The reconstructions have the correct values of the pitch angle and gyroradius and also the relative intensities for all monoenergetic distributions. Some artefacts cause the signals at $\rho = 3.1$ and 4.3 cm to be partitioned in the pitch direction, but reconstructions have the correct width in pitch angle.

6.5.2 Velocity-space sensitivity

Noise prevents perfect reconstructions of the ground truth pinhole velocity-space distribution functions. The question is how this affects the sensitivity of the reconstructions when different

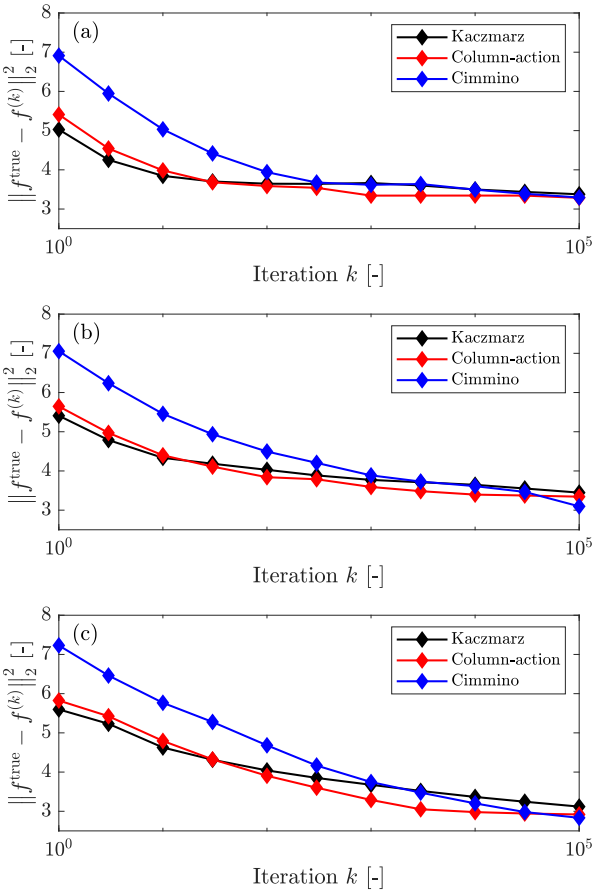

Figure 6.7: The error histories $\left\|f^{\text{true}} - f^{(k)}\right\|_2$ for Kaczmarz's method, the column-action method, and Cimmino's method for (a) one, (b) two, and (c) three monoenergetic distributions in pinhole velocity space populated by fast ions. Observe that semi-convergence seems to occur around $k = 10^5$ iterations with no risk of divergence for iterations $k > 10^5$. The fastest convergence occurs for the column-action method around $k = 1000$ iterations.

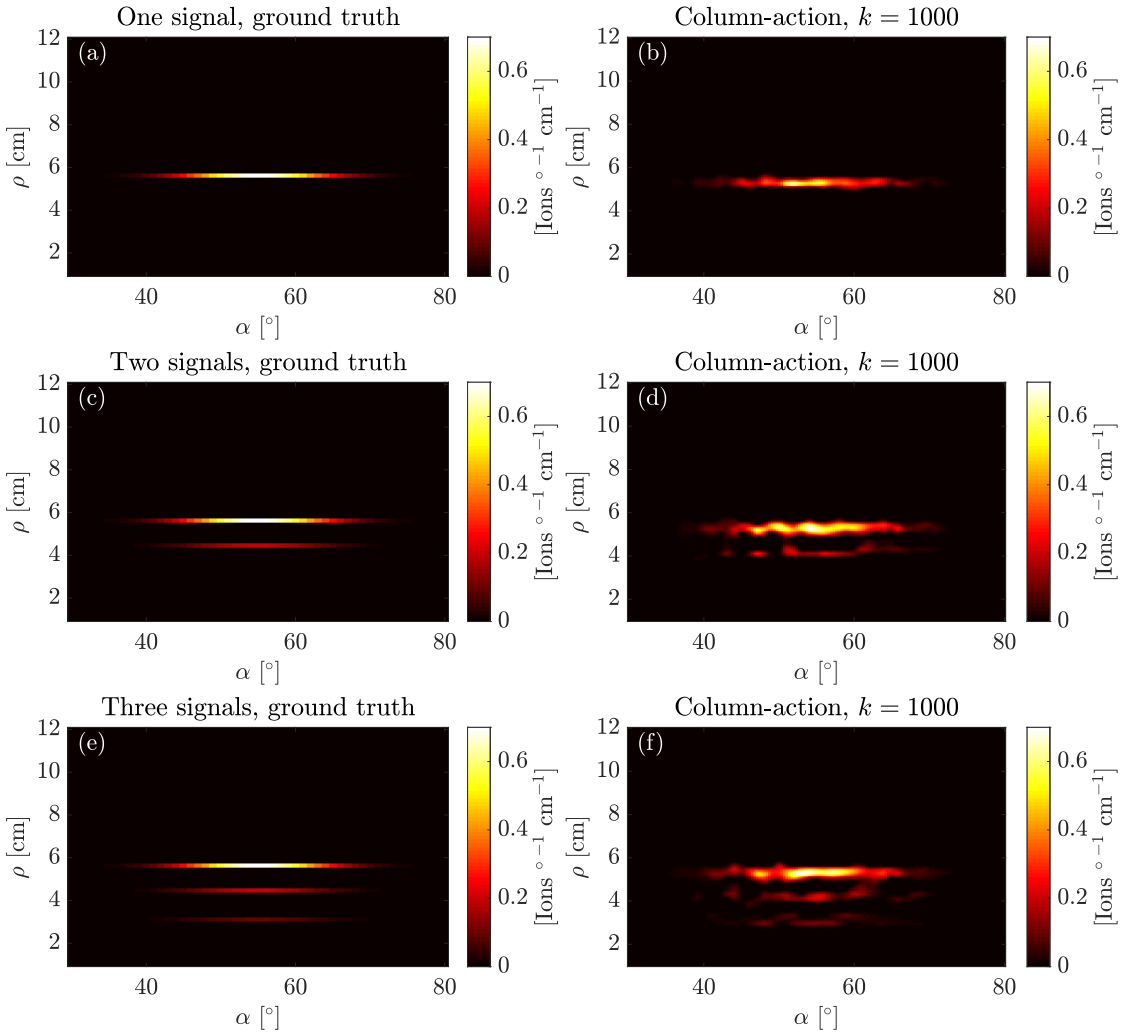

Figure 6.8: Reconstructions of 1-3 signals using the column-action method for $k = 1000$ iterations. The ground truths are shown in subfigures (a), (c), and (e), and the reconstructions in subfigures (b), (d), and (f). Observe that the signal in the reconstruction has the correct location in both pitch and gyroradius, the correct spread in pitch angle, and the correct relative intensities between all signals.

distributions are separated by just a few degrees in pitch angle and a few millimeters in gyroradius. We investigate the same monoenergetic distributions as above without the third energy component at $\rho = 3.1$ cm, so only the two distributions at $\rho = 4.3$ and 5.4 cm are included. Their intensities are both normalized to one.

The results are illustrated in Fig. 6.9. To achieve separation of the signals in the reconstruction, a greater number of iterations are now required, exacerbating the artefacts. The artefacts are small 'blobs' in the reconstructed distributions in pitch angle instead of a continuous signal. This effect is caused by the noise; without noise in the signal, the reconstructions do not contain any blobs; see Fig. 6.6. The spread in gyroradius of the blobs is caused by the overlap of the skew-Gaussian distributions in gyroradius in the model of the forward problem.

To investigate the gyroradius and pitch angle resolution of the current model, we computed reconstructions of two distributions with different distances in gyroradius and pitch angle between their central locations. For the gyroradius resolution, the distributions were assumed to be monoenergetic. For the pitch angle resolution, the assumption of monoenergetic distributions was dropped and distributions with a spread in gyroradius considered. The results are shown in Figs. 6.9 and 6.10. The lowest possible resolution at a gyroradius of $\rho \approx 5$ cm is $\delta\rho = 0.8$ cm. For the same gyroradius value, the pitch angle sensitivity is $\delta\alpha = 4°$.

6.5.3 Resolution dependent on location in velocity space

The ability to distinguish between two peaks in the pinhole distribution separated by just a few millimeters or degrees depends on the locations of the signals in velocity space. The sensitivity in velocity space is, in turn, dependent on the FILD geometry, as characterized by its gross weight function as shown in Fig. 6.3(b).

The gross weight function shows that the sensitivity depends on both the pitch angle and the gyroradius. Where the sensitivity is *high* in the gross weight function, the gyroradius resolution is *low*. This is because near high-sensitivity regions, ions can impact this location from many different locations in pinhole velocity space. Thus, it is difficult to determine where in pinhole velocity space a given scintillator measurement came from at high-sensitivity locatioins. Thus, the reconstructions with the *worst* gyroradius resolution occur for distributions at $\rho \approx 8$ cm at $\alpha = 40 - 60°$. The best gyroradius resolution occurs for $\rho < 3$ cm for all α.

This effect occurs since ions with smaller gyroradii can impact locations on the scintillator corresponding to higher gyroradii. This effect is slightly increased by the skew-Gaussian model in FILDSIM modelling the weight functions, where the upper tails overestimate the strike point locations; see Fig. 6.11(a).

The reconstruction resolution in pitch angle is better for the smallest possible pitch angles. This effect cannot be seen directly from the gross weight function matrix since it is dominated by the skewness effect in the gyroradius direction. However, in the forward model, the width of the fitted Gaussian distributions to the FILDSIM data increases in width with increasing pitch angle independent of the gyroradius; see Fig. 6.11(b). Reconstructions of distributions at 70° have a resolution of approximately 5°, whereas distributions at 35° have a resolution below 2°; see Fig. 6.12 for an illustration of such reconstructions. The error histories associated with these reconstructions are shown in Fig. 6.13. Note that reconstructions of signals with good resolution also achieve semi-convergence much faster.

It follows, therefore, that when constructing FILDs, it is necessary to consider the locations of the signals in velocity space that will be measured if detailed pinhole velocity-space distribution functions are desired. To obtain detailed tomographic reconstructions, FILDs optimized for different parts of velocity space could be constructed.

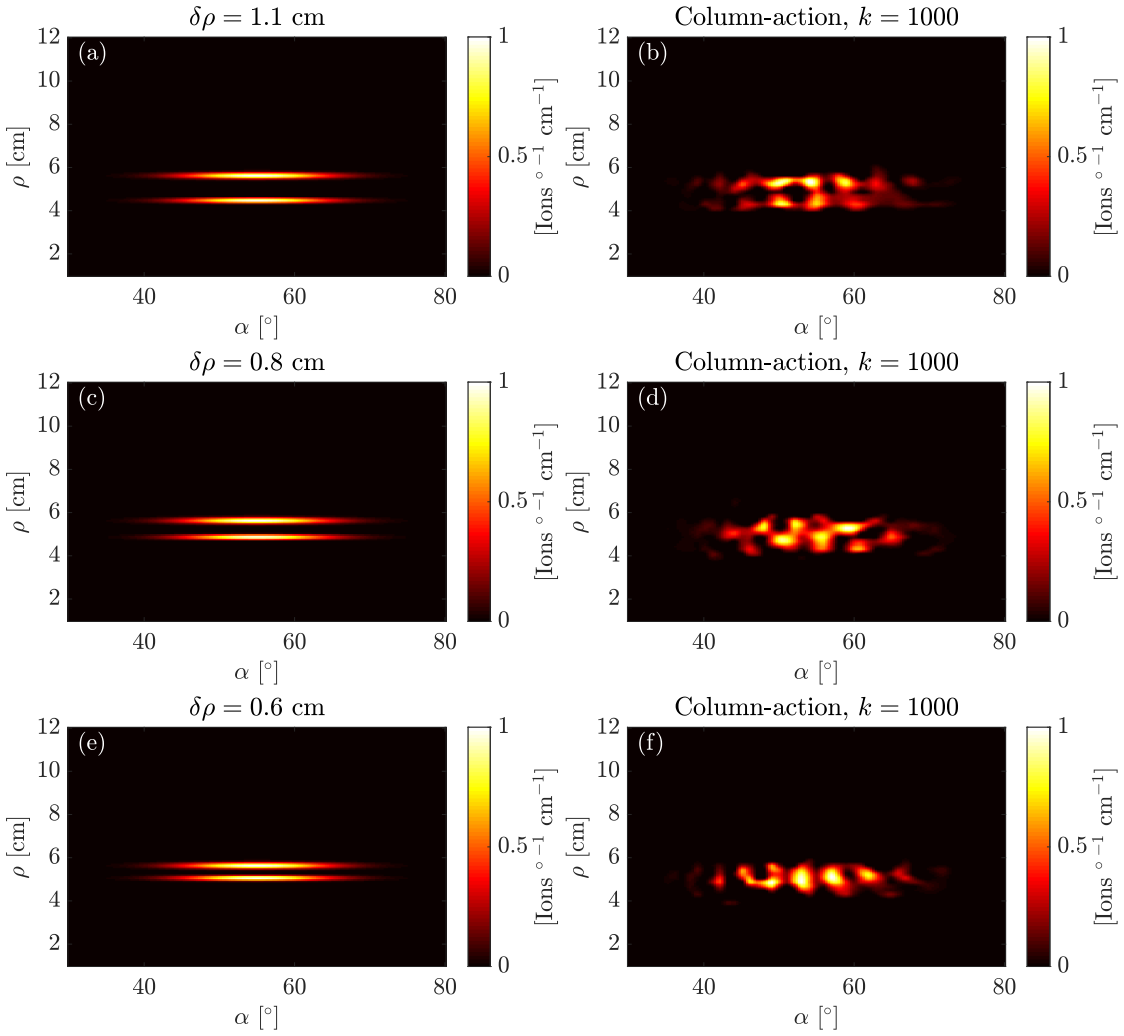

Figure 6.9: Reconstructions of two separate ion locations with decreasing distance in gyroradius between their central locations. The ground truths are shown in subfigures (a), (c), and (e), and the reconstructions are shown in subfigures (b), (d), and (f).

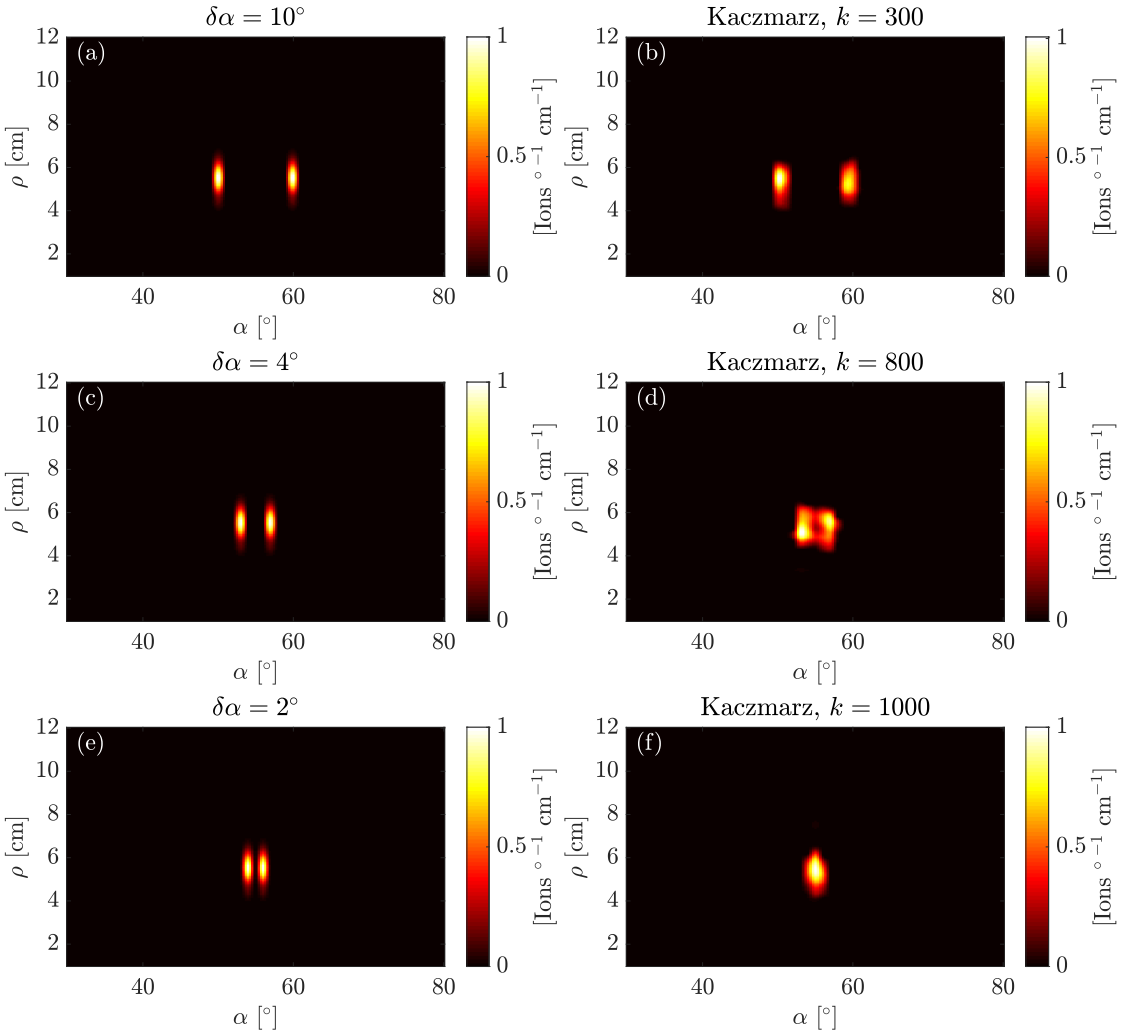

Figure 6.10: Reconstructions of two separate ion locations with decreasing pitch angle between their central locations. The ground truths are shown in subfigures (a), (c), and (e), and the reconstructions are shown in subfigures (b), (d), and (f).

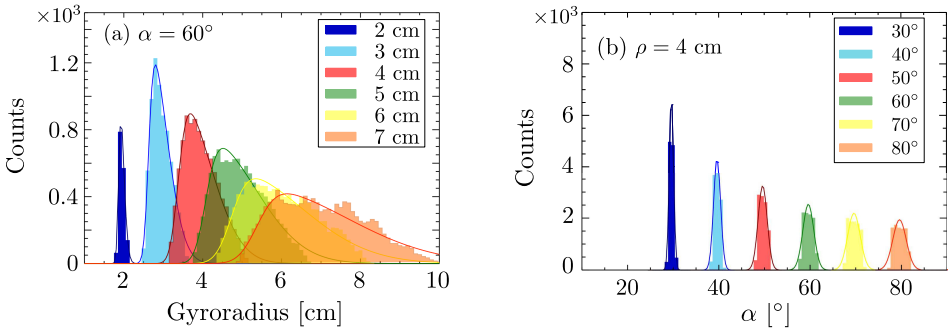

Figure 6.11: (a) Impact locations in gyroradius for ions initialized with gyroradii $\rho = 2, 3, 4, 5, 6,$ and 7 cm and $\alpha = 60°$ in the FILD pinhole. The fits of the skew-Gaussian models are indicated. (b) Impact locations in pitch angle for ions initialized with pitch angles $\alpha = 30°, 40°, 50°, 60°, 70°,$ and 80° in the FILD pinhole. The fits of the Gaussian models are indicated. From Galdon-Quiroga, Garcia-Munoz, Salewski, et al. (2018), p. 3.

6.6 Conclusion and outlook

The pinhole-scintillator relation for a specific FILD can be modeled as $Wf = s$ for a weight function matrix W, pinhole velocity distribution f, and scintillator velocity distribution s. The weight function matrix W characterizes the FILD. From W, it is possible to compute a gross strike map indicating the highest probabilities of impinging ions for a uniform distribution in scintillator velocity space and a gross weight function indicating the how many ions at a given position in pinhole velocity space impinge somewhere on the detector. The highest sensitivities for FILD1 at ASDEX Upgrade occur for pitch angles $30 - 45°$ and gyroradii of $6 - 8$ cm.

The algebraic iterative reconstruction techniques Kaczmarz's method, the column-action method, and Cimmino's method can find high quality reconstructions of pinhole velocity distributions for FILD1 at ASDEX Upgrade. Since the only requirements to perform the reconstructions are weight functions output from FILDSIM computations, the techniques can be used to perform reconstructions of pinhole velocity distributions for all FILDs. In fact, the techniques can be applied to any problem of the form $s = Wf$ and may, therefore, also be suitable to obtain reconstructions for other fast-ion diagnostics that can be modeled in this manner. The techniques provide different solutions than Tikhonov regularization, which is the primary technique that has been used to obtain reconstructions in the fast-ion community.

Tikhonov regularization and ARTs can compute perfect reconstructions when committing inverse crime. However, artefacts occur due to noise in the signal for both techniques in the form of localized blobs instead of a single continuous signal.

The flat error histories for reconstructions of velocity distributions relevant for prompt NBI losses at ASDEX Upgrade indicate that increasing the number of iterations improves the reconstructions. However, other signals may not have the same behavior; error histories depend on the signal complexity and the signal locations in velocity space. Thus, if other synthetic measurements lead to semi-convergence after which the reconstructions may be worsened by additional iterations needs to be investigated. In this case, implementing optimal stopping criteria should be considered.

Furthermore, the step size $\omega^{(k)}$ for each iteration k has been set to 1 for simplicity in these investigations. This value of $\omega^{(k)}$ seemed to be sufficient for our investigations. However, the exact value of $\omega^{(k)}$ may be important for optimal convergence. Future work should consider optimal

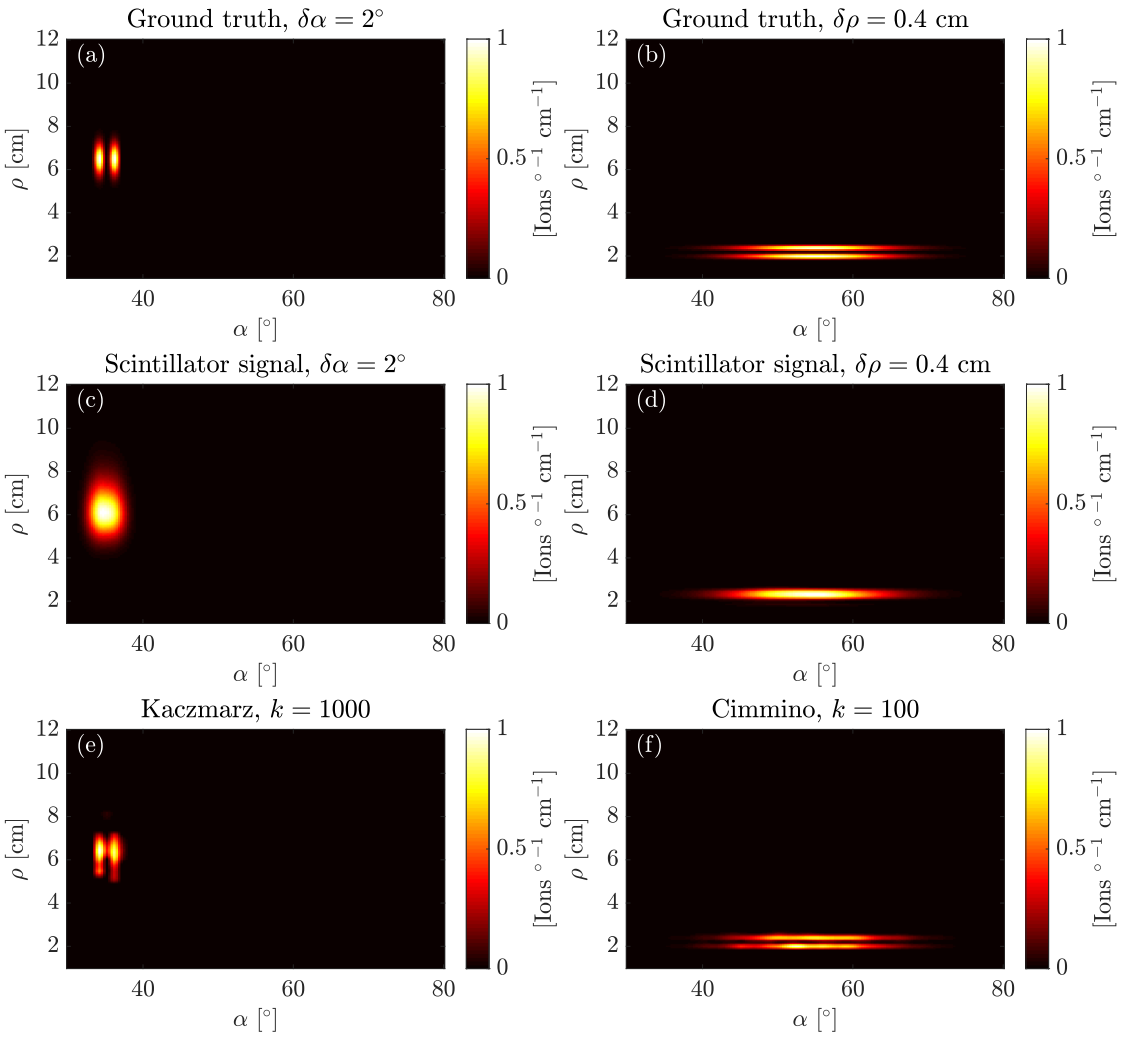

Figure 6.12: Subfigures (a), (c), and (e) show the ground truth, scintillator measurement, and tomographic reconstruction for a location in velocity space for FILD1 at ASDEX Upgrade with resolution below 2° in pitch angle. Subfigures (b), (d), and (f) show the ground truth, scintillator measurement, and tomographic reconstruction for a location in velocity space for FILD1 at ASDEX Upgrade with resolution below 0.4 cm in gyroradius.

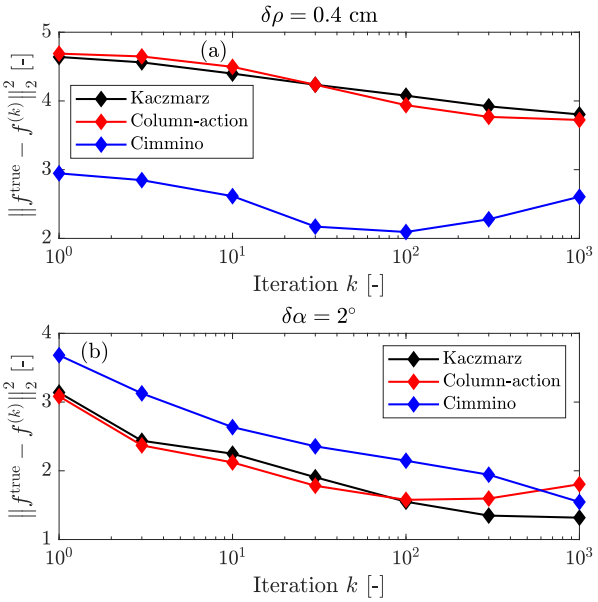

Figure 6.13: The error histories showing the semi-convergence of Kaczmarz's method, the column-action method, and Cimmino's method for locations in velocity space where the reconstructions have the resolution below (a) $\delta\rho = 0.4$ cm and (b) $\delta\alpha = 2°$. The reconstructions are almost identical to the ground truth.

choices of $\omega^{(k)}$ for each iteration k.

Finally, the three ARTs studied here are just a small subset of the current existing number of ARTs. Other techniques can be studied to investigate their applicability to obtain reconstructions.

Chapter 7

Neural networks for reconstructions

This chapter presents the paper "Tomographic reconstructions of fast-ion loss detector measurements using deep neural networks", to be submitted.

7.0 Abstract

This paper applies a deep learning approach to solve ill-posed inverse problems in nuclear fusion science, particularly inverse problems for data analysis of fast-ion loss detector (FILD) measurements in tokamaks. First, we develop a deep neural network to determine the numerical value of the regularization parameter required for performing zeroth-order Tikhonov regularization. We show that the regularization parameter values provided by a trained deep neural network produce high-quality tomographic reconstructions on both synthetic and experimental FILD measurements. Second, a different deep neural network is trained to directly compute tomographic reconstructions of the lost fast-ion velocity-space distribution function from FILD measurements, eliminating the need for regularization. The tomographic reconstructions produced by the deep neural network are superior to those obtained using zeroth-order Tikhonov regularization.

7.1 Introduction

Deep learning and neural networks have shown potential in addressing complex problems. The ability of deep neural networks (DNNs) to model nonlinear relationships, manage high-dimensional data, and generalize from training sets has proven beneficial.

When analysing physical systems, it is sometimes necessary to solve inverse problems. These inverse problems are typically ill-posed, meaning noise in the measurements prevents a stable solution. One typical approach to mitigate this issue is to regularize the problem by applying Tikhonov regularization. The choice of an appropriate value of the regularization parameter is then crucial, as it directly affects the balance between fitting the data and imposing constraints on the solution, ultimately influencing the accuracy and reliability of the recovered solution.

In nuclear fusion science, measurements of lost fast ions play an important role in understanding their general behaviour and their role in sustainable energy production. The analysis of such data requires robust and accurate computational techniques to interpret the underlying physics.

In this paper, we present a DNN-based approach for determining the optimal regularization

parameter value when using Tikhonov regularization, and we demonstrate its effectiveness in improving the tomographic reconstructions of fast-ion loss detector (FILD) measurements. Further, we investigate applying trained DNNs to perform tomographic reconstructions of synthetic and experimental data from FILD measurements. Our objective is to develop a data-driven approach that can accurately process the FILD measurements to retrieve information about the lost fast-ion velocity distribution function in fusion plasmas. This information is essential for understanding and optimizing the performance of fusion devices.

We begin by providing an overview of the inverse problem for FILD measurement data analysis and discuss the challenges associated with traditional tomographic reconstruction techniques. Subsequently, we introduce the proposed DNN-based method for determining the optimal regularization parameter and for computing tomographic reconstructions directly, detailing its architecture, training process, and evaluation metrics. We also present a comparison of the DNN-based method with Tikhonov regularization, the current standard used in velocity-space tomography in nuclear fusion science, demonstrating the improvements that can be achieved using our approach.

The effectiveness of the trained DNN is demonstrated by applying it to experimental data from FILD2 at ASDEX Upgrade. The results showcase the ability of the neural network to accurately recover the lost fast-ion velocity-space distribution function from FILD measurements, outperforming current implementations using Tikhonov regularization.

Section 2 describes fast-ion loss detectors and the physical model resulting in having to solve an inverse problem. Section 3 explains Tikhonov regularization and its application to velocity-space tomography. Section 4 details the evaluation metrics for the trained neural networks, the details of the training dataset generation, and determines the optimal network architectures for a feedforward neural network and a convolutional neural network to predict the regularization parameter for zeroth-order Tikhonov regularization. Section 5 applies the best of the two trained neural networks to predict the regularization parameters for experimental data from ASDEX Upgrade. Section 6 investigates using a trained deep neural network to compute tomographic reconstructions on the same experimental data from Section 5 and compares the two approaches. Section 7 provides a discussion and conclusion.

7.2 Fast-ion loss detectors

Superthermal ions play an important role in key aspects of magnetically confined fusion plasmas. The ions are termed ‘fast ions’ and are characterized by having energies larger than the bulk plasma, typically on the order of tens of keVs to MeVs. Their confinement is crucial for the optimal operation of fusion devices since fast-ion losses may lead to irreversible damage to the plasma-facing components.

One way to investigate the mechanisms leading to fast-ion losses is using FILDs. Several types of FILDs exist. This study considers scintillator FILDs, but the results are independent of the exact type. Scintillator FILDs consist of a scintillator plate mounted in a probe head placed near the plasma. During their motion, the lost fast ions may reach the pinhole in the probe head and pass through a collimator filtering the ions. These measurements are used to determine the velocity-space distribution function of the lost fast ions. See Fig. 7.1 for an illustration of the working mechanism of a scintillator FILD.

The forward model of the FILD instrument can be formulated as an integral equation relating the fast-ion velocity-space distribution function to a FILD measurement through a weight function. The integral is over gyroradius ρ and pitch angle α, two variables that can describe the velocity space of ions in a plasma. Typically, the variables $v_\parallel$ and $v_\perp$ are used, where $v_\parallel$ is the velocity of the ions along the magnetic field and $v_\perp$ the velocity perpendicular to the magnetic field. The

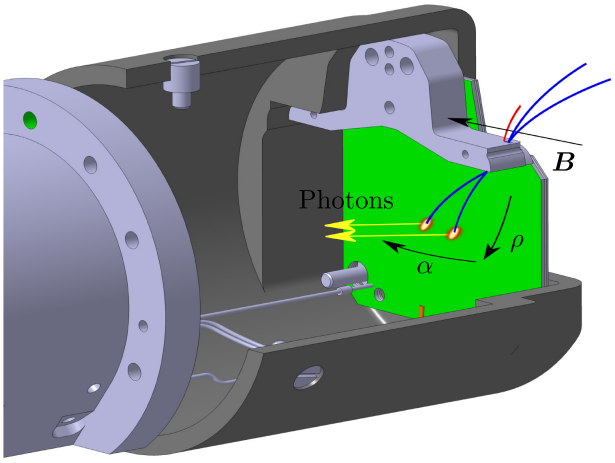

Figure 7.1: A typical FILD probe head (dark gray) and the scintillator (green). fast-ion orbits shown in blue pass through the collimator and fast-ion orbits in red are blocked. From Poley-Sanjuan et al. (2023).

four variables are related by the equations

$$\cos\alpha = \frac{v_\parallel}{v}, \tag{7.1}$$

$$\rho = \frac{mv_\perp}{ZeB}, \tag{7.2}$$

where $v = \sqrt{v_\parallel^2 + v_\perp^2}$. The forward problem can be expressed as

$$s(\rho_1, \rho_2, \alpha_1, \alpha_2) = \int_0^\pi \int_0^\infty w(\rho_1, \rho_2, \alpha_1, \alpha_2, \rho, \alpha) f(\rho, \alpha)\, \mathrm{d}\rho\, \mathrm{d}\alpha, \tag{7.3}$$

where $s(\rho_1, \rho_2, \alpha_1, \alpha_2)$ is the FILD measurement in the gyroradius range $[\rho_1, \rho_2]$ and pitch angle range $[\alpha_1, \alpha_2]$, f the velocity-space distribution function of the lost fast ions, and $w(\rho_1, \rho_2, \alpha_1, \alpha_2, \rho, \alpha)$ the weight function modelling the detector characteristics for scintillator measurements in the specific gyroradius and pitch angle ranges. Since the weight function w can be obtained by computational modelling, and the FILD measurements s are obtained through experiments, the objective is to solve Eq. (7.3) for f given s and w. This is an inverse problem.

The inverse problem of obtaining f given s and W is ill-posed. Ill-posed inverse problems are sensitive to perturbations in the measurements resulting in the lack of unique and stable solutions, i.e., small perturbations in the measurement can produce large perturbations in the reconstructed solutions. Typically, regularization techniques are applied to address the ill-posed nature of the problem by introducing additional penalties on undesired features of the reconstructed solution. In the subsequent sections, we explore the use of deep neural networks to determine the value of the optimal regularization parameter and to solve the inverse problem directly.

7.3 Tikhonov regularization

Solving the ill-posed inverse problem in Eq. (7.3) in practice requires discretizing velocity space. This turns the equation into the matrix-vector equation

$$Wf = s, \tag{7.4}$$

where $W \in \mathbb{R}^{m \times n}$ is the weight function matrix, $s \in \mathbb{R}^m$ is the measurement vector, and $f \in \mathbb{R}^n$ is the desired solution. Regularization is needed to compute a stable solution. Typically, Tikhonov regularization is used to determine the velocity-space distribution functions in velocity-space tomography. This section gives a brief overview of Tikhonov regularization and the associated challenges in selecting an appropriate regularization parameter.

Tikhonov regularization is a widely used technique for regularizing ill-posed inverse problems. The ill-posed inverse problem is regularized by adding a regularization term to the objective function, penalizing different aspects of the solution as defined by the regularization operator L. Mathematically, Tikhonov regularization can be expressed as:

$$f^* = \underset{f}{\operatorname{argmin}} \|Wf - s\|_2^2 + \lambda \|Lf\|_2^2, \tag{7.5}$$

where L is a linear operator promoting desired properties in the solution, and λ is the regularization parameter. The regularization parameter determines the trade-off between fitting the measured data and the operator penalty. A larger value results in a solution emphasizing the operator penalty with less emphasis on fitting the data, while a smaller value prioritizes fitting the data at the expense of the penalty. The choice of the value of the regularization parameter can therefore impact the solution's accuracy, reliability, and interpretability.

Determining the optimal regularization parameter is not straightforward, since it depends on the specific problem, the noise in the data, and the desired properties of the solution. Several methods exist to select the value of the regularization parameter, including the discrepancy principle, the L-curve, and generalized cross-validation. However, these methods usually determine values of the regularization parameter within an order of magnitude but systematically different, so the solutions systematically have higher or lower noise levels depending on the method used. Therefore, the choice of regularization parameter is typically left to the user's intuition, which results in better reconstructions. We propose to teach a deep neural network to choose the optimal value of the regularization parameter.

7.4 Determining the optimal regularization parameter

In this section, we present the results of our DNN-based approach for determining the optimal regularization parameter for zeroth-order Tikhonov regularization applied to synthetic and experimental scintillator FILD measurements. The performance of the networks on synthetic data is evaluated using the R^2 coefficient and the slope α of the straight line ℓ fitted to data containing the DNN predictions for the optimal value of the regularization parameter λ_{DNN} vs. the true optimal values λ^{true}. The line ℓ models the relationship between the predicted regularization parameter values and the true optimal regularization parameter values. Ideally, the line has slope $\alpha = 1$ and intercept 0. The R^2 coefficient is defined as

$$R^2 = 1 - \frac{\sum_{i=1}^{n} \left(\lambda_{\mathrm{DNN},i} - \ell\left(\lambda_{\mathrm{true},i}\right)\right)^2}{\sum_{i=1}^{n} \left(\lambda_{\mathrm{DNN},i} - \mu_{\mathrm{DNN}}\right)^2}, \tag{7.6}$$

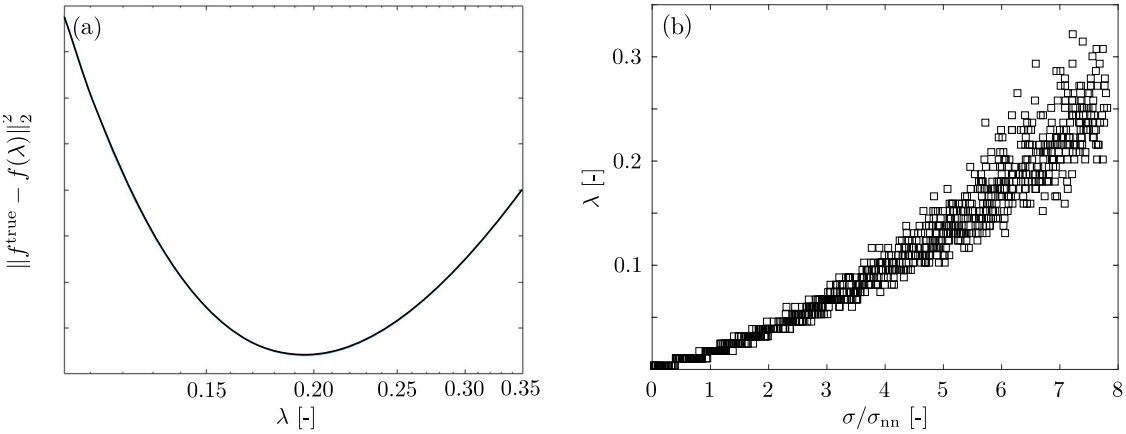

Figure 7.2: (a) The curved shape of $g(\lambda) = \|f^{\text{true}} - f(\lambda)\|_2^2$ for a scintillator FILD measurement indicating the optimal choice of λ at the minimum. (b) The optimal choice of λ as a function of the normalized standard deviation $\sigma/\sigma_{\text{nn}}$ of the scintillator FILD measurement.

where n is the size of the dataset, and μ_{DNN} is the mean of the DNN predictions. The numerator is the *sum of squared residuals*, since $\lambda_{\text{DNN},i} - \ell\left(\lambda_{\text{true},i}\right)$ is the ith residual for the DNN-predicted regularization parameter values relative to the model ℓ. The sum of squared residuals measures the discrepancy between the predicted regularization parameter values and the model ℓ. The denominator is the *total sum of squares* and is proportional to the variance of the predictions. The fraction can be interpreted as the fraction of unexplained variance since the variance of the model errors is compared with the total variance of the data. The sum of squared residuals is zero for a perfect match between the model ℓ and the predictions, and $R^2 = 1$. Here, we call a model always predicting the mean μ_{DNN} the 'baseline model' with $R^2 = 0$. A model worse than the baseline model has $R^2 < 0$.

We compare the performance of a feedforward neural network (FFNN) and a convolutional neural network (CNN) to assess the effectiveness of different network architectures. Furthermore, we apply the best trained neural network as determined by its performance on the synthetic scintillator FILD measurements to experimental FILD measurements from discharge #34559 at ASDEX Upgrade and illustrate the reconstructions computed using the regularization parameter values suggested by the network.

7.4.1 Details of the training dataset generation

The DNNs are trained and validated on synthetic FILD measurements. The inputs are synthetic FILD measurements, and the training targets are the optimal value of the regularization parameter. The optimal value is determined as follows. Tomographic reconstructions are computed using non-negative zeroth-order Tikhonov regularization for a wide range of regularization parameter values. The function $g(\lambda) \coloneqq \|f^{\text{true}} - f(\lambda)\|_2^2$ then has a minimum for the optimal value of the regularization parameter, where f^{true} is the known ground truth and $f(\lambda)$ the tomographic reconstruction. The curved shape is illustrated in Fig. 7.2(a).

The synthetic FILD measurements s are generated by computing $s = Wf$ for a physically relevant pinhole velocity-space distribution function f. Normally-distributed noise with 10% standard deviation is added to the synthetic FILD measurements. Let the noise level be represented by its standard deviation σ, and let σ_{nn} be the standard deviation of all pixels of the synthetic

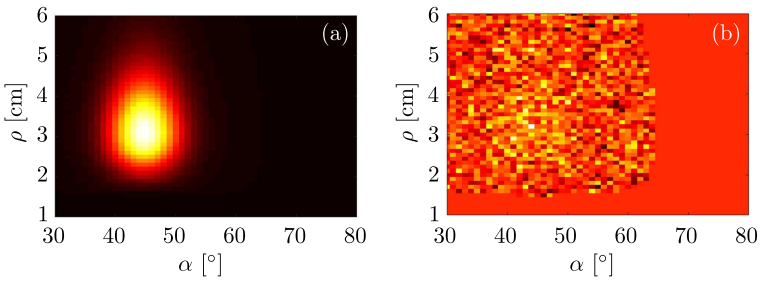

Figure 7.3: Dataset 1: Example fast-ion velocity-space distribution functions for (a) $\sigma/\sigma_{\mathrm{nn}} = 1$ and (b) $\sigma/\sigma_{\mathrm{nn}} = 8$.

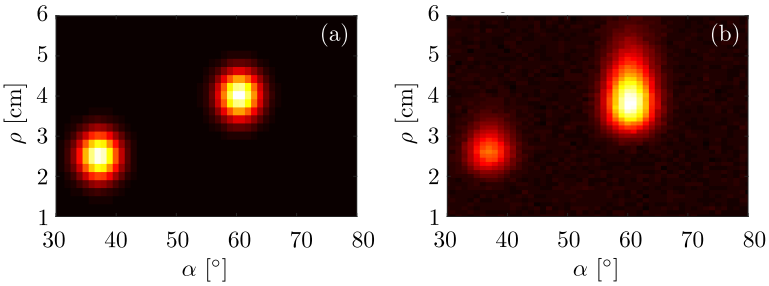

Figure 7.4: Dataset 2: The fast-ion velocity-space distribution function (a) at the pinhole and (b) on the scintillator.

measurement. The parameter σ_{nn} is estimated for the whole synthetic measurement and is used to normalize the noise level relative to the standard deviation of the measurement. See Fig. 7.2(b) for a plot of the numerical value of the optimal regularization parameter λ as a function of $\sigma/\sigma_{\mathrm{nn}}$ for dataset 1, to be described below. The optimal value of the regularization parameter increases with the noise level, as it should. Note that for large noise levels $\sigma/\sigma_{\mathrm{nn}} \gtrsim 3$, the method used to determine the optimal numerical value of λ identifies different λs for the same noise level, with the range of λs increasing as the level of noise increases. This spread in λ occurs since different noise realizations for the same σ result in different values of the regularization parameter being optimal.

Three different datasets consisting of 1000 measurements each, to be referred to as 'dataset 1', 'dataset 2', and 'dataset 3', are generated with an increasing number of velocity-space locations populated by lost fast ions. Examples of synthetic FILD measurements from each dataset are illustrated in Figs. 7.3, 7.4, and 7.5. Measurements in dataset 1 consist of a single Gaussian distribution in a region of velocity space that has previously been observed to contain measurements in experiments at ASDEX Upgrade. The noise added to dataset 1 ranges from no noise, i.e., $\sigma/\sigma_{\mathrm{nn}} = 0$, to a very high level of noise, i.e., $\sigma/\sigma_{\mathrm{nn}} = 8$, where the measurement becomes indistinguishable from the noise; see Fig. 7.3. Including such extreme measurements are thought to improve the robustness of the DNNs and their generalizability to unknown data. Dataset 2 consists of Gaussian distributions in two locations in velocity space with noise with 10% standard deviation; see Fig. 7.4. Dataset 3 consists of Gaussian distributions in nine locations in velocity space also with noise with 10% standard deviation; see Fig. 7.5.

FILD measurements are collected in an array with the ith row corresponding to a specific value of the gyroradius and the jth column to a specific value of the pitch angle. The matrix

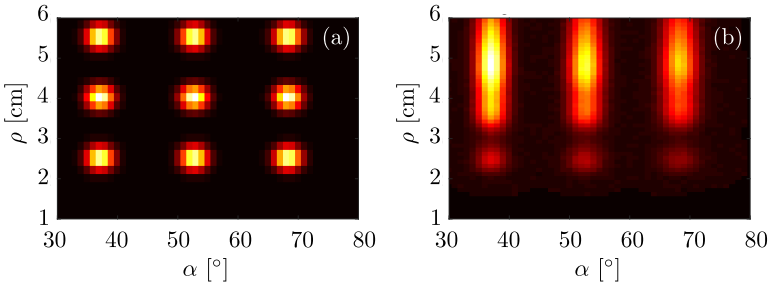

Figure 7.5: Dataset 3: The fast-ion velocity-space distribution function (a) at the pinhole and (b) on the scintillator.

dimensions are 91×81. As input for the FFNN, the matrix is transformed to a 1D vector with 7371 entries. The 2D array is used as input to the CNN.

7.4.2 Network architectures

Deep neural networks with architectures corresponding to a feedforward neural network (FFNN) and a convolutional neural network (CNN) were trained on the three datasets with the optimal values of the regularization parameter as training targets. We used an 80/20 split for training and validation for all three datasets. To evaluate the performance of the DNNs, the predictions of the regularization parameter values are plotted as data points $(\lambda^{\text{true}}, \lambda_{\text{pred}})$. A linear regression is then performed with the correlation coefficient R^2 and the slope α of the fitted line used as evaluation metrics. Both R^2 and α equal one for 100% accurate predictions.

The architectures of the DNNs are optimized in terms of several parameters evaluated by their effect on the resulting predictive performance of the DNNs according to the evaluation metrics R^2 and α. These parameters are

- Number and type of layers
- Number of nodes
- Activation function
- CNN kernel size
- Max pooling
- Stride length
- Dropout layers
- Padding

The activation functions considered are ReLU and tanh to account for non-linearities, where

$$\text{ReLU}(x) = \begin{cases} x & \text{if } x > 0, \\ 0 & \text{otherwise}, \end{cases} \tag{7.7}$$

$$\tanh x = \frac{\sinh x}{\cosh x} = \frac{\mathrm{e}^{x} - \mathrm{e}^{-x}}{\mathrm{e}^{x} + \mathrm{e}^{-x}} = \frac{\mathrm{e}^{2x} - 1}{\mathrm{e}^{2x} + 1}. \tag{7.8}$$

Max pooling is used and preferred over average pooling since max pooling works as a noise reduction and dimensionality reduction mechanism, which is helpful for better predictions with noisy and high-dimensional data. The size of the CNN kernel is important. Dropout is used to avoid possible overfitting. Different padding schemes may affect the predictions as the array is processed differently by the kernel of the CNN for different padding schemes. Finally, we use the 'Adam' optimizer and the mean squared error as loss function.

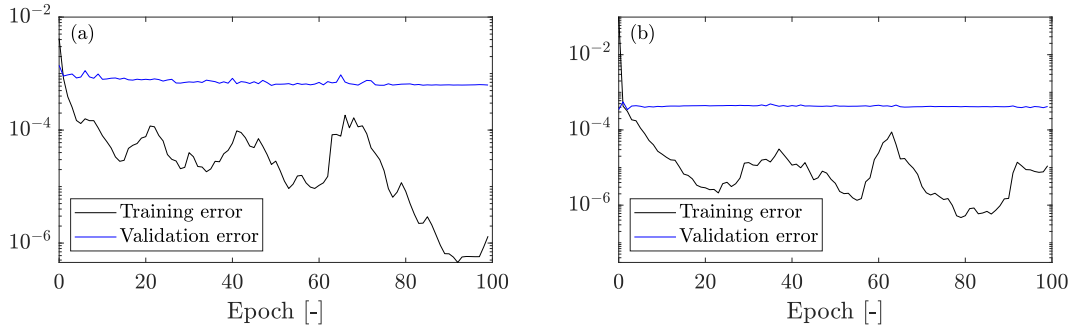

Figure 7.6: Training histories of (a) the FFNN and (b) the CNN on dataset 1 for the first 1000 epochs.

Architecture	Baseline	Ideal	6 layers	10 layers	11 layers	12 layers
R^2	0	1	0.8478	0.8966	0.9012	0.9012
α	0	1	0.8382	0.8606	0.9655	0.8660

Table 7.1: The performance of the FFNN as a function of the number of layers. The best performance is achieved for 11 layers with 1024 nodes in the input layer.

7.4.3 Feedforward neural network

The optimal architecture for the FFNN was determined by testing the number of dense layers and the number of nodes in each layer resulting in improvements in the two evaluation metrics R^2 and α compared to a baseline model always predicting the mean μ_{DNN}, so $R^2 = 0$. A model worse than the baseline model has $R^2 < 0$. This can happen, e.g., if the model predicts a decreasing relation, whereas the relation should be increasing. This testing was performed on all three datasets. A batch size of 20 and 100 epochs were used in the training. The neural networks had almost converged after 100 epochs with only minor improvements to be gained by additional epochs as indicated by the training history of the FFNN on dataset 1; see Fig. 7.6(a). With a loss value of 10^{-6} after 100 epochs, no further optimization is needed since a deviation of the numerical value of the regularization parameter on the order of 10^{-3} or less for λ values around 10^{-1} does not result in any appreciable changes in the recovered solution to the ill-posed tomography problem. There seems to be some overfitting indicated by the decreasing training error compared to the almost constant validation error. However, the performance is high on the experimental data set evidenced by the improved tomographic reconstructions, as discussed in Section 7.5.

The same performance increases occurred for the same architectural changes across all three datasets. The number of nodes in each layer was chosen as 2^n for $n = 0, 1, 2, \ldots$ counting from the output layer. The performance of the network was found to be the best for 11 layers with $R^2 = 90.12\%$ and $\alpha = 0.9655$; see Table 7.1. Note that the R^2 are comparable for most tests, but the accuracy of the prediction as given by α is best for 11 layers. The choice of activation function makes no appreciable difference. Implementing dropout layers with 10% dropout increases R^2, but the value of the slope deviates more from one; see Table 7.2. Thus, no dropout layers were used. The architecture is illustrated in Fig. 7.7(a). The predictions of the optimal FFNN vs. the true values for dataset 1 are illustrated in Fig. 7.8(a) with the R^2 and the slope of the fitted line indicated.

The FFNN performs worse on datasets 2 and 3. The correlation coefficient is $R^2 = 9.285\%$

Dropout	Baseline	Ideal	0 layers	1 layer	2 layers	4 layers	6 layers
R^2	0	1	0.9012	0.9110	0.9045	0.9221	0.9314
α	0	1	0.9655	0.8658	0.8652	0.8156	0.7053

Table 7.2: The performance of the FFNN with the indicated number of dropout layers with 10% dropout. The dropout layers are implemented after layers 1-6. Note that R^2 improves slightly, but α decreases significantly with more dropout layers.

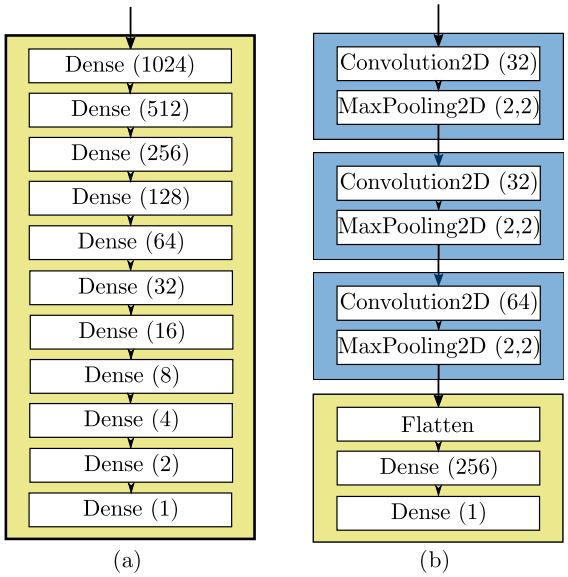

Figure 7.7: The architectures of the (a) feedforward neural network and (b) convolutional neural network used to determine the optimal value of the regularization parameter for zeroth-order Tikhonov regularization on scintillator FILD measurements.

and $\alpha = 0.5674$ for dataset 2 and $R^2 = 57.02\%$ and $\alpha = 0.7856$ for dataset 3; see Table 7.5. The reason for the large performance drop for dataset 2 is unknown. However, the maximal deviation from the true optimum λ is approximately 0.004, which is not a sufficiently large deviation to cause the tomographic reconstructions to worsen significantly. Therefore, although the FFNN scores poorly on our chosen evaluation metrics, the suggested regularization parameters are still useful. The predictions of the optimal FFNN vs. the true values for dataset 2 are illustrated in Fig. 7.9(a). The large spread in the data around the fitted line results in the low value of R^2. The significant underregularization gives the value of the slope far from one.

7.4.4 Convolutional neural network

Similar testing strategies as was used to find the FFNN architecture were used to find the optimal CNN architecture. The architecture was then tested for different kernels, padding, max pooling sizes, stride length, and dropout layers. See Table 7.3 and 7.4 for the specific performance evaluations for stride length and padding. The final architecture is illustrated in Fig. 7.7(b). The optimal CNN has a (2, 2) kernel size, no padding, a (2, 2) max pooling size, a stride length of (1, 1), and no dropout layers. The CNN was trained using a batch size of 10 and for 100 epochs, as

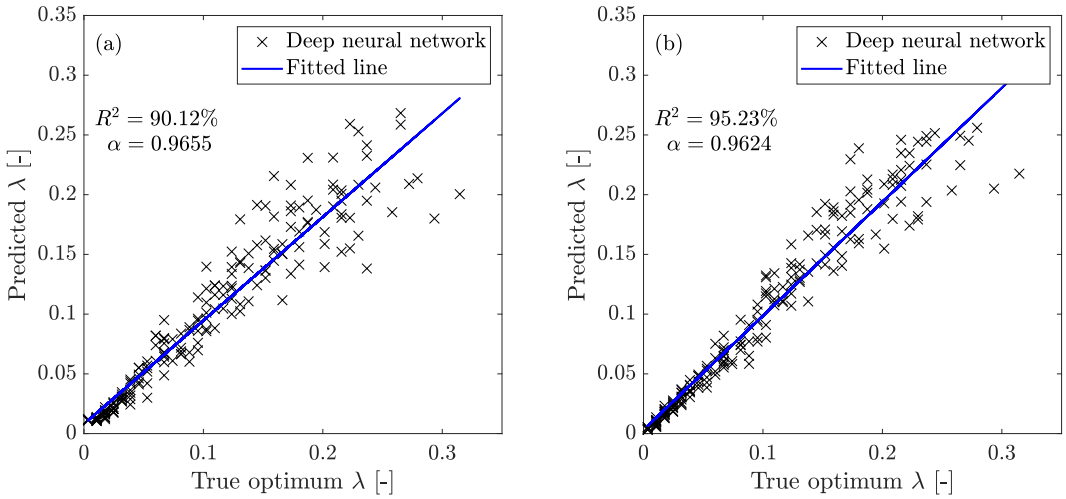

Figure 7.8: The deep neural network predictions of the numerical value of the regularization parameter λ in zeroth-order Tikhonov regularization vs. the true optimal value of λ for (a) a feedforward neural network and (b) a convolutional neural network on dataset 1.

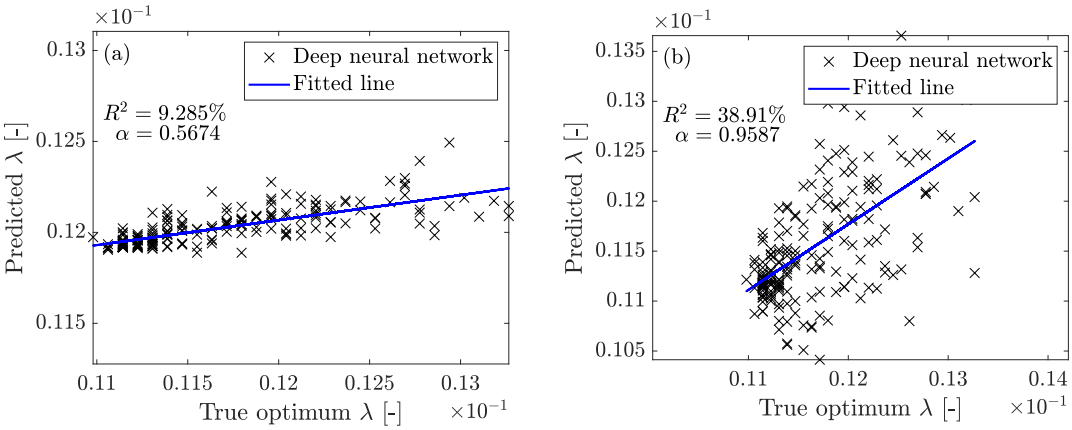

Figure 7.9: The deep neural network predictions of the numerical value of the regularization parameter λ in zeroth-order Tikhonov regularization vs. the true optimal value of λ for (a) a feedforward neural network and (b) a convolutional neural network on dataset 2.

shown in Fig. 7.6(b). The training was terminated at 100 epochs for the same reasons as given for the FFNN. See Table 7.5 for the performance evaluation for the CNN on datasets 1, 2, and 3. The predictions of the CNN vs. the true optimum λ are illustrated for datasets 1 and 2 in Figs. 7.8(b) and 7.9(b).

Note that $\alpha < 1$ for both the FFNN and CNN on all three datasets and for all investigated network parameter values. This indicates that the networks tend to underregularize compared to the optimum.

Stride length	(1, 1)	(2, 1)	(1, 2)	(2, 2)
R^2	0.9523	0.9270	0.9334	0.9385
α	0.9624	0.9077	0.9185	0.9342

Table 7.3: CNN performance as a function of the stride length.

Padding	None ("valid")	Keep size ("same")
R^2	0.9523	0.9436
α	0.9624	0.9323

Table 7.4: CNN performance as a function of the padding.

7.5 Optimal regularization parameter estimation for experimental FILD measurements

Since the trained CNN outperforms the trained FFNN on both evaluation metrics by having a value of R^2 and α closer to one, we use the CNN in the following. The CNN was applied to experimental FILD measurements from FILD2 at ASDEX Upgrade during discharge #34559. The time resolution of FILD2 is 20 ms. The measurements are made for three seconds resulting in 150 measurements. Discharge #34559 investigated the impact of magnetic perturbations generated by magnetic perturbation coils on fast-ion losses. The magnetic activity is measured using a magnetic probe, and a FILD measures the lost fast ions. Using the measurements from the photomultiplier tubes (PMTs) in the FILD, it is possible to compare the frequency of the lost fast ions with the frequencies measured by the magnetic probes.The frequency of the measurements of the magnetic probe and the PMTs are illustrated in Fig. 7.10. The magnetic perturbations around 100 kHz

FFNN	Dataset 1	Dataset 2	Dataset 3
R^2	0.9012	0.09285	0.5702
α	0.9655	0.5674	0.7856
CNN	Dataset 1	Dataset 2	Dataset 3
R^2	0.9460	0.3891	0.3215
α	0.9608	0.9587	0.8814

Table 7.5: Performance of the FFNN and CNN.

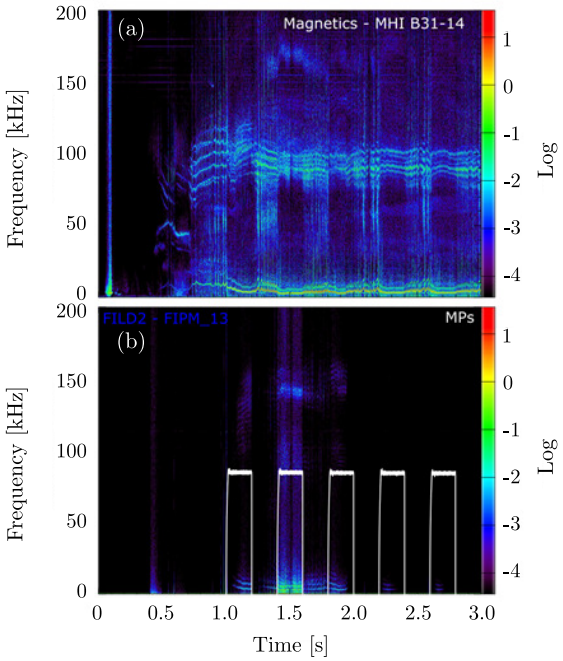

Figure 7.10: Measurements of magnetic activity from a (a) magnetic probe and (b) FILD photomultiplier tubes during discharge #34559 at ASDEX Upgrade. The white line in (b) indicates the current in the the magnetic perturbation coil. Provided by Joaquín Galdon-Quíroga.

correspond to Alfvén eigenmodes transporting ions outward toward the low field side. The 10-20 kHz signals are low-frequency modes likely to be neoclassical tearing modes. The white line is the magnetic perturbation coil current. The interactions observed between modes and fast ions occur primarily during the time interval when the magnetic perturbation coil was turned on at $t = 1.5$ s.

When reconstructing the velocity-space distribution function, a single value of the regularization parameter is typically used to compute reconstructions of a full discharge. This is done because the value of the regularization parameter has to be chosen specific to a given measurement, which is impractical for an entire discharge. Thus, an average value of the regularization parameter is used, which works approximately well for all measurements. This, however, does not produce optimal reconstructions for each measurement. For example, for discharge #34559, the FILD measurements vary significantly during the discharge due to the current in the magnetic perturbation coil. To evaluate the performance of the CNN, we compare tomographic reconstructions computed using zeroth-order Tikhonov regularization with $\lambda = 0.1$ and $\lambda = 0.05$ to the tomographic reconstructions computed using the regularization parameter value suggested by the CNN. The CNN provides the optimal regularization parameter values for zeroth-order Tikhonov regularization for individual measurements to reconstruct the pinhole velocity-space distribution function of the lost ions for all 150 measurements.

Tomographic reconstructions of the FILD measurement at $t = 0.9403$ s using the values $\lambda = 0.1$, $\lambda = 0.05$, and the value suggested by the trained CNN are shown in Fig. 7.11. A timeline of the discharge is indicated at the top of the figure showing the power of the NBI (horizontal black line) and when the magnetic perturbation coils are active (blue line). The vertical black line on the

timeline indicates the time of the measurement. Figure 7.12 shows the values of the regularization parameter suggested by the neural network as a function of time with the magnetic perturbation coil current overlaid and the user-defined λ values of 0.1 and 0.05 indicated. Note that the values suggested by the neural network remain far from the user-defined values throughout the discharge.

The CNN suggests an optimal value of the regularization parameter of $\lambda = 0.0115$ for the FILD measurement at $t = 0.9403$ s. The reconstruction using the value suggested by the CNN indicates an improvement over the two user-defined values. It must be stressed here that if a human were to perform tomographic reconstructions on just this one measurement, he would be able to choose an optimal value of the regularization parameter such as that suggested by the CNN. The strength of the CNN approach is that the CNN can provide an approximate optimal value of the regularization parameter for hundres of measurements and adjust the lambda accordingly and do it automatically. For the user, the value of the regularization parameter supplied by the CNN also suggests an approximate range for the regularization parameter, so the user does not have to investigate many reconstructions computed using different values of the regularizatoin parameter. In fact, the CNN could suggest a single regularization parameter value that could be used to perform reconstructions for an entire discharge. The values of the regularization parameter suggested by the CNN for discharge #34559 do not deviate much from measurement to measurement, and an average value would produce useful tomographic reconstructions.

The tomographic reconstruction obtained using $\lambda = 0.0115$ produces a more localized pinhole velocity-space distribution function, which better reflects the pinhole velocity-space distribution function of the lost fast ions. This can be seen both qualitatively by the shape of the high-intensity locations in velocity space and by the values of the colorbar: the signal intensities in the CNN-assisted reconstruction are higher by an order of magnitude than the manually chosen value. The integral of the reconstructions over all of velocity space are identical, but the number of ions is more localized in the CNN-assisted reconstruction. Further, the tails occurring in the gyroradius direction do not appear in the CNN-assisted reconstruction, and these ions are instead at the center of the distribution. The tails are erroneous artefacts introduced in the reconstruction, as can be seen by comparison with the FILD measurement. The larger values of the regularization parameter better suppress the noise in the FILD measurement; see, e.g., the higher intensity dot at around $(38°, 2\,\text{cm})$ in the reconstruction using the CNN-suggested value of the regularization parameter.

The CNN finds a good balance between under- and overregularizing. Overregularizing produces solutions that are too smooth, indicate velocity-space locations of the fast ions that are too large, and contain artefacts such as the tails in Fig. 7.11(b). A lower value of the regularization parameter by a factor of 10, $\lambda = 0.001$, significantly amplifies the noise in the reconstruction, which is undesirable; see Fig. 7.13.

The CNN is trained to predict the optimal value of the regularization parameter based on the noise in the measurement and the complexity of the measurement. That the regularization parameter is relatively constant throughout the discharge, as indicated by the timeline in Fig. 7.12, makes sense since the noise can be assumed to not deviate much from a given mean value during the discharge, and the complexity, as understood by the trained neural network, also does not change. However, the number of different velocity-space locations indicating lost fast ions as measured on the scintillator changes from 0 to 3, with the intensity of the losses highest during the second interval the magnetic perturbation coil current was turned on around 1.5 s. See Fig. 7.14 for an illustration of the different measurement complexity and relatively constant noise level. In the same figure, tomographic reconstructions obtained using the values suggested by the CNN are illustrated. The reconstructions do not indicate more localized distributions in pinhole velocity space as expected. However, noise is reduced. Note the constancy of the regularization parameter around $\lambda = 0.0120$ for all five reconstructions.

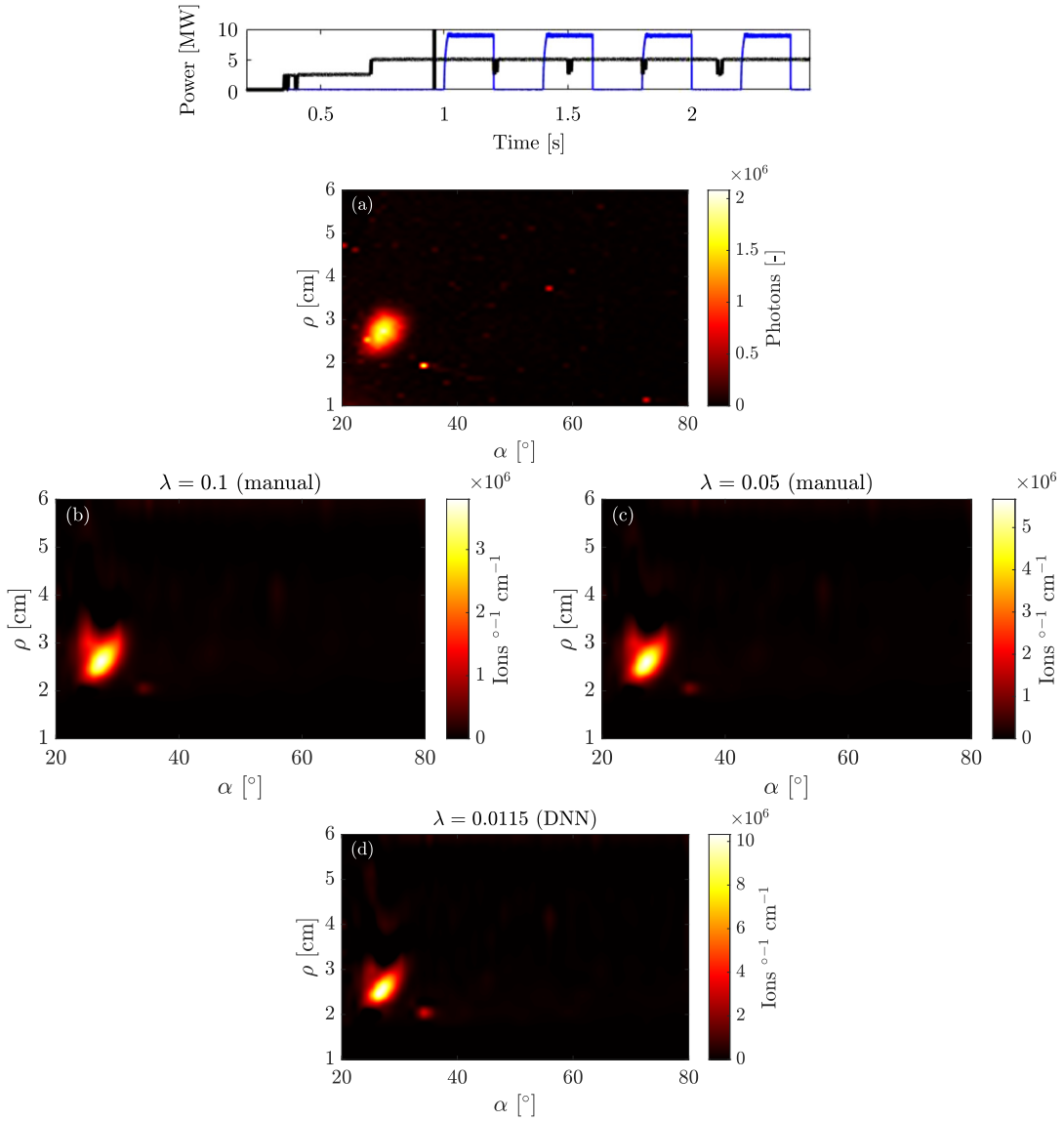

Figure 7.11: (a) The scintillator velocity-space distribution at $t = 0.9403$ s as measured by FILD2 during discharge #34559 indicated by the vertical black line in the time bar at the top of the figure. (b)-(c) Tomographic reconstructions using the manually chosen value of the regularization parameter $\lambda = 0.1$ and $\lambda = 0.05$. (d) Tomographic reconstruction using the value of the regularization parameter suggested by the trained DNN.

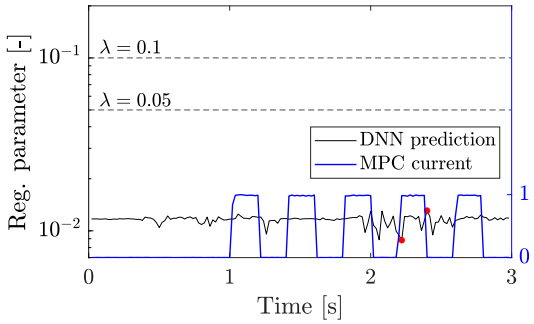

Figure 7.12: The values of the regularization parameter for zeroth-order Tikhonov regularization suggested by a trained deep neural network (DNN) as a function of time during discharge #34559. The blue line indicates the current in the magnetic perturbation coil (MPC current). '0' indicates the current is off, and '1' indicates it is on. The two red dots indicate the smallest and largest values of the regularization parameter suggested by the trained DNN.

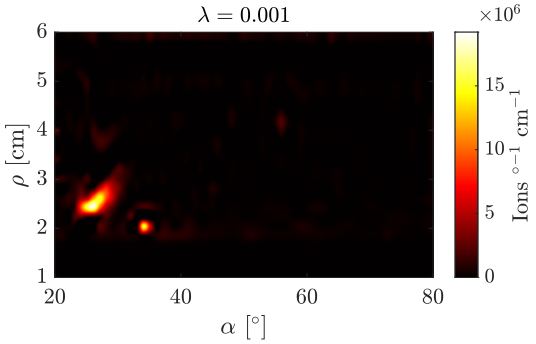

Figure 7.13: Tomographic reconstruction using a value of the regularization parameter smaller than the DNN-suggested value of the regularization parameter by a factor of 10, which significantly amplifies the noise in the reconstruction.

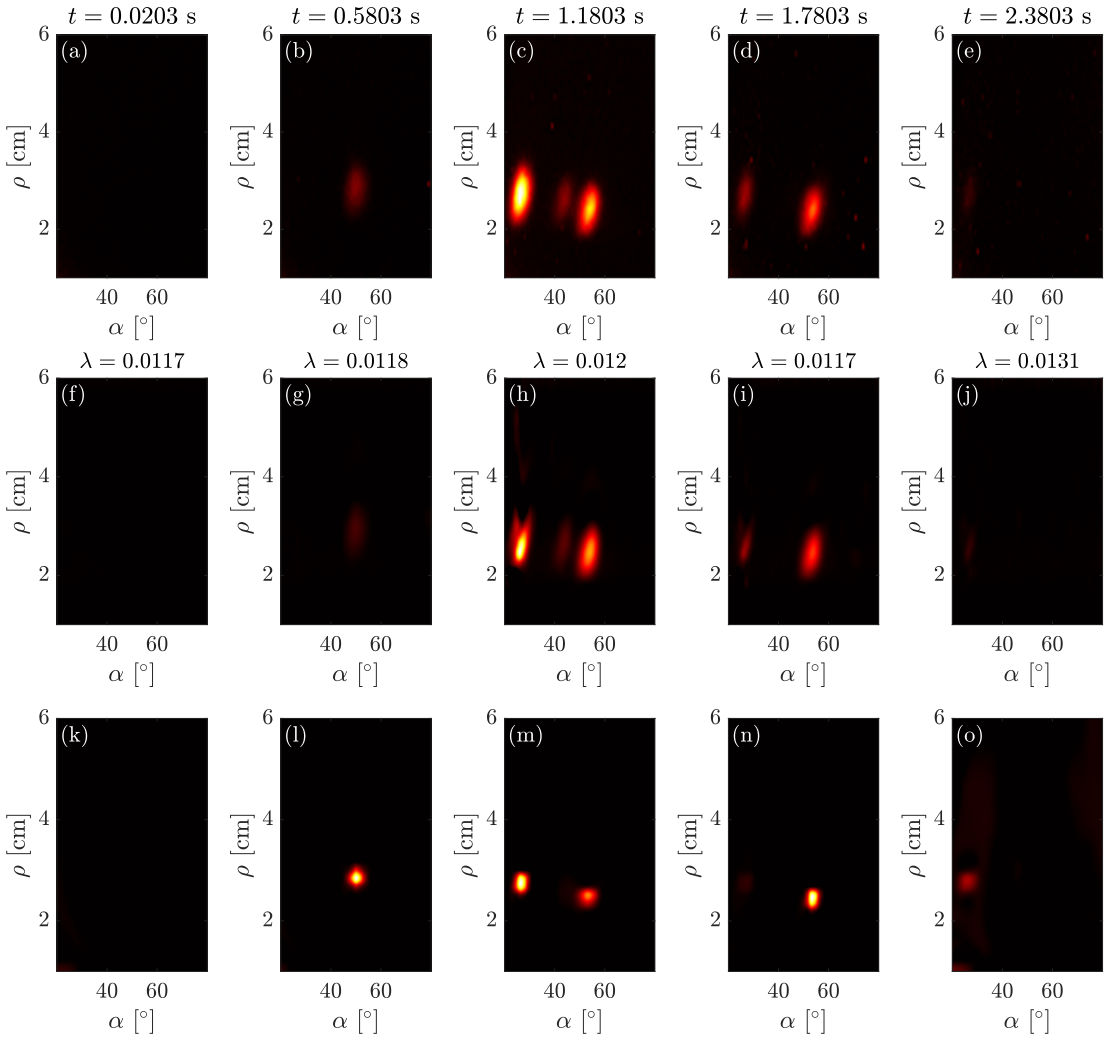

Figure 7.14: (a-e) FILD measurements at different times throughout the discharge normalized to the same colorbar values illustrating the different complexities and approximately constant noise level. (f-j) Tomographic reconstructions computed using the indicated values of the regularization parameter suggested by the trained deep neural network. (k-o) Tomographic reconstructions computed directly by a trained deep neural network different from that used in (f-j).

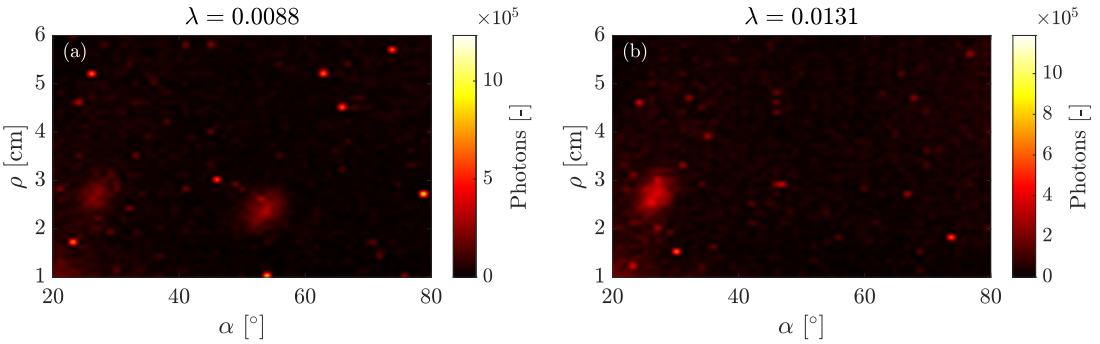

Figure 7.15: The FILD measurements from discharge #34559 with the (a) smallest regularization parameter predicted by the DNN at $t = 2.2203$ s and (b) the largest regularization parameter predicted by the DNN at $t = 2.4003$ s. The DNN downregulates the value of the regularization parameter when it detects what corresponds to actual lost ion measurements, and upregulates the value when it detects noise.

The explanation for the constancy of the optimal value of the regularization parameter is the following: the trained CNN can interpret what a measurement of lost fast ions is and what noise is, even for faint measurements with intensities comparable to the noise. The CNN then suggests the value of the regularization parameter accordingly: if it interprets a given input as signal, it suggests a smaller value of the regularization parameter to better fit the measured data, and if it interprets the input as noise, it provides a larger value of the regularization parameter to reduce the fit to the data. This effect is illustrated in Fig. 7.15. The FILD measurement shown in Fig. 7.15(a) was made at $t = 2.2203$ s and corresponds to the CNN-prediction with the smallest value of λ, and that in Fig. 7.15(b) at 2.4003 s and corresponds to the CNN-prediction with the largest value of λ. These times are indicated by the two red dots in Fig. 7.12. In (a), the two faint spots at around $(28°, 2.8\,\text{cm})$ and $(55°, 2.5\,\text{cm})$ are noticeable, whereas in (b), only the one at $(28°, 2.8\,\text{cm})$ remains. Where there is a spot indicating lost fast ions in (a), there is noise in (b). With other parts of the measurement remaining almost identical, this difference between an actual measurement and noise leads the trained CNN to predict an upregulated value of the regularization parameter to suppress the noise. This capability likely comes from the training on dataset 1, where some training examples have noise levels making the signal almost indistinguishable from the noise.

7.6 DNNs for direct tomographic reconstructions

In this section, we use trained DNNs to directly perform tomographic reconstructions of velocity-space distribution functions of lost fast ions. This is achieved by training a DNN on synthetic FILD measurements with known velocity-space distribution functions of lost fast ions as targets.

Similar investigations as described in the previous section show that a CNN is superior to an FFNN for computing tomographic reconstructions of synthetic FILD measurements. The details of this investigation are not given here as it closely mimics that of the previous section. The resulting CNN architecture employed for direct tomographic reconstructions consists of six CNNs with 64 nodes with 50% dropout layers between each CNN. The kernel size used was $(3, 3)$. The training set consisted of 10,000 input-target pairs with a batch size of 100 used in training. Similar to the previous section, the 'Adam' optimizer was used and the mean squared error as loss

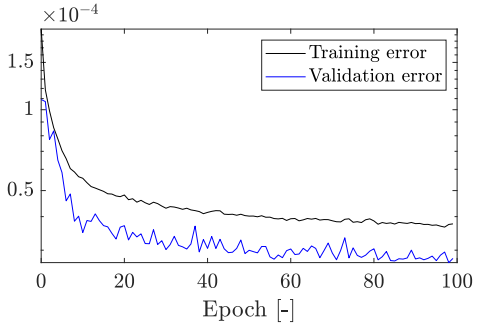

Figure 7.16: Training history of a convolutional neural network to compute tomographic reconstructions of the velocity-space distribution function of lost fast ions.

function. The training was run for 100 epochs; see Fig. 7.16.

The training set contains synthetic measurements similar to experimental FILD measurements measured at ASDEX Upgrade and TCV. Some deviations from experimental measurements are purposefully introduced to allow for greater generalization capabilities of the DNN. The training set consists of 10,000 pinhole-scintillator velocity distribution function pairs with single Gaussian distributions with varying standard deviation in gyroradius and pitch angle centered at different gyroradii $\rho_0 \in [1, 6]$ cm and pitch angles $\alpha_0 \in [20°, 80°]$. These ranges cover the measurable velocity space for FILD2 at ASDEX Upgrade and the FILD at TCV. The equation for the Gaussian distributions used to generate the data is

$$f(\alpha, \rho) = \frac{1}{2\pi\sigma_\alpha\sigma_\rho}\exp\left(-\frac{1}{2}\left(\frac{\rho_0 - \rho}{\sigma_\rho}\right)^2 - \frac{1}{2}\left(\frac{\alpha_0 - \alpha}{\sigma_\alpha}\right)^2\right) \tag{7.9}$$

with appropriate values of σ_ρ and σ_α chosen randomly. The single Gaussian distributions were positioned uniformly all over the measurable velocity space. The input and target distributions were all normalized to be independent of the actual photon counts to allow for tomographic reconstructions of measurements from different FILDs at different machines. Five examples of these 10,000 input-target training pairs are shown in Fig. 7.17. These examples showcase velocity-space distribution functions of lost ions measured at TCV and ASDEX Upgrade.

We have applied the trained DNN to the experimental data from FILD2 at ASDEX Upgrade measured during discharge #34559. The tomographic reconstruction produced by the DNN for $t = 0.9403$ s is shown in Fig. 7.19(b). This reconstruction is a large improvement over the tomographic reconstruction obtained using zeroth-order Tikhonov regularization for several reasons. Firstly, lost fast ions are expected to originate from a precise location in velocity space, i.e., the high-intensity location in the pinhole velocity-space distribution function should be localized without much width. The pinhole velocity-space distribution function provided by the DNN is significantly more localized than that obtained using Tikhonov regularization, cf. Fig. 7.11(c). Secondly, the high-intensity noise in the scintillator measurements is removed by the DNN, and only the correct measurement appears in the reconstruction. However, the DNN misses the faintest of the three peaks in the scintillator measurement as shown in Figs. 7.14(c) and (m), and the faintest of the two peaks in Figs. 7.14(d) and (n). This is reasonable since the training set only includes synthetic scintillator measurements of one peak. In fact, that the DNN is able to reconstruct two peaks shows the DNN can generalize well from its training and go beyond the contents of its training set.

Additional tomographic reconstructions of the discharge computed using the trained DNN

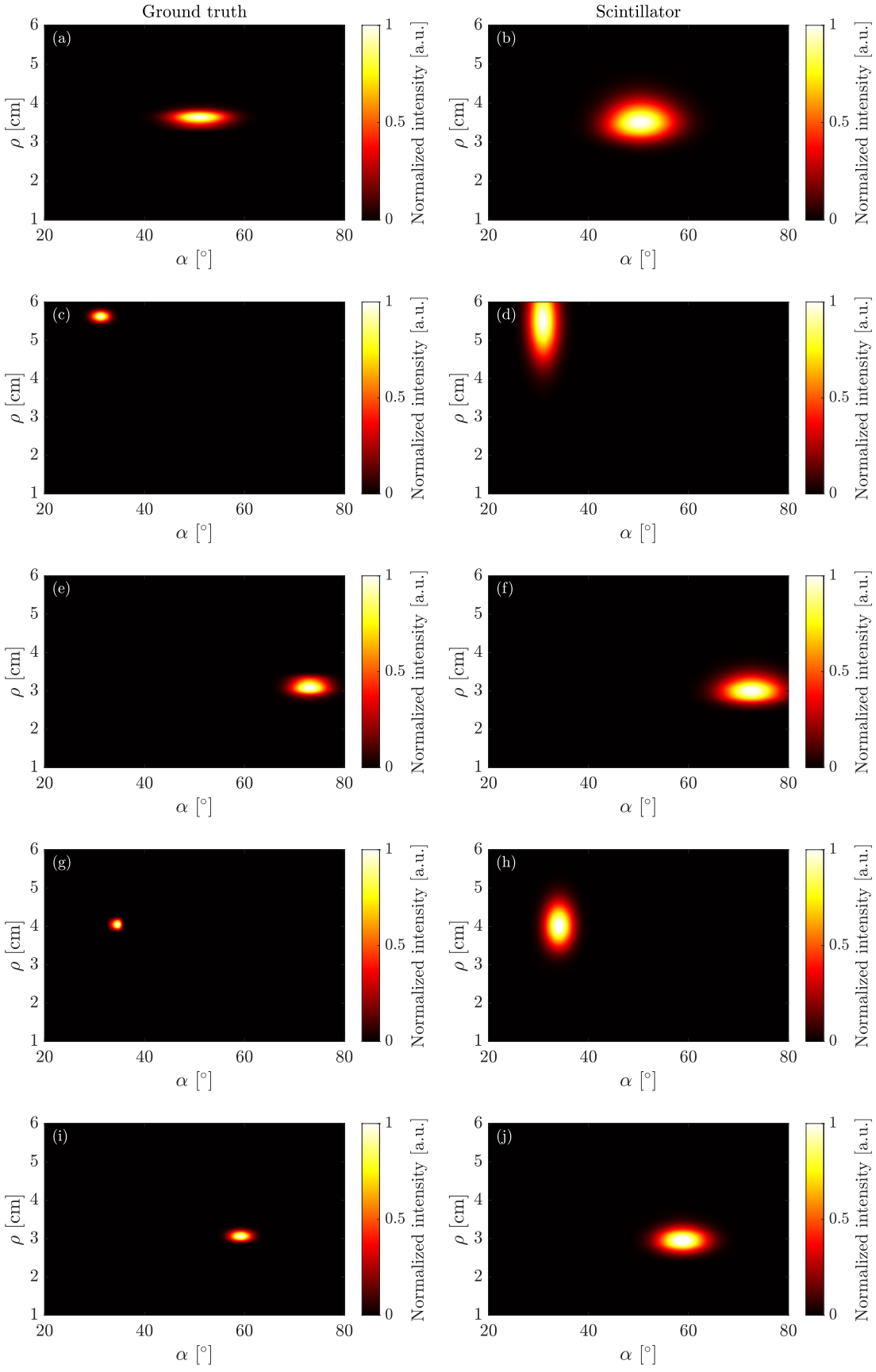

Figure 7.17: The left column shows five examples of pinhole velocity-space distribution functions ('ground truth') in the training set for CNN-based tomographic reconstructions of FILD measurements. The right column illustrates the corresponding scintillator measurements.

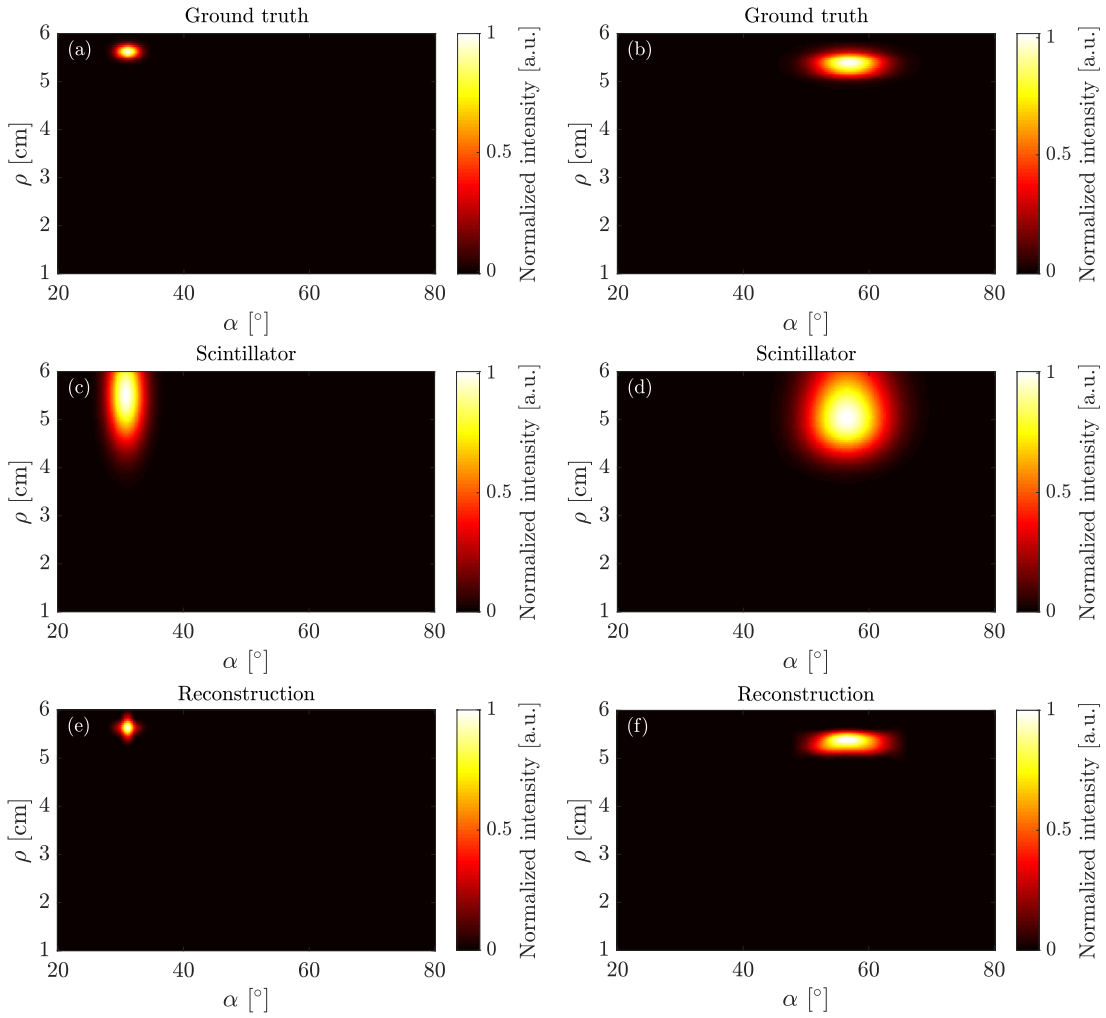

Figure 7.18: Subfigures (a) and (b) show two pinhole velocity-space distribution functions. Subfigures (c) and (d) show the corresponding scintillator measurements for the pinhole velocity-space distribution functions shown in (a) and (b). Subfigures (e) and (f) show the neural network reconstructions based on the synthetic scintillator data.

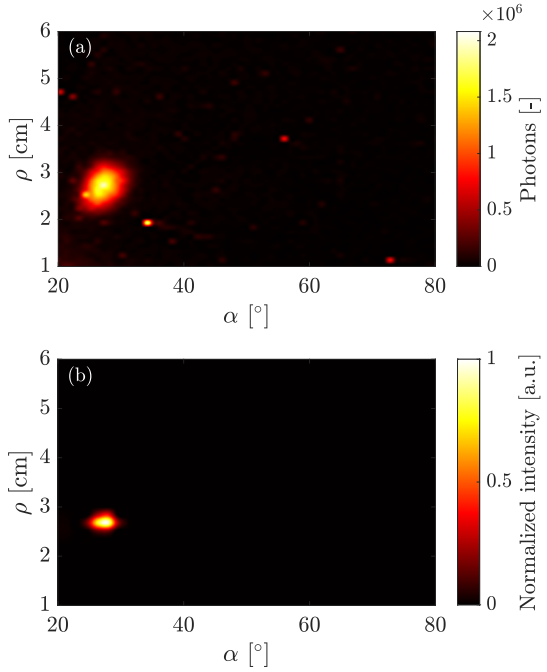

Figure 7.19: (a) Scintillator velocity-space distribution function measured by FILD2 during discharge #34559 at $t = 0.9403$ s. (b) Tomographic reconstruction obtained from the trained deep neural network.

are illustrated in Fig. 7.14(k-o). The trained DNN predicts pinhole velocity-space distribution functions of the lost fast ions that are much more localized than those obtained using Tikhonov regularization. This is in accordance with the expectations of the pinhole velocity-space distribution functions. Further, the network removes the noise almost entirely.

7.7 Discussion and conclusion

This paper investigates the capability of deep neural networks to invert fast-ion loss detector measurements in two distinct ways. One is to predict the optimal numerical value of the regularization parameter used in zeroth-order Tikhonov regularization. The other is to perform direct tomographic reconstructions of experimental fast-ion loss detector measurements. For the regularization parameter prediction, a feedforward neural network and a convolution neural network are optimized in terms of their architectures and relevant training parameters. The performance of the networks is evaluated by plotting the neural network predictions vs. the known true optimal regularization parameters for three different synthetic datasets and evaluated by how close the correlation coefficient R^2 and the slope α of the line fitted to the data points are to 1.

Both networks perform well on dataset 1. The CNN outperforms the FFNN by a small margin, achieving $R^2_{\text{CNN}} = 0.9523$ vs. $R^2_{\text{FFNN}} = 0.9012$, and $\alpha_{\text{CNN}} = 0.9624$ vs. $\alpha_{\text{FFNN}} = 0.9655$. The values of R^2 and α close to 1 indicate the networks' capacity to model the relation between the input data and the value of the optimal regularization parameter. Dataset 1 contains measurements with both low and high levels of noise. Therefore, the good performance indicates that neural networks can be trained to identify a large range of noise levels in FILD measurements. The

network performance is worse on datasets 2 and 3. This is expected since the datasets are more complex. The exact reason for this performance drop needs to be investigated further. Perhaps it can be remedied by training the network on additional data.

Since the CNN outperforms the FFNN, the CNN was used to predict the optimal value of the regularization parameter for zeroth-order Tikhonov regularization for 150 experimental FILD measurements made using FILD2 at ASDEX Upgrade during discharge #34559. Typically, when processing an entire discharge using Tikhonov regularization, a single value of the regularization parameter is used. The CNN suggests an optimal value for the regularization parameter for each measurement. The regularization parameter predicted by the CNN provides a good trade-off between under- and overregularizing. The network detected the presence of two loss regions in an image and selected a low regularization parameter. In another image, the network detected a large amount of noise and accordingly selected a high regularization parameter.

Furthermore, we train a CNN to perform tomographic reconstructions directly, which does not require explicit regularization altogether to compute tomographic reconstructions from FILD measurements. The CNN is trained on synthetic data consisting of scintillator velocity-space distribution functions obtained from FILD measurements as input and pinhole velocity-space distribution functions as output. The trained CNN was applied to the 150 experimental measurements from FILD2 during discharge #345559. The tomographic reconstructions provided by the CNN have a more precise velocity-space location of the lost fast ions compared to those obtained using zeroth-order Tikhonov regularization, and measurement noise is suppressed. The CNN is able to compute accurate reconstructions of scintillator measurements containing several peaks, which shows its capacity to generalize beyond its training set. This capability can potentially enhance the quality and interpretability of FILD measurements, thereby contributing to a better understanding of complex plasma phenomena.

In conclusion, feedforward and convolutional neural networks can be trained to predict values of the regularization parameter for zeroth-order Tikhonov regularization to reconstruct the lost fast-ion velocity-space distribution function from synthetic and experimental scintillator FILD measurements. Furthermore, convolutional neural networks can be trained to compute tomographic reconstructions of synthetic and experimental scintillator FILD measurements, with significant improvements over tomographic reconstructions computed using zeroth-order Tikhonov regularization.

Chapter 8

FILDSIM model improvements and computation speed optimization

This chapter presents the methods developed in the paper "FILDSIM model improvements and faster tomographic reconstructions of fast-ion loss detector measurements", to be submitted.

8.0 Abstract

This paper presents FILDSIM model improvements, enabling more accurate modelling of the ion trajectories as they pass from the pinhole in the probe head of a fast-ion loss detector to the scintillator plate. The weight functions generated by the improved FILDSIM model are more accurate than the present standard FILDSIM model. They produce superior tomographic reconstructions of fast-ion velocity-space distribution functions from fast-ion loss detector measurements. We showcase this improvement for the FILD currently installed at TCV on synthetic and experimental data from discharge #75620. We also demonstrate that the improved FILDSIM model can be used to optimize a balance between computation time and reconstruction quality using algebraic iterative reconstruction techniques. We argue this optimization technique can provide inter-shot FILD data tomographic reconstructions and analysis.

8.1 Introduction

The presence of superthermal ions is crucial for plasma heating in fusion plasmas. These ions are called 'fast ions' and are generated by injection of high-energy neutrals (NBI), ion cyclotron range of frequencies (ICRF) heating, and alpha particles from DT reactions. Fast ions are characterized by their relatively high energies, from tens of keVs to several MeVs. In nuclear fusion experiments, fast ions can escape confinement and interact with the plasma-facing components of the device, causing damage and reducing the efficiency of the reactor. Such undesirable radial transport can occur, e.g., due to fast-ion interactions with magnetohydrodynamic (MHD) activity. Current fusion devices utilize fast ions generated via NBI and ICRF heating to study radial transport resulting from MHD activity, such as edge-localized modes (ELMs). We need accurate estimates of the fast-ion velocity-space distribution function to understand and mitigate these effects.

To improve the performance of fusion devices, it is crucial to understand the mechanisms leading to fast-ion losses. fast-ion loss detectors (FILDs) provide information on the velocity space of lost fast ions through measurements at the plasma edge. This information is typically given in terms of the pitch angle α and gyroradius ρ given by

$$\alpha = \cos \frac{v_{\parallel}}{v}, \tag{8.1}$$

$$\rho = \frac{mv_{\perp}}{ZeB}, \tag{8.2}$$

where $v_{\parallel}$ is the ion velocity parallel to the magnetic field, $v_{\perp}$ the ion velocity perpendicular to the magnetic field, and $v = \sqrt{v_{\parallel}^2 + v_{\perp}^2}$. Thus, FILDs work as magnetic spectrometers by dispersing the lost fast ions onto a plate since the gyroradius is determined by the magnetic field. The information from FILD measurements can aid in identifying the causes of losses of fast ions and enable researchers to mitigate their negative impact on fusion device performance. FILDs are installed at several fusion devices, including ASDEX Upgrade (AUG), DIII-D, JET, NSTX, MAST-U, EAST, KSTAR, LHD, and TCV. Additionally, FILDs are currently being designed for ITER and JT-60SA, highlighting the importance of the diagnostic.

Since a FILD can measure some of the lost fast ions from MHD activity, a FILD can be used as a direct measure of MHD activity. However, due to the blurring effect of the fast-ion velocity space, FILD measurements do not indicate the fast ions' exact locations. Such information is valuable when seeking to optimize experimental conditions between subsequent discharges. Therefore, it is desirable to compute an accurate estimate of the lost fast-ion velocity-space distribution function. In this paper, we propose reconstruction techniques optimized in terms of reconstruction quality and computation time that can perform FILD velocity-space tomographic reconstructions fast enough for intra-shot analysis.

The paper is structured as follows. Section 2 presents the forward model for the pinhole-scintillator relation and the working principles of the FILD simulation code FILDSIM. Section 3 explains our proposed optimization of the model distributions and illustrates the improvements for simulated FILD impact distributions in gyroradius (energy) and pitch angle. Section 4 illustrates the present standard and new weight functions produced by running the present standard and new FILDSIM models, computes tomographic reconstructions of synthetic and experimental data, and characterizes the FILD TCV in terms of its gross strike map and gross weight function. Section 5 presents previous techniques for inverting the scintillator velocity space to obtain the pinhole velocity space and also presents the fast algebraic iterative reconstruction techniques for tomographic reconstructions. Section 6 applies the algebraic iterative reconstruction techniques to data from discharge #35336 at ASDEX Upgrade. Section 7 presents the computation speed and optimization framework in terms of quality and computation time for the fast algorithms. Section 8 discusses the results and concludes.

8.2 FILDSIM

In a scintillator-based FILD, ions pass through a pinhole in the probe head of the FILD equipped with a 3D collimator. The probe head is placed close to the plasma, in the far scrape-off layer. After passing through the pinhole, the collimated ions impact on a scintillator plate, where the scintillating material emits photons subsequently captured by a camera setup. The spatial locations on the scintillator plate of the emitted photons can be converted to velocity-space coordinates through FILDSIM modelling. This will be briefly described in the following. See Fig. 8.1 for an illustration of the working principle for the FILD installed at TCV.

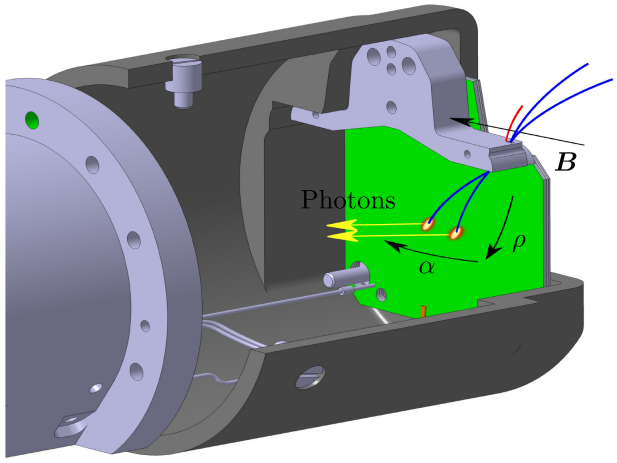

Figure 8.1: The blue trajectories illustrate collimated lost fast ions passing through the FILD pinhole and hitting a plate coated with a scintillating material (green). Photons (yellow) are emitted at the impact locations. The red trajectory of a lost fast ion impacts the collimator and does not pass through the pinhole. From Poley-Sanjuan et al. (2023).

A FILD measurement is a smeared representation of the lost fast-ion velocity-space distribution function of the ions passing through the pinhole. The sought velocity distribution is that of the ions passing through the pinhole, to be denoted "pinhole velocity space". The measured velocity space will be denoted "scintillator velocity space".

The pinhole and scintillator velocity-space distribution functions can be modelled using FILDSIM. FILDSIM simulates ion trajectories through a FILD's pinhole and detects collisions with 3D elements of the FILD detector. The ion trajectories are assumed to be helical since assuming a constant local magnetic field is a reasonable approximation. For example, in tokamaks such as ASDEX Upgrade, the magnetic field variation is less than 1% across the FILD probe head. Consequently, it is unnecessary to solve the Lorentz equation of motion to obtain the ion trajectories, and the analytical solution for ion orbits in a constant magnetic field is used. FILDSIM initializes N ions with fixed gyroradius ρ and pitch angle α with random positions in the FILD pinhole and random gyrophases in the interval $[0, 2\pi]$. Only the few ions within the gyrophase acceptance cone passes through the collimator. The number of ions N is chosen to be large enough to achieve good statistics.

Typically, the gyroradius and pitch angle are used as velocity-space variables for FILD measurements. The velocity-space distribution function as a function of $v_\parallel$ and $v_\perp$ can then be calculated from the relations

$$v_\perp = \Omega\rho, \tag{8.3}$$

$$v_\parallel = \frac{\lambda}{\sqrt{1-\lambda^2}}\, v_\perp, \tag{8.4}$$

where Ω is the ion cyclotron frequency, and $\lambda = v_\parallel / v$ is the pitch. The perpendicular energy can also be used instead of the gyroradius, since

$$E_\perp = \frac{1}{2} m \frac{\Omega^2 \rho^2}{1-\lambda^2}. \tag{8.5}$$

The gyroradius and pitch angle variables are used to describe velocity-space distribution functions

from ASDEX Upgrade, and energy and pitch are used for the same functions at TCV.

The random initial location of a lost fast ion in the FILD pinhole and its random initial gyrophase result in a distribution of impact locations for ions initialized with the same gyroradius and pitch angle (or energy and pitch). It is possible to identify all possible locations on the scintillator plate that ions with a specific gyroradius and pitch angle can hit by modelling a sufficiently large number of ions and collecting their impact locations on the scintillator plate. The centroid of the resulting distribution is used as the location on the scintillator corresponding to that exact gyroradius and pitch angle. Repeating such modelling for all gyroradii and pitch angles under consideration produces a strike map. The strike map for a specific FILD, its vessel location, and the plasma conditions is then used to map spatial locations on the FILD to scintillator velocity space.

The FILD signal s measured in the gyroradius range $[\rho_1, \rho_2]$ and pitch angle range $[\alpha_1, \alpha_2]$, with the ranges determined by the spatial resolution of the FILD camera, can be modelled as the integral equation

$$s(\rho_1, \rho_2, \alpha_1, \alpha_2) = \int_0^{\pi} \int_0^{\infty} w\left(\rho_1, \rho_2, \alpha_1, \alpha_2, \alpha_\mathrm{p}, \rho_\mathrm{p}\right) f(\alpha_\mathrm{p}, \rho_\mathrm{p})\, \mathrm{d}\rho_\mathrm{p}\, \mathrm{d}\alpha_\mathrm{p}, \tag{8.6}$$

where $(\alpha_\mathrm{p}, \rho_\mathrm{p})$ are the velocity-space coordinates of the pinhole, w is a weight function, and f is the velocity-space distribution function of the ions passing through the pinhole. Scintillator velocity-space coordinates will be written without a subscript, and pinhole velocity-space coordinates with a subscript 'p'. Weight functions have units of [photons per ion] and indicate if an ion at a given location in pinhole velocity space can produce a signal at a given location in scintillator velocity space. The units of f are [ions rad^{-1} m^{-1}], and s is measured in photons.

With a suitable discretization of the gyroradius and pitch angle, the integral equation (8.6) can be transformed to the matrix-vector equation

$$Wf = s. \tag{8.7}$$

Thus, having a FILD measurement s and the FILDSIM-modelled weight function matrix W, it is possible to obtain f by solving the inverse problem in Eq. (8.7).

8.3 FILDSIM model improvements

As described above, the specific location of the ion in the pinhole and its gyrophase result in a distribution of impact locations on the scintillator of ions with the same gyroradius and pitch angle and hence also a distribution of locations in velocity space. FILDSIM outputs these distributions in gyroradius (or energy) and pitch angle (or pitch). See Figs. 8.2 and 8.3 for examples for FILD1 at ASDEX Upgrade and the FILD at TCV. Distributions for the specific pitch angle $\alpha = 60°$ and different gyroradii overlap. The overlap increases with increasing gyroradius. As illustrated in Fig. 8.2(a), ions with a gyroradius of 5-7 cm can impact the scintillator at the same location as ions with a gyroradius of 4 cm. The distributions in pitch angle for a specific gyroradius for FILD1 at ASDEX Upgrade are better separated as illustrated in Fig. 8.3(a). The overlap is more extreme in both energy and pitch for the FILD at TCV; see Figs. 8.2(b) and 8.3(b).

These simulations show that the blurred scintillator velocity-space distribution function is not generated by ions at the same locations in pinhole velocity space due to the different ion locations and gyroangles. With knowledge of the discharge conditions, it is possible to guesstimate the locations in pinhole velocity space of the lost ions when interpreting FILD measurements. For example, during a discharge with NBI aroud 30 keV, measurements at 30 and 15 keV are expected as prompt losses from the first and half energy components. However, this remains a guess, and a

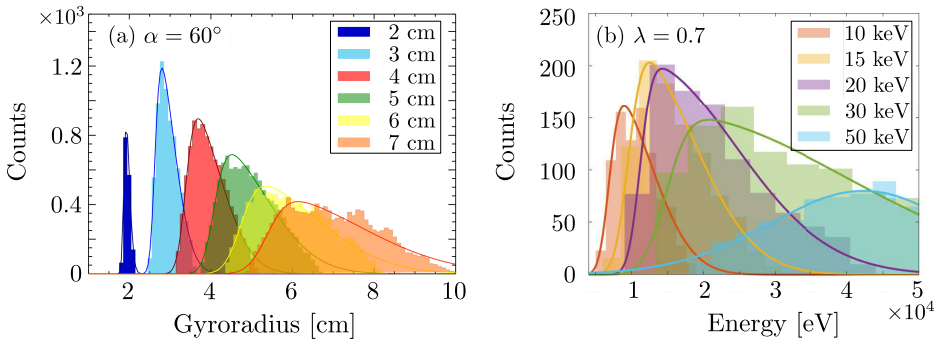

Figure 8.2: FILDSIM gyroradius distributions for N markers initiated at the pinhole with different gyroradii (energy) for (a) FILD1 at AUG and (b) the FILD at TCV. From Galdon-Quíroga *et al.* (2018c) and Stipani (2021).

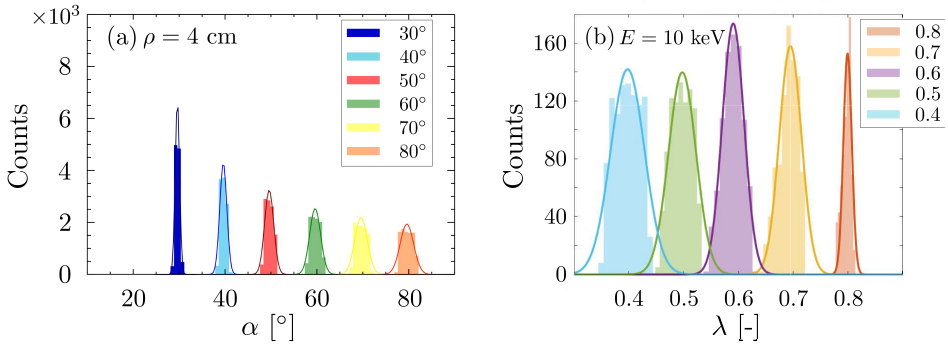

Figure 8.3: FILDSIM pitch angle distributions for N markers initiated at the pinhole with diferrent pitch angles for (a) FILD1 at AUG and (b) the FILD at TCV. From Galdon-Quíroga *et al.* (2018c) and Stipani (2021).

much more reliable inference can be made by computing the pinhole velocity space by solving the inverse problem in Eq. (8.7). This also assumes that the mechanisms resulting in the lost fast ions are known or can be guessed, which might not be the case.

The centroids of the simulated distributions are used to indicate the location on the scintillator corresponding to a specific value in pinhole velocity space. Current FILDSIM modelling uses a skew-Gaussian distribution to fit the distributions in gyroradius and a Gaussian for the pitch angle, i.e.,

$$f_\rho(\rho, \rho_0) = \frac{1}{\sqrt{2\pi}\sigma_\rho} \exp\left[-\frac{(\rho_0 - \rho)^2}{2\sigma_\rho^2}\right]\left[1 + \mathrm{erf}\left(\beta_\rho \frac{\rho_0 - \rho}{\sqrt{2}\sigma_\rho}\right)\right], \tag{8.8}$$

$$f_\alpha(\alpha, \alpha_0) = \frac{1}{\sqrt{2\pi}\sigma_\alpha} \exp\left[-\frac{(\alpha_0 - \alpha)^2}{2\sigma_\alpha^2}\right], \tag{8.9}$$

where ρ_0 and α_0 are the initialized parameter values of the fast ions in the pinhole. The combined

model therefore becomes

$$\begin{aligned} f(\rho, \alpha, \rho_0, \alpha_0) &= f_\rho(\rho) f_\alpha(\alpha) \\ &= \frac{f_{\text{col}}}{2\pi\sigma_\alpha\sigma_\rho} \exp\left(-\frac{(\alpha_0-\alpha)^2}{2\sigma_\alpha^2} - \frac{(\rho_0-\rho)^2}{2\sigma_\rho^2}\right) \\ &\times \left(1 + \operatorname{erf}\left(\beta_\rho \frac{\rho_0-\rho}{\sqrt{2}\sigma_\rho}\right)\right), \end{aligned} \tag{8.10}$$

where $f_{\text{col}} = N_s/N_p$ is the collimator factor giving the number of ions impacting the scintillator N_s divided by the number of ions initialized at the pinhole N_p. The full model for a weight function is a product of the above distribution and a yield function describing the number of photons emitted as a function of the energy of the impacting ion.

The parameters ρ_0 and α_0 are the centroids of the distributions, and σ_ρ and σ_α control the width of the distribution. The function 'erf' is the error function that, when multiplied with a Gaussian distribution, produces a skew-Gaussian distribution, with β_ρ controlling the skewness of the distribution. When computing the weight functions, these parameters are estimated from the lost fast-ion trajectory simulations.

8.3.1 Skewness and kurtosis

The distributions described above have some insufficiencies when modelling the impact distributions in the velocity space of the ions initialized in the pinhole. For the gyroradius distributions, there is a gap in the upper tail between the model and the true ion counts, indicating an overestimation of the fit at higher gyroradii and energies; see Fig. 8.2. The gap increases with increasing gyroradius and energy. For the pitch angle distributions, the tails of the Gaussians severely overestimate the true width of the simulated distributions; see Fig. 8.3. Furthermore, the Gaussians are too narrow at the top of the distribution. As we now show, other distributions can model the gyroradius and pitch angle distributions more precisely. Modifying the FILDSIM model to these distributions increases the accuracy of the FILD weight functions, improving the accuracy of the tomographic reconstructions of pinhole velocity-space distribution functions.

Distributions are typically characterized in terms of their mean μ and the standard deviation σ, i.e., the zeroth and first moment. It is possible further to characterize them by their third and fourth moments called the *skewness* and *kurtosis*. For univariate data, the skewness s and kurtosis k is given by[1]

$$s = \frac{\mathbb{E}\left[(x-\mu)^3\right]}{\sigma^3}, \tag{8.11a}$$

$$k = \frac{\mathbb{E}\left[(x-\mu)^4\right]}{\sigma^4}. \tag{8.11b}$$

Skewness is a measure of the lack of symmetry in the distribution, and kurtosis is a measure of how much data is in the tails of the distribution. Distributions with heavier tails have a larger value of kurtosis.

Thus, desirable modifications to the current FILDSIM model in gyroradius is the same skewness and slightly less kurtosis. For the pitch angle distributions, the improved model needs a skewness of zero and significantly less kurtosis. Possible distributions for the gyroradius include a raised cosine distribution f, a Cauchy distribution g, and a logistic distribution h, described by

[1] "Measures of Skewness and Kurtosis" in *NIST/SEMATECH e-Handbook of Statistical Methods*.

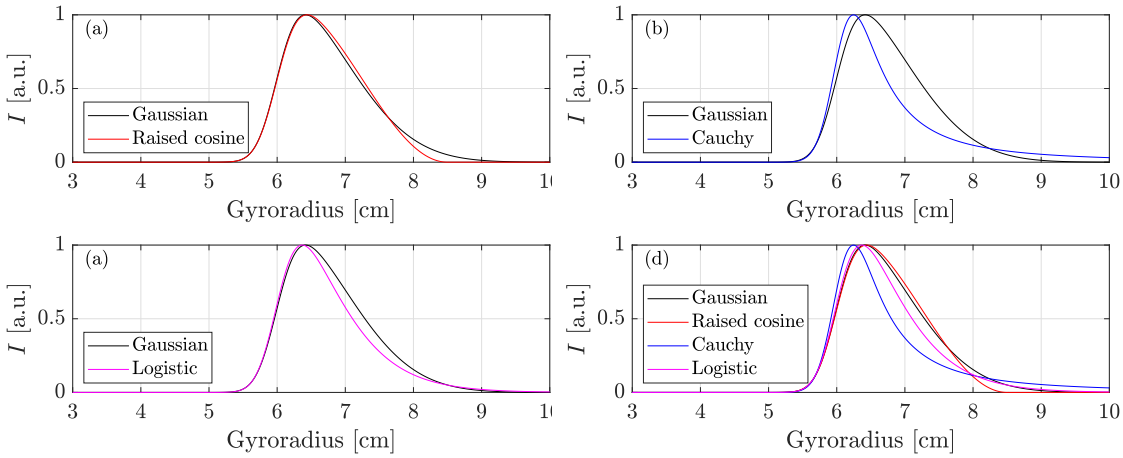

Figure 8.4: The (a) raised cosine, (b) Cauchy, and (c) logistic distribution functions plotted with a skew-Gaussian distribution function. Subfigure (d) shows the distribution functions in the same plot. Observe that the raised cosine distribution function has the shortest upper tail of the four distributions.

the probability density functions

$$f(x;\mu,\sigma) = \frac{1}{2\sigma}\left[1+\cos\left(\frac{x-\mu}{\sigma}\pi\right)\right] \tag{8.12}$$

$$g(x;\mu,\gamma) = \frac{1}{\pi\gamma}\frac{1}{1+\left(\frac{x-\mu}{\gamma}\right)^2}, \tag{8.13}$$

$$h(x;\mu,\sigma) = \frac{\exp\left(-\frac{x-\mu}{\sigma}\right)}{\sigma\left(1+\exp\left(-\frac{x-\mu}{\sigma}\right)\right)^2}, \tag{8.14}$$

where $f(x;\mu,\sigma)$ is supported on $[\mu-\sigma,\mu+\sigma]$, and γ is the half width at half-maximum of the Cauchy distribution. See Fig. 8.4 for an illustration of the three distributions. The distributions are all multiplied by the skewness parameter function

$$\Phi(x;\mu,\sigma) = 1+\operatorname{erf}\left(\beta_s\frac{x-\mu}{\sqrt{2}\sigma}\right) \tag{8.15}$$

to model the skewness as seen in the output from the FILDSIM simulations, as was done for the Gaussian distribution in Eq. (8.8).

Numerical testing shows the best fit to the FILDSIM simulated distributions to be the raised cosine distribution. The skewness and kurtosis of the distributions are displayed in Table 8.1. As desired, the raised cosine has the same skewness as the skew-Gaussian and slightly smaller kurtosis.

A suitable probability distribution function modelling the pitch angle distributions is Wigner's semicircle

$$W(\alpha) = \frac{2}{\pi R^2}\sqrt{R^2-\alpha^2} \tag{8.16}$$

for pitch angles satisfying $-R \le \alpha \le R$, and $W(\alpha) = 0$ if $\alpha > R$. This function has the desirable qualities required to properly model the pitch angle distributions: short tails and a greater width near the top of the distribution.

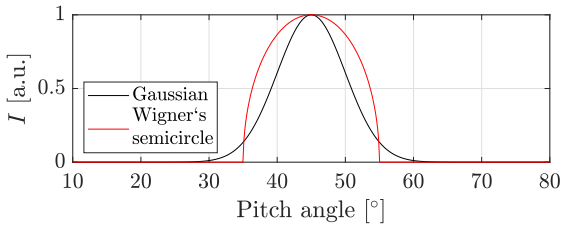

Figure 8.5: Wigner's semicircle distribution function with a Gaussian distribution function. Note the significantly greater FWHM and the shorter tails of Wigner's semicircle.

Table 8.1: Values of skewness and kurtosis for the improved gyroradius and pitch angle models for the 1D models displayed in Figs. 8.4 and 8.5.

	Gyroradius		Pitch angle	
	Skew-Gaussian	Raised cosine	Gaussian	Wigner's semicircle
s	1.8	1.8	0	0
k	4.8	4.7	4.1	2.6

8.4 TCV implementation

We have implemented the improved FILDSIM models as detailed in the previous subsection in FILDSIM at TCV. The 1D distributions in gyroradius and pitch resulting from the skew-Gaussian/Gaussian model and the skew raised cosine/Wigner's semicircle model are illustrated in Fig. 8.6. From here on, we will refer to these models as the 'standard Gaussian model', abbreviated as SGM, and the 'raised cosine model', abbreviated as RCM, respectively. The fit of the raised cosine model for the 1D distributions is significantly better than the fit made using the standard Gaussian models. The gap at the upper tails is no longer apparent for the gyroradius distributions, ensuring improved resolution in gyroradius. Similarly, the tails of the Gaussian distributions for the pitch distributions are completely removed, ensuring improved resolution in pitch. In the following, we consider the standard Gaussian model and the raised cosine model weight functions and their role in computing tomographic reconstructions of FILD measurements.

8.4.1 Weight functions

An ion initialized at a specific location (α, ρ) in velocity space can be modelled as a delta function $f = \delta(\alpha, \rho)$. Computing all possible impact locations from ions at this location in velocity space produces a strike map. With strike maps of all positions in pinhole velocity space, it is possible to compute which positions in pinhole velocity space can impact a given position in scintillator velocity space. This is a weight function. To each location in scintillator velocity space corresponds a weight function indicating the pinhole velocity-space locations able to impact the scintillator at that specific location. Weight functions have units [photons per ion]. Thus, the weight function shows the sensitivity in pinhole velocity space for a given measurement on the scintillator: how many photons an ion at a given position in pinhole velocity space can produce at a given position on the scintillator.

In the following, we investigate the standard Gaussian model and the raised cosine model weight functions resulting from the improved FILDSIM model for the FILD installed at TCV. In

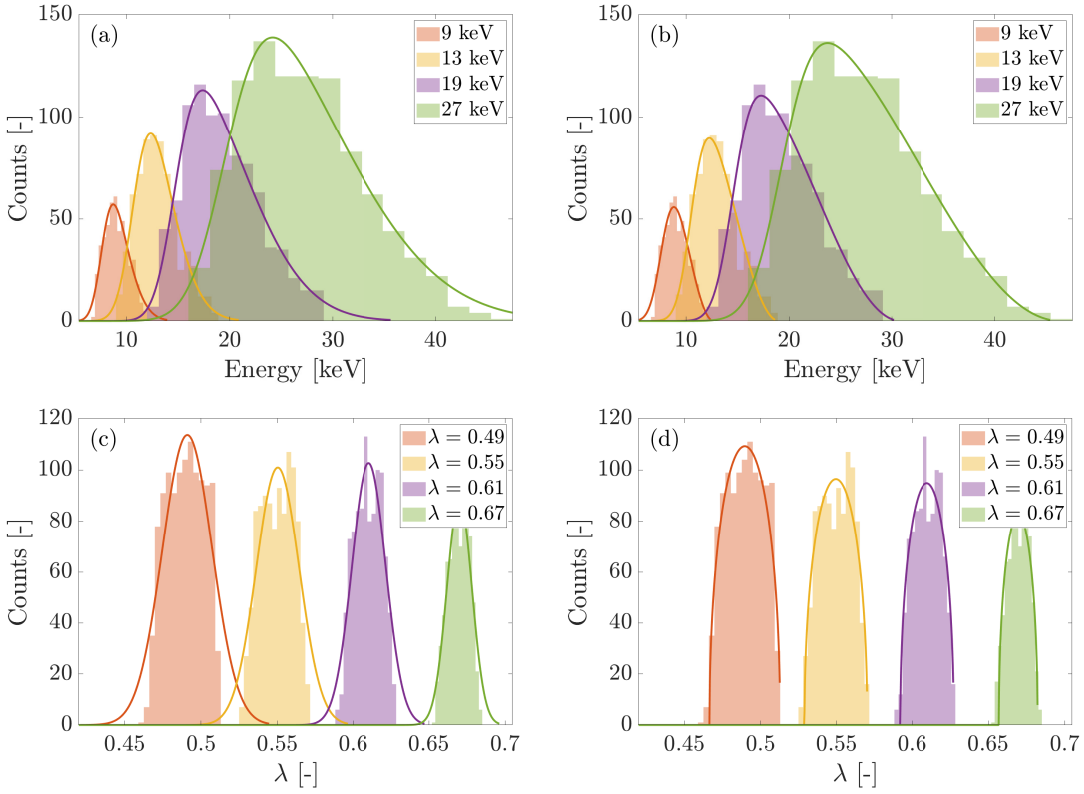

Figure 8.6: (a) The standard Gaussian model and (b) the raised cosine model for the 1D gyroradius distributions implemented at TCV for $\lambda = 0.6$. (c) The standard Gaussian model and (d) the raised cosine model for the 1D pitch distributions implemented at TCV for $E = 25$ keV.

particular, we consider the weight function corresponding to the scintillator velocity-space location $\rho = 25$ keV and $\lambda = 0.59$. The true weight function as simulated by FILDSIM is illustrated in Fig. 8.7(a), the standard Gaussian model weight function in 8.7(b), and the raised cosine model weight function in 8.7(c). The new weight function is much more accurate in both pitch and energy; the cut-off in pitch is now as sharp as the simulated weight function, and the upper and lower tails resemble the tails of the simulated weight function.

The precision of the model can be quantified and illustrated by considering the residual weight function w_R calculated as

$$w_R = w_{\text{sim}} - w_{\text{model}}, \tag{8.17}$$

where w_{sim} is the simulated weight function and W_{model} the weight function modelled using the standard Gaussian model or the raised cosine model. The residual weight functions are denoted by a lowercase w to avoid risking confusing them with the weight function matrix W.

The residual weight function matrix for the standard Gaussian model $w_{R,\text{SGM}}$ is illustrated in Fig. 8.7(d) and for the raised cosine model in Fig. 8.7(e). The erroneous larger width in pitch and the long tails in the standard Gaussian model are evident. To further characterize the deviation from the simulated weight function, the absolute error

$$E_{\text{A},k} \equiv \sum_i \sum_j |w_{R,k}| \tag{8.18}$$

can be computed for each residual matrix $w_{R,\mathrm{SGM}}$ and $w_{R,\mathrm{RCM}}$, where the sum runs over the rows i and columns j, and k indicates either the standard Gaussian model or the raised cosine model. The result is

$$E_{A,\mathrm{SGM}} = 186, \tag{8.19}$$

$$E_{A,\mathrm{RCM}} = 95. \tag{8.20}$$

According to this measure, the raised cosine model is a 49% improvement over the standard Gaussian model.

Some features in the simulated weight function are not captured by the raised cosine model. The highest intensity of the simulated weight function occurs at $\lambda = 0.59$ and $E = 25$ keV, but this is not the center of the weight function. Instead, the parts of pinhole velocity space able to impact at this location in scintillator velocity space occur predominantly for ions with smaller pitch values. Thus, it seems that the distribution is skewed towards lower pitch values. This asymmetry is the feature that creates most of the deviation in $w_{R,\mathrm{RCM}}$ as illustrated in Fig. 8.7(e).

8.4.2 Tomographic reconstruction comparison

With a FILD measurement s and the FILDSIM-modelled weight function matrix W, it is possible to compute f by solving the inverse problem in Eq. (8.7). Since the problem is ill-posed, regularization is required to produce a meaningful solution. Tikhonov regularization is typically used to regularize the problem in velocity-space tomography. For the inverse problem in Eq. (8.7), the solution found using Tikhonov regularization can be written as

$$f^* = \underset{f}{\operatorname{argmin}} \|Wf - s\|_2^2 + \lambda \|Lf\|_2^2, \tag{8.21}$$

where L is the regularization matrix promoting desired properties in the solution, and λ is the regularization parameter. The value of the regularization parameter determines the emphasis on the operator penalty and the emphasis on fitting the data. The choice of the numerical value of the regularization parameter is, therefore, crucial, as the accuracy, reliability, and interpretability of the solution are affected by it.

8.4.3 Reconstructions of synthetic FILD measurements

We investigate the effects of the improved weight functions in the tomographic reconstructions for synthetic and experimental data. An example of a synthetic pinhole velocity-space distribution function is shown in Fig. 8.8(a). The corresponding scintillator measurement according to the standard Gaussian model is illustrated in Fig. 8.8(b) and according to the raised cosine model in Fig. 8.8(c). The raised cosine model produces measurements that are much more like actual measurements: the width in pitch seen in the standard Gaussian model is not seen in experiments and is not prevalent in the synthetic measurements of the raised cosine model, and the long tail in energy is also not seen in experiments. The tomographic reconstructions using the standard Gaussian model and the raised cosine model are shown in Fig. 8.8(d) and 8.8(e), respectively. Both reconstructions are excepted to be good since the same model was used to generate the data, so this particular example does not show much improvement in the tomographic reconstructions using the standard Gaussian model or the raised cosine model.

Since the tomographic reconstructions were computed for synthetic data, it is important to note that no inverse crime were committed when computing them. If the same grid is used to compute the tomographic reconstruction as was used to generate the synthetic measurements, the problem becomes artificially easy for the computer algorithm to solve. Thus, we note here that

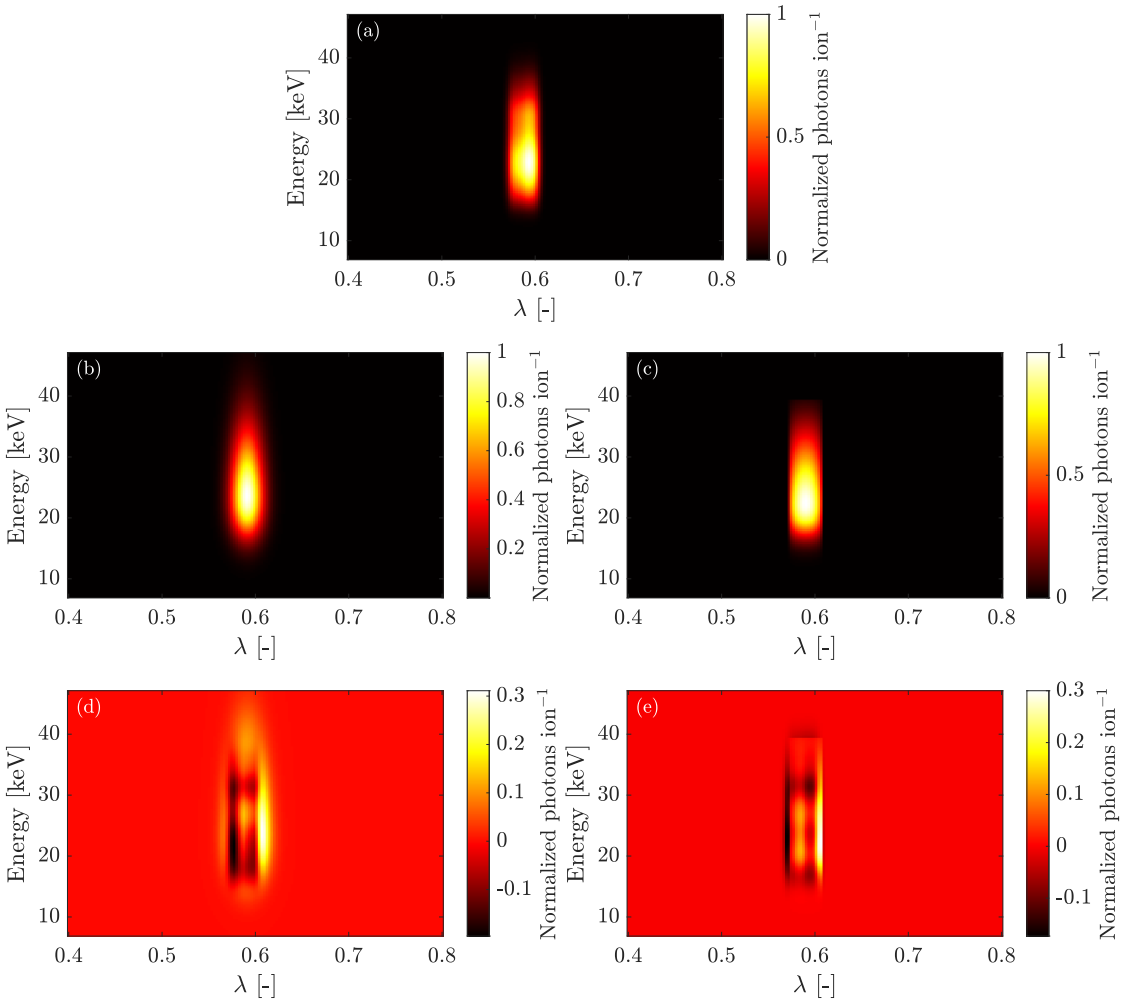

Figure 8.7: (a) FILDSIM simulation of the weight function at $\rho = 25$ keV and $\lambda = 0.59$. Subfigures (b) and (c) illustrate the standard Gaussian model and the raised cosine model weight functions obtained using the modelling described in the previous sections. Subfigures (d) and (e) illustrate the residual weight functions $w_{R,\mathrm{SGM}}$ and $w_{R,\mathrm{RCM}}$ corresponding to the difference between the simulated weight function and the model-fitted weight functions.

the forward grid size used to generate the synthetic measurements was $[150, 150]$ in energy and pitch, and the inversion grid size was $[100, 100]$.

8.4.4 Reconstructions of experimental FILD measurements: discharge #75620

Next, we compute tomographic reconstructions using the standard Gaussian model and the raised cosine model weight functions on experimental FILD measurements from the TCV FILD. We consider the FILD measurement at $t = 1.005$ s during discharge #75620 illustrated in Fig. 8.9. The illustration in Fig. 8.9(a) shows the FILD measurement in (x, y)-coordinates before mapping it to velocity space. The raised cosine strike map is overlaid in white. The scintillator velocity space is shown in Fig. 8.9(b). This is the signal to invert.

The reconstruction results are shown in Fig. 8.10. To investigate the behaviour of the reconstructions, reconstructions of what is thought to be underregulatization, a good reconstruction, and overregularization are computed. The good reconstruction using the standard Gaussian model identifies a large (~ 8) number of isolated locations in pinhole velocity space, whereas the good reconstruction using the raised cosine model contains around 4 isolated locations in pinhole velocity space and is more smooth. This is surprising since the raised cosine model provides clearer distinctions between both gyroradius and pitch distributions.

To compare and interpret the tomographic reconstructions, we ran an ASCOT simulation for the discharge conditions at $t = 1.005$ s to obtain the velocity space of the lost fast ions at the FILD probe head. The simulation was run as a full orbit simulation with Coulomb collisions and a 5 ms simulation duration. The result is shown in Fig. 8.11(a). Some features seen in the reconstructions are in the pinhole velocity-space distribution function produced by ASCOT, and some are not. First, observe the smoothness of the ASCOT simulation, indicating that the smoothness of the raised cosine model is preferable to the standard Gaussian model. Second, high intensities are found at energies around 13-14 keV and pitch around 0.7 in both the reconstructions and the ASCOT simulation and at energies of 11-12 keV and 0.58 pitch. The faint circular populated area in the reconstruction using the raised cosine model is also in the ASCOT simulation. The most intense location in the ASCOT simulation at 27 keV and 0.7 pitch is not in the reconstructions. The ions from the NBI are injected with energies of 27 keV, which is likely the reason for the high-intensity area in the ASCOT simulation. They were not measured by the FILD, however.

The FILD measurement corresponding to the ASCOT simulation can be computed from the forward model $Wf = s$. The result using the standard Gaussian model is shown in Fig. 8.11(b) and using the raised cosine model in Fig. 8.11(c). The differences in the two forward models are reflected in a more narrow measurement with energies extending to around 38 keV in the raised cosine model compared to the standard Gaussian model. These aspects are closer to the actual scintillator measurement shown in Fig. 8.9(b). This indicates that the raised cosine model is favourable to the standard Gaussian model.

8.4.5 TCV FILD characterization: gross strike map and gross weight function

The FILDSIM model improvements refine the characterization of FILDs by improving the precision of the computation of the gross strike map and gross weight function. Letting $f = \delta(\alpha, \rho)$ ions keV^{-1} in Eq. (8.6) produces a strike map. A gross strike map showing where, on average, ions will strike the scintillator, can be computed by setting $f = 1$ ions keV^{-1}. The interpretation is as follows: "Initializing the same amount of ions at all locations in pinhole velocity space, where are the ions most likely to impact the scintillator?" The answer is given by the gross strike map,

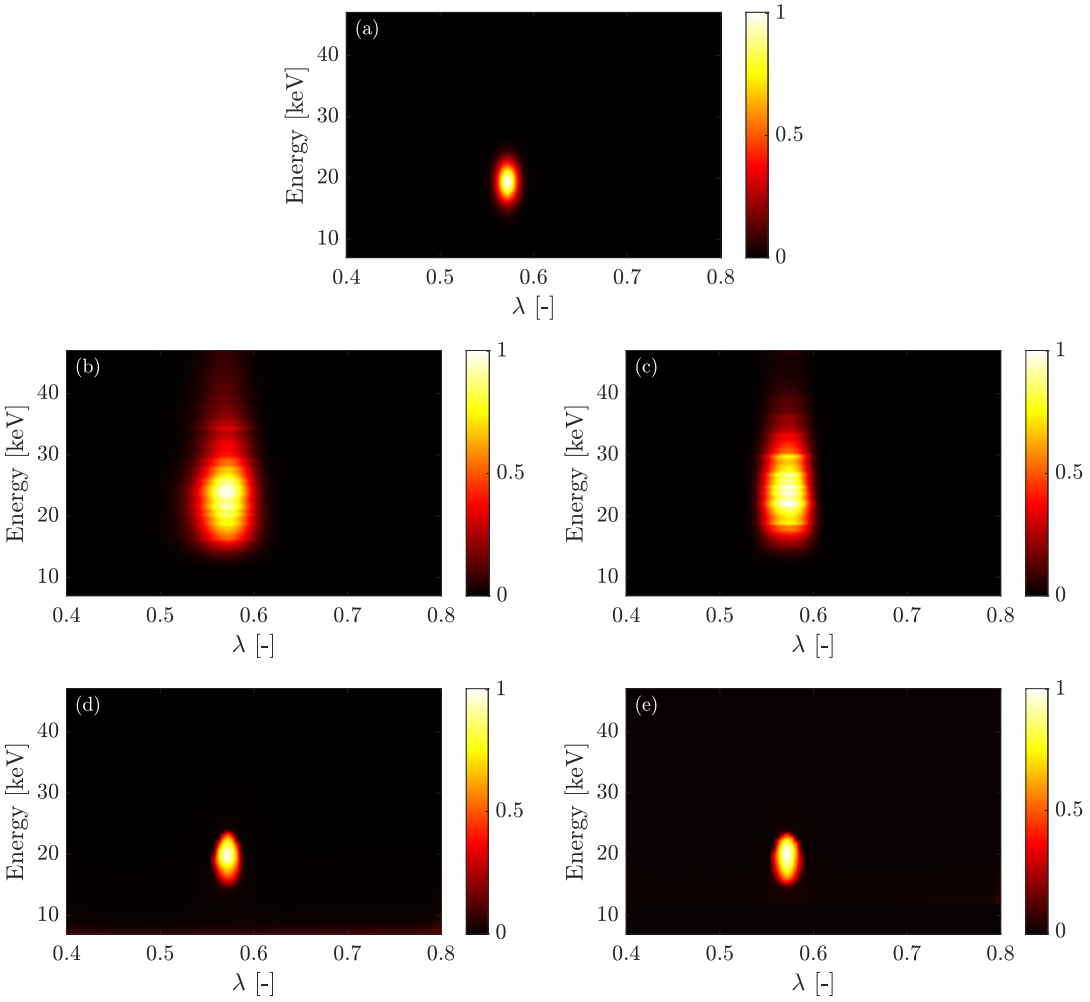

Figure 8.8: (a) Example synthetic pinhole velocity-space distribution function. The corresponding scintillator measurement generated using (b) the standard Gaussian model weight functions and (c) the raised cosine model weight functions. The tomographic reconstruction computed using (d) the standard Gaussian model weight functions and (e) the raised cosine model weight functions.

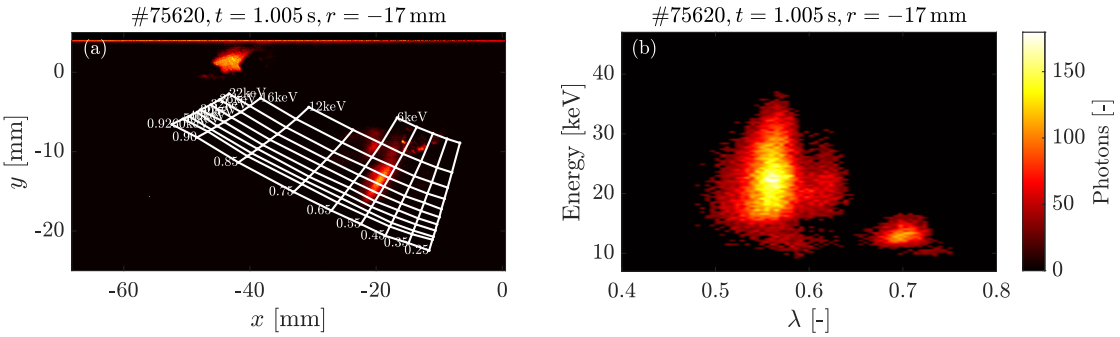

Figure 8.9: (a) The FILD measurement in (x, y)-coordinates with the FILDSIM-modelled strike map overlaid computed using the raised cosine model for discharge #75620 at $t = 1.005$ s at a radial distance of $r = -17$ mm from the plasma. (b) Scintillator velocity space mapped from the FILD measurement.

which is determined by the FILD geometry, the characteristics of the machine, and the location of the detector.

A weight function for a specific scintillator velocity-space location shows which parts of pinhole velocity space can impact the scintillator at this scintillator velocity-space location. The intensity of the weight function indicates the number of photons each position in pinhole velocity space produces at that measurement position. Summing all weight functions produces a gross weight function. The gross weight function shows the average number of photons generated per ion in pinhole velocity space. Again, this number is unique to a specific FILD depending on the FILD geometry, the characteristics of the machine, and the location of the detector.

Since these constructions depend on the weight functions and hence on the FILDSIM modelling, the two characterizations of a FILD using the standard Gaussian model and the raised cosine model are different. Here, we highlight the differences in the gross strike map and the gross weight function between the two models for the TCV FILD. The gross strike map and and the gross weight function of the TCV FILD are illustrated in Fig. 8.12 computed using the standard Gaussian model and the raised cosine model. The gross strike maps are shown in the first column, and the gross weight functions in the second column.

According to the gross strike map of the standard Gaussian model, the most impacts on the scintillator occur at 45 keV and 0.45 pitch. According to the gross strike map of the raised cosine model, the most impacts on the scintillator occur at 38 keV and 0.73 pitch. The reduction in energy occurs since the overestimation of the upper tails of the gyroradius distributions with the standard Gaussian model is corrected with the raised cosine model. Furthermore, the standard Gaussian model makes a worse overestimation of the tails of the pitch distributions for low values of the pitch compared to larger values of pitch; see Fig. 8.6. This correction decreases the number of impacts that occur at lower pitch values in the strike map, so the relative value of larger pitch values increases.

According to the gross weight function of the standard Gaussian model, ions at 35 keV and 0.45 pitch generate the most photons by a significant margin. On the other hand, according to the gross weight function of the raised cosine model, the number of photons generated per ion is close to independent of the pitch and occurs for energies around 30-35 keV, with a slight increase from low to high pitch. The number of photons emitted by ions at energies above 35 keV is also significantly reduced in the raised cosine model compared to the standard Gaussian model.

The increase in intensity from lower to higher energies in both the gross strike map and the

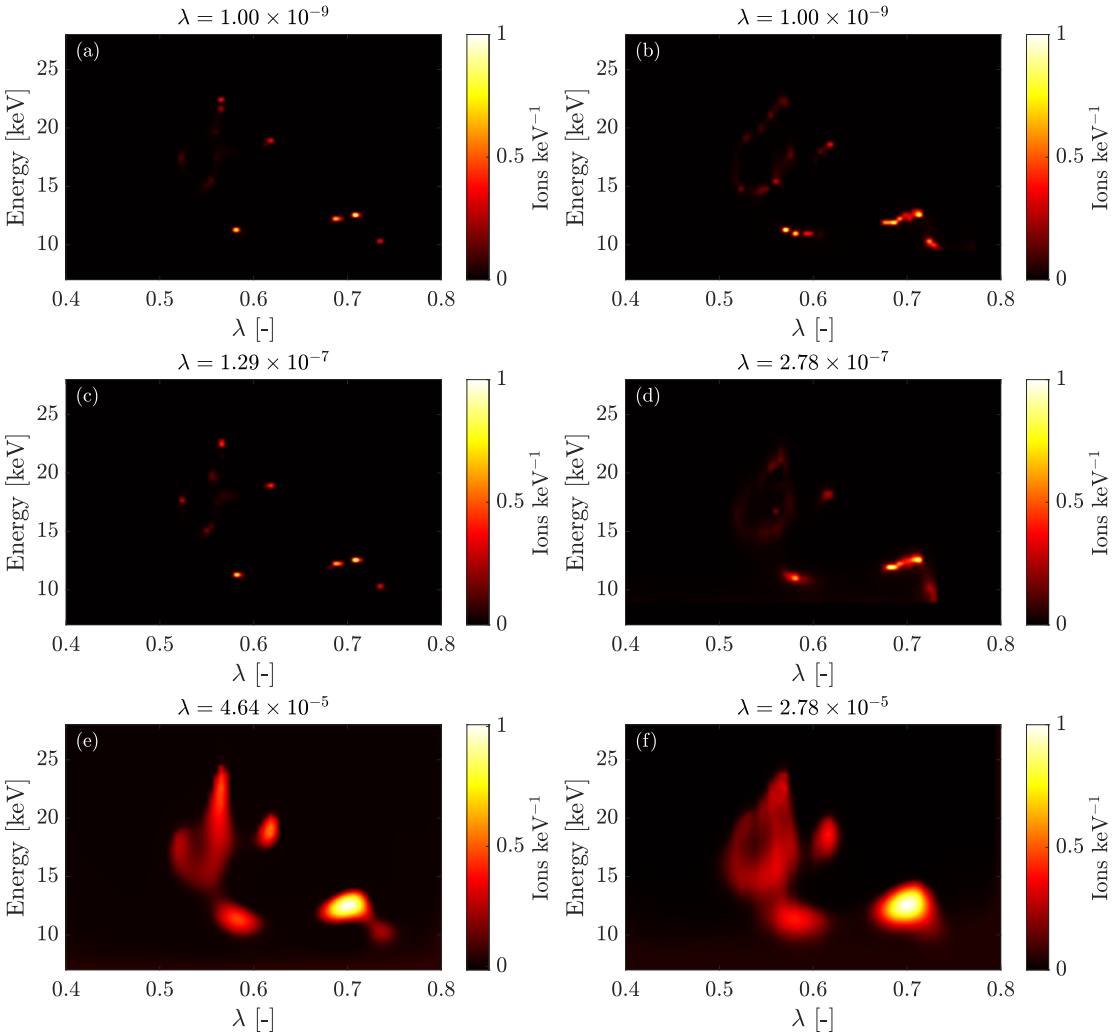

Figure 8.10: Tomographic reconstructions of the FILD measurement at $t = 1.005$ s during discharge #75620 computed using the standard Gaussian model in the left column and the raised cosine model in the right column. The reconstructions are computed using the values of the regularization parameter indicated above each figure. The chosen values correspond to underregularization (top row), a good reconstruction (middle row), and overregularization (bottom row).

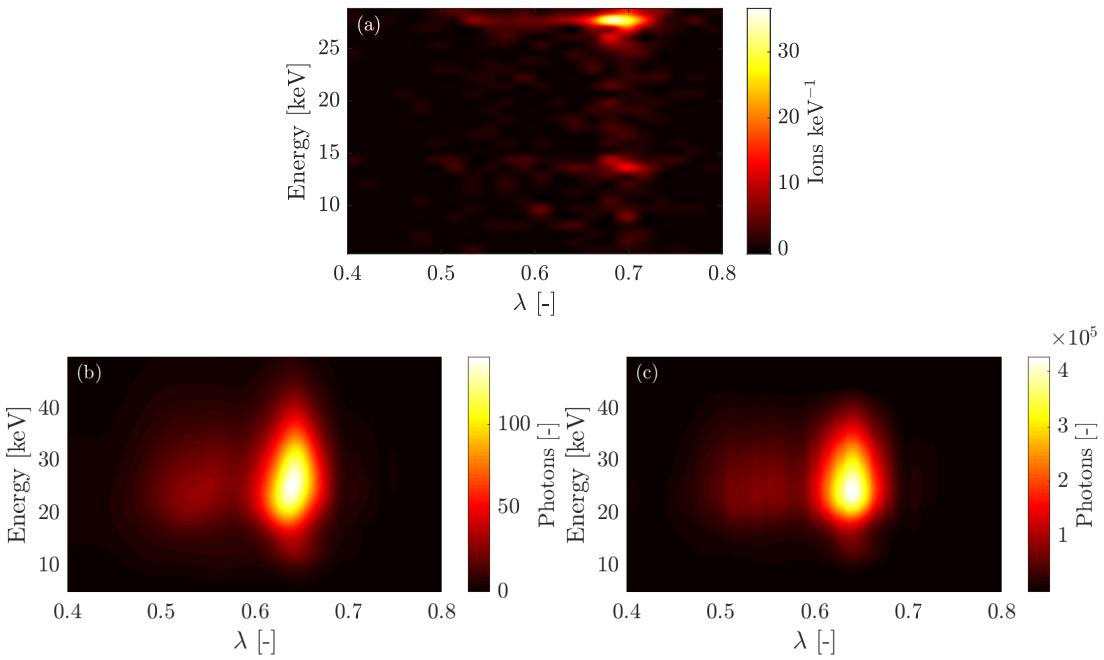

Figure 8.11: (a) ASCOT simulated pinhole velocity space for discharge #75620 at $t = 1.005$ s. See the main text for further details of the simulation. (b) Scintillator velocity space computed using the forward model $Wf = s$ using the standard Gaussian model weight functions. (c) Scintillator velocity space computed using the raised cosine model weight functions.

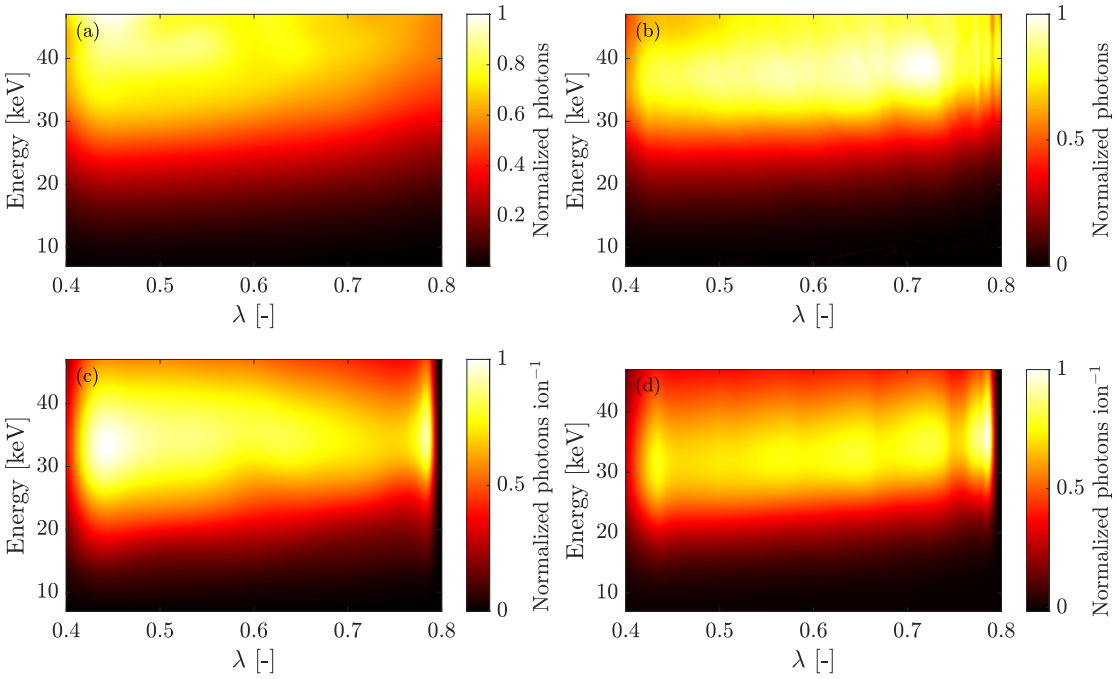

Figure 8.12: For the TCV FILD: (a) The gross strike map using the standard Gaussian model and (b) using the raised cosine model. (c) The gross weight function using the standard Gaussian model and (d) using the raised cosine FILDSIM model.

gross weight function is expected in both models since the number of ions passing through the collimator increases with the energy, see Fig. 8.6.

8.5 Tomographic reconstructions using algebraic iterative reconstruction techniques

The pinhole velocity-space distribution function is obtained by solving the inverse problem in Eq. (8.7). This problem is ill-posed, meaning noise in the measurement can produce large, unphysical values in the reconstruction. Thus, regularization is needed to stabilize the problem. Previously, zeroth and first order Tikhonov regularization has been applied to obtain tomographic reconstructions of pinhole velocity-space distribution functions. Using Tikhonov regularization, the solution f^* is found by solving

$$f^* = \underset{f}{\operatorname{argmin}} \|Wf - s\|^2 + \lambda \|Lf\|^2, \tag{8.22}$$

where W is the weight function matrix, s the data vector, L is a linear operator that promotes desired properties in the solution, such as smoothness by penalizing gradients, and λ is the regularization parameter.

The regularization parameter determines the trade-off between the goodness-of-fit ($Wf \approx s$) and imposing the constraint (Lf) on the solution. For an operator L imposing smoothness, a larger value of λ results in a smoother solution, while a smaller value fits the data better at

the expense of the smoothness of the solution. Thus, the value of the regularization parameter significantly impacts the recovered solution, and determining the value of the regularization parameter producing the solution closest to the ground truth when reconstructing velocity-space distribution functions from experimental data becomes crucial.

Determining the optimal value of the regularization parameter is challenging, and the choice is typically made based on intuition: different reconstructions are computed, and the one thought to be most correct by the user is chosen. To avoid the arbitrary choice made by selecting the regularization parameter based on intuition, several methods have been proposed for selecting the optimal value of the regularization parameter, including the discrepancy principle, the L-curve, and generalized cross-validation[2]. However, these methods rarely give the same value of the regularization parameter since the methods emphasize different aspects of the solution. Thus, there is no consistent way of obtaining optimal results for experimental data.

Recent results indicate the applicability of algebraic iterative reconstruction techniques (ART) for reconstructions of FILD data[3]. Typically, ARTs exhibit *semi-convergence*, where the optimal reconstruction is found for a specific iteration number k^*. Reconstructions stopping at iteration numbers $k < k^*$ do not fit the data optimally, and reconstructions stopping at larger iteration numbers $k > k^*$ overfit the noise in the data. However, for FILD data, the optimal reconstruction f^* is approached asymptotically as $k \to \infty$, where additional iterations keep improving the reconstruction by a smaller and smaller margin. Thus, optimal reconstructions can be performed by choosing a sufficiently large iteration number. This removes the need to determine an optimal regularization parameter when performing tomographic reconstructions of FILD measurements.

Another advantage of ARTs, which we highlight in this paper, is the fast convergence and computation time of the iterative techniques. The fast computation time combined with the improved quality reconstructions from the FILDSIM model improvements described in the previous sections opens the doors to optimizing the tomographic reconstructions in terms of their quality and computation time. Performing one iteration with the current MATLAB implementation on a modern laptop takes approximately 10 ms. Thus, the algebraic techniques can produce up to 100 frames per second depending on the desired reconstruction quality.

The ARTs considered in this work are Kaczmarz' method, the column-action method, and Cimmino's method. We briefly describe each of the three ARTs in the following.

For each iteration k in Kaczmarz's method, each row r_i of W is cycled through. Therefore, every iteration performs m steps. Every step satisfies one of the m equations in the forward model $Wf = s$. For the ith row, $r_i f^{(k^i)} = s_i$. The update to the solution vector is

$$\Delta f = \frac{s_i - r_i f^{(k)}}{\|r_i\|_2^2} r_i^T. \tag{8.23}$$

Each iteration is projected onto $\mathcal{C} = \mathbb{R}_+^n$ to apply a non-negativity constraint. For a relaxation parameter $\omega^{(k)}$ satisfying $0 < \omega^{(k)} \leq 1$, steps are

$$f^{(k^i)} = \mathcal{P}_{\mathcal{C}} \left(f^{(k^{i-1})} + \omega^{(k^i)} \frac{s_i - r_i f^{(k^{i-1})}}{\|r_i\|_2^2 + t^{(k)}} r_i^T \right) \tag{8.24}$$

for $i = 1, \ldots, m$. Note that each step in Kaczmarz's method divides by the row norm $\|r_i\|_2^2$. Some rows have either zero or very small but nonzero norm which may result in noise amplification. To avoid this problem, a small damping parameter $t^{(k)}$ is added to the denominator such that the division in each iterative step is $\|r_i\|_2^2 + t^{(k)}$. This damping parameter is dependent on the iteration step k, but we choose $t^{(k)} = 0.1$ for all k for simplicity.[4]

[2] Hansen (2010), p. 89 ff.
[3] Schmidt *et al. Reconstruction methods for velocity-space tomography of fast-ion loss detectors* (to be submitted).
[4] This approach is validated in Andersen and Hansen (2014).

Instead of the rows, the column-action method operates on the columns c_j. Similar to Kaczmarz's method, the column-action method operates cyclically now in the direction of the unit vectors e_j, where e_j has a 1 at the jth location and 0s elsewhere. At each iteration, we update $f^{(k+1)} = f^{(k)} + \alpha_k e_j$ with $j \equiv k \pmod{n}$ for

$$\alpha_k = \frac{c_j^T (s - W f^{(k)})}{\|c_j\|^2}. \tag{8.25}$$

Projecting onto $\mathbb{R}^n_+$ and with relaxation parameter ω_k, the iterations are

$$f^{(k+1)} = \mathcal{P}_{\mathcal{C}} \left(f^{(k)} + \omega^{(k)} \frac{c_j^T (s - W f^{(k)})}{\|c_j\|^2 + t^{(k)}} e_j \right). \tag{8.26}$$

Similar to Kaczmarz's method, a damping parameter $t^{(k)} = 0.1$ was used.

General simultaneous iterative reconstruction techniques (SIRT) have a diagonal matrix $D \in \mathbb{R}^{n \times n}$ and a weighting matrix $M \in \mathbb{R}^{m \times m}$ with iterative steps

$$f^{(k+1)} = f^{(k)} + \omega^{(k)} D W^T M (s - W f^k). \tag{8.27}$$

For simplicity, we choose $D = I^{n \times n}$. To obtain faster convergence, we use a SIRT with

$$M = \operatorname{diag} \left(\frac{1}{m \|r_i\|_2^2} \right). \tag{8.28}$$

This method is Cimmino's method. Again, we project onto $\mathcal{C} = \mathbb{R}^n_+$.

All three methods start with an initial guess for the solution, denoted $f^{(0)}$, which can be the zero vector or a guess based on prior information. The methods terminate when a stopping criterion is met, in our case when a maximum number of iterations is met, as indicated in the discussion below.

To illustrate the applicability of the iterative techniques to experimental data and their convergence properties, we apply the reconstruction techniques to data from FILD1 at ASDEX Upgrade from discharge #35336. Afterward, we describe how to optimize the tomographic reconstruction using these techniques in terms of the reconstruction quality and computation time.

8.6 Discharge #35336 at ASDEX Upgrade

Discharge #35336 at ASDEX Upgrade concerns actuation of toroidal Alfvén eigenmodes (TAEs) using electron cyclotron current drive (ECCD). Localized ECCD modifies the local magnetic shear causing TAEs not to develop if the plasma pressure gradient exceeds a critical value[5]. The plasma was heated using ICRF heating and a combined NBI power of 5 MW. The measurements are from FILD1 at ASDEX Upgrade. The scintillator measurements appear around $\rho = 2$ cm to $\rho = 8$ cm for pitch angles around 65°. See Fig. 8.13 for the scintillator measurement at $t = 1.7328$ s.

First, we investigate the convergence rate of the three different ARTs by visual inspection of the tomographic reconstructions of the pinhole velocity-space distribution functions. This shows the number of iterations required for a reconstruction produced by a specific method to show the details in pinhole velocity space, indicating the precise locations of the lost fast ions. Zeroth-order Tikhonov regularization is used as a benchmark for comparison.

[5] Galdon-Quíroga *et al.* (2019).

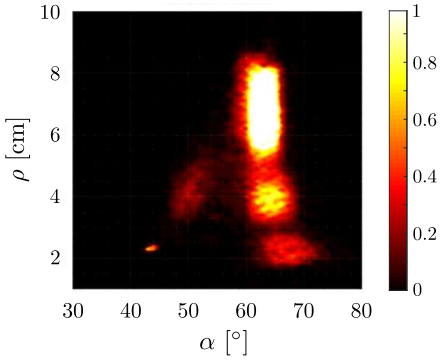

Figure 8.13: The scintillator measurement $t = 1.7328$ s in FILD1 during discharge #35336 at ASDEX Upgrade.

The tomographic reconstructions of the scintillator measurement shown in Fig. 8.13 for $t = 1.7328$ s for the iteration numbers $k = 5, 10, 20$, and 50 are shown in Fig. 8.14. The four numbers for k were chosen to be representative of fast convergence ($k \leq 10$), medium-speed convergence ($k \approx 20$), and slow convergence ($k \geq 50$).

All methods reconstruct five high-intensity regions with approximate velocity-space coordinates

$$(67°, 2.5 \text{ cm}), (65°, 4 \text{ cm}), (62°, 7 \text{ cm}), (64°, 7 \text{ cm}), (43°, 2.5 \text{ cm}) \tag{8.29}$$

for sufficiently large k's. The high-intensity region at $(43°, 2.5 \text{ cm})$ is an artefact and can be disregarded.

Of the three different methods, Kaczmarz's method converges the fastest. The reconstructions using Kaczmarz's method indicate precise velocity-space locations for $k = 5$, whereas this is not the case for Cimmino's method nor the column-action method. Note that the location of the high-intensity regions around 7 cm in gyroradius occurs for lower gyroradii in the Kaczmarz reconstruction than in the Tikhonov reconstruction. The column-action method converges slower than Kaczmarz's method but faster than Cimmino's. Cimmino's method converges slowly and requires around 500 iterations to converge.

All three methods have artefacts at $\rho = 2$ cm for all pitch angles. These occur after the very first iteration and persist for all iterations. The artefacts occur due to the large gradient at $\rho = 2$ cm, where the weight functions drop to zero. Since they are known to be artefacts, they can be disregarded.

In the next section, we optimize the quality of the reconstruction in terms of the computation time.

8.7 Optimized tomographic reconstructions in terms of quality and computation time

Knowledge of the lost fast-ion velocity-space distribution functions is highly desirable for discharge analysis when FILD measurements are relevant. The distribution functions may provide evidence of fast-ion interactions with particular modes or prompt losses from NBI. In particular, it is highly desirable to have the fast-ion velocity-space distribution functions between discharges to optimize discharge conditions. Due to the improved reconstruction quality from the FILDSIM model improvements described in Section 8.3, it is possible to compute an optimized reconstruction

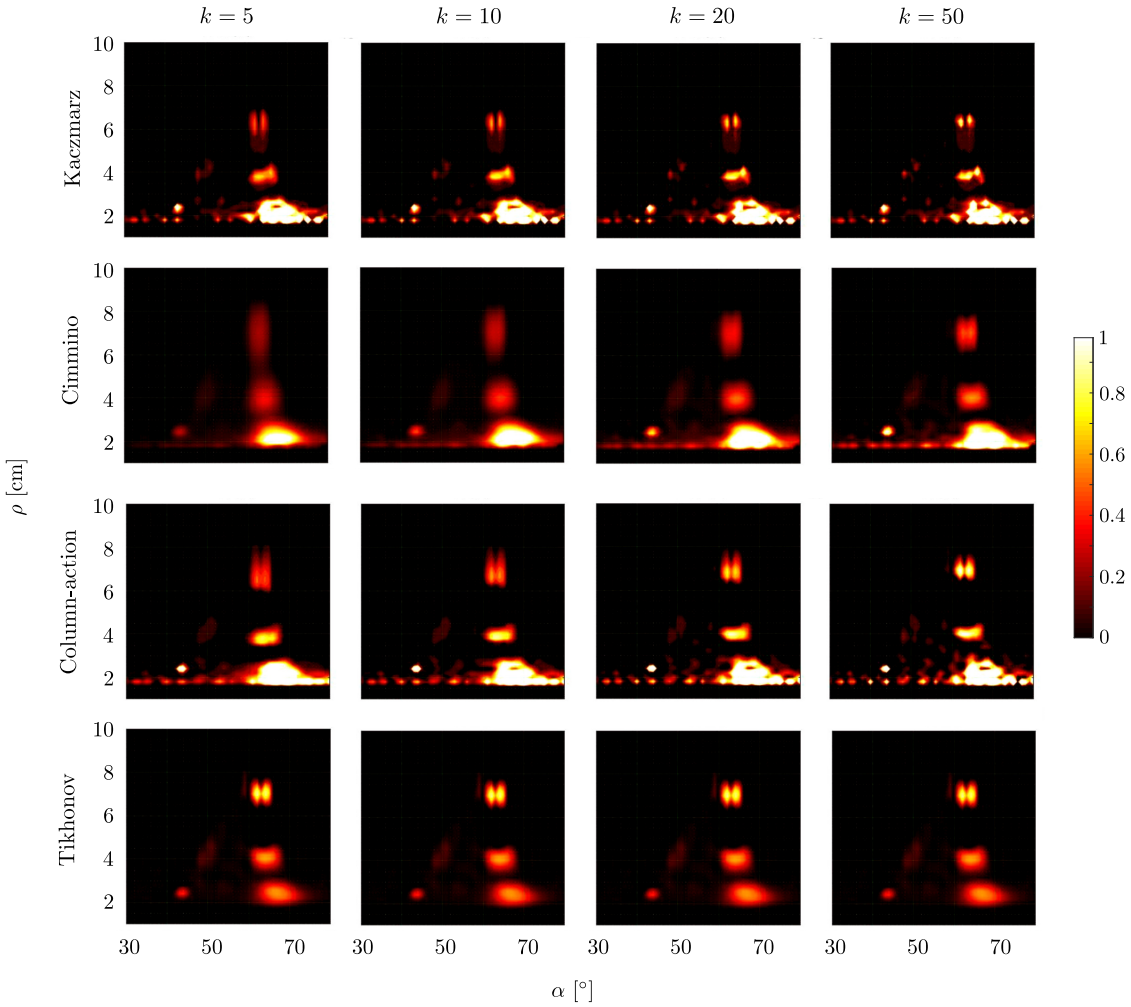

Figure 8.14: The reconstructions for each method as a function of the iteration number. The Tikhonov reconstruction is calculated for $\lambda = 0.5$.

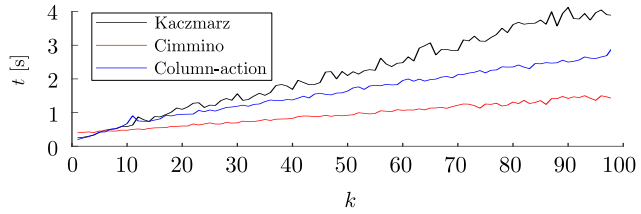

Figure 8.15: The computation times for each method as a function of iteration number k for $t = 1.7328$ s in discharge #35336.

	Iterations	Kaczmarz	Cimmino	Column-action	Tikhonov
35336	$k = 5$	0.3854	0.4288	0.3442	5.3368
	$k = 10$	0.5842	0.4807	0.5610	
	$k = 20$	0.9813	0.5827	0.8400	
	$k = 50$	2.2331	0.8922	1.4973	

Table 8.2: Computation times in seconds for each method for the number of iterations indicated.

in terms of both reconstruction quality and computation time. This optimization can produce optimized videos of entire discharges available within minutes.

The three iterative techniques are applied to compute reconstructions of 100 FILD1 measurements from discharge #35336 at ASDEX Upgrade from $t = 1.700$ s to $t = 1.800$ s. The reconstruction computation time is computed as the average computation time for all 100 frames for a given iteration number k. The computation time for the most efficient non-negative zeroth-order Tikhonov regularization MATLAB routine *lsqlin* as it is currently implemented in MATLAB is given for comparison since it is currently the standard technique used for computing reconstructions. We set the regularization parameter $\lambda = 0.5$ since that produces a good reconstruction and use that as the comparison value. The computation times are illustrated in Fig. 8.15 for each method as a function of k, and the exact numerical values for specific iteration numbers are displayed in Table 8.2.

Kaczmarz's method is the fastest of the four methods for few iteration numbers ($k < 5$). The method even produces a good reconstruction after the second iteration. Fig. 8.16 shows the tomographic reconstruction using Kaczmarz's method for $k = 2$ compared to the optimal Tikhonov reconstruction. The tomographic reconstruction from Kaczmarz's method correctly identifies the two high-intensity locations around 6-7 cm in gyroradius and 62° and 64° in pitch angle. It takes Cimmino's method several iterations to find the distinction in pitch angle. The total computation time was 0.2748 s, around 20 times as fast as the Tikhonov reconstruction. Note that the locations of the high-intensity regions around 6-7 cm in gyroradius are slightly lower in gyroradius in the Kaczmarz reconstruction than in the Tikhonov reconstruction. The reason for this is unknown.

The computation time increases linearly for all three techniques. The computation time for the first 100 iterations for all three methods is shown in Fig. 8.15. Kaczmarz's method and the column-action method are the slowest after $k \approx 5$, after which Cimmino's method is the fastest. Cimmino's method is faster than Kaczmarz's method and the column-action method but converges much slower. The first iteration requires initializing the algorithm, which is why the curves in Fig. 8.15 do not intersect $(0, 0)$. The time for an additional iteration for all methods is on the order of 10 ms.

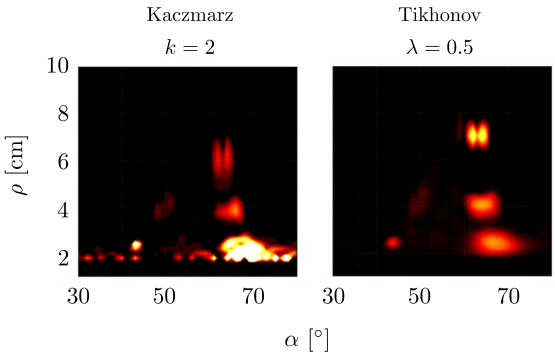

Figure 8.16: Tomographic reconstructions for $k = 2$ using Kaczmarz's method and $\lambda = 0.5$ for Tikhonov regularization.

8.7.1 Reconstruction quality vs. computation time

In this section we develop a figure of merit to optimize the reconstruction quality and the computation time. The description here is kept brief. See the appendix for additional details.

Define the residual matrix $R^{(k)} \equiv \hat{s} - \widehat{Wf^{(k)}}$ for the kth iteration with entries $\left(r_{ij}^{(k)}\right)$, where a hat indicates normalization. When applying ARTs to FILD data, the better the reconstruction, the closer $R^{(k)}$ is to 0. One way to measure the goodness of a reconstruction is the number of entries with $\left|r_{ij}^{(k)}\right| > \tau$ for some threshold τ, where τ is a non-negative scalar. Since $\hat{s}$ and $\widehat{Wf^{(k)}}$ are normalized, τ can be interpreted as a lower bound on the percentage point deviation of the actual measurement from the measurement corresponding to the reconstruction computed as $Wf^{(k)}$. Let m_i denote the ith method used for performing the reconstruction, and let $\pi\left(R^{(k)} \mid m_i, \tau\right)$ be a counting function for the kth iteration of method m_i and threshold τ counting the number of entries with values above τ. Let $T\left(k \mid m_i\right)$ be the computation time for k iterations for the ith method. Then, it takes method m_i the time $T\left(k \mid m_i\right)$ to produce a reconstruction with $\pi\left(R^{(k)} \mid m_i, \tau\right)$ entries deviating by τ percentage points from the measurement. Let Kaczmarz's method, Cimmino's method, and the column-action method be numbered 1-3.

The counting function π as a function of the iteration number is illustrated in Fig. 8.17 for the tomographic reconstruction using the column-action method and a threshold $\tau = 0.1$. The lower bound is $\pi\left(R^k \mid m_3, 0.1\right) = 28$ for $k \geq 35$. Thus, the tomographic reconstruction obtained using the column-action method will have at least 28 entries with a deviation above 10 percentage points from the measurement entries and does not improve beyond $k = 35$.

Numerical testing shows the functional relation between T and π follows a power expression of the form

$$\pi = bT^a + u_0 \tag{8.30}$$

with $a < 0$, $b > 0$, and u_0 is a non-negative constant representing the lower bound on π as $k \to \infty$. For example, for $t = 1.7328$ s during discharge #35336, a fit using Eq. (8.30) gives $R^2 = 0.8517$, indicating a relatively good model.

Define $u(T, \pi) \equiv \pi - bT^a$. Optimizing the tomographic reconstruction in terms of reconstruction quality and computation time can then be formulated as the optimization problem

$$E(\alpha, \beta, u) = \min_{T,\pi} \alpha T + \beta\left(N - \pi\right) \quad \text{subject to} \quad u(T, \pi) = u. \tag{8.31}$$

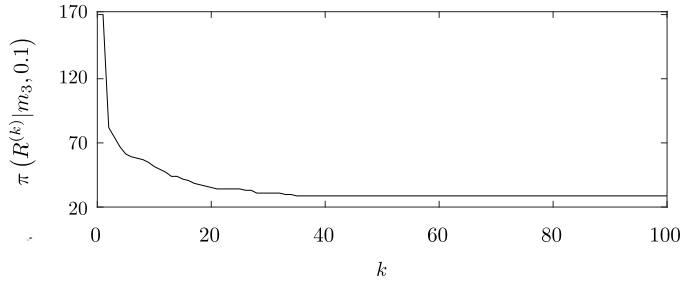

Figure 8.17: The counting function $\pi\left(R^{(k)} \mid m_3, 0.1\right)$ computed for tomographic reconstructions obtained using the column-action method with threshold $\tau = 0.1$ for the scintillator measurement at $t = 1.7328$ s during discharge #35536.

The solution function $h^*(\alpha, \beta, u)$ is

$$h^*(\alpha, \beta, u) = \left(\left(\frac{\alpha}{-ab\beta} \right)^{1/(a-1)}, b \left(\frac{\alpha}{-ab\beta} \right)^{a/(a-1)} + u \right). \tag{8.32}$$

See the appendix for a derivation.

8.7.2 Optimized tomographic reconstructions for discharge #35336

The optimal combination of computation time and the corresponding number of entries in the residual matrix above τ can be computed after having estimated values for α and β. The optimal iteration number k^* follows from the linearity between the computation time and the number of iterations.

A power regression for π as a function of k for the column-action method for the scintillator measurements at $t = 1.7324$ s during discharge #35336 gives

$$\pi = 7.073T^{-1.892} + 649 \quad \text{with} \quad R^2 = 0.8517. \tag{8.33}$$

Note that the number of significant digits does not reflect physical uncertainties. The coefficients are $a = -1.892$, $b = 7.073$, and $u = 649$.

Suppose the value one puts on obtaining a good reconstruction compared to faster computation time is $100 : 1$. Then $\alpha = 100$ and $\beta = 1$, and

$$h^*(100, 1, 649) = (0.4988 \text{ s}, 675.4), \tag{8.34}$$

The linearity between the computation time and the number of iterations for the column-action method is $T = 0.0114k + 0.3482$ with $R^2 = 0.9837$. Thus, $k = 87.72T - 3.054$, and $k^* = 41$. For this particular case, $R^{(k)}$ does not improve for $k \geq 35$, so a ratio of $100 : 1$ overestimates the number of iterations needed to obtain the optimal tomographic reconstruction. A ratio of $200 : 1$ for $\alpha : \beta$ gives $T^* = 0.3925$ s, so $k^* = 31$ with $\pi^* = 690$. A ratio of $300 : 1$ gives $T^* = 0.3412$ s, so $k^* = 27$ with $\pi^* = 703$. The decrease in computation time from the ratio $100 : 1$ to the ratio $200 : 1$ is around 20 % and from $200 : 1$ to $300 : 1$ around 10 %. It is possible to determine an optimal ratio by considering many frames from different discharges and finding a common ratio that produces optimal reconstructions. This remains to be investigated.

8.8 Conclusion

This paper presents advancements in FILDSIM modelling and execution of tomographic reconstructions. The FILDSIM model improvements include more accurate models of the 1D FILDSIM distributions in energy for a given pitch and the distributions in pitch for a given energy. The improvements are made by implementing a skewed raised cosine distribution in gyroradius and Wigner's semicircle distribution in pitch. The weight functions resulting from the FILDSIM improvements more accurately model the upper tail and width of simulated weight functions. The improved weight functions generate synthetic data that are more like experimental FILD measurements. Furthermore, we show a significant improvement in the characterization of the TCV FILD in terms of its gross strike map and gross weight function using the updated FILDSIM model.

This paper also presents a way to utilize algebraic iterative reconstruction techniques to compute tomographic reconstructions optimized in terms of the reconstruction quality and computation time. This allows faster tomographic reconstructions of entire discharges completed within minutes. Thus, this optimization strategy is particularly valuable for inter-discharge FILD data tomographic reconstructions and analysis.

Appendix

In this section, we derive the solution as given in Eq. (8.32) to the optimization problem in Eq. (8.31).

Let Kaczmarz's method, Cimmino's method, and the column-action method be numbered 1-3. Note that as k increases, $R^{(k)}$ should decrease. This is indeed the case. For example, the counting function π as a function of the iteration number is illustrated in Fig. 8.17 for the tomographic reconstruction using the column-action method and a threshold $\tau = 0.1$. The lower bound, and hence the best the reconstruction can do, is $\pi\left(R^k \mid m_3, 0.1\right) = 28$ for $k \geq 35$. Thus, the tomographic reconstruction obtained using the column-action method will have at least 28 entries with a deviation above ten percentage points from the measurement entries and does not improve beyond $k = 35$. Therefore, one termination criterion for the algebraic iterative reconstruction techniques is when reaching the situation for $k = 35$ in the above example. Determining when this situation occurs can be accomplished by, e.g., computing the slope of an interpolated spline of the points (π, k) and terminating the algorithm when the slope is zero for a pre-specified number of iterations. This presents a way to avoid running the iterative algorithms for a larger number of iterations.

However, *a priori*, it is impossible to say for which iteration number this termination criterion is satisfied. Terminating the iteration algorithms at an earlier iteration number may also be desirable if another appropriate figure of merit is satisfied. This may result in a reconstruction of equal quality with a faster computation time. The counting function π can be used for this.

Let $T\left(k \mid m_i\right)$ be the computation time for k iterations for the ith method. Then, it takes method m_i the time $T\left(k \mid m_i\right)$ to produce a reconstruction with $\pi\left(R^{(k)} \mid m_i, \tau\right)$ entries deviating by τ percentage points from the measurement. Let N be the total number of entries in s. Then it is possible to determine a maximum value M such that

$$\alpha T\left(k \mid m_i\right) + \beta\left(N - \pi\left(R^{(k)} \mid m_i, \tau\right)\right) \leq M \tag{8.35}$$

for some $\alpha, \beta \in \mathbb{R}_+$. The parameter α represents the cost of a higher computation time and β the cost of obtaining a better reconstruction as measured as the number of entries in the reconstruction not deviating by more than τ from the measurement. Note that as the tomographic reconstruction

improves, π decreases, so $N - \pi$ increases and β can be correctly interpreted as the cost of a better reconstruction.

Numerical testing shows that the functional relation between T and π follows a power expression of the form

$$\pi = bT^a + u_0 \tag{8.36}$$

with $a < 0$ since the number of error above the threshold τ decreases as the computation time increases, $b > 0$ since the number of errors for $T \geq 0$ is positive, and u_0 is a non-negative constant representing the lower bound on π as $k \to \infty$. This model is appropriate for tomographic reconstructions of experimental FILD data. For example, for $t = 1.7328$ s during discharge #35336, a fit using Eq. (8.30) produces $R^2 = 0.8517$, indicating a relatively good model.

Define $u(T, \pi) \equiv \pi - bT^a$. Given a method m_i and a measurement s, a value $u = u_0$ is uniquely determined such that all possible values of (T, π) must lie on the curve $u_0 = \pi - bT^a$. The optimal combination (T^*, π^*) makes M a minimum. In this case, the cost for both the reconstruction quality and the computation time is minimized. Thus, optimizing the tomographic reconstruction in terms of reconstruction quality and computation time can be formulated as the optimization problem

$$E(\alpha, \beta, u) = \min_{T,\pi} \alpha T + \beta (N - \pi) \quad \text{subject to} \quad u(T, \pi) = u. \tag{8.37}$$

The solution function $h^*(\alpha, \beta, u)$ can be determined as follows. Write the Lagrangian function $\mathcal{L}$ as

$$\mathcal{L}(T, \pi, \lambda) = \alpha T + \beta(N - \pi) + \lambda (u - (\pi - bT^a)) . \tag{8.38}$$

Then

$$\frac{\partial \mathcal{L}}{\partial T} = \alpha + \lambda ab T^{a-1} = 0, \tag{8.39}$$

$$\frac{\partial \mathcal{L}}{\partial \pi} = -\beta + \lambda = 0, \tag{8.40}$$

$$\frac{\partial \mathcal{L}}{\partial \lambda} = u - \pi + bT^a = 0. \tag{8.41}$$

Thus,

$$\frac{\alpha}{\beta} = -abT^{a-1}, \tag{8.42}$$

so

$$T = \left(\frac{\alpha}{-ab\beta} \right)^{1/(a-1)}, \tag{8.43}$$

and

$$\pi = bT^a + u = b \left(\frac{\alpha}{-ab\beta} \right)^{a/(a-1)} + u. \tag{8.44}$$

Therefore,

$$h^*(\alpha, \beta, u) = \left(\left(\frac{\alpha}{-ab\beta} \right)^{1/(a-1)}, b \left(\frac{\alpha}{-ab\beta} \right)^{a/(a-1)} + u \right). \tag{8.45}$$

Note that since $a < 0$ and b, α, and β are all positive, $(T, \pi) \in \mathbb{R}^2$ and is well-defined. The behaviour of T^* and π^* can be interpreted in terms of the cost of T and π. It follows from Eq.

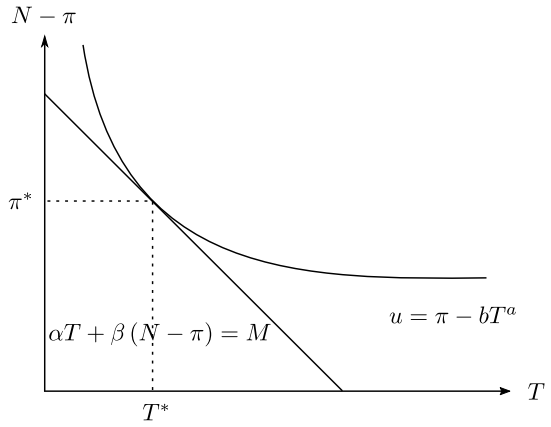

Figure 8.18: A graphical interpretation of the minimization problem to determine the optimal parameters (T^*, π^*) and consequently the optimal number of iterations k.

(8.45) that

$$T^* \sim \left(\frac{\alpha}{\beta}\right)^{1/(a-1)}, \tag{8.46a}$$

$$\pi^* \sim \left(\frac{\alpha}{\beta}\right)^{a/(a-1)}. \tag{8.46b}$$

Since $a < 0$, the fraction $1/(a-1) < 0$, so the optimal computation time T^* decreases with increasing α. This behaviour occurs because having a higher computation time is more costly. The optimal computation time increases with increasing β since having the same number of errors becomes more expensive, so the computation time must increase to reduce the number of entries in the residual matrix with values below τ.

The optimal error count π^* increases with increasing α, since when computation time cost increases, it becomes more expensive to reduce the reconstruction error to reduce π. The optimal error count π^* decreases with increasing β because it becomes more expensive to have more errors in the reconstruction.

Graphically, obtaining this solution corresponds to determining the point of tangency between the curve $\alpha T + \beta (N - \pi) = M$ and the function $u = \pi - bT^a$. This occurs exactly when

$$\frac{\alpha}{\beta} = -\frac{\partial u/\partial T}{\partial u/\partial \pi} = \frac{\mathrm{d}\pi}{\mathrm{d}T} = abT^{a-1}. \tag{8.47}$$

This point of tangency and the optimal values of T and π are illustrated in Fig. 8.18.

Chapter 9

Grid dependence in Tikhonov regularization

This chapter presents the paper "Dependence of the reconstruction error on the grid size in ill-posed inverse problems", to be submitted.

9.0 Abstract

In this paper, we investigate how the discretization of the domain of a linear operator A impacts the solution of an ill-posed inverse problem. We model a physical system via a matrix-vector relationship $Ax = b$ and solve it using zeroth- and first-order Tikhonov regularization. Our findings show that an increase in the number of grid points correlates with a reduction in both the optimal value of the regularization parameter and the reconstruction error of the solution.

The results apply to the specific model of determining fast-ion velocity-space distribution functions from projections of fast-ion velocities in fusion plasmas. In this case, our results show that the dependence of the reconstruction error on the grid discretization depends almost entirely on the grid resolution in the parallel-velocity direction.

9.1 Introduction

Inverse problems occur in various scientific disciplines and involve the process of deduction from effect to cause. In mathematical parlance, modelling an inverse problem can be written in the general form

$$Ax = b, \tag{9.1}$$

where A is a matrix representing the physical system, b is a data vector obtained from measurements, and x is the unknown vector to deduce.

Inverse problems often present issues of ill-posedness. The ill-posedness arises when small changes in b lead to large changes in x, making the solution unstable. This occurs when a measurement contains noise. It could also be that no solution exists, or multiple distinct x could correspond to a given b, making the solution non-unique. Therefore, challenges when dealing with inverse problems comprise obtaining existence, uniqueness, and stable solutions. Regularization methods are used to constrain the solution space to obtain such solutions.

Solving inverse problems involves discretizing a continuous model to solve it on computers.

The resolution of the discretization is determined by the grid size, which determines the level of detail in the discrete model. A smaller grid size, with a larger number of grid points, provides higher resolution, potentially resulting in computing more accurate solutions. However, the size of the system matrix A grows with the number of grid points, so the higher resolution comes at the cost of increased computational time. A larger grid size, with fewer grid points, reduces computational requirements. However, this coarser representation can lead to a loss in accuracy, as less detail from the original continuous problem is captured in the discretized version.

In this paper, we investigate the impact of the grid size on the reconstruction. The data considered arise from projections of fast-ion velocities in fusion plasmas. Section 2 describes how regularization is used to solve ill-posed inverse problems and the concept of inverse crime. Section 3 presents the physical model of projections. Section 4 details our investigations, including the generation of the synthetic measurement used to compute reconstructions and how we compute the optimal value of the regularization parameter. Section 5 investigates the grid dependence when using zeroth- and first-order Tikhonov regularization. Section 6 provides a conclusion.

9.2 Solving ill-posed inverse problems

An approximate solution to the ill-posed inverse problem can be computed using regularization techniques. One such regularization technique is Tikhonov regularization. Tikhonov regularization introduces a penalty term that penalizes undesirable characteristics of the solution. This problem can be formulated as

$$x^* = \underset{x}{\operatorname{argmin}} \left(\|Ax - b\|_2^2 + \lambda \|Lx\|_2^2 \right), \tag{9.2}$$

where L is a linear operator, and λ is the regularization parameter. A wide range of regularization can be computed using different Ls. The corresponding normal equations are

$$\left(A^T A + \lambda L^T L\right) x = A^T b, \tag{9.3}$$

with solution

$$x^* = \left(A^T A + \lambda L^T L\right)^{-1} A^T b. \tag{9.4}$$

9.2.1 Inverse crime

An inverse crime is committed when the same discretization of the mathematical model is used to generate the synthetic measurement and to compute the subsequent reconstruction. For the system matrix A, we generate a synthetic measurement b by computing

$$b = Ax^{\text{true}}, \tag{9.5}$$

where x^{true} is the ground truth. If we compute x^{true} from b using the same system matrix A and the same discretization, we are committing an inverse crime. Committing an inverse crime results in an over-optimistic assessment of the reconstruction method's performance, and the reconstruction will seem more accurate than it otherwise would be on experimental data. Avoiding committing an inverse crime requires using different grid sizes for the forward and inverse problems. This notion forms the bedrock of this paper.

Note that all computations in this paper are performed using "synthetic data". This term refers to data used for method development, testing, and to indicate the viability of a specific reconstruction approach.

When modelling a physical system to generate synthetic data, we must discretize the physical domain, creating a grid that spans the region of interest. Call this grid the 'forward grid' and

denote the corresponding system matrix A_{cont}. The abbreviation 'cont' is short for 'continuous', since the forward grid represents the continuous physical process. Let the number of grid points in each direction of the grid be $[N_1, N_2]$. To solve the inverse problem using synthetic data generated using the forward grid, we use the same system matrix discretized on the same domain, but with a different grid size with the number of grid points $[n_1, n_2]$. This translates into A having a different number of columns but the same number of rows as the number of measurements remains the same. This grid is called the 'inverse grid' and is denoted A_{inv}.

9.3 The physical model: projections

In plasma physics, the term 'projections' refers to an analytical methodology used to infer the velocity-space distribution function of fast ions along a particular direction of observation called the 'line of sight'. The velocity of any particle within a plasma system is three-dimensional. However, the experimental ability to directly measure this velocity is limited. We rely on measurements along a specific line of sight and extract the projection of the velocity vector along this line. These projections are used to infer the fast-ion velocity-space distribution function. The task involves solving an inverse problem.

In a magnetically confined fusion plasma, fast ions gyrate around magnetic field lines. Their velocity can be described in terms of a parallel velocity $v_\parallel$ and a perpendicular velocity vector $\boldsymbol{v}_\perp$. The velocity component $v_\parallel$ is the velocity of the ion parallel to the magnetic field, and $\boldsymbol{v}_\perp = (v_{\perp,1}, v_{\perp,2})$ are the ion velocities perpendicular to the magnetic field. In cylindrical coordinates, it is possible to write $\boldsymbol{v} = (v_\parallel, v_\perp, \gamma)$, where

$$v_{\perp,1} = v_\perp \cos\gamma, \tag{9.6}$$

$$v_{\perp,2} = v_\perp \sin\gamma, \tag{9.7}$$

as illustrated on Fig. 9.1(a), and

$$v_\perp = \sqrt{v_{\perp,1}^2 + v_{\perp,2}^2}. \tag{9.8}$$

The parameter γ is called the gyroangle, indicating the angle between $\boldsymbol{v}_\perp$ and $\hat{\boldsymbol{v}}_{\perp,1}$. The fast gyration around the magnetic fields lines results in azimuthal symmetry in 3D velocity space. The gyroangle γ therefore becomes ignorable, and velocity space reduces to $(v_\parallel, v_\perp)$.[1]

An expression for the projected velocity $\boldsymbol{u} = u\hat{\boldsymbol{u}}$ onto a line of sight of a diagnostic, where $\hat{\boldsymbol{u}}$ is a unit vector in the direction of the line of sight, can be obtained as follows. Define a coordinate system with ion velocity

$$\boldsymbol{v} = v_\parallel \hat{\boldsymbol{B}} + v_\perp \cos\gamma\, \hat{\boldsymbol{v}}_{\perp,1} - v_\perp \sin\gamma\, \hat{\boldsymbol{v}}_{\perp,2}. \tag{9.9}$$

Let ϕ be the angle between $\boldsymbol{B}$ and $\boldsymbol{u}$, so

$$\hat{\boldsymbol{u}} = \cos\phi\, \hat{\boldsymbol{B}} + \sin\phi\, \hat{\boldsymbol{v}}_{\perp,1}. \tag{9.10}$$

The projected velocity u is then

$$u = \boldsymbol{v} \cdot \hat{\boldsymbol{u}} = v_\parallel \cos\phi + v_\perp \sin\phi \cos\gamma. \tag{9.11}$$

See Fig. 9.1(b) for an illustration of the geometry.

[1] Moseev and Salewski (2019).

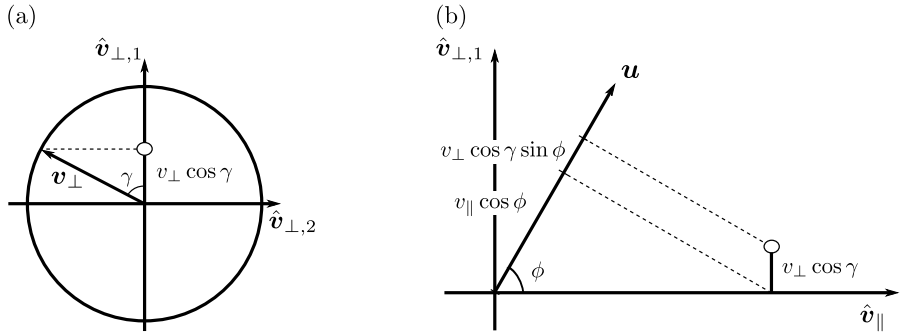

Figure 9.1: A geometric description of the projection of the 3D ion velocities $\boldsymbol{v} = (v_\parallel, v_\perp \cos\gamma, v_\perp \sin\gamma)$ onto the velocity $\boldsymbol{u}$ in the direction of the line of sight of the diagnostic. Subfigure (a) shows the projection onto the $v_{\perp 1}$-axis, and (b) the projection in the direction of $\boldsymbol{u}$. Adapted from Salewski et al. (2011) and Salewski, Geiger, Moseev, et al. (2014).

9.3.1 The system matrix

The system matrix consists of so-called "weight functions". Weight functions provide the relation between a detected signal s and the 2D velocity-space distribution function f. In velocity space, the weight functions are defined as the kernel of the equation

$$s(u_1, u_2, \phi) = \int_{-\infty}^{\infty} \int_{0}^{\infty} w(u_1, u_2, \phi, v_\parallel, v_\perp) f(v_\parallel, v_\perp) \, \mathrm{d}v_\perp \, \mathrm{d}v_\parallel \tag{9.12}$$

for a projected velocity range u_1 to u_2 and viewing angle ϕ. Thus, the weight functions $w = w(u_1, u_2, \phi, v_\parallel, v_\perp)$ depend on the projected velocity range u_1 to u_2, the viewing angle ϕ, and the location in velocity space $(v_\parallel, v_\perp)$. The weight function w represents the relative contributions of different areas of velocity space to the detected signal s for a given projected velocity range u_1 to u_2 and a given viewing angle ϕ. Areas where the weight functions are positive are called 'observable regions.'

Weight functions contain the probabilities that a given projected velocity is within the projected velocity range u_1 to u_2. Thus, to obtain the system matrix, we need the probability $\mathrm{prob}(u_1 < u < u_2 \mid \phi, v_\parallel, v_\perp)$ that the projected velocity of the fast ion is between u_1 and u_2. Given that $v_\perp \neq 0$ and the projection angle $\phi \neq 0$, solving Eq. (9.11) for the gyroangle γ gives

$$\gamma = \arccos \frac{u - v_\parallel \cos\phi}{v_\perp \sin\phi}. \tag{9.13}$$

One solution γ is found for $0 < \gamma < \pi$, and a second solution for $\pi < \gamma' < 2\pi$ given by $\gamma' = 2\pi - \gamma$. The total probability is therefore

$$\begin{aligned} \mathrm{prob}\left(u_1 < u < u_2 \mid \phi, v_\parallel, v_\perp\right) = {} & \mathrm{prob}\left(\gamma_1 < \gamma < \gamma_2 \mid \phi, v_\parallel, v_\perp\right) \\ & + \mathrm{prob}\left(\gamma_1' < \gamma < \gamma_2' \mid \phi, v_\parallel, v_\perp\right), \end{aligned} \tag{9.14}$$

where $\gamma_1, \gamma_2, \gamma_1'$, and γ_2' correspond to the limits u_1 and u_2. Assuming a uniform probability density, which is a valid assumption due to the fast gyromotion of the ions, we get

$$\mathrm{prob}\left(u_1 < u < u_2 \mid \phi, v_\parallel, v_\perp\right) = \frac{\gamma_1 - \gamma_2}{2\pi} + \frac{\gamma_2' - \gamma_1'}{2\pi} = \frac{\gamma_1 - \gamma_2}{\pi}. \tag{9.15}$$

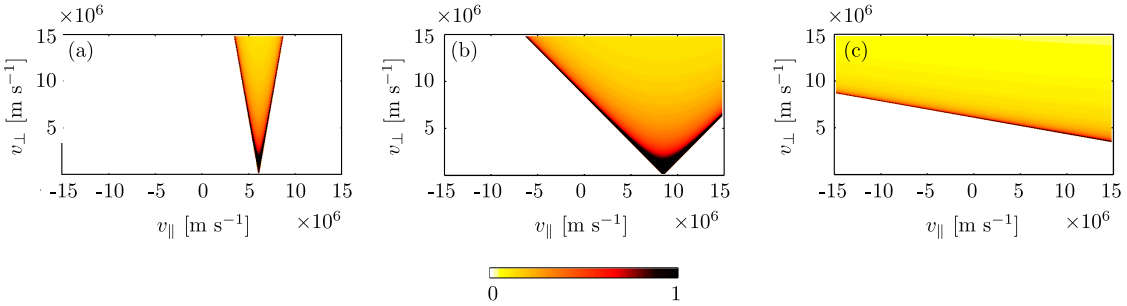

Figure 9.2: Projection weight functions in $(v_\parallel, v_\perp)$ coordinates for $u = 6 \times 10^6$ m s^{-1} and (a) $\phi = 10°$, (b) $\phi = 45°$, and (c) $\phi = 85°$. Adapted from Salewski et al. (2011).

Substituting γ from Eq. (9.13) gives

$$\text{prob}\left(u_1 < u < u_2 \mid \phi, v_\parallel, v_\perp\right) = \frac{1}{\pi}\left(\arccos\frac{u_1 - v_\parallel \cos\phi}{v_\perp \sin\phi} - \arccos\frac{u_2 - v_\parallel \cos\phi}{v_\perp \sin\phi}\right). \tag{9.16}$$

We use this expression to calculate the weight functions. Note that the equation is singular for $v_\perp = 0$ or $\phi = 0$. In those cases,

$$\text{prob}(u_1 < u < u_2 \mid \phi, v_\parallel, v_\perp = 0) = \begin{cases} 1 & \text{for } \frac{u_1}{\cos\phi} < v_\parallel < \frac{u_2}{\cos\phi}, \\ 0 & \text{otherwise,} \end{cases} \tag{9.17}$$

and

$$\text{prob}(u_1 < u < u_2 \mid \phi = 0, v_\parallel, v_\perp) = \begin{cases} 1 & \text{for } u_1 < v_\parallel < u_2, \\ 0 & \text{otherwise.} \end{cases} \tag{9.18}$$

The weight functions have a characteristic triangular structure in $(v_\parallel, v_\perp)$ coordinates indicating the observable and unobservable regions in velocity space for a given viewing angle. Example weight functions for $\phi = 10^\circ, 45°$, and $85°$ are illustrated in Fig. 9.2.

9.4 Data generation

Discretizing Eq. (9.12) as done in Salewski et al. (2012), we obtain a matrix-vector equation of the form

$$Wf = s, \tag{9.19}$$

where W is the system matrix containing the weight functions, s is a vector containing the projected velocities, and f the velocity-space distribution function. The objective is to compute the velocity-space distribution function f given W and s.

For all synthetic measurements, the noise e is assumed to be added noise, so an observation s_i can be written as

$$s_i = s_i^{\text{exact}} + e_i, \tag{9.20}$$

where s^{exact} is the exact data without noise. A noise level of 10% is added to all synthetic measurements, approximating the noise levels of experimental diagnostic equipment used in fusion experiments. To incorporate a background level of noise, a synthetic noisy data vector s is generated as

$$s = s^{\text{exact}} + \eta \left\langle s^{\text{exact}} \right\rangle \mathcal{N}\left[0, \max\left(\sigma_{\min}, \sqrt{s^{\text{exact}}}\right)\right]. \tag{9.21}$$

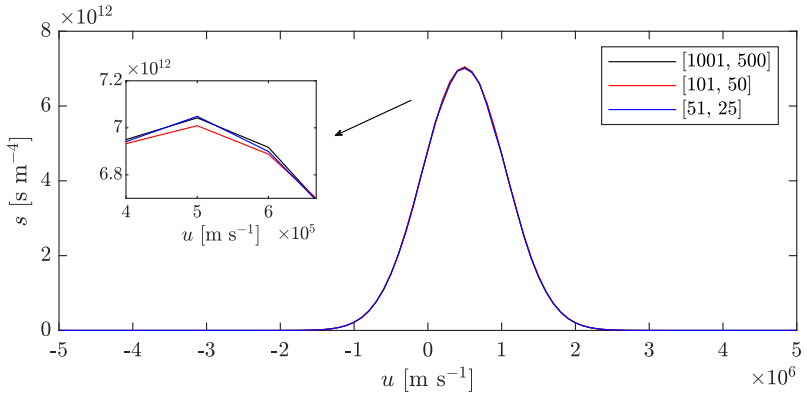

Figure 9.3: Three synthetic spectra generated using different sizes of the forward grid. The black line corresponds to $[N_{v_\parallel}, N_{v_\perp}] = [1001, 500]$, the red line [101, 50], and the blue line [51, 25]. The inset highlights the peak of the spectrum.

The parameter η controls the noise level, and $\mathcal{N}\left[0, \max\left(\sigma_{\min}, s^{\text{exact}}\right)\right]$ is a normal distribution with mean 0 and standard deviation equal to the maximum of either $\sigma_{\min}$, mimicking the background noise, or $\sqrt{s^{\text{exact}}}$. Thus, the noisy synthetic data have a background noise or a noise dependent on the measurement.

The system matrix W_{cont} was computed using a grid of size $[N_{v_\parallel}, N_{v_\perp}] = [1001, 500]$ on the domain $v_\parallel/[10^6 \text{ m s}^{-1}] \in [-4, 4]$ and $v_\perp/[10^6 \text{ m s}^{-1}] \in [0, 4]$. This number of grid points in the forward model represents a fine approximation of the continuous physical process generating the measurements. The number of grid points $N_{v_\parallel}$ in the $v_\parallel$-direction was chosen to be an odd number to include 0 m s^{-1} in the discretization. Generating the synthetic spectra using coarser grids such as [51, 25] and [101, 50] results in a loss of details at the peaks; see Fig. 9.3.

For the projected velocities, $u/[10^6 \text{ m s}^{-1}] \in [-5, 5]$ with resolution 0.1×10^6 to obtain 101 points in the measured spectra. In this study, we investigate the reconstructions using five lines of sight with viewing angles $\phi = 10°$, 20°, 40°, 70°, and 85°. The weight functions are computed for each line of sight using Eq. (9.16) for the given range of projected velocities and combined in the matrix W_{cont}.

The Maxwellian 3D velocity-space distribution function

$$f_{\text{3D}}\left(v_\parallel, v_{\perp,1}, v_{\perp,2}\right) = \frac{n_e}{\pi^{3/2} v_{\text{th},\parallel} v_{\text{th},\perp}^2} \exp\left(-\left(\frac{v_\parallel - v_{\text{d}}}{v_{\text{th},\parallel}}\right)^2 - \left(\frac{v_\perp}{v_{\text{th},\perp}}\right)^2\right) \tag{9.22}$$

is used to model a velocity-space distribution function relevant for fusion-plasma conditions. Here,

$$v_{\text{d}} = 0.5 \times 10^6 \text{ m s}^{-1}, \tag{9.23}$$

$$v_{\text{th},\parallel} = 0.8 \times 10^6 \text{ m s}^{-1}, \tag{9.24}$$

$$v_{\text{th},\perp} = 0.8 \times 10^6 \text{ m s}^{-1}. \tag{9.25}$$

The corresponding 2D velocity-space distribution function is obtained by integrating over the gyroangle γ, giving

$$f_{\text{2D}}\left(v_\parallel, v_\perp\right) = 2\pi v_\perp f_{\text{3D}}\left(v_\parallel, v_{\perp,1}, v_{\perp,2}\right). \tag{9.26}$$

Using the modelled weight function matrix, we obtain the synthetic measurements by first computing the noise-free signal $s = W_{\text{cont}} f$ and subsequently adding noise as described above.

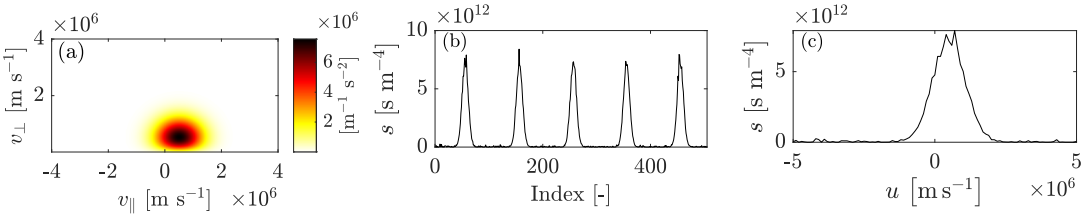

Figure 9.4: (a) Ground truth fast-ion velocity-space distribution function. (b) Synthetic spectra from five lines of sight with viewing angles $\phi = 10°$, $20°$, $40°$, $70°$, $85°$. (c) A single spectrum with 10% noise with the projected velocity on the x-axis.

The 2D velocity distribution and the corresponding synthetic measurements are illustrated in Fig. 9.4. The system matrix W_{inv} used to compute the reconstructions are computed as W_{cont} but with a coarser grid. The exact grids used will be indicated where relevant. Lastly, W_{inv} and s are normalized before computing the reconstructions.

9.5 Computing the optimal value of the regularization parameter

This investigation considers the dependence of the optimal value of the regularization parameter and the resulting reconstruction error $\|f^{\text{true}} - f\|_2^2$ on the grid size when computing solutions to the inverse problem in Eq. (9.1) using zeroth- and first-order Tikhonov regularization. A range of the regularization parameter $\lambda \in [10^{-6}, 10^{6}]$ was used for all investigations. Within this range, 50 linearly log-spaced values were used to compute a solution as given in Eq. (9.4). All 50 solutions were then compared to the ground truth. The solution with minimum squared error defined as

$$\Delta := \sum_i \left(f_i^{\text{true}} - f_i\right)^2, \tag{9.27}$$

was then determined as the solution corresponding to the optimal value of the regularization parameter. We denote this search the "first iteration". A second iteration was then conducted around this optimum value of the regularization parameter. This search includes 50 values spaced linearly between the two points closest to the optimum value in the previous search grid. This ensures that the minimum occurs for values included within the second iteration. Furthermore, the second search is sufficiently fine that any discrepancy between the actual true optimum value of the regularization parameter and that found by the search deviates by less than 10^{-3}. This minor discrepancy does not result in any significant changes to the reconstruction error of the optimal solution. As for the first iteration, the solution with minimum Δ was chosen as the solution corresponding to the optimum value of the regularization parameter. We call Δ the *reconstruction error*. Examples of the results of such a search of the optimum λ are illustrated in Fig. 9.5(a) and (b).

When conducting such a search for the optimum value of the regularization parameter, the reconstructed solution f needs to be compared with the ground truth f^{true}. This comparison requires that the two arrays have the same dimensions. This is not the case initially due to the

different grid sizes of the forward and inverse grid. The ground truth was computed using the forward grid with $[N_{v_\parallel}, N_{v_\perp}] = [1001, 500]$ number of grid points, and the reconstruction using the inverse grid $[n_{v_\parallel}, n_{v_\perp}]$ with a significantly smaller number of grid points. There are then three choices: either the reconstruction is interpolated onto the finer grid of the ground truth, the ground truth is interpolated onto the coarser grid of the reconstruction, or both the ground truth and the reconstruction are interpolated onto some other grid, e.g., grid sizes halfway between the larger and smaller grid-size values.

Interpolating one way or the other results in radically different values of the optimal regularization parameter and, therefore, different solutions. The differences are illustrated in Fig. 9.5. Interpolating the ground truth onto the coarser inverse grid produces the results for the regularization parameter search and corresponding reconstruction shown in subfigures (a) and (c). Interpolating the reconstruction onto the fine forward grid produces the results shown in subfigures (b) and (d). The optimal values of the regularization parameter using each method is $\lambda^{\text{opt}} = 0.0097$ and $\lambda^{\text{opt}} = 0.5756$ when interpolating the fine ground truth onto the coarse grid and when interpolating the coarse reconstruction onto the fine grid, respectively. Thus, an erroneous artificial smoothing is applied on the reconstructed solution when interpolating from coarse to fine. Compared to the ground truth illustrated in Fig. 9.4(a), the solution found when interpolating the ground truth onto the coarse inverse grid is preferable.

The significantly larger value of the optimal regularization parameter when interpolating the reconstructed solution onto the fine grid occurs since array entries with wrong values on the finer pixels are more likely to be introduced when interpolating the coarse reconstruction onto a finer grid. This is not the case when interpolating a fine solution onto a coarse grid. Only some details that can be captured on a finer grid might be lost, but no erroneous array entries are introduced. This is reflected in the larger value of the optimal regularization parameter when interpolating onto the fine grid: the optimal value of the regularization parameter is larger compared to interpolating the ground truth onto the coarse grid, indicating a solution with more smoothing and less details is better, i.e., the erroneous pixels are penalized.

Alternatively, the ground truth and the reconstruction could both be interpolated onto some other grid of choice, e.g., grid sizes halfway between the larger and smaller grid size values. However, our investigations show that such interpolation produces the same results as when the reconstruction is interpolated onto the fine grid. This is because of the above-mentioned effect from interpolating a coarse reconstruction onto a finer grid.

Thus, our investigations are performed by interpolating the fine ground truth onto the coarse inverse grid to determine the optimal value of the regularization parameter and the corresponding solution with lowest reconstruction error.

9.6 Grid-dependence in zeroth- and first-order Tikhonov regularization

This section investigates how the number of grid points used in the inverse grid $[n_{v_\parallel}, n_{v_\perp}]$ influences the optimal value of the regularization parameter and the reconstruction error.

We compute the optimal value of the regularization parameter and the reconstruction error for different grid sizes, where the number of grid points in one dimension is kept constant and the other varied. One-dimensional plots of the optimal value of the regularization parameter and the reconstruction error can then be plotted as a function of the variable number of grid points. The results are shown in Fig. 9.6.

In subfigures (a) and (b), $n_{v_\parallel}$ is kept constant at the values indicated and $n_{v_\perp}$ varied from 10 to 51. The optimal value of the regularization parameter decreases with an increasing number of

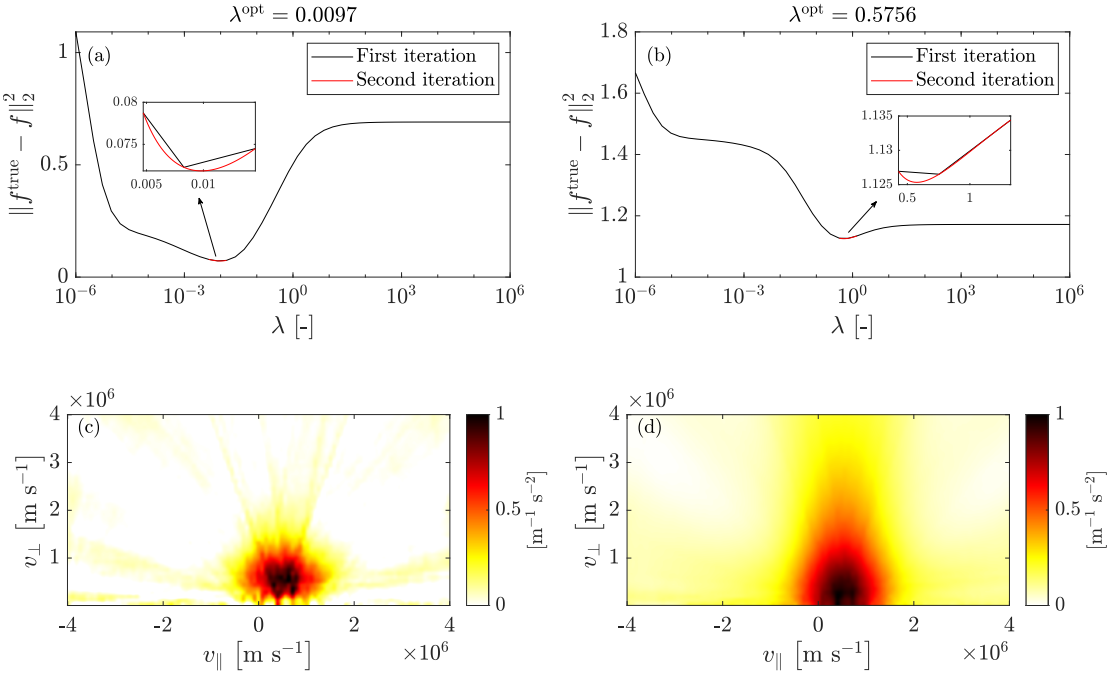

Figure 9.5: (a) The optimal regularization parameter for the synthetic measurement shown in Fig. 9.4(b) computed using zeroth-order Tikhonov regularization by interpolating the ground truth onto the dimensions of the inverse grid with $[n_{v_\parallel}, n_{v_\perp}] = [101, 50]$, and (b) by interpolating the reconstruction onto the grid dimensions of the ground truth with $[N_{v_\parallel}, N_{v_\perp}] = [1001, 500]$. Subfigures (c) and (d) illustrate the normalized reconstructions computed using the optimal values of the regularization parameters as determined by the minima of the curves in (a) and (b).

grid points, indicating a *reduced* need for regularization, i.e., the data-fitting term $\|Wf - s\|_2^2$ is valued higher in the trade-off between the data-fitting and the regularization term when discretizing using more grid points. This decrease continues until $n_{v_\perp} \approx 30$, after which the optimal value of the regularization parameter and the reconstruction error remain constant. The same effect is observed when keeping $n_{v_\perp}$ constant and varying $n_{v_\parallel}$. The cases with $n_{v_\perp} = 25, 40$, and 50 and $n_{v_\parallel}$ varied from 10 to 101 are illustrated in subfigures 9.6(c) and (d).

Typically, including additional measurements in the signal data vector s improves the computed reconstruction and reduces the reconstruction error.[2] To ensure that the effect observed in Fig. 9.6 results from the grid discretization and an insufficient amount of data, we perform the same computations with ten spectra, i.e., an increase of 100% in the amount of data. The additional data results in an improved solution, as seen by its lower reconstruction error; see Fig. 9.7. The discretization effect is still prevalent with a constant value of the optimal regularization parameter and reconstruction error occurring for grid sizes with $n_{v_\perp} \approx 30$.

Next, we illustrate the above results in two dimensions. The optimal value of the regularization parameter and the reconstruction error for all grid sizes $n_{v_\parallel}, n_{v_\perp} \in [10, 51]$ are plotted in Fig. 9.8. Again the trend of a decreasing optimal value of the regularization parameter and a decreasing value of the reconstruction error with an increasing number of grid points is apparent. From Fig. 9.8(b), we see that the number of grid points in $v_\parallel$ plays a significantly larger role than the

[2] Schmidt et al. (2023).

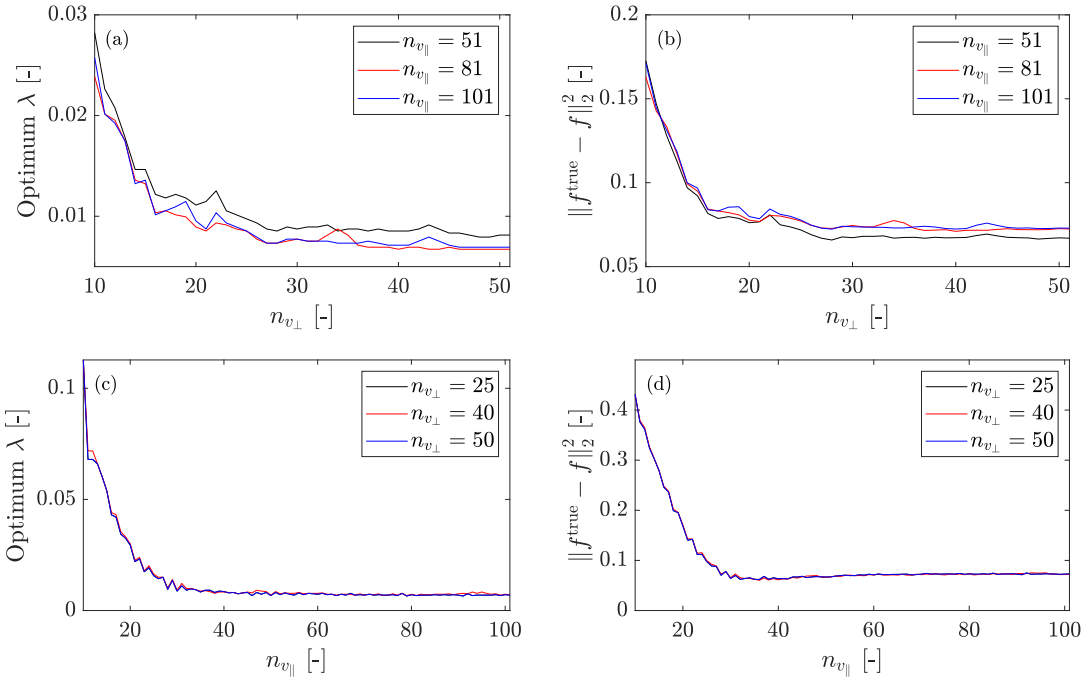

Figure 9.6: (a) Optimal value of the regularization parameter and (b) reconstruction error for $n_{v_\parallel} = 51, 81$, and 101 as a function of $n_{v_\perp}$. (c) Optimal value of the regularization parameter and (d) reconstruction error for $n_{v_\perp} = 25, 40$, and 50 as a function of $n_{v_\parallel}$.

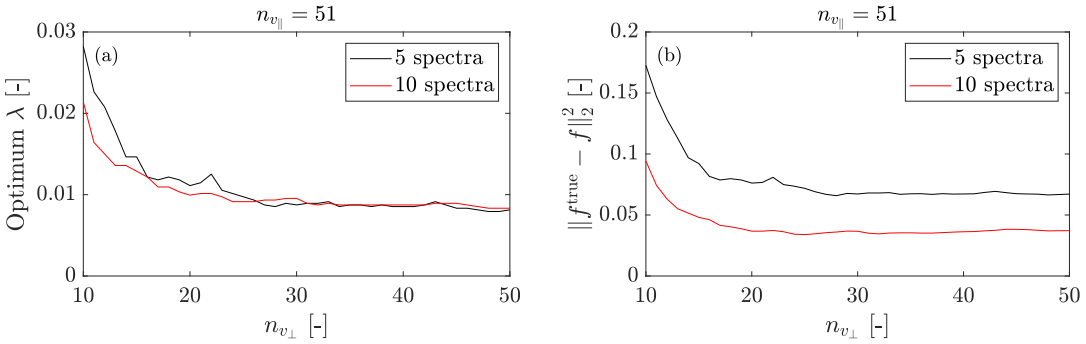

Figure 9.7: (a) Optimal value of the regularization parameter and (b) reconstruction error for $n_{v_\parallel} = 51$ as a function of $n_{v_\perp}$ for measurements consisting of 5 and 10 spectra.

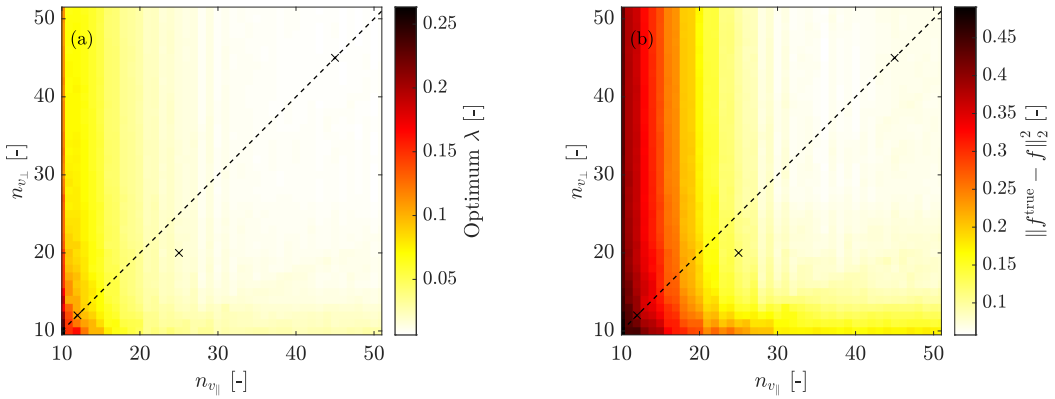

Figure 9.8: (a) Optimal value of the regularization parameter and (b) reconstruction error for $n_{v_\parallel}$ and $n_{v_\perp}$ in the range [10, 51]. The three black crosses at (12, 12), (25, 20), and (45, 45) indicate the locations used for Fig. 9.9. The dashed line indicates the locations used for Figs. 9.11 and 9.12.

number of grid points in $v_\perp$. Only increasing $n_{v_\parallel}$ reduces the reconstruction error considerably. A small effect is seen for $n_{v_\perp} \gtrsim 10$, where the grid is so coarse that increases in $n_{v_\perp}$ also improves the reconstruction error.

Figure 9.9 provides example reconstructions at different grid sizes. The figure shows the ground truth interpolated to grids of different sizes in the first column, the corresponding optimal reconstruction in the second column, and the normalized absolute residual matrix R in the third column. The normalized absolute residual matrix is computed as

$$R \equiv \frac{|f^{\text{true}} - f|}{\max(|f^{\text{true}} - f|)}. \tag{9.28}$$

The matrix R illustrates the locations in velocity space where the reconstruction deviates from the ground truth. For the coarse grid [12, 12] in the top row of Fig. 9.9, the solution significantly overestimates the extent of the distribution in $v_\perp$. Increasing the resolution in $v_\perp$ by adding additional grid points does not improve the reconstruction, as can be seen from Fig. 9.8(b). Thus, the number of grid points is too low in $v_\parallel$ for the solution to improve the coverage in $v_\perp$. The explanation for this is the discretization of the weight functions.

Inspection of the weight functions shows that the sensitivities of the weight functions in the system matrix modelling the physical system depend primarily on the number of grid points in $v_\parallel$, and not $v_\perp$. For example, consider the weight function for $\phi = 10°$ and $u = 0$ m s^{-1} illustrated in Fig. 9.10. The weight function is computed using a different number of grid points. The observable region of this weight function is centered at $u = 0$ m s^{-1} and extends into $v_\perp$. Using a coarse grid, the weight function loses its sensitivity for $v_\perp \leq 1.8 \times 10^6$ m s^{-1}. Increasing the number of grid points in $v_\perp$ does not improve this sensitivity. Instead, an increas in the number of grid points in $v_\parallel$ is required to improve the sensitivity in $v_\perp$. This effect is what gives rise to the phenomenon in Fig. 9.8: for a given $n_{v_\parallel}$, the reconstruction error remains the same independent of $n_{v_\perp}$. The details of the weight function increases when increasing the number of grid points in $v_\parallel$.

Thus, one reason for the poor reconstructions is a loss of detail in the weight functions of the system matrix.

Thus, as the number of grid points in $v_\parallel$ increases, the detail and information carried in the inverse grid increases. When $n_{v_\parallel}$ is sufficiently large, which occurs around $n_{v_\parallel} \approx 30$, the edges

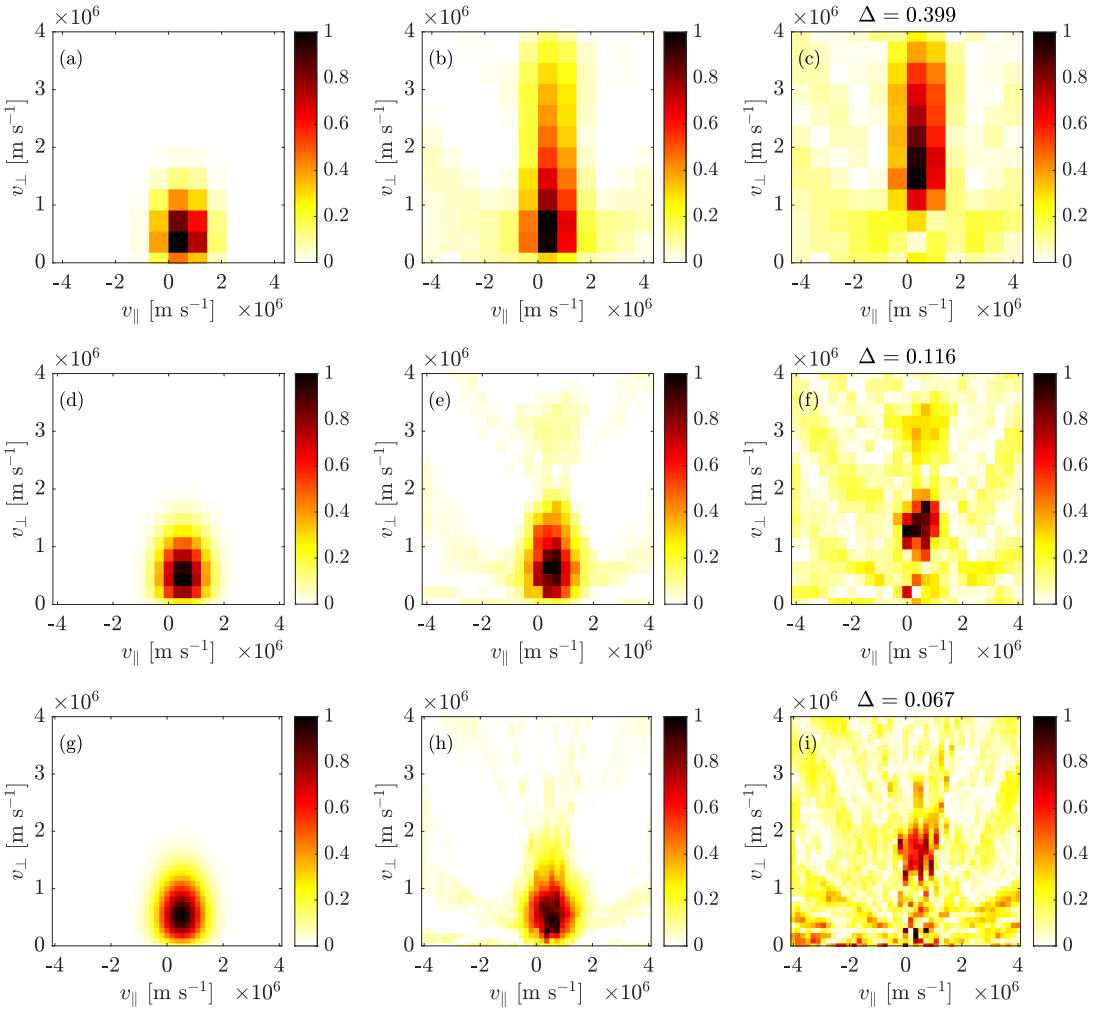

Figure 9.9: Subfigures (a), (d), and (g) illustrate the ground truth for the grid sizes $[12, 12]$, $[25, 20]$, and $[45, 45]$. The locations of these grid sizes are indicated on the 2D reconstruction error plot on Fig. 9.8(b). Subfigures (b), (e), and (h) illlustrate the reconstruction using these grid sizes as the inverse grid. Subfigures (c), (f), and (i) illustrate the normalized residual matrix.

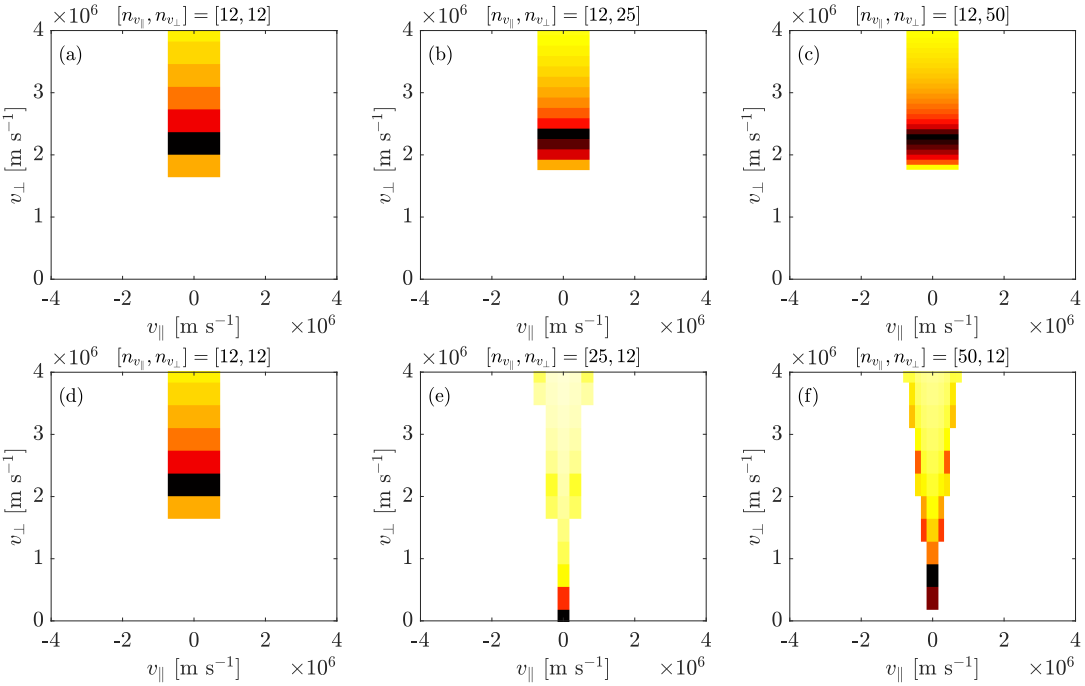

Figure 9.10: Subfigures (a), (b), and (c) illustrate the weight function for $\phi = 10°$ and $u = 0$ m s^{-1} computed using the number of grid points indicated, with an increasing number of grid points in $v_\perp$ from left to right. Subfigures (d), (e), and (f) illustrate the weight function for $\phi = 10°$ and $u = 0$ m s^{-1} computed using the number of grid points indicated, with an increasing number of grid points in $v_\parallel$ from left to right. The colorbar is removed for simplicity, but the same colorbar as shown in Fig. 9.9 was used.

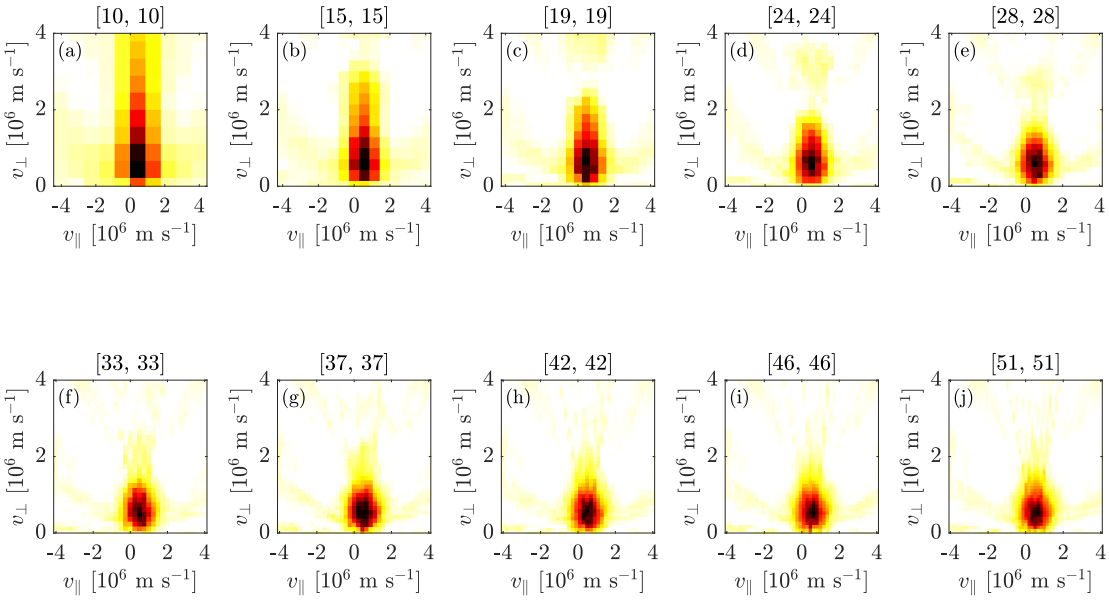

Figure 9.11: Zeroth-order Tikhonov regularization: Reconstructions of the ground truth in Fig. 9.4(a) computed using the grid size indicated above each subfigure. The colorbar used is identical to that in Fig. 9.9.

of the observable regions of the weight functions have a significantly higher sensitivity than the centers of the observable regions. When $v_\parallel$ is too coarse, the weight functions do not indicate this difference, and detail is lost in the system matrix.

The solutions computed using zeroth-order Tikhonov regularization as a function of the number of grid points are illustrated in Fig. 9.11. The grid sizes were chosen along the dashed diagonal indicated in Fig. 9.8 to produce solutions with a high to low reconstruction error. The increasingly detailed weight functions with coverage closer to $v_\perp = 0$ m s^{-1} allows the solution to extend less into high values of $v_\perp$.

The same effect as described above occurs for first-order Tikhonov regularization. In this case, the operator L is chosen such that

$$L^T L = \nabla_{v_\parallel}^T \nabla_{v_\parallel} + \nabla_{v_\perp}^T \nabla_{v_\perp}, \tag{9.29}$$

where $\nabla_{v_\parallel}$ and $\nabla_{v_\perp}$ are first-order finite-difference approximations of the partial derivatives with respect to $v_\parallel$ and $v_\perp$.[3] The solutions computed in this manner as a function of the number of grid points are very similar to those computed using zeroth-order Tikhonov regularization. See Fig. 9.12 for the solutions computed using first-order Tikhonov regularization for the same grid sizes as in Fig. 9.11.

[3] Jacobsen (2015).

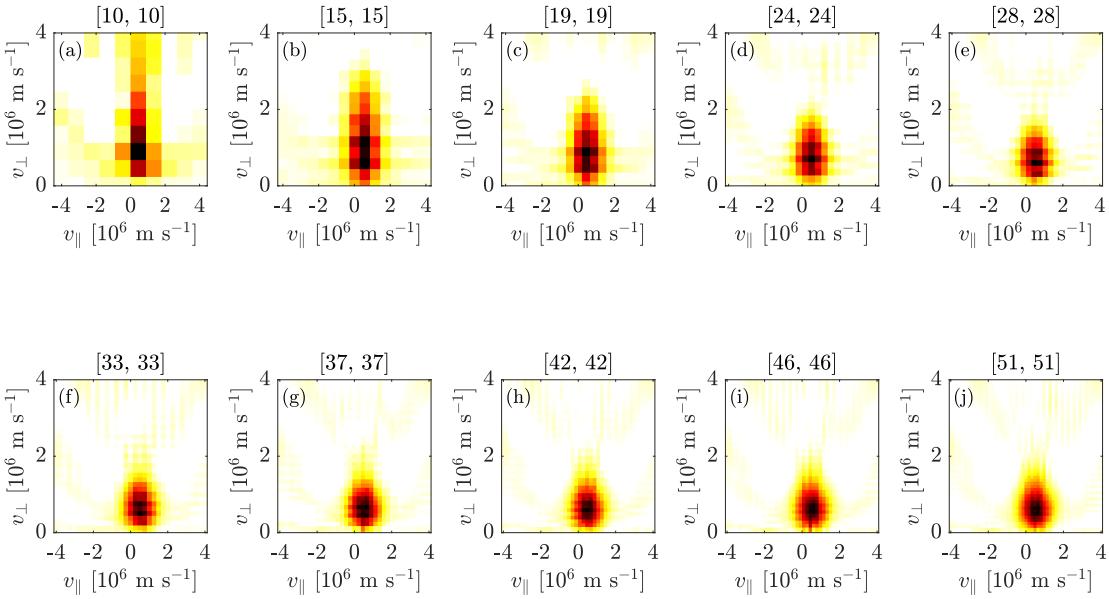

Figure 9.12: First-order Tikhonov regularization: Reconstructions of the ground truth in Fig. 9.4(a) computed with the grid size indicated above each subfigure. Axes are not of equal length for illustration purposes. The colorbar used is identical to that used in Fig. 9.9.

9.7 Conclusion

In this work, we have systematically investigated the influence of the grid discretization on the optimal value of the regularization parameter and the reconstruction error for an ill-posed inverse problem, specifically in the context of projections of fast-ion velocities in fusion plasmas.

When investigating a reconstruction approach to solve an ill-posed inverse problem using synthetic data, reconstructions computed using said approach must be compared with a ground truth. The reconstructions and the ground truth are typically not of the same dimensions. The decision on whether to interpolate the reconstructed solution onto the fine grid of the ground truth or to interpolate the fine ground truth onto the coarse grid of the reconstructed solution significantly affects the optimal value of the regularization parameter and the solution deemed to be optimal. Our study suggests that interpolating the fine ground truth onto the coarse grid of the reconstructed solution results in solutions closer to the ground truth.

The discretization of the domain of the matrix used to solve the inverse problem is important when investigating the performance of a reconstruction method. Specifically for reconstructing fast-ion velocity-space distribution functions using projections of fast-ion velocities in fusion plasmas, a coarse grid with less than 30 grid points in the $v_\parallel$-direction produces solutions with increasing reconstruction error the smaller number of grid points used in the discretization. The number of grid points in the $v_\perp$-direction does not play a large role in the value of the reconstruction error.

The poor reconstruction error results from loss of significant detail in the weight functions of the system matrix. An insufficient number of grid points in the $v_\parallel$-direction results in loss of weight function sensitivity in $v_\perp$. The weight functions discretized using around ten points in $v_\parallel$ are zero up to $v_\perp = 1.8 \times 10^6$ m s^{-1}. Thus, sensitivities of a large region of velocity space is neglected. Furthermore, weight functions on coarse grids lose their high sensitivities near the boundaries of the observable regions and instead have a constant value for a wide interval in $v_\parallel$.

Chapter 10

Conclusion and outlook

The research during this Ph.D. has contributed to advancements in fast-ion diagnostics in fusion plasmas, providing new methodologies and strategies to address ill-posed inverse problems in velocity-space tomography.

The research has successfully developed and applied the technique of slowing-down physics regularization to obtain fast-ion phase-space distribution functions of fast ions from projected velocities. The technique will be developed further to provide additional details of the fast-ion behaviour, with significant research effort already being devoted to this by the fast-ion group at the Plasma Physics and Fusion Energy section at DTU Physics. Therefore, the research in this Ph.D. has laid the foundation for future developments of the technique.

The 2D ion cyclotron emission weight functions developed provide improved fast-ion analysis and are the first of their kind. Notably, the weight functions and the associated reconstruction methods can be used to determine the velocity-space location of ions emitting ion cyclotron emission.

This research has explored alternative regularization methods to Tikhonov regularization, assessing their potential application in determining the fast-ion velocity-space distribution function in fusion plasmas. Iterative algebraic reconstruction techniques were evaluated and compared with Tikhonov regularization, providing insights into their relative strengths and weaknesses.

The raised cosine model for FILDSIM provides more accurate modelling of the pinhole-scintillator relation in a FILD. With its ability to facilitate enhanced precision and increased computational speed, this model could pave the way for efficient inter-shot reconstructions of FILD measurements from full discharges. Further testing at other FILDs besides the FILD at TCV should be performed to investigate the performance improvement using the raised cosine model compared to the standard Gaussian model.

The potential of the application of deep neural networks in velocity-space tomography was investigated. The research indicates a significant potential for applying deep neural networks, with significant improvements in the reconstruction capability of a trained deep neural network on experimental FILD measurements. This also provides instantaneous reconstructions of the fast-ion velocity-space distribution function, both supplementing current reconstruction methods and paving the way for improved control of fusion plasmas using fast-ion diagnostics.

It is important to note that while these advancements offer promising avenues for future work, further investigations are required to validate these methods on a broader scale and in different fusion reactors. The findings of this research form the foundation for these future explorations and pave the way for continued innovations in the realm of fast-ion diagnostics in fusion plasmas.

Bibliography

Adelberger, E. G. et al. (2011). "Solar fusion cross sections. II. the pp chain and CNO cycles". *Reviews of Modern Physics* **83**(1), pp. 195–245.

AGU, A. G. U. (2019). *Position Statement on Climate Change: Society Must Address the Growing Climate Crisis Now*. `https://www.agu.org/Share-and-Advocate/Share/Policymakers/Position-Statements/Position_Climate`. Accessed: 09-02-2023.

Anderegg, W. R. et al. (2010). "Expert credibility in climate change". *Proceedings of the National Academy of Sciences of the United States of America* **107**(27), pp. 12107–12109.

Andersen, M. S. and P. C. Hansen (2014). "Generalized Row-Action Methods for Tomographic Imaging". *Numerical Algorithms* **67**(1), pp. 121–144.

Anton, M. et al. (1996). "X-ray tomography on the TCV tokamak". *Plasma Physics and Controlled Fusion* **38**(11), pp. 1849–1878.

Appel, L. C. et al. (2008). "Compressional alfvén eigenmodes on MAST". *Plasma Physics and Controlled Fusion* **50**(11), p. 115011.

APS, A. P. S. (2007). *07.1 Climate Change*. `https://www.aps.org/policy/statements/07_1.cfm`. Accessed: 23-05-2023.

Ayllon-Guerola, J. et al. (2021). "Thermo-mechanical assessment of the JT-60SA fast-ion loss detector". *Fusion Engineering and Design* **167**, p. 112304.

Baeumel, S. et al. (2004). "Scintillator probe for lost alpha measurements in JET". *Review of Scientific Instruments* **75**(10), pp. 3563–3565.

Belikov, V. S. and Y. I. Kolesnichenko (1975). "Magnetoacoustic cyclotron instability in a thermonuclear plasma". *Sov. Phys. Tech. Phys.* **20**(9), pp. 1146–1151.

Birks, J. B. (1951). "Scintillations from organic crystals - Specific flourescence and relative response to different radiations". *Proceedings of the Physical Society of London Section a* **64**(382), pp. 874–877.

Bonofiglo, P. J. et al. (2020). "Improvements to the Faraday cup fast ion loss detector and magnetohydrodynamic induced fast ion loss measurements in Joint European Torus plasmas". *Review of Scientific Instruments* **91**(9), p. 093502.

Bornatici, M. et al. (1983). "Electron cyclotron emission and absorption in fusion plasmas". *Nuclear Fusion* **23**(9), pp. 1153–1257.

Budny, R. et al. (1995). "Simulations of alpha parameters in a TFTR DT supershot with high fusion power". *Nuclear Fusion* **35**(12), pp. 1497–1508.

Buli, N. and S. Jacobsen (2021). *Analysis: Weak winds worsened Europe's power crunch; utilities need better storage*. `https://www.reuters.com/markets/commodities/weak-winds-worsened-europes-power-crunch-utilities-need-better-storage-2021-12-22/`. Accessed: 11-02-2023.

Bustos, A. et al. (2011). "Kinetic simulations of fast ions in stellarators". *Nuclear Fusion* **51**(8), p. 083040.

Cairns, R. A. (1985). *Plasma physics*. Blackie [u.a.]

Carbajal, L. et al. (2014). “Linear and nonlinear physics of the magnetoacoustic cyclotron instability of fusion-born ions in relation to ion cyclotron emission”. *Physics of Plasmas* **21**(1), p. 012106.
— (2017). “Quantifying Fusion Born Ion Populations in Magnetically Confined Plasmas using Ion Cyclotron Emission”. *Physical Review Letters* **118**(10), p. 105001.
Cauffman, S. et al. (1995). “Alfvenic behaviour of alpha particle driven ion cyclotron emission in TFTR”. *Nuclear Fusion* **35**(12), pp. 1597–1602.
Cauffman, S. and R. Majeski (1995). “Ion-cyclotron emission on the Tokamak Fusion Test Reactor”. *Review of Scientific Instruments* **66**(1), pp. 817–819.
Chang, J. F. et al. (2016). “Scintillator-based fast ion loss measurements in the EAST”. *Review of Scientific Instruments* **87**(11), 11E728.
Chapman, B. et al. (2017). “Sub-microsecond temporal evolution of edge density during edge localized modes in KSTAR tokamak plasmas inferred from ion cyclotron emission”. *Nuclear Fusion* **57**(12), p. 124004.
Chapman, B. et al. (2018). “Nonlinear wave interactions generate high-harmonic cyclotron emission from fusion-born protons during a KSTAR ELM crash”. *Nuclear Fusion* **58**(9), p. 096027.
— (2019). “Interpretation of suprathermal emission at deuteron cyclotron harmonics from deuterium plasmas heated by neutral beam injection in the KSTAR tokamak”. *Nuclear Fusion* **59**(10), p. 106021.
Chapman, B. et al. (2020). “Origin of ion cyclotron emission at the proton cyclotron frequency from the core of deuterium plasmas in the ASDEX-Upgrade tokamak”. *Plasma Physics and Controlled Fusion* **62**(9), p. 095022.
Chen, F. F. (2016). *Introduction to Plasma Physics and Controlled Fusion*. Springer.
Cook, J. W., R. O. Dendy, and S. C. Chapman (2013). “Particle-in-cell simulations of the magnetoacoustic cyclotron instability of fusion-born alpha-particles in tokamak plasmas”. *Plasma Physics and Controlled Fusion* **55**(6), p. 065003.
Cottrell, G. A. and R. O. Dendy (1988). “Superthermal radiation from fusion products in JET”. *Physical Review Letters* **60**(1), pp. 33–36.
Cottrell, G. A. et al. (1993). “Ion-cyclotron emission measurements during JET deuterium-tritium experiments”. *Nuclear Fusion* **33**(9), pp. 1365–1387.
Crocker, N. A. et al. (2022). “Novel internal measurements of ion cyclotron frequency range fast-ion driven modes”. *Nuclear Fusion* **62**(2), p. 026023.
Darrow, D. S. (2008). “Scintillator based energetic ion loss diagnostic for the National Spherical Torus Experiment”. *Review of Scientific Instruments* **79**(2), p. 023502.
Darrow, D. S. et al. (2004). “Design and construction of a fast ion loss Faraday cup array diagnostic for Joint European Torus”. *Review of Scientific Instruments* **75**(10), pp. 3566–3568.
Darwin, C. (1920). “LI. The dynamical motions of charged particles”. *London, Edinburgh, and Dublin Philosophical Magazine and Journal of Science* **39**(233), pp. 537–551.
DeGrandchamp, G. H. et al. (2022). “Mode structure measurements of ion cyclotron emission and sub-cyclotron modes on DIII-D”. *Nuclear Fusion* **62**(10), p. 106033.
Degrave, J. et al. (2022). “Magnetic control of tokamak plasmas through deep reinforcement learning”. *Nature* **602**(7897), pp. 414–419.
Dendy, R. O., C. N. Lashmoredavies, and K. F. Kam (1992). “A possible excitation mechanism for observed superthermal ion-cyclotron emission from tokamak plasmas”. *Physics of Fluids B-plasma Physics* **4**(12), pp. 3996–4006.
— (1993). “The magnetoacoustic cyclotron instability of an extended shell distribution of energetic ions”. *Physics of Fluids B-plasma Physics* **5**(7), pp. 1937–1944.
Dendy, R. O. and K. G. McClements (2015). “Ion cyclotron emission from fusion-born ions in large tokamak plasmas: A brief review from JET and TFTR to ITER”. *Plasma Physics and Controlled Fusion* **57**(4), p. 044002.

Dendy, R. O. et al. (1994). "The excitation of obliquely propagating fast Alfvén waves at fusion ion-cyclotron harmonics". *Physics of Plasmas* **1**(6), pp. 1918–1928.

Dendy, R. O. et al. (1995). "Ion cyclotron emission due to collective instability of fusion products and beam ions in TFTR and JET". *Nuclear Fusion* **35**(12), pp. 1733–1742.

Dendy, R. O. et al. (2023). "Mechanism for Collective Energy Transfer from Neutral Beam-Injected Ions to Fusion-Born Alpha Particles on Cyclotron Timescales in a Plasma". *Physical Review Letters* **130**(10), p. 105102.

Donné, A. J. H. et al. (2007). "Chapter 7: Diagnostics". *Nuclear Fusion* **47**(6), S337.

Duong, H. H. et al. (1993). "Loss of energetic beam ions during TAE instabilities". *Nuclear Fusion* **33**(5), pp. 749–765.

Earth System Research Laboratories, G. M. L. (2023). *NOAA Mauna Loa CO_2 record*. `https://gml.noaa.gov/dv/iadv/graph.php?code=MLO&program=ccgg&type=ts`. Accessed: 11-02-2023.

Eriksson, J. et al. (2019). "Measuring fast ions in fusion plasmas with neutron diagnostics at JET". *Plasma Physics and Controlled Fusion* **61**(1), p. 014027.

Fasoli, A. et al. (2007). "Chapter 5: Physics of energetic ions". *Nuclear Fusion* **47**(6), S05.

Fisher, R. A. (1959). *Statistical methods and scientific inference, 2. ed.* Oliver and Boyd,

Fisher, R. K. et al. (2010). "Scintillator-based diagnostic for fast ion loss measurements on DIII-D". *Review of Scientific Instruments* **81**(10), p. 10D307.

Fredrickson, E. D. et al. (2001). "Observation of compressional Alfvén modes during neutral-beam heating on the National Spherical Torus Experiment". *Physical Review Letters* **87**(14), p. 145001.

Fredrickson, E. D. et al. (2019). "Emission in the ion cyclotron range of frequencies (ICE) on NSTX and NSTX-U". *Physics of Plasmas* **26**(3), p. 032111.

Fredrickson, E. D. et al. (2021). "Chirping ion cyclotron emission (ICE) on NSTX-U". *Nuclear Fusion* **61**(8), p. 086007.

Frieden, B. R. (1988). "Applications to optics and wave mechanics of the criterion of maximum Cramer-Rao bound". *Journal of Modern Optics* **35**(8), pp. 1297–1316.

Friedlingstein, P. et al. (2022). *Global Carbon Budget 2022*.

Friedman, I. (1953). "Deuterium content of natural waters and other substances". *Geochimica Et Cosmochimica Acta* **4**(1-2), pp. 89–103.

Galdon-Quiroga, J., M. Garcia-Munoz, M. Salewski, et al. (2018). "Velocity-space sensitivity and tomography of scintillator-based fast-ion loss detectors". *Plasma Physics and Controlled Fusion* **60**(10), p. 105005.

Galdon-Quiroga, J., M. Garcia-Munoz, L. Sanchis-Sanchez, et al. (2018). "Velocity space resolved absolute measurement of fast ion losses induced by a tearing mode in the ASDEX Upgrade tokamak". *Nuclear Fusion* **58**(3), p. 036005.

Galdon-Quiroga, J. et al. (2019). "Observation of accelerated beam ion population during edge localized modes in the ASDEX Upgrade tokamak". *Nuclear Fusion* **59**(6), p. 066016.

Galdon-Quiroga, J. (2018). "Velocity-space resolved measurements of fast-ion losses due to magnetohydrodynamic instabilities in the ASDEX Upgrade tokamak".

Garcia-Munoz, M. (2006). "Fast Response Scintillator Based Detector for MHD Induced Energetic Ion Losses in ASDEX Upgrade".

Garcia-Munoz, M., H. U. Fahrbach, and H. Zohm (2009). "Scintillator based detector for fast-ion losses induced by magnetohydrodynamic instabilities in the ASDEX upgrade tokamak". *Review of Scientific Instruments* **80**(5), p. 053503.

Garcia-Munoz, M. et al. (2010). "Fast-ion losses induced by ACs and TAEs in the ASDEX Upgrade tokamak". *Nuclear Fusion* **50**(8), p. 084004.

Garcia-Munoz, M. et al. (2013). "Fast-ion losses induced by ELMs and externally applied magnetic perturbations in the ASDEX Upgrade tokamak". *Plasma Physics and Controlled Fusion* **55**(12), p. 124014.

Garcia-Munoz, M. et al. (2016). "Conceptual design of the ITER fast-ion loss detector". *Review of Scientific Instruments* **87**(11), p. 11D829.

Goldberg, R. (1964). *Methods of real analysis*.

Gonzalez-Martin, J. et al. (2018). "First measurements of a scintillator based fast-ion loss detector near the ASDEX Upgrade divertor". *Review of Scientific Instruments* **89**(10), p. 10I106.

Gonzalez-Martin, J. et al. (2019). "First measurements of a magnetically driven fast-ion loss detector on ASDEX Upgrade". *Journal of Instrumentation* **14**(11), p. C11005.

Goodfellow, I. et al. (2016). *Deep learning*. The MIT Press, xxii, 775 Seiten (unknown).

Gorelenkov, N. N. (2016). "Ion cyclotron emission studies: Retrospects and prospects". *Plasma Physics Reports* **42**(5), pp. 430–439.

Grierson, B. A. et al. (2018). "Orchestrating TRANSP simulations for interpretative and predictive tokamak modeling with OMFIT". *Fusion Science and Technology* **74**(1-2), pp. 101–115.

Hansen, P. C. (1992). "Analysis of discrete ill-posed problems by means of the L-curve". *Siam Review* **34**(4), pp. 561–580.

Hansen, P. C. (2008). *Regularization Tools: A MATLAB Package for Analysis and Solution of Discrete Ill-Posed Problems*. `https://www.imm.dtu.dk/~pcha/Regutools/`. Described in: P. C. Hansen, *Regularization Tools Version 4.0 for Matlab 7.3*, Numerical Algorithms, 46 (2007), pp. 189-194.

— (2010). *Discrete Inverse Problems: Insight and Algorithms*. Society for Industrial and Applied Mathematics.

— (2019). *Inverse Problems - New challenges and new methods*. Presentation at IDA Matematik, 24-09-2019.

Hansen, P. C., T. K. Jensen, and G. Rodriguez (2007). "An adaptive pruning algorithm for the discrete L-curve criterion". *Journal of Computational and Applied Mathematics* **198**(2), pp. 483–492.

Heidbrink, W. W. (2010). "Fast-ion Dalpha measurements of the fast-ion distribution". *Review of Scientific Instruments* **81**(10), p. 10D727.

Heidbrink, W. W. and G. J. Sadler (1994). "The behavior of fast ions in tokamak experiments". *Nuclear Fusion* **34**(4), pp. 535–615.

Heidbrink, W. W. and R. B. White (2020). "Mechanisms of energetic-particle transport in magnetically confined plasmas". *Physics of Plasmas* **27**(3), p. 030901.

Heidbrink, W. W. et al. (2006). "Observation of compressional Alfvén eigenmodes (CAE) in a conventional tokamak". *Nuclear Fusion* **46**(2), pp. 324–334.

Heidbrink, W. W. et al. (2007). "Measurements of fast-ion acceleration at cyclotron harmonics using Balmer-alpha spectroscopy". *Plasma Physics and Controlled Fusion* **49**(9), pp. 1457–1475.

Heidbrink, W. et al. (2021). "Phase-space sensitivity (weight functions) of 3 MeV proton diagnostics". *Plasma Physics and Controlled Fusion* **63**(5), p. 055008.

Helander, P. (2014). "Theory of plasma confinement in non-axisymmetric magnetic fields". *Reports on Progress in Physics* **77**(8), p. 087001.

Hirvijoki, E. et al. (2014). "ASCOT: Solving the kinetic equation of minority particle species in tokamak plasmas". *Computer Physics Communications* **185**(4), pp. 1310–1321.

Hopf, C. (2013). *Operational Diagrams of the NBI on AUG*. `https://www.aug.ipp.mpg.de/foswiki/bin/view/ITED/NiauOpDiagrams`. Accessed: 26-05-2023.

Ichimura, M. et al. (2008). "Observation of spontaneously excited waves in the ion cyclotron frequency range on JT-60U". *Nuclear Fusion* **48**(3), p. 035012.

IEA, I. E. A. (2021). *Renewables 2021*. https://www.iea.org/reports/renewables-2021. Accessed: 21-03-2023.

ILO, I. L. O. (2022). *Renewable energy jobs hit 12.7 million globally*. https://www.ilo.org/global/about-the-ilo/newsroom/news/WCMS_856515/lang--en/index.htm. Accessed: 21-03-2023.

International Energy Agency (2022a). *World Energy Outlook 2022*. https://iea.blob.core.windows.net/assets/830fe099-5530-48f2-a7c1-11f35d510983/WorldEnergyOutlook2022.pdf. Accessed: 11-02-2023.

— (2022b). *World Energy Outlook 2022: Executive Summary*. https://www.iea.org/reports/world-energy-outlook-2022/executive-summary. Accessed: 11-02-2023.

Internet Geography (2023). *Why is energy consumption increasing*. https://www.internetgeography.net/topics/why-is-energy-consumption-increasing/. Accessed: 11-02-2023.

IPCC, I. P. C. C. (2022). *IPCC Fifth Assessment Report: Summary for Policymakers*. https://www.ipcc.ch/site/assets/uploads/2018/02/ipcc_wg3_ar5_summary-for-policymakers.pdf. Accessed: 09-02-2023.

ITER (2014). *Who "invented" fusion?* https://www.iter.org/mag/3/29. Accessed: 13-02-2023.

— (2022a). *Deuterium: a precious gift from the Big Bang*. https://www.iter.org/newsline/167/631. Accessed: 13-02-2023.

— (2022b). *ITER: Tritium Breeding*. https://www.iter.org/mach/TritiumBreeding. Accessed: 13-02-2023.

— (2022c). *Measuring the behaviour of fast ions in the plasma*. https://www.iter.org/newsline/-/3799. Accessed: 21-02-2023.

— (2022d). *What is ITER?* https://www.iter.org/proj/inafewlines. Accessed: 21-02-2023.

Jacobsen, A. S. et al. (2017). "Velocity-space sensitivities of neutron emission spectrometers at the tokamaks JET and ASDEX upgrade in deuterium plasmas". *Review of Scientific Instruments* **88**(7), p. 073506.

Jacobsen, A. S. (2015). "Methods to determine fast-ion distribution functions from multi-diagnostic measurements".

Jacobsen, A. S. et al. (2015). "Velocity-space sensitivity of neutron spectrometry measurements". *Nuclear Fusion* **55**(5), p. 053013.

Jacobsen, A. S. et al. (2016a). "Benchmark and combined velocity-space tomography of fast-ion D-alpha spectroscopy and collective Thomson scattering measurements". *Plasma Physics and Controlled Fusion* **58**(4), p. 042002.

— (2016b). "Benchmark and combined velocity-space tomography of fast-ion D-alpha spectroscopy and collective Thomson scattering measurements". *Plasma Physics and Controlled Fusion* **58**(4), p. 042002.

Jansen Van Vuuren, A. et al. (2022). "Conceptual Design of a Scintillator-Based Fast-Ion Loss Detector for the Wendelstein 7-X Stellarator". *Ieee Transactions on Plasma Science* **50**(11), pp. 4114–4119.

Järleblad, H. et al. (2021). "Fast-ion orbit sensitivity of neutron emission spectroscopy diagnostics". *Review of Scientific Instruments* **92**(4), p. 043526.

Järleblad, H. et al. (2022). "Fast-ion orbit sensitivity of neutron and gamma-ray diagnostics for one-step fusion reactions". *Nuclear Fusion* **62**(11), p. 112005.

Jiménez-Ramos, M. C. et al. (2014). "Characterization of scintillator materials for fast-ion loss detectors in nuclear fusion reactors". *Nuclear Instruments and Methods in Physics Research, Section B: Beam Interactions With Materials and Atoms* **332**, pp. 216–219.

Karpushov, A. N. (2022). *Neutral Beamns on TCV*. Presentation at SPC, 25-03-2022.

Kazakov, Y. O. et al. (2020). "Plasma heating and generation of energetic D ions with the 3-ion ICRF + NBI scenario in mixed H-D plasmas at JET-ILW". *Nuclear Fusion* **60**(11), p. 112013.

Kenstler, B. (2016). *Cyclical Learning Rate*. `https://github.com/bckenstler/CLR`.
Kim, J. et al. (2012). "Initial measurements of fast ion loss in KSTAR". *Review of Scientific Instruments* **83**(10), p. 10D305.
Kress, R. (2014). *Linear Integral Equations*. Springer New York.
Lazerson, S. A. et al. (2020). "Validation of the BEAMS3D neutral beam deposition model on Wendelstein 7-X". *Nuclear Fusion* **60**(7), p. 076020.
Lazerson, S. A. et al. (2021). "Modeling and measurement of energetic particle slowing down in Wendelstein 7-X". *Nuclear Fusion* **61**(9), p. 096005.
Levitus, S. et al. (2012). "World ocean heat content and thermosteric sea level change (0-2000m), 1955-2010". *Geophysical Research Letters* **39**(10), p. L10603.
Liu, L., R. Ochoukov, and A. Anders (2023). *Interpretation of ion cyclotron emission from sub-Alfvénic beam injected ions heated plasmas during L-H mode transition in EAST*. Submitted to Nuclear Fusion.
Liu, L. N. et al. (2019). "Ion cyclotron emission diagnostic system on the experimental advanced superconducting tokamak and first detection of energetic-particle-driven radiation". *Review of Scientific Instruments* **90**(6), p. 063504.
Liu, L. et al. (2021). "Explanation of core ion cyclotron emission from beam-ion heated plasmas in ASDEX Upgrade by the magnetoacoustic cyclotron instability". *Nuclear Fusion* **61**(2), p. 026004.
Loffelmann, V. et al. (2016). "Minimum Fisher Tikhonov regularization adapted to real-time tomography". *Fusion Science and Technology* **69**(2), pp. 505–513.
Madsen, B., J. Huang, et al. (2020). "Fast-ion velocity-space tomography using slowing-down regularization in EAST plasmas with co- and counter-current neutral beam injection: Paper". *Plasma Physics and Controlled Fusion* **62**(11), p. 115019.
Madsen, B., M. Salewski, et al. (2020). "Tomography of the positive-pitch fast-ion velocity distribution in DIII-D plasmas with Alfvén eigenmodes and neoclassical tearing modes". *Nuclear Fusion* **60**(6), p. 066024.
Madsen, B. et al. (2018). "Velocity-space tomography using prior information at MAST". *Review of Scientific Instruments* **89**(10), p. 10D125.
Mantsinen, M. J. et al. (2007). "Analysis of ICRF-accelerated ions in ASDEX upgrade". *Aip Conference Proceedings* **933**(1). Ed. by P. M. Ryan and D. Rasmussen, pp. 99–102.
McClements, K. G. and R. O. Dendy (1993). "Ion-cyclotron harmonic wave generation by ring protons in space plasmas". *Journal of Geophysical Research-space Physics* **98**(A7), pp. 11689–11700.
McClements, K. G. et al. (1996). "Interpretation of ion cyclotron emission from sub-Alfvénic fusion products in the Tokamak Fusion Test Reactor". *Physics of Plasmas* **3**(2), pp. 543–553.
McClements, K. G. et al. (1999). "Ion cyclotron emission from JET D-T plasmas". *Physical Review Letters* **82**(10), pp. 2099–2102.
McClements, K. G. et al. (2015). "Fast particle-driven ion cyclotron emission (ICE) in tokamak plasmas and the case for an ICE diagnostic in ITER". *Nuclear Fusion* **55**(4), p. 043013.
McNeely, P. et al. (2020). "Commissioning and initial operation of the W7-X neutral beam injection heating system". *Fusion Engineering and Design* **161**, p. 111997.
Mencke, J. E. et al. (2022). "Characterization of correlations of fast-ion H-alpha measurement volumes in Wendelstein 7-X by particle tracking". *Review of Scientific Instruments* **93**(12), p. 123503.
Moseev, D. et al. (2021). "Development of the ion cyclotron emission diagnostic for the W7-X stellarator". *Review of Scientific Instruments* **92**(3), p. 033546.
Moseev, D. and M. Salewski (2019). "Bi-Maxwellian, slowing-down, and ring velocity distributions of fast ions in magnetized plasmas". *Physics of Plasmas* **26**(2), p. 020901.

Moseev, D. et al. (2018). "Recent progress in fast-ion diagnostics for magnetically confined plasmas". *Reviews of Modern Plasma Physics* **2**(1), 7 (68 pp.)

NASA, N. (2023a). *How Do We Know Climate Change Is Real?* `https://climate.nasa.gov/evidence/`. Accessed: 09-02-2023.

— (2023b). *Is the Sun causing global warming?* `https://climate.nasa.gov/faq/14/is-the-sun-causing-global-warming/`. Accessed: 11-02-2023.

— (2023c). *NASA Says 2022 Fifth Warmest Year on Record, Warming Trend Continues.* `https://www.nasa.gov/press-release/nasa-says-2022-fifth-warmest-year-on-record-warming-trend-continues/`. Accessed: 11-02-2023.

— (2023d). *The Causes of Climate Change.* `https://climate.nasa.gov/causes/`. Accessed: 11-02-2023.

Nerem, R. S. et al. (2018). "Climate-change–driven accelerated sea-level rise detected in the altimeter era". *Proceedings of the National Academy of Sciences of the United States of America* **115**(9), pp. 2022–2025.

Nishiura, M. et al. (2004). "Scintillator probe diagnostic for high energy particles escaped from Large Helical Device". *Review of Scientific Instruments* **75**(10), pp. 3646–3648.

Nocente, M., A. D. Molin, et al. (2020). "MeV range particle physics studies in tokamak plasmas using gamma-ray spectroscopy". *Plasma Physics and Controlled Fusion* **62**(1), p. 014015.

Nocente, M., Y. Kazakov, et al. (2020). "Generation and observation of fast deuterium ions and fusion-born alpha particles in JET D-³He plasmas with the 3-ion radio-frequency heating scenario". *Nuclear Fusion* **60**(12), p. 124006.

Ochoukov, R., R. Bilato, V. Bobkov, B. Chapman, et al. (2019). "Core plasma ion cyclotron emission driven by fusion-born ions". *Nuclear Fusion* **59**(1), p. 014001.

Ochoukov, R., K. McClements, et al. (2019). "Interpretation of core ion cyclotron emission driven by sub-Alfvénic beam-injected ions via magnetoacoustic cyclotron instability: Paper". *Nuclear Fusion* **59**(8), p. 086032.

Ochoukov, R. et al. (2020). "High frequency Alfvén eigenmodes detected with ion-cyclotron-emission diagnostics during NBI and ICRF heated plasmas on the ASDEX Upgrade tokamak: Paper". *Nuclear Fusion* **60**(12), p. 126043.

Ochoukov, R. et al. (2023). "Analysis of high frequency Alfvén eigenmodes observed in ASDEX Upgrade plasmas in the presence of RF-accelerated NBI ions". *Nuclear Fusion* **63**(4), p. 046001.

Ogawa, K. et al. (2019). "Energy-and-pitch-angle-resolved escaping beam ion measurements by Faraday-cup-based fast-ion loss detector in Wendelstein 7-X". *Journal of Instrumentation* **14**(9), p. C09021.

Ohlendorf, N. and W. P. Schill (2020). "Frequency and duration of low-wind-power events in Germany". *Environmental Research Letters* **15**(8), p. 084045.

Our World in Data (2023). *Energy Production and Consumption.* `https://ourworldindata.org/energy-production-consumption`. Accessed: 11-02-2023.

Ozaki, T. et al. (2012). "Perpendicular and tangential angularly resolved multi-sight neutral particle analyzer system in LHD". *Review of Scientific Instruments* **83**(10), p. 10D920.

Pankin, A. et al. (2004). "The tokamak Monte Carlo fast ion module NUBEAM in the national transport code collaboration library". *Computer Physics Communications* **159**(3), pp. 157–184.

Poley-Sanjuan, J. et al. (2023). *Simultaneous measurement of co- and counter-current ions with a Fast IOn Loss Detector on the TCV tokamak.* 5th European Conference on Plasma Diagnostics (ECPD), 2023.

Rae, J. W. et al. (2021). "Atmospheric CO_2 over the past 66 million years from marine archives". *Annual Review of Earth and Planetary Sciences* **49**(1), pp. 609–641.

Reidmiller, D. et al. (2018). *Impacts, Risks, and Adaptation in the United States: Fourth National Climate Assessment, Volume II*.

Reman, B. C. G. (2018). Ph.D. dissertation, University of Warwick.

Reman, B. C. G. et al. (2019). "Interpreting observations of ion cyclotron emission from large helical device plasmas with beam-injected ion populations". *Nuclear Fusion* **59**(9), p. 096013.

Reman, B. C. G. et al. (2022). "First observation and interpretation of spontaneous collective radiation from fusion-born ions in a stellarator plasma". *Plasma Physics and Controlled Fusion* **64**(8), p. 085008.

Rivero-Rodriguez, J. F. et al. (2018). "A rotary and reciprocating scintillator based fast-ion loss detector for the MAST-U tokamak". *Review of Scientific Instruments* **89**(10), p. 10I112.

Rivero-Rodriguez, J. F. et al. (2019). "A fast model to resolve the velocity-space of fast-ion losses detected in ASDEX Upgrade and MAST Upgrade". *Journal of Instrumentation* **14**(9), p. C09015.

Rodriguez-Ramos, M. et al. (2017). "First absolute measurements of fast-ion losses in the ASDEX Upgrade tokamak". *Plasma Physics and Controlled Fusion* **59**(10), p. 105009.

Saito, K. et al. (2009). "Measurement of ion cyclotron emissions by use of ICRF heating antennas in LHD". *Fusion Engineering and Design* **84**(7-11), pp. 1676–1679.

Saito, K. et al. (2013). "Measurement of ion cyclotron emissions by using high-frequency magnetic probes in the LHD". *Plasma Science and Technology* **15**(3), pp. 209–212.

Salewski, M., B. Geiger, A. Jacobsen, et al. (2018). "Deuterium temperature, drift velocity, and density measurements in non-Maxwellian plasmas at ASDEX Upgrade". *Nuclear Fusion* **58**(3), p. 036017.

Salewski, M., M. Nocente, A. Jacobsen, F. Binda, C. Cazzaniga, et al. (2018). "Bayesian Integrated Data Analysis of Fast-Ion Measurements by Velocity-Space Tomography". *Fusion Science and Technology* **74**(1-2), pp. 23–36.

Salewski, M., M. Nocente, B. Madsen, et al. (2018). "Alpha-particle velocity-space diagnostic in ITER". *Nuclear Fusion* **58**(9), p. 096019.

Salewski, M. (2019). "Fast-ion diagnostic in fusion plasmas by velocity-space tomography".

— (2022). *Lecture notes for 10400 Plasma Physics*. Technical University of Denmark.

Salewski, M., B. Geiger, A. Jacobsen, et al. (2016). "High-definition velocity-space tomography of fast-ion dynamics". *Nuclear Fusion* **56**(10), p. 106024.

Salewski, M., B. Geiger, A. S. Jacobsen, et al. (2014). "Measurement of a 2D fast-ion velocity distribution function by tomographic inversion of fast-ion D-alpha spectra". *Nuclear Fusion* **54**(2), p. 023005.

Salewski, M., B. Geiger, D. Moseev, et al. (2014). "On velocity-space sensitivity of fast-ion D-alpha spectroscopy". *Plasma Physics and Controlled Fusion* **56**(10), p. 105005.

Salewski, M., B. Geiger, et al. (2015). "Doppler tomography in fusion plasmas and astrophysics". *Plasma Physics and Controlled Fusion* **57**(1), p. 014021.

Salewski, M., M. Nocente, G. Gorini, et al. (2015). "Velocity-space observation regions of high-resolution two-step reaction gamma-ray spectroscopy". *Nuclear Fusion* **55**(9), p. 093029.

Salewski, M., M. Nocente, G. Gorini, et al. (2016). "Fast-ion energy resolution by one-step reaction gamma-ray spectrometry". *Nuclear Fusion* **56**(4), p. 046009.

Salewski, M. et al. (2011). "On velocity space interrogation regions of fast-ion collective Thomson scattering at ITER". *Nuclear Fusion* **51**(8), p. 083014.

Salewski, M. et al. (2012). "Tomography of fast-ion velocity-space distributions from synthetic CTS and FIDA measurements". *Nuclear Fusion* **52**(10), p. 103008.

Salewski, M. et al. (2013). "Combination of fast-ion diagnostics in velocity-space tomographies". *Nuclear Fusion* **53**(6), p. 063019.

Salewski, M. et al. (2017). "MeV-range velocity-space tomography from gamma-ray and neutron emission spectrometry measurements at JET". *Nuclear Fusion* **57**(5), p. 056001.

Sato, S. et al. (2010). "Observation of Ion Cyclotron Emission Owing to DD Fusion Product H Ions in JT-60U". *Plasma and Fusion Research* **5**, S2067 (4 pp.)

Schmidt, B. S. et al. (2021). "Determining 1D fast-ion velocity distribution functions from ion cyclotron emission data using deep neural networks". *Review of Scientific Instruments* **92**(5), p. 053528.

Schmidt, B. S. et al. (2023). "4D and 5D phase-space tomography using slowing-down physics regularization". *Nuclear Fusion* **63**(7), p. 076016. URL: https://dx.doi.org/10.1088/1741-4326/acd6a6.

Sisternes, F. J. de, J. D. Jenkins, and A. Botterud (2016). "The value of energy storage in decarbonizing the electricity sector". *Applied Energy* **175**, pp. 368–379.

Skilling, J. (1989). *Maximum Entropy and Bayesian Methods : Cambridge, England, 1988*. Ed. by J. Skilling. Springer.

Smith, L. N. (2017). "Cyclical learning rates for training neural networks". *Proceedings - 2017 Ieee Winter Conference on Applications of Computer Vision, Wacv 2017*, pp. 464–472.

SPC, S. P. C. (2023a). *SPC Wiki: TCV General Information*. https://spcwiki.epfl.ch/wiki/TCV_general_information. Accessed: 15-02-2023.

— (2023b). *SPC Wiki: Technical data*. https://www.epfl.ch/research/domains/swiss-plasma-center/research/tcv/research_tcv_tokamak/tcv-technical-data/. Accessed: 25-05-2023.

Spitzer, L. (1962). *Physics of fully ionized gases*. Interscience,

Sree Harsha, N. R. (2018). "The tightly bound nuclei in the liquid drop model". *European Journal of Physics* **39**(3), p. 035802.

Stagner, L. and W. W. Heidbrink (2017). "Action-angle formulation of generalized, orbit-based, fast-ion diagnostic weight functions". *Physics of Plasmas* **24**(9), p. 092505.

Stagner, L. et al. (2022). "Orbit tomography of energetic particle distribution functions". *Nuclear Fusion* **62**(2), p. 026033.

Stipani, L. (2021). "A Fast Ion Loss Detector for the TCV Tokamak".

Stix, T. H. (1972). "Heating of toroidal plasmas by neutral injection". *Plasma Physics* **14**(4), pp. 367–&.

Su, J. et al. (2021). "Reconstructions of velocity distributions from fast-ion D-alpha (FIDA) measurements on EAST". *Plasma Science and Technology* **23**(9), p. 095103.

Sumida, S. et al. (2018). "Study on ion cyclotron emission excited by DD fusion produced ions on JT-60U". *45th Eps Conference on Plasma Physics, Eps 2018* **2018-**, pp. 589–592.

Sumida, S. et al. (2021). "Identification of slow-wave ion cyclotron emission on JT-60U". *Nuclear Fusion* **61**(11), p. 116036.

Sumida, S. et al. (2017). "Comparison of dispersion model of magneto-acoustic cyclotron instability with experimental observation of3He ion cyclotron emission on JT-60U". *Journal of the Physical Society of Japan* **86**(12), p. 124501.

Sydora, R. D. (1999). "Low-noise electromagnetic and relativistic particle-in-cell plasma simulation models". *Journal of Computational and Applied Mathematics* **109**(1-2), pp. 243–259.

Team, G. (2023). *GISS Surface Temperature Analysis (GISTEMP), version 4*. https://data.giss.nasa.gov/gistemp/. NASA Goddard Institute for Space Studies. Accessed: 11-02-2023.

Thatipamula, S. G. et al. (2016). "Dynamic spectra of radio frequency bursts associated with edge-localized modes". *Plasma Physics and Controlled Fusion* **58**(6), p. 065003.

Thome, K. E. et al. (2018). "Radio frequency measurements of energetic-particle-driven emission using the ion cyclotron emission diagnostic on the DIII-D tokamak". *Review of Scientific Instruments* **89**(10), p. 10I102.

Thome, K. E. et al. (2019). "Central ion cyclotron emission in the DIII-D tokamak". *Nuclear Fusion* **59**(8), p. 086011.

Tibshirani, R. (1996). "Regression shrinkage and selection via the Lasso". *Journal of the Royal Statistical Society Series B-methodological* **58**(1), pp. 267–288.

Velicogna, I. et al. (2020). "Continuity of Ice Sheet Mass Loss in Greenland and Antarctica From the GRACE and GRACE Follow-On Missions". *Geophysical Research Letters* **47**(8), e2020GL087291.

Verdolini, E., F. Vona, and D. Popp (2018). "Bridging the gap: Do fast-reacting fossil technologies facilitate renewable energy diffusion?" *Energy Policy* **116**, pp. 242–256.

Veshchev, E. A. et al. (2009). "Fast Particle Loss-Cone Measurements by Angular Resolved Multi-Sightline Neutral Particle Analyzer (ARMS-NPA) in Large Helical Device (LHD)". *Journal of Plasma and Fusion Research SERIES* **8**, pp. 1084–1088.

Weiland, M. et al. (2016). "Enhancement of the FIDA diagnostic at ASDEX Upgrade for velocity space tomography". *Plasma Physics and Controlled Fusion* **58**(2), p. 025012.

Weiland, M. et al. (2017). "Phase-space resolved measurement of 2nd harmonic ion cyclotron heating using FIDA tomography at the ASDEX Upgrade tokamak: Paper". *Nuclear Fusion* **57**(11), p. 116058.

Wesson, J. (2004). *Tokamaks*. 3rd ed. Oxford University Press Inc., New York.

— (2011). *Tokamaks*. 4th ed. Oxford University Press Inc., New York.

Wittmann, F. M. (2019). *Learning rate finder for Keras*. `https://github.com/WittmannF/LRFinder`.

Zalzali, A. I. et al. (2021). "Simulations of ion cyclotron emission from DIII-D tokamak plasmas". *47th EPS Conference on Plasma Physics, EPS 2021* **2021-**, pp. 784–787.

Zhang, Y. et al. (2013). "Investigation of the slowing down of neutral beam-injected energetic ions in the HL-2A plasma with various environments".

Zweben, S. J. (1989). "Pitch angle resolved measurements of escaping charged fusion products in TFTR". *Nuclear Fusion* **29**(5), pp. 825–833.

Zweben, S. J. et al. (1990). "Loss of alpha-like MeV fusion products from TFTR". *Nuclear Fusion* **30**(8), pp. 1551–1574.

Index